Hybrid Digital-Analog Transmission Systems: Design and Evaluation

Von der Fakultät für Elektrotechnik und Informationstechnik
der Rheinisch-Westfälischen Technischen Hochschule Aachen
zur Erlangung des akademischen Grades eines Doktors
der Ingenieurwissenschaften genehmigte Dissertation

vorgelegt von

Diplom-Ingenieur

Matthias Rüngeler

aus Paderborn

Berichter: Universitätsprofessor Dr.-Ing. Peter Vary
Universitätsprofessorin Dr.-Ing. Anke Schmeink

Tag der mündlichen Prüfung: 30. März 2015

AACHENER BEITRÄGE ZU DIGITALEN NACHRICHTENSYSTEMEN

Herausgeber:

Prof. Dr.-Ing. Peter Vary
Institut für Nachrichtengeräte und Datenverarbeitung
Rheinisch-Westfälische Technische Hochschule Aachen
Muffeter Weg 3a
52074 Aachen
Tel.: 02 41-80 26 956
Fax: 02 41-80 22 186

Bibliografische Information der Deutschen Bibliothek
Die Deutsche Bibliothek verzeichnet diese Publikation in der Deutschen Nationalbibliografie; detaillierte bibliografische Daten sind im Internet über `http://dnb.ddb.de` abrufbar

1. Auflage Aachen:
Wissenschaftsverlag Mainz in Aachen
(Aachener Beiträge zu Digitalen Nachrichtensystemen, Band 40)
ISSN 1437-6768
ISBN 978-3-95886-034-6

Wissenschaftsverlag Mainz
Süsterfeldstr. 83, 52072 Aachen
Tel.: 02 41 / 2 39 48 oder 02 41 / 87 34 34
Fax: 02 41 / 87 55 77
www.verlag-mainz.de

Herstellung: Druckerei Mainz GmbH
Süsterfeldstr. 83, 52072 Aachen
Tel.: 02 41 / 87 34 34
Fax: 02 41 / 87 55 77
www.druckereimainz.de

Gedruckt auf chlorfrei gebleichtem Papier

D 82 (Diss. RWTH Aachen University, 2015)

To Bettina

Acknowledgments

This thesis was written during my time as research assistant at the *Institute of Communication Systems and Data Processing* (IND) at the *Rheinisch-Westfälische Technische Hochschule Aachen* (RWTH Aachen University). First, I would like to express my sincere gratitude to my supervisor Prof. Dr.-Ing. Peter Vary. His continuous support and interest, numerous ideas and suggestions as well as his outstanding ability to create an inspiring, co-operative, quality-driven working environment combined with a great amount of flexibility and friendliness makes time at the IND exceptional. I am also indebted to my co-supervisor Prof. Dr.-Ing. Anke Schmeink for showing her interest in my work. Furthermore, I would like to thank my current and former colleagues at the IND for providing a very enjoyable working atmosphere, for fruitful discussions and collaboration, as well as very valuable proof readings. Thank you, Andreas Heitzig, Andreas Welbers, Annika Böttcher, Aulis Telle, Bastian Sauert, Benedikt Eschbach, Bernd Geiser, Birgit Schotsch, Christiane Antweiler, Christoph Nelke, Daniel Haupt, Florian Heese, Hauke Krüger, Heiner Löllmann, Helge Lüders, Kim Nguyen, Laurent Schmalen, Magnus Schäfer, Marc Adrat, Marco Jeub, Markus Niermann, Matthias Pawig, Max Mascheraux, Meik Dörpinghaus, Moritz Beermann, Roswitha Fröhlich, Simone Sedgwick, Stefan Liebich, Sylvia Sieprath, Thomas Esch, Thomas Schlien, Tim Schmitz, and Tobias Breddermann. I would also like to express my appreciation to all the students who made significant contributions to my work.

I wish to thank my parents for giving me the fundament for everything: Love, exemplifying endurance while nourishing creativity and always providing the necessary support. Papa, I wish you could have lived to enjoy the fruits harvested in the last eleven years.

Finally, I wish to thank my wonderful wife Bettina for her caring love and encouragement, for founding a family with our son Andreas creating so many happy hours.

Aachen, 2015 Matthias Rüngeler

Abstract

During the last 25 years, most of the communication systems have been converted to purely digital technology, although the transmitted content mostly is analog by nature. The principal advantages of digital communication are compression by source encoding, bit error protection by channel coding and robust transmission over noisy channels by appropriate modulation. Digital systems are usually designed for worst case channel conditions. However, often the channel quality is much better, which is not reflected in an improved end-to-end transmission quality due to inevitable quantization noise produced by the source encoder.
In this thesis, the focus is set on systems which

- are not purely digital anymore,
- benefit from increasing channel qualities, and
- avoid the saturation effect using discrete-time, continuous-amplitude techniques.

In the first part, purely analog, i.e., discrete-time and continuous-amplitude transmission systems are considered – with linear or nonlinear components. Theoretical performance limits are discussed and a new rate-distortion upper bound is derived which can be evaluated semi-analytically. The performance of linear transmission systems is derived analytically while simulations assess several nonlinear systems including the famous *Archimedes spiral*. A new class of nonlinear discrete-time analog coding systems, i.e., the *Analog Modulo Block Codes* (AMBCs) is developed. One important observation is that nonlinear discrete-time, continuous-amplitude systems can be decomposed into a discrete and a continuous-amplitudes part. The considered systems exhibit a considerable gap to capacity but they all circumvent the saturation effect due to the continuous-amplitude components.
In the main part of the thesis, these findings are turned into a design principle. *Hybrid Digital-Analog* (HDA) transmission systems consist of separate digital and analog branches while each is constructed independently. By combining both worlds – digital and continuous-amplitude transmission – new concepts emerge which fuse their advantages: capacity achieving performance in the digital branch with a huge variety of conventional digital codes plus avoiding the saturation effect in the analog branch. The performance of HDA systems is assessed theoretically as well as by simulations. These *Hybrid Digital-Analog* (HDA) transmission systems outperform both purely digital and continuous-amplitude concepts. HDA transmission is an attractive solution for wireless systems such as microphones, loudspeakers or distributed sensors.

Contents

Chapter 1

Introduction

Not too long ago, wireless communication was purely analog. Radio, television, or telephony used *analog* transmission systems with continuous-amplitude processing to protect the content against channel noise. These analog transmission systems, such as AM or FM radio, relied on the available technology, featuring a transmission quality which improved gradually with increasing channel quality.

In 1948, Shannon [Sha48] split the transmitter into two logical units: the source and the channel encoder. The source encoder uses a model of the content, e.g., statistical properties of the source symbols, to generate a representation with as few bits as possible while in the channel encoder additional bits are introduced for the protection against channel noise. It has been shown that this separation principle may achieve the theoretical performance limits at the cost of an increased complexity and delay. This insight, combined with the rapid technological evolution of integrated circuits, was the essential basis for the "digital revolution" in communications. Since then, researchers and engineers have succeeded to build efficient *digital* communication systems such as digital audio broadcast (DAB), digital television (DVB) and mobile telephony (GSM, UMTS, UMTS LTE). High complex transmission schemes with long block lengths are utilized in order to achieve the performance bounds predicted by Shannon [BGT93, CFRU01, Cle06, Lüd10, Sch11, 3GP11]. These transmission schemes are the perfect choice for digital content such as text or data.

However, a lot of content, e.g., audio, video, or sensor data is analog by nature. The term "analog" is used for continuous-amplitude discrete-time variables or signals throughout this work. The signal analysis employed in the source encoder first extracts continuous-amplitude parameters. Then, they are quantized in a second step to yield a compact representation in bits. As a result, the quantizer limits the resolution of the reproduction in the receiver due to the inevitable quantization noise.

In a transmission system, depending on the available resources – transmission power, channel bandwidth, and channel quality – a compromise between the resolution of the quantization and the strength of the channel coding (error protection) has to be made. The transmission in a cellular communication system, for example, has to be designed such, that it covers also the "worst case" channel conditions

experienced at the cell edge. Thus, operating at the cell edge requires a strong channel coding while a low resolution in the source encoder is chosen. Closer to the cell center, the receiver experiences a better channel quality, but the resolution of the reproduction is limited due to the worst case design. Hence, the end-to-end transmission quality saturates.

One solution to this design conflict is the *Adaptive Multi Rate* (AMR) transmission concept [ETS98]. The transmitter obtains information about the current channel quality via feedback channel and reacts with a favorable compromise between quantization resolution and error protection. Unfortunately, the AMR concept is not applicable in scenarios when feedback is not available: several receivers (broadcast), fast changing channel conditions or too slow or delayed feedback, and transmitters which are unable to adapt to the current channel quality due to cost or complexity constraints.

For this reason, a new concept is sought which offers an alternative solution to the design conflict. The main questions are: How can discrete-time and continuous-amplitude content be transmitted using a non-adaptive transmitter while the end-to-end transmission quality improves with increasing channel quality? How can a modern transmission system be designed with the favorable properties that are inherent in analog transmission systems?

The transmission chain has to be rethought. The principle of a discrete-time representation of the band-limited signal and the separation of source and channel coding is maintained, but the representation in bits of the continuous-amplitude content is questioned. The source encoder is modified to output the undistorted continuous-amplitude model parameters, e.g., by omitting the final quantization step. These continuous-amplitude parameters or samples are then transmitted using systems which are especially designed for discrete-time, continuous-amplitude (analog) input. In this thesis, the focus is set on the design and evaluation of transmission systems for continuous-amplitude parameters.

As the first step, purely analog transmission systems are analyzed. These systems can be classified into linear and nonlinear systems. The performance of linear transmission is predicted analytically for the case of *Linear Analog Block Codes* (LABCs) [RSV09], while it is shown that these results also hold for any other linear analog system. One interesting special case is transmitting Gaussian source symbols with no additional redundancy [Gas02]. Here, capacity is achieved, but, as soon as it is deviated from this setup (especially when adding redundancy) linear analog systems show a poor performance.

Nonlinear systems promise better results specifically when adding redundancy, but their analysis is more cumbersome. Computer simulations are employed to quantify their performance. Considered nonlinear examples are *Companding Systems* and *Space Filling Curves* including the famous *Archimedes spiral* [FR06, HV06, RSV10a, HGFL11, BSGF13]. Based on the results of the investigation, a new class of nonlinear transmission systems combining the block coding concept of

LABCs and a modulo operation as the mandatory nonlinearity is proposed and analyzed: the *Analog Modulo Block Codes* (AMBCs) [SRV15].

All known purely analog transmission systems, including further examples in the literature, such as *Orthogonal Polynomials* [WSR09], *Shift Maps* [VC03], or *Chaotic Dynamical Systems* [CW98], have one disadvantage in common. They cannot operate even close to the theoretical limits since the design or the operation is either impossible or not feasible for long block lengths.

In consequence, a further approach has been introduced which combines digital and analog transmission in one single *hybrid* system. *Hybrid Digital-Analog* (HDA) transmission systems known in literature use numerical optimization for the design of all components [SPA02]. However, due to the tremendous complexity during design and even operation, again only small block lengths are feasible and the theoretical limits are out of reach.

In this thesis, a new design approach for HDA transmission is introduced, combining the advantages of both, the analog and the digital world. The insights and knowledge gained in the last decades to build capacity achieving digital transmission systems on the one side and continuous-amplitude processing circumventing the saturation effect even for non-adaptive transmitters on the other side are unified. These HDA transmission systems use conventional purely digital transmission and additionally transmit the quantization error using continuous-amplitude discrete-time means [RV13a, RV13b, RBV14, RV15].

In thorough assessments, the newly proposed design of HDA systems is compared to purely digital systems. In the performed theoretical derivations and computer simulations, the used resources – channel bandwidth, transmission power, and channel quality – are chosen to be the same for a fair comparison. It will be shown theoretically, that to any purely digital parameter transmission system, a superior HDA transmission system can be created. Corresponding constructive guidelines enable to design practical systems which prove their superiority in computer simulations. It is interesting to note, that the additional complexity to purely digital transmission is negligible.

The analysis of HDA systems leads to further very promising observations. For purely digital transmission systems not achieving capacity, e.g., due to complexity or delay constraints, the analog branch of the corresponding HDA system partially compensates the imperfectness of the digital branch leading to decodability at lower channel qualities. Furthermore, even the AMR systems can be enhanced incorporating the HDA transmission concept to transmit successfully at lower channel qualities.

Structure of the Thesis

In Chapter 2, the fundamentals of digital and analog transmission are reviewed. The differences and similarities between purely digital and analog transmission systems are detailed. Thereby, especially the effect of nonlinearities in analog

transmission systems to yield discrete-valued and continuous-amplitude dimensions and their necessity to achieve a good performance is described. Furthermore, the separation of source and channel coding is reviewed also for continuous-amplitude transmission.

Chapter 3 introduces several performance bounds to define the theoretical limits for digital, analog, and HDA transmission. The performance of purely linear transmission systems is derived and the *Optimum Performance Theoretically Attainable* (OPTA) [BT67] is stated for different channel models including HDA channels.

Rate-distortion theory is an integral component for the derivation of performance bounds. Here, a new rate-distortion upper bound with an innovative construction rule is proposed which provides an upper bound for the information rate at which a certain mean-square error distortion could be achieved by a source encoder for a given source distribution.

Additionally, the influence of the block length of a transmission system on the performance and the need for long block lengths is reviewed to motivate the use of HDA systems.

In Chapter 4, nonlinear analog transmission schemes are considered. The functionality of the simplest continuous-amplitude transmission systems, i.e., *Companding Systems* and *Space Filling Curves*, is to map usually just one source symbol to channel symbols using continuous-amplitude (non)-linear functions. Systems mapping just one source symbol to one channel symbol (1:1) or the famous Archimedes spiral which uses one additional redundant channel symbol per source symbol (1:2) are analyzed and further numerically optimized.

Chapter 5 combines the gained insights and proposes a new class of codes. Motivated by digital block codes, the performance of *Linear Analog Block Codes* (LABCs) has been assessed, but due to the lack of a nonlinearity only a very limited performance is achieved. Therefore, a new system using a real-valued matrix multiplication with an additional modulo operation as the nonlinearity is proposed and analyzed. Different decoders exploit the special structure of these *Analog Modulo Block Codes* (AMBCs) with their discrete-valued and continuous-amplitude dimensions.

In Chapter 6 the observation of the existence and necessity of discrete-valued and continuous-amplitude dimensions is turned into a design principle. One innovative concept is to enable the independent construction of the digital and the analog branch while the power and flexibility of digital transmission systems is exploited. The inherent quantization error is additionally transmitted using continuous-amplitude methods in the analog branch. Several receivers with different types of estimators, operating either independently in the digital and analog branch, or using joint estimation are proposed. The most powerful receivers, iterative source channel decoders are adapted to HDA to even exploit the analog branch as additional side information. The separation in HDA transmission into two branches

enables new degrees of freedom in the design such as unequal power distribution or adding redundancy in the analog branch.

The HDA systems are assessed both theoretically and via computer simulations under the same conditions for a fair comparison.

Chapter 7 describes an application example of HDA transmission systems including a source encoder. Correlated source symbols, which may emerge from, e.g., band-limited speech, audio, or video signals, are encoded using block transform coding to source parameters which are then transmitted using an HDA system. Also here, HDA transmission and purely digital transmission are compared while the source encoder in the HDA transmission system enables the transmission of undistorted model parameters.

At the end, in Chapter 8 the properties of several proposed transmission systems are compared. A special scenario is considered for which all systems including linear analog systems, nonlinear Archimedes spirals, AMBCs, and HDA systems may be parametrized. Here, the results and findings from the previous chapters are confirmed.

Parts of the results of this thesis have been prepublished in the following references: [RSV09, RSV10a, RSV10b, ERHV10a, ERHV10b, ERHV12, DRM12, RV13a, RV13b, RKBV13, RBV14, RV15, SRV15]. These references are marked by an underlined label throughout this thesis.

Chapter 2

Digital versus Analog Transmission

2.1 Introduction

In this chapter, first the generic transmission model and its system parameters are introduced. Then, light is shed on the basic principles and on the reasons why purely digital transmission works. Furthermore, the idea of discrete-time, continuous-amplitude (analog) transmission is described, what is actually meant by the term "analog" and which new aspects arise, such as the necessity of nonlinearities and the resulting "large" and "small" decoding errors when dealing with analog transmission systems. Following the insights on purely digital transmission, some design criteria for analog systems are derived and the relationship between both systems is briefly touched.

2.2 Transmission Model and System Parameters

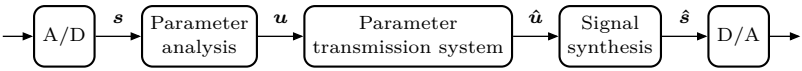

Figure 2.1: Transmission of source parameters $\boldsymbol{u}$ generated from source signal $\boldsymbol{s}$ by model based source coding.

Figure 2.1 shows a generic transmission system for continuous-amplitude, real world sampled source signals. First, the samples of the signal are converted using an analog to digital (A/D) block to enable analysis and encoding using digital signal processing. The last block in the transmission chain consists of a digital to analog (D/A) converter. Throughout this thesis, it is assumed that these A/D and D/A converters exhibit a sufficiently high precision so the quantization error introduced here can be neglected.

After conversion, the source signal $\boldsymbol{s}$, which could be an audio signal, video or sensor data is fed to a parameter analysis which uses a model of the content and extracts parameters which describe the signal as closely as possible. These parameters could be, e.g., Linear Predictive Coding (LPC) coefficients, samples of

the prediction error signal or block transform coefficients generated in video encoding. These continuous-amplitude and discrete-time parameters $\boldsymbol{u}$, which are also called "analog" parameters, are transmitted using a parameter transmission system and are then decoded as $\hat{\boldsymbol{u}}$ with potential distortions. A signal synthesis algorithm then reconstructs the signal $\hat{\boldsymbol{s}}$. In this thesis, the focus is set on improvements of the parameter transmission system. The specific type of signal and the employed signal model in the parameter analysis are not in focus since it is assumed that an improved transmission quality of the parameters leads to a refinement of the reconstruction of the signal $\hat{\boldsymbol{s}}$. With regard to reproducibility of the results, the parameters $\boldsymbol{u}$ are described using random variables which are *independent identically distributed* (i.i.d.) or, as in Chapter 7, a correlated Gauss-Markoff source is employed.

The performance of the whole transmission system is measured in the end-to-end symbol *Signal to Noise Ratio* (SNR) which is the ratio between the energy[1] of the source symbols and the *Mean-Square Error* (MSE) between the source symbols $\boldsymbol{s}$ and the estimated symbols $\hat{\boldsymbol{s}}$:

$$\mathrm{sSNR} = \frac{\mathrm{E}\left\{\|\boldsymbol{s}\|^2\right\}}{\mathrm{E}\left\{\|\boldsymbol{s}-\hat{\boldsymbol{s}}\|^2\right\}}. \tag{2.1}$$

The performance of the transmission of the parameters generated by the parameter analysis are measured in the end-to-end parameter SNR. This is the ratio between the energy of the source symbols and the MSE between the source symbols $\boldsymbol{u}$ and the estimated symbols $\hat{\boldsymbol{u}}$:

$$\mathrm{pSNR} = \frac{\mathrm{E}\left\{\|\boldsymbol{u}\|^2\right\}}{\mathrm{E}\left\{\|\boldsymbol{u}-\hat{\boldsymbol{u}}\|^2\right\}}. \tag{2.2}$$

The pSNR[2] measures the performance of the parameter transmission system in Figure 2.1 and is the usually applied figure of merit in this thesis. If a parameter analysis outputs several types of continuous-amplitude parameters, e.g., LPC coefficients and samples of the prediction error signal, an individual pSNR for each type could be of interest for assessment. In this thesis, just one type of parameter and hence just one type of pSNR is considered.

Although, the continuous-amplitude discrete-time parameters $\boldsymbol{u}$ which are transmitted by the parameter transmission system are not the real world source symbols originally processed by the parameter analysis, $\boldsymbol{u}$ will be denoted "source

[1] The average power of one source symbol s is denoted $\sigma_s^2 = \mathrm{E}\{s^2\}$. The expectation of the vector norm of $\boldsymbol{s}$ integrates over the average power of each symbol with the duration T. Thus, with the length $\ell_{\boldsymbol{s}}$ of the vector $\boldsymbol{s}$, $\mathrm{E}\{\|\boldsymbol{s}\|^2\} = \sigma_s^2 \cdot \ell_{\boldsymbol{s}} \cdot T$ denotes the average energy of the vector $\boldsymbol{s}$. Therefore, fractions of average energies of vectors of equal lengths equal fractions of their powers. As common in signal processing, the symbol duration is normalized to unity ($T = 1$) in this work.

[2] In image processing an alike SNR is used. The Peak SNR (PSNR) is defined differently and therefore, to avoid confusion, here the "p" is written in lower case.

symbols" in the following and the parameter transmission system "transmission system" for simplicity.

The usually considered baseband model of the general transmission system is depicted in Figure 2.2.

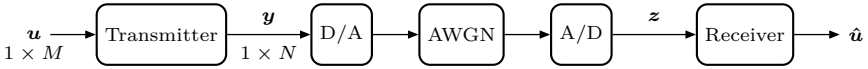

Figure 2.2: Baseband model of general parameter transmission system.

The source symbols u follow the *probability density function* (pdf) $\mathrm{p}(u)$ and are combined to M-dimensional source vectors $\boldsymbol{u}$.

A transmitter which may use purely digital operations or also continuous-amplitude functions transforms the source vector to a channel vector $\boldsymbol{y}$ with N dimensions. The dimension N of $\boldsymbol{y}$ also describes the number of *channel uses* which are needed for transmission. The elements of the channel vector $\boldsymbol{y}$ may have a discrete or continuous-amplitude nature, depending on the concepts used in the transmitter. The overall rate of the transmitter is denoted by

$$r = \frac{M}{N}. \tag{2.3}$$

Before sending the channel symbols $\boldsymbol{y}$ over the *Additive White Gaussian Noise* (AWGN) channel, the symbols are converted using a D/A block. An A/D block digitizes the samples received from the AWGN channel. Again, is it assumed that these convertors exhibit a sufficiently high precision, so the quantization error introduced here can be neglected.

In the AWGN channel, the symbols are disturbed by additive Gaussian noise $\boldsymbol{n}$ and received as $\boldsymbol{z}$:

$$\boldsymbol{z} = \boldsymbol{y} + \boldsymbol{n}. \tag{2.4}$$

A receiver generates an estimate $\hat{\boldsymbol{u}}$ of the source symbols.

The influence of signaling, matched filtering and sampling need not to be considered here. Transmission with matched filtering, no intersymbol interference and a minimum bandwidth ideal rectangle shape in the spectrum are assumed. All signals are represented by vectors in the real baseband.

The channel quality can be expressed as the channel SNR (cSNR) which relates the average energy of the channel vector to the average energy of the noise vector:

$$\mathrm{cSNR} = \frac{\mathrm{E}\left\{\|\boldsymbol{y}\|^2\right\}}{\mathrm{E}\left\{\|\boldsymbol{n}\|^2\right\}}. \tag{2.5}$$

In case of the above assumptions (matched filtering, no intersymbol interference and a minimum bandwidth ideal rectangle spectrum), the very popular channel quality measure E_s/N_0 is equivalent to the above defined cSNR:

$$E_s/N_0 = \text{cSNR}. \tag{2.6}$$

The E_s/N_0 relates the transmitted transmission energy of the channel symbols to N_0 which is twice the noise power spectral density $N_0/2$ on the channel. To enable a fair comparison of the performance of digital transmission systems with different code rates and different modulation schemes, another channel quality measure is frequently used. The E_b/N_0 relates the transmission energy which is spent per source bit to N_0. Using the spectral efficiency ρ, the E_b/N_0 and the E_s/N_0 measure are connected as follows:

$$E_b/N_0 \ = E_s/N_0 \cdot \frac{1}{\rho}. \tag{2.7}$$

The spectral efficiency ρ describes the number of bits which are transmitted per channel symbol, while it is assumed that the system is designed such, that they can also be decoded successfully.

In the context of continuous-amplitude source symbols, the overall rate $r = \frac{M}{N}$ (2.3) denotes the number of source symbols which are transmitted per channel symbol. Thus, r is the continuous-amplitude equivalent of the spectral efficiency ρ. Inspired by (2.7), a similar measure is used for continuous-amplitude source symbols: The E_u/N_0 relates the transmission energy per source symbol to twice the the noise power spectral density $N_0/2$:

$$E_u/N_0 = E_s/N_0 \cdot \frac{1}{r} = E_s/N_0 \cdot \frac{N}{M}. \tag{2.8}$$

With (2.6) it holds:

$$E_u/N_0 = \text{cSNR} \cdot \frac{1}{r} = \text{cSNR} \cdot \frac{N}{M}. \tag{2.9}$$

In Figure 2.2 only real-valued (and not complex-valued) variables are used. This approach is motivated by its simplicity and the correspondence to a baseband transmission system which just allows real-valued channel symbols. Complex modulation schemes such as *Quadrature Phase Shift Keying* (QPSK) which are employed in the complex baseband when describing band-pass transmission are also included in the above model: The real and the imaginary part of the complex symbol are interpreted as two real symbols which are concatenated in the real valued channel vector.

2.3 Purely Digital Transmission

Conventional purely digital transmission systems whose aim is the transmission of bits and not continuous-amplitude values, usually consist of a concatenation of

digital channel coding and digital modulation. The m-dimensional information words are encoded to n-dimensional code words which are then mapped by digital modulation to N-dimensional channel vectors. The n-dimensional coding space allows for 2^n different points while only $2^m < 2^n$ points are selected as valid code words, each code word corresponding to one information word. The digital modulation then maps groups of the encoded bits to constellation points forming the channel symbols. These channel symbols compose the channel vector. This vector describes one point in the N-dimensional channel space which corresponds to one valid code word in the n-dimensional coding space and to one m-dimensional information word. Not all possible points in the channel space are valid, just a points given by the structure of the digital channel code are sent.

An AWGN channel disturbs the channel symbols, shifting each sent symbol in each dimension by a random distance. To eliminate the effect of the noise, the decoder at the receiver assigns the received vector to the nearest valid point in the N-dimensional channel space. The region, from which received vectors are assigned to one valid point, is called "Voronoi region". A decoding error occurs, if the Euclidean length of the disturbing noise vector is large enough to reach a neighboring Voronoi region.

To minimize decoding errors, the pairs of valid points in the N-dimensional channel space should exhibit a maximum Euclidean distances. However, the (squared) distance of one valid point to the origin directly corresponds to the transmission power which on the other hand shall be minimized. The optimum solution in this conflict of objectives is positioning valid points such that the minimum distance between any pair of points is maximum. This leads to similar error probabilities for valid point and to Voronoi regions which approximate hyperspheres to fill the channel space as densely as possible. Interestingly, the higher the channel dimension N, the closer is the approximation of the Voronoi region to a hypersphere. This effect is described by the sphere packing bound (Section 3.6).

This way the word error rate, i.e., the probability of decoding errors between valid points can be minimized. The bit error rate can additionally be minimized when neighboring valid points correspond to information bit vectors which differ just in very few bit positions. Thus a "neighborhood" relation which the information bit vectors exhibit (two vectors are neighbors if they have a small Hamming distance) shall be preserved in the channel space, so the corresponding valid points are still neighbors (now in terms of Euclidean distance).

In total, a purely digital transmission system with digital channel coding and digital modulation can be understood as a direct mapping of m-dimensional information bit vectors via n-dimensional code words after channel encoding to valid points after modulation in the N-dimensional channel space.

2.4 Nonlinear Analog Transmission and Hybrid Digital-Analog Transmission

2.4.1 What is "Analog"?

Throughout this work, the term "analog" is used for continuous-amplitude discrete-time variables.

Although, the ideas and the design of the analog and hybrid transmission systems are driven by the idea of truly continuous-amplitude variables, in practice, all operations and analog functions are conducted using digital signal processing. It is assumed that the resolution of the necessary A/D and D/A conversion is sufficiently high, so the introduced quantization error can be neglected.

2.4.2 The Necessity and Effects of Nonlinearities

To achieve a pSNR which is significantly greater than the channel noise cSNR, more than one channel use per source symbol ($N > M \Leftrightarrow r < 1$) has to be employed (Section 3.4). The transmission of one source symbol by several channel uses can, e.g., be facilitated employing linear methods, i.e., continuous-amplitude linear operations such as sums and multiplications with constants. Linearity is given when encoding $\boldsymbol{u}_1$ and $\boldsymbol{u}_2$ leads to $\boldsymbol{y}_1$ and $\boldsymbol{y}_2$, respectively, encoding the sum $\boldsymbol{u}_3 = \boldsymbol{u}_1 + \boldsymbol{u}_2$ yields the sum $\boldsymbol{y}_3 = \boldsymbol{y}_1 + \boldsymbol{y}_2$. The simplest solution for a linear system is a repetition code which transmits the (normalized) source symbol u by 2 channel uses y_1 and y_2. The maximum performance achievable with linear operations is derived in Section 3.2. Regarding the cSNR, doubling the number of channel uses improves the performance in terms of pSNR by 3 dB. For linear systems, no gain is achievable at all by additional channel uses if the channel quality measure $\mathrm{E_u/N_0}$ is considered for a fair comparison between systems with different rates r.

However, the *Optimum Performance Theoretically Attainable* (OPTA) predicts a possible gain in cSNR which rises exponentially with the number of channel uses (3.49). Thus, nonlinear processing may be the solution to go beyond the linear processing performance and reach the theoretical performance limits, e.g., [FR06].

Comparable to digital transmission systems, analog transmission systems can also be characterized by valid code words which are transmitted as channel symbols. Due to the continuous-amplitude nature of the source symbols, there are infinitely many different channel symbols, which still form a pattern in the channel space. In Figure 2.3 several analog modulation schemes are depicted which encode scalar ($M = 1$) uniformly distributed source symbols as $N = 2$ channel symbols (y_1 and y_2). The range of the source symbols is $-1 < u < 1$ and the average power of the channel symbols is $\mathrm{E}\left\{\|\boldsymbol{y}\|^2\right\}/N = 1$. The correspondence of a selection of channel symbols to their source values is depicted in the figures.

One example of a *linear* analog modulation scheme is shown in Figure 2.3a. A linear system always comprises just one (flat) hyperplane such as, e.g., the straight

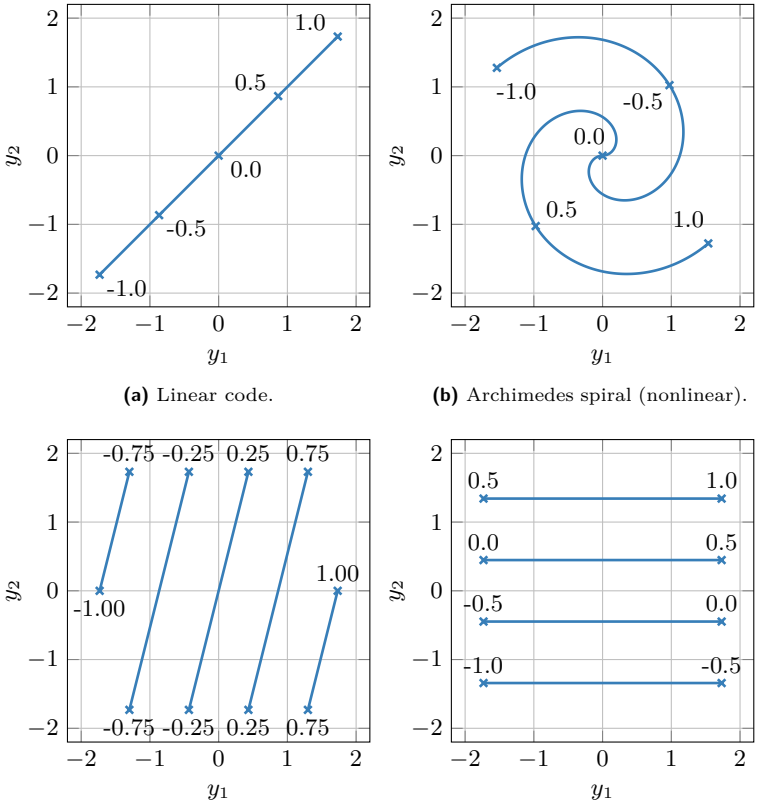

(a) Linear code.

(b) Archimedes spiral (nonlinear).

(c) *Analog Modulo Block Code* (AMBC) (nonlinear).

(d) *Hybrid Digital-Analog* (HDA) transmission (nonlinear).

Figure 2.3: Different analog modulation schemes and their channel symbols. All schemes encode $M = 1$ analog source symbol with $-1 < u < 1$ forming 2-dimensional ($N = 2$) channel symbols with $\mathrm{E}\left\{\|\boldsymbol{y}\|^2\right\}/N = 1$.

line (or arm) in the 1-dimensional ($M = 1$) case. In a nonlinear system, this one (flat) hyperplane could, e.g., either be not flat anymore but bent or curved, and/or the hyperplane could be split up into several hyperplanes.

One example of a *nonlinear* analog modulation scheme are space filling curves (Chapter 4) which could be designed using, e.g., Archimedes spirals. Here, the line is rolled up to a spiral yielding several spiral arms (Figure 2.3b).

In Chapter 5 a different class of analog codes, the *Analog Modulo Block Codes* (AMBCs), are examined while one example is shown in Figure 2.3c. The arm is still straight, but it is cut into shorter segments which are arranged in parallel and tilted with respect to the coordinate axis.

Other candidates are *Hybrid Digital-Analog* (HDA) systems as described in Chapter 6. The straight arm is cut into segments and arranged in parallel, but here all segments have the same length and they are in parallel to the coordinate axis (Figure 2.3d).

A common feature of all shown nonlinear modulation schemes is that for a constant transmission power, the length of the arm is increased compared to a linear system. Furthermore, the neighborhood relationship of the source symbols is preserved on the channel. A performance comparison of these analog modulation schemes is given in Section 8.3.

2.4.3 Small and Large Errors – Analog and Discrete Directions

In nonlinear analog transmission systems, two types of decoding errors can be observed. This is illustrated in Figure 2.4. An *Analog Modulo Block Code* (AMBC) may encode the source symbol $u = 0.9$ to $\boldsymbol{y}(u = 0.9)$. Two examples of noise vectors $\boldsymbol{n}_1$ and $\boldsymbol{n}_2$ with the same length but different direction disturb the channel symbol and lead to received symbols which are decoded by a *Maximum Likelihood* (ML) decoder. The decoder splits the noise vector into two orthogonal components. One components is in parallel to the hyperplane (i.e., the arm) and another components is orthogonal to the hyperplane. As long as the orthogonal components of the noise (as in case of $\boldsymbol{n}_1$) is small enough not to cross the decision border between two neighboring arms, the decoder can eliminate the influence of the orthogonal components of the noise vector. This results in a decoded symbol whose corresponding channel symbol $\hat{\boldsymbol{y}}(\hat{u}_1)$ is on the correct hyperplane. If the received symbol is across the decision border to a neighboring arm, e.g., at half the distance for ML decoding (as in case of $\boldsymbol{n}_2$), the decoder chooses a point ($\hat{\boldsymbol{y}}(\hat{u}_2)$) on the neighboring arm as the estimate of the received symbol. In the example in Figure 2.4, the estimated symbol is $\hat{u}_2 = 0.4$ whose error to the original source symbol is much higher than for $\hat{u}_1 = 0.96$. The corresponding source symbol on the neighboring arm significantly differs in terms of MSE from the sent source symbol, hence, a "large" decoding error occurs. This error is sometimes also called "threshold" error, since it dominates the overall performance at just below a certain channel quality [Tim70]. The parallel components of the noise vector result in an

estimated symbol which is just along the arm. The neighborhood relationship of the symbols on the arm leads to a "small" decoding error in terms of MSE.

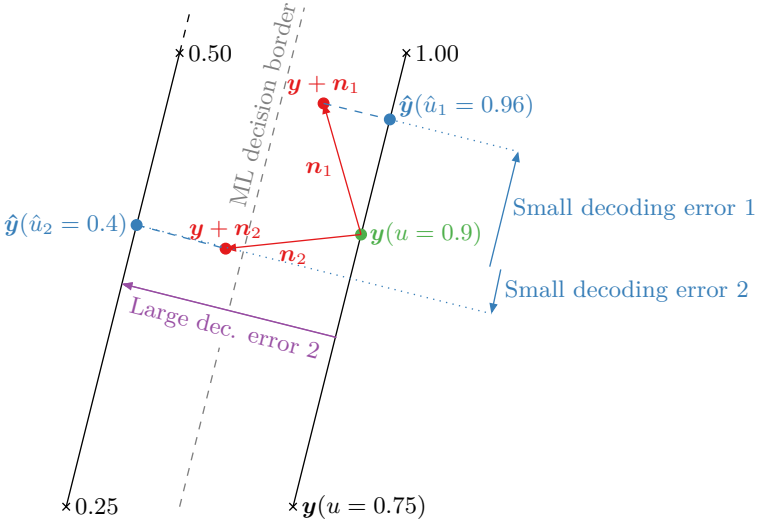

Figure 2.4: Different types of errors. The AMBC in Figure 2.3c is used.

The direction of the components orthogonal to the hyperplane can be called "discrete" direction and the direction which is in parallel to the hyperplanes "analog" direction. The choice of the discrete and analog direction depends on the nonlinearity of the analog transmission system. In systems which exhibit parallel hyperplanes (e.g., Figures 2.3c and 2.3d), the discrete direction is always the same for all channel symbols. This does not hold for other analog transmission systems such as, e.g., the Archimedes spiral (Figure 2.3b). Since here the arms are bent, the direction which is in parallel or orthogonal to the arms is different for each channel symbol.

Even though all entries of the channel vector are analog and exhibit continuous amplitudes, there are still the discrete dimensions, in which only discrete values occur. This leads to an interesting observation: A nonlinear analog transmission system (with $N > M$) always comprises discrete dimensions! This observation answers the open question posed, e.g., in [Rez03], why a system with N continuous-amplitude channel symbols and nonlinearities does not achieve the expected performance.

The number of discrete dimensions of a transmission system can be derived as follows. For systems with parallel hyperplanes, the channel space could be rotated, such that the hyperplanes are in parallel to M coordinate axes. Thus M vector entries are needed to represent the analog direction and hence $N-M$ entries remain for the discrete directions which are orthogonal to the hyperplanes. It follows that if a nonlinear analog transmission system transmits M-dimensional source vectors

over an N-dimensional channel, $N - M$ channel symbols are discrete. For systems without parallel hyperplanes (e.g., the Archimedes spiral), the same observation can be made. However, here, the angle of the rotation to align the analog direction with the coordinate axis is dependent on the considered channel symbol (Figure 2.3b).

Another conclusion is that since any nonlinear analog transmission system with more channel uses (N) than source dimensions (M) exhibits discrete and analog directions, this property may directly be used as a design principle as shown in Chapter 6.

2.4.4 Design Criteria

In the design process of nonlinear analog transmission systems, two main criteria have to be considered: On the one hand, the stretching effect, i.e., the area of the hyperplane (i.e., the length of the line for $M = 1$) should be as large as possible to combat the components of the channel noise which are parallel to the hyperplanes. The size of the area of the hyperplanes is also responsible for the performance of the transmission system at such a high channel quality, that ambiguity about the hyperplane during decoding improbable [FR06] (e.g., Section 5.3.4 for *Linear Analog Block Codes* (LABCs)). On the other hand, the Euclidean distance between the hyperplanes should be as large as possible to eliminate the influence of the large errors resulting from the components of the channel noise orthogonal to the hyperplanes. Furthermore, the transmission power should be as low as possible.

It is not obvious how to find the optimal compromise between these requirements. Since in the previous section, the observation is made that a nonlinear analog transmission system can be described in terms of discrete and analog dimensions, the design criteria from purely digital transmission systems (Section 2.3) can be used for the digital dimensions: As many points as possible should be positioned as such that the minimum distance between any pair of points is maximum while exhibiting a low transmission power. In the analog dimensions a large hypersphere is desired, also with a low transmission power. These insights are used in the design of *Hybrid Digital-Analog* (HDA) codes in Chapter 6.

Chapter 3

Performance Bounds

3.1 Introduction

Theoretical performance bounds are useful to assess the performance of practical transmission systems in order to evaluate the potential of further improvement.

First, in Section 3.2, the performance of linear analog transmission systems is analytically derived. One candidate, the *Linear Analog Block Codes* (LABCs) is analyzed for different estimators, namely the *Maximum Likelihood* (ML) and the *Linear Minimum Mean-Square Error* (LMMSE) estimator.

To assess the performance of a source encoder, the rate-distortion function is a widely used instrument. A source encoder always strives to use as few bits as possible to find a description of the content with the smallest possible distortion. The rate-distortion function gives the minimum rate (bits/symbol) necessary to describe source symbols with a given *probability density function* (pdf) and a given distortion (usually the mean-square error distortion). Well known rate-distortion functions and a new approach for a rate-distortion bound (Section 3.3.3) are described in Section 3.3.

The *Optimum Performance Theoretically Attainable* (OPTA) combines the concept of the rate-distortion function with the transmission over a channel. OPTA gives the minimum distortion for the transmission of source symbols with a given pdf using multiple or partial channel uses of a specific transmission channel with a certain channel quality. In Section 3.4 this bound is evaluated for the *Additive White Gaussian Noise* (AWGN) channel, the *Binary Symmetric Channel* (BSC) for bipolar hard decision transmission, the *Binary-Input Additive White Gaussian Noise* (BIAWGN) channel for bipolar soft decision transmission and combinations of these channels to model *Hybrid Digital-Analog* (HDA) transmission channels.

The different variants of OPTA and the performance of LABCs are compared in Section 3.5.

Usually, the performance of a transmission system is influenced by its coding rate and its block length, i.e., the number of channel uses which are considered at once. In Section 3.6 the idea of the *Sphere Packing Bound* (SPB) is briefly reviewed and the general influence of finite block lengths is evaluated.

3.2 Linear Analog Codes

Linear analog codes only employ continuous-amplitude linear operations such as sums of source vector entries and multiplications with constants. All linear analog codes can be described by matrix multiplications at the transmitter and at the receiver. The source vector $\boldsymbol{u}$ with dimension[1] $M \times 1$ is multiplied with the encoding matrix $\boldsymbol{P}$ with dimension $N \times M$. The decoding of the received vector $\boldsymbol{z}$ is conducted by a multiplication with $\boldsymbol{Q}$ with dimension $M \times N$. This coding scheme is called *Linear Analog Block Code* (LABC) with the following encoding, transmission and decoding relations:

$$\boldsymbol{y} = \boldsymbol{P} \cdot \boldsymbol{u}, \tag{3.1}$$

$$\boldsymbol{z} = \boldsymbol{y} + \boldsymbol{n}, \tag{3.2}$$

$$\hat{\boldsymbol{u}} = \boldsymbol{Q} \cdot \boldsymbol{z}. \tag{3.3}$$

To facilitate the following analysis, an arbitrary, but fixed energy constraint is imposed. After multiplication with $\boldsymbol{P}$, the total energy of the zero mean channel input vector $\boldsymbol{y}$ shall be the same as of the zero mean source vector $\boldsymbol{u}$:

$$\mathrm{E}\left\{\|\boldsymbol{u}\|^2\right\} = \mathrm{E}\left\{\boldsymbol{u}^{\mathrm{T}} \cdot \boldsymbol{u}\right\} = M \cdot \sigma_u^2 = N \cdot \sigma_y^2 = \mathrm{E}\left\{\boldsymbol{y}^{\mathrm{T}} \cdot \boldsymbol{y}\right\} = \mathrm{E}\left\{\|\boldsymbol{y}\|^2\right\}. \tag{3.4}$$

To normalize an arbitrary given matrix $\boldsymbol{P}'$ to meet (3.4), a scalar factor α is used

$$\boldsymbol{P} = \alpha \cdot \boldsymbol{P}', \tag{3.5}$$

which is calculated as follows:

$$\begin{aligned}
& \mathrm{E}\left\{\boldsymbol{u}^{\mathrm{T}} \cdot \boldsymbol{u}\right\} = \mathrm{E}\left\{\boldsymbol{y}^{\mathrm{T}} \cdot \boldsymbol{y}\right\} \\
\Leftrightarrow \quad & M \cdot \sigma_u^2 = \mathrm{E}\left\{\alpha^2 \cdot \boldsymbol{u}^{\mathrm{T}} \cdot \boldsymbol{P}'^{\mathrm{T}} \cdot \boldsymbol{P}' \cdot \boldsymbol{u}\right\} \\
\Leftrightarrow \quad & M \cdot \sigma_u^2 = \alpha^2 \cdot \mathrm{E}\left\{\boldsymbol{P}'^{\mathrm{T}} \cdot \boldsymbol{P}'\right\} \cdot \sigma_u^2 \\
\Leftrightarrow \quad & \alpha = \sqrt{\frac{M}{\mathrm{trace}\left(\boldsymbol{P}'^{\mathrm{T}} \cdot \boldsymbol{P}'\right)}}.
\end{aligned} \tag{3.6}$$

Using this normalization, the following relationships w.r.t. the matrix $\boldsymbol{P}$ and the cSNR hold:

$$\mathrm{trace}\left(\boldsymbol{P}^{\mathrm{T}} \cdot \boldsymbol{P}\right) = M, \tag{3.7}$$

$$\mathrm{cSNR} = \frac{\sigma_y^2}{\sigma_n^2} = \frac{M \cdot \sigma_u^2}{N \cdot \sigma_n^2}. \tag{3.8}$$

[1] In this dissertation, usually row vectors are used, but in Section 3.2, column vectors are employed to conform with the formulas in [RSV09].

3.2.1 Maximum Likelihood Estimator

The properties and performance bounds of LABCs for an arbitrary choice of $\boldsymbol{P}$ and a *Maximum Likelihood* (ML) decoder are derived in, e.g., [RSV09]. For Gaussian additive noise, a *Least Squares* (LS) estimator is also the ML decoder [Kay93]. Thus, it suffices to use the pseudo inverse of $\boldsymbol{P}$ as the decoder matrix $\boldsymbol{Q}$, since this is the LS optimal solution. Additionally, since no probabilistic assumptions about the data (and the noise) can be made, the estimator is independent of the channel quality. The decoding matrix is defined as follows:

$$\boldsymbol{Q} = (\boldsymbol{P}^{\mathrm{T}} \cdot \boldsymbol{P})^{-1} \cdot \boldsymbol{P}^{\mathrm{T}}, \tag{3.9}$$

and the end-to-end pSNR of the system can be calculated in dependency of the encoding matrix [RSV09]:

$$\mathrm{pSNR}_{\mathrm{LABC,ML}} = \mathrm{cSNR} \cdot \frac{1}{\frac{1}{M}\sum_{i=1}^{M} \frac{1}{\gamma_i}} \cdot \frac{N}{M} \qquad , \gamma_i = \left|\mathrm{eig}(\boldsymbol{P}^{\mathrm{T}} \cdot \boldsymbol{P}, i)\right|. \tag{3.10}$$

To achieve the maximum performance by choosing the best $\boldsymbol{P}$, Lagrange optimization is conducted [RSV09], leading to the result that all eigenvalues γ_i should be 1: $\gamma_i = \left|\mathrm{eig}(\boldsymbol{P}^{\mathrm{T}} \cdot \boldsymbol{P}, i)\right| = 1$. This is given, e.g., for the identity matrix with padded zeros, a repetition code or a Hadamard matrix. The maximum performance achievable with LABCs, thus, is:

$$\begin{aligned} \mathrm{pSNR}_{\mathrm{LABC,ML,max}} &= \mathrm{cSNR} \cdot \frac{N}{M} && (3.11) \\ &= \mathrm{cSNR} \cdot \frac{1}{r} \\ &\overset{(2.9)}{=} \mathrm{E_u/N_0}. && (3.12) \end{aligned}$$

Equation (3.11) supposes that for a constant cSNR, the performance is increased with a rising N/M. Doubling the number of channel uses per source symbol yields a gain of 3 dB in terms of pSNR. The same gain of 3 dB could be achieved, if the transmission energy could be doubled, thus, increasing the channel quality by 3 dB.

This effect is incorporated in the $\mathrm{E_u/N_0}$ channel quality measure[2] (Section 2.2) which allows a fair comparison of systems with different rates. Then, (3.12) shows, that independently of the rate r, the performance in terms of pSNR just depends on the channel quality. Therefore, for a given noise power spectral density $\mathrm{N_0}/2$ on the channel, and a fixed transmission energy per source symbol, the performance does not increase if the rate r is lowered. Thus, in case of LABCs, coding and hence employing more channel uses and energy is not favorable to just increasing the transmission energy. In total, with LABCs and considering the $\mathrm{E_u/N_0}$ measure, the performance is the same for a system transmitting the source symbol just once without more channel uses or repetitively transmitting the source symbol with more channel uses.

[2] Here, the definition of $\mathrm{E_u/N_0}$ is by 3 dB different to [RSV09, Rü09]

3.2.2 Linear Minimum Mean-Square Error Estimator

An *Linear Minimum Mean-Square Error* (LMMSE) estimator employs only linear operations using first and second order statistics of the data and the noise to yield a minimum mean-square error. For a linear transmission model, Gaussian source symbols and Gaussian additive noise, the LMMSE estimator yields the same performance as an *Minimum Mean-Square Error* (MMSE) estimator [Kay93]. The LMMSE estimator is also known as the Wiener filter.

For zero mean source and noise symbols and for a certain channel quality, which is known at the receiver, the decoding matrix for an LABC can be derived as follows [Kay93, p. 391]

$$\begin{aligned}\boldsymbol{Q} &= \left(\boldsymbol{C}_u^{-1} + \boldsymbol{P}^{\mathrm{T}} \cdot \boldsymbol{C}_n^{-1} \cdot \boldsymbol{P}\right)^{-1} \cdot \boldsymbol{P}^{\mathrm{T}} \cdot \boldsymbol{C}_n^{-1} \\ &= \left(\mathbb{1}_{M\times M} \cdot \sigma_u^{-2} + \boldsymbol{P}^{\mathrm{T}} \cdot \mathbb{1}_{N\times N} \cdot \sigma_n^{-2} \cdot \boldsymbol{P}\right)^{-1} \cdot \boldsymbol{P}^{\mathrm{T}} \cdot \mathbb{1}_{N\times N} \cdot \sigma_n^{-2} \\ &= \left(\mathbb{1}_{M\times M} \cdot \frac{\sigma_n^2}{\sigma_u^2} + \boldsymbol{P}^{\mathrm{T}} \cdot \boldsymbol{P}\right)^{-1} \cdot \boldsymbol{P}^{\mathrm{T}} \\ &= \left(\mathbb{1}_{M\times M} \cdot \frac{M}{N \cdot \mathrm{cSNR}} + \boldsymbol{P}^{\mathrm{T}} \cdot \boldsymbol{P}\right)^{-1} \cdot \boldsymbol{P}^{\mathrm{T}}, \end{aligned} \tag{3.13}$$

using the covariance matrices of the source and noise symbols:

$$\boldsymbol{C}_u = \mathbb{1}_{M\times M} \cdot \sigma_u^2, \tag{3.14}$$

$$\boldsymbol{C}_n = \mathbb{1}_{N\times N} \cdot \sigma_n^2. \tag{3.15}$$

The covariance of the estimation error and, thus, the MSE are given by [Kay93, p. 391]

$$\boldsymbol{e} = \boldsymbol{u} - \hat{\boldsymbol{u}}, \tag{3.16}$$

$$\boldsymbol{C}_{\boldsymbol{e}} = \left(\boldsymbol{C}_u^{-1} + \boldsymbol{P}^{\mathrm{T}} \cdot \boldsymbol{C}_n^{-1} \cdot \boldsymbol{P}\right)^{-1} \tag{3.17}$$

$$= \left(\mathbb{1}_{M\times M} \cdot \sigma_u^{-2} + \boldsymbol{P}^{\mathrm{T}} \cdot \boldsymbol{P} \cdot \sigma_n^{-2}\right)^{-1}, \tag{3.18}$$

$$\mathrm{MSE} = \mathrm{E}\left\{\boldsymbol{e}^{\mathrm{T}} \cdot \boldsymbol{e}\right\} = \mathrm{trace}\left(\boldsymbol{C}_{\boldsymbol{e}}\right) \tag{3.19}$$

$$= \sum_{i=1}^{M} \frac{1}{\lambda_i} \tag{3.20}$$

$$= \sum_{i=1}^{M} \frac{1}{\sigma_u^{-2} + \sigma_n^{-2} \cdot \gamma_i} \tag{3.21}$$

$$= \sum_{i=1}^{M} \frac{\sigma_u^2}{1 + \mathrm{cSNR} \cdot \frac{N}{M} \cdot \gamma_i}, \tag{3.22}$$

with the eigenvalues

$$\lambda_i = \left|\mathrm{eig}\left(\mathbb{1}_{M\times M}\cdot\sigma_u^{-2} + \boldsymbol{P}^{\mathrm{T}}\cdot\boldsymbol{P}\cdot\sigma_n^{-2}, i\right)\right| \tag{3.23}$$

$$= \sigma_u^{-2} + \sigma_n^{-2}\cdot\gamma_i \qquad \gamma_i = \left|\mathrm{eig}\left(\boldsymbol{P}^{\mathrm{T}}\cdot\boldsymbol{P}, i\right)\right|. \tag{3.24}$$

For an arbitrary choice of $\boldsymbol{P}$, the overall performance of the LABC with an LMMSE estimator is, thus:

$$\mathrm{pSNR}_{\mathrm{LABC,LMMSE}} = \frac{\mathrm{E}\left\{\boldsymbol{u}^{\mathrm{T}}\cdot\boldsymbol{u}\right\}}{\mathrm{MSE}} \tag{3.25}$$

$$= \frac{M\cdot\sigma_u^2}{\sum_{i=1}^{M}\frac{\sigma_u^2}{1+\mathrm{cSNR}\cdot\frac{N}{M}\cdot\gamma_i}} \tag{3.26}$$

$$= \frac{1}{\frac{1}{M}\sum_{i=1}^{M}\frac{1}{1+\mathrm{cSNR}\cdot\frac{N}{M}\cdot\gamma_i}}. \tag{3.27}$$

Also here, the best transmission fidelity can be achieved with a matrix $\boldsymbol{P}$ with $\gamma_i = \left|\mathrm{eig}\left(\boldsymbol{P}^{\mathrm{T}}\cdot\boldsymbol{P}, i\right)\right| = 1 \quad \forall 1 \le i \le M$, yielding the maximum performance:

$$\mathrm{pSNR}_{\mathrm{LABC,LMMSE,max}} = \frac{M}{\frac{M}{1+\mathrm{cSNR}\cdot\frac{N}{M}}} \tag{3.28}$$

$$= 1 + \mathrm{cSNR}\cdot\frac{N}{M} \tag{3.29}$$

$$\overset{(2.9)}{=} 1 + \mathrm{E_u/N_0}. \tag{3.30}$$

The decoding matrix and the overall performance of the LMMSE approach their equivalent of the ML estimator with increasing cSNR. But for low channel qualities, the LMMSE estimator outperforms the ML estimator and additionally yields a performance which is always greater than 0 dB.

3.3 Rate-Distortion Function

The rate-distortion function states the minimum rate $\mathfrak{R}(\mathfrak{D})$ which is necessary to describe one source symbol with a limited distortion $\mathfrak{D}$ [CT06]. Here, for the distortion the mean-square error distortion is used and the rate is measured in bits or nats, while the latter will be used in all derivations. To convert between bits and nats, the following relations are used:

$$\mathfrak{R}_{\mathrm{bit}} = \mathfrak{R}_{\mathrm{nat}}\cdot\mathrm{ld(e)}, \tag{3.31}$$

$$\mathfrak{R}_{\mathrm{nat}} = \mathfrak{R}_{\mathrm{bit}}\cdot\ln(2). \tag{3.32}$$

The mean-square error distortion is defined as follows for the source symbol u and its estimation $\hat{u}$:

$$\mathfrak{D} = \mathrm{E}\left\{(u-\hat{u})^2\right\}. \tag{3.33}$$

The rate-distortion function is dependent on the source statistics such as the pdf or correlation. Here, just *independent identically distributed* (i.i.d.) symbols are considered and, thus, only the source pdf is of importance to obtain the rate-distortion function.

3.3.1 Shannon Upper Bound

For Gaussian source symbols u with variance σ_u^2 and the mean-square error distortion $\mathfrak{D}$, the rate-distortion function can directly be stated, e.g., [CT06, Theorem 10.3.2]:

$$\mathfrak{R}(\mathfrak{D}) = \begin{cases} \frac{1}{2} \ln\left(\frac{\sigma_u^2}{\mathfrak{D}}\right) & \text{for } 0 \leq \mathfrak{D} \leq \sigma_u^2 \\ 0 & \text{for } \mathfrak{D} > \sigma_u^2 \end{cases}. \tag{3.34}$$

This rate-distortion function holds for Gaussian source symbols and additionally is an upper bound for the rate for non-Gaussian source pdfs for a given distortion [Sha48]. Therefore, (3.34) is also denoted as Shannon upper bound.

3.3.2 Shannon Lower Bound

Shannon also published a lower bound for the rate-distortion function for arbitrary source pdfs $\mathrm{p}_{\mathcal{U}}(u)$ [Sha59a]:

$$\mathfrak{R}(\mathfrak{D}) \geq h(\mathcal{U}) - \frac{1}{2} \ln\left(2\pi e \mathfrak{D}\right), \tag{3.35}$$

with the differential entropy

$$h(\mathcal{U}) = -\int \mathrm{p}_{\mathcal{U}}(u) \cdot \ln\left(\mathrm{p}_{\mathcal{U}}(u)\right) \, \mathrm{d}u, \tag{3.36}$$

while the integral is taken over the support of the random variable.

3.3.3 New Rate-Distortion Upper Bound

In 2005, Guo et al. published a relationship (*Guo-Shamai-Verdú* (GSV) theorem) between the mutual information and the MMSE achievable over an AWGN channel [GSV05]. In [RSV10b], this relationship is used in the context of rate-distortion theory. These findings were proven to be a new quite tight upper bound for the rate-distortion function [DRM12] for arbitrary source pdfs.

To calculate the new rate-distortion upper bound for source symbols u with the pdf $\mathrm{p}_{\mathcal{U}}(u)$, first, u is regarded as the input of the AWGN channel (c.f. Figure 2.2, $y = u$, $\mathrm{p}_{\mathcal{Y}}(y) = \mathrm{p}_{\mathcal{U}}(u)$). Then, the mutual information $I(\mathcal{Y}; \mathcal{Z})$ of the AWGN channel $z = y + n$ with noise variance σ_n^2 is calculated and finally using the GSV theorem, the MMSE is derived from the mutual information. Taking the MMSE as

the distortion $\mathfrak{D}$ and the mutual information as the rate $\mathfrak{R}(\mathfrak{D})$, different operating points on the rate-distortion bound can be attained, while varying the noise variance of the AWGN channel.

The aim is to state the input-output mutual information $I(\mathcal{Y};\mathcal{Z})$ of the AWGN channel as the sum of the Gaussian channel capacity and a *Kullback-Leibler distance* (KLD). For that, an auxiliary variable $\mathcal{Z}'$ is introduced which follows a zero-mean Gaussian pdf $\mathrm{p}_{\mathcal{Z}'}$ with the same variance as $\mathcal{Z}$ ($\sigma_{z'}^2 = \sigma_z^2$). Furthermore, the KLD is defined as $\mathrm{KLD}(f(a)||g(a)) = \int f(a) \ln\left(\frac{f(a)}{g(a)}\right) \mathrm{d}a$ [CT06, (8.46)] and the steps from (3.37) to (3.38) are detailed further down:

$$\begin{aligned}
I(\mathcal{Y};\mathcal{Z}) =& h(\mathcal{Z}) - h(\mathcal{Z}|\mathcal{Y}) \\
=& h(\mathcal{Z}) - h(\mathcal{Y}+\mathcal{N}|\mathcal{Y}) \\
=& h(\mathcal{Z}) - h(\mathcal{N}|\mathcal{Y}) \\
=& h(\mathcal{Z}) - h(\mathcal{N}) \\
=& -\int \mathrm{p}_{\mathcal{Z}}(z) \cdot \ln\left(\mathrm{p}_{\mathcal{Z}}(z)\right) \mathrm{d}z - h(\mathcal{N}) \\
=& -\int \mathrm{p}_{\mathcal{Z}}(z) \cdot \ln\left(\mathrm{p}_{\mathcal{Z}}(z)\frac{\mathrm{p}_{\mathcal{Z}'}(z)}{\mathrm{p}_{\mathcal{Z}'}(z)}\right) \mathrm{d}z - h(\mathcal{N}) \\
=& -\int \mathrm{p}_{\mathcal{Z}}(z) \cdot \ln\left(\mathrm{p}_{\mathcal{Z}'}(z)\right) \mathrm{d}z - \int \mathrm{p}_{\mathcal{Z}}(z) \cdot \ln\left(\frac{\mathrm{p}_{\mathcal{Z}}(z)}{\mathrm{p}_{\mathcal{Z}'}(z)}\right) \mathrm{d}z - h(\mathcal{N}) \qquad (3.37) \\
=& -\int \mathrm{p}_{\mathcal{Z}'}(z) \cdot \ln\left(\mathrm{p}_{\mathcal{Z}'}(z)\right) \mathrm{d}z - \int \mathrm{p}_{\mathcal{Z}}(z) \cdot \ln\left(\frac{\mathrm{p}_{\mathcal{Z}}(z)}{\mathrm{p}_{\mathcal{Z}'}(z)}\right) \mathrm{d}z - h(\mathcal{N}) \qquad (3.38) \\
=& h(\mathcal{Z}') - \mathrm{KLD}(\mathrm{p}_{\mathcal{Z}}||\mathrm{p}_{\mathcal{Z}'}) - h(\mathcal{N}). \qquad (3.39)
\end{aligned}$$

The conversion from (3.37) to (3.38) can also be found in [CT06, (8.72)-(8.76)] but is elaborated with more detail for convenience in the following.

$$\begin{aligned}
-\int \mathrm{p}_{\mathcal{Z}}(z) \cdot \ln\left(\mathrm{p}_{\mathcal{Z}'}(z)\right) \mathrm{d}z =& -\int \mathrm{p}_{\mathcal{Z}}(z) \cdot \ln\left(\frac{1}{\sqrt{2\pi\sigma_{z'}^2}} \cdot \mathrm{e}^{\frac{-z^2}{2\sigma_{z'}^2}}\right) \mathrm{d}y \\
=& \ln\left(\sqrt{2\pi\sigma_{z'}^2}\right) \cdot \underbrace{\int \mathrm{p}_{\mathcal{Z}}(z)\,\mathrm{d}z}_{=1} + \frac{1}{2\sigma_{z'}^2} \cdot \underbrace{\int z^2 \mathrm{p}_{\mathcal{Z}}(z)\,\mathrm{d}z}_{=\sigma_z^2} \\
=& \ln\left(\sqrt{2\pi\sigma_{z'}^2}\right) \cdot \underbrace{\int \mathrm{p}_{\mathcal{Z}'}(z)\,\mathrm{d}z}_{=1} + \frac{1}{2\sigma_{z'}^2} \cdot \underbrace{\int z^2 \mathrm{p}_{\mathcal{Z}'}(z)\,\mathrm{d}z}_{=\sigma_{z'}^2} \\
=& -\int \mathrm{p}_{\mathcal{Z}'}(z) \cdot \ln\left(\mathrm{p}_{\mathcal{Z}'}(z)\right) \mathrm{d}z. \qquad (3.40)
\end{aligned}$$

Equation (3.39) can be further reformulated using the differential entropy of a continuous-amplitude Gaussian random variable [CT06]:

$$\begin{aligned} I(\mathcal{Y};\mathcal{Z}) =& h(\mathcal{Z}') - h(\mathcal{N}) - \mathrm{KLD}(\mathrm{p}_{\mathcal{Z}}||\mathrm{p}_{\mathcal{Z}'}) \\ =& \frac{1}{2}\ln\left(2\pi\mathrm{e}\sigma_{z'}^2\right) - \frac{1}{2}\ln\left(2\pi\mathrm{e}\sigma_n^2\right) - \mathrm{KLD}(\mathrm{p}_{\mathcal{Z}}||\mathrm{p}_{\mathcal{Z}'}) \\ =& \frac{1}{2}\ln\left(\frac{\sigma_{z'}^2}{\sigma_n^2}\right) - \mathrm{KLD}(\mathrm{p}_{\mathcal{Z}}||\mathrm{p}_{\mathcal{Z}'}) \\ =& \frac{1}{2}\ln\left(\frac{\sigma_n^2+\sigma_y^2}{\sigma_n^2}\right) - \mathrm{KLD}(\mathrm{p}_{\mathcal{Z}}||\mathrm{p}_{\mathcal{Z}'}) \\ =& \frac{1}{2}\ln\left(1+\mathrm{cSNR}\right) - \mathrm{KLD}(\mathrm{p}_{\mathcal{Z}}||\mathrm{p}_{\mathcal{Z}'}). \end{aligned} \tag{3.41}$$

The first term of (3.41) is the well known channel capacity for AWGN channels. The output pdf $\mathrm{p}_{\mathcal{Z}}$ of the AWGN channel which is needed to calculate the KLD is the convolution of the input pdf $\mathrm{p}_{\mathcal{Y}}$ and the Gaussian pdf $\mathrm{p}_{\mathcal{N}}$ of the noise ($\mathrm{p}_{\mathcal{Z}} = \mathrm{p}_{\mathcal{Y}} * \mathrm{p}_{\mathcal{N}}$). Therefore, the KLD and hence the mutual information can be obtained analytically for pdfs which allow closed form convolution and integration. For other pdfs, convolution and integration are carried out semi-analytically.

In [GSV04] an analytical relationship between the mutual information in nats and the MMSE of arbitrarily distributed input symbols y and their observations z through an AWGN channel (GSV theorem) is derived:

$$\mathrm{MMSE}(\mathrm{cSNR}) = 2 \cdot \frac{\partial}{\partial \mathrm{cSNR}} I(\mathcal{Y};\mathcal{Z},\mathrm{cSNR}). \tag{3.42}$$

Inserting (3.41) into (3.42) yields:

$$\mathrm{MMSE}(\mathrm{cSNR}) = \frac{1}{1+\mathrm{cSNR}} - 2\frac{\partial}{\partial \mathrm{cSNR}} \mathrm{KLD}(\mathrm{p}_{\mathcal{Z}}||\mathrm{p}_{\mathcal{Z}'},\mathrm{cSNR}). \tag{3.43}$$

For a varying channel quality cSNR, the mutual information in equation (3.41) and the MMSE in equation (3.43) are used as the rate $\mathfrak{R}$ and the distortion $\mathfrak{D}$ for the operating points of the rate-distortion upper bound, respectively.

In the following, the new upper bound is evaluated for different source pdfs. For comparison, the Shannon upper bound (3.34), the Shannon lower bound (3.35) and the numerical results for the rate-distortion function calculated by the Blahut-Arimoto [Bla72, Ari72] algorithm are shown. Figure 3.1a shows the results for a uniform source pdf, Figure 3.1b for a Laplacian source pdf, and Figure 3.2 for a bipolar source pdf, respectively. The properties of the employed pdfs are listed in Appendix D for convenience. For the bipolar source symbols, the Shannon lower bound cannot be evaluated, since the differential entropy $h(\mathcal{Y})$ is not defined here.

All figures show, that the new upper bound is quite tight to the rate-distortion function obtained by the Blahut-Arimoto algorithm.

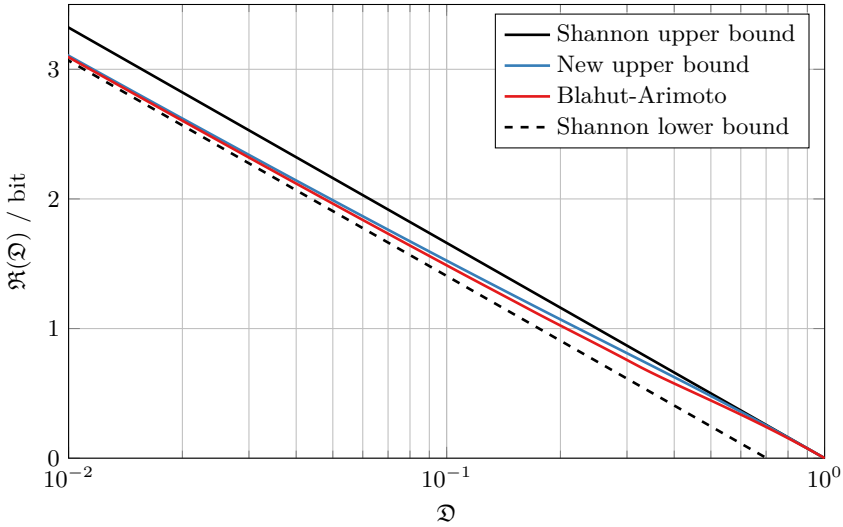

(a) Uniform source pdf.

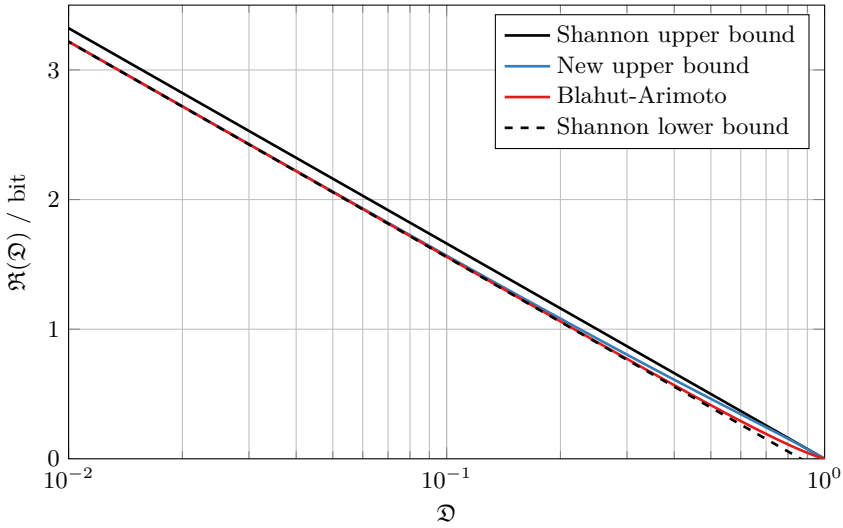

(b) Laplacian source pdf.

Figure 3.1: Rate-distortion functions and bounds for different source pdf.

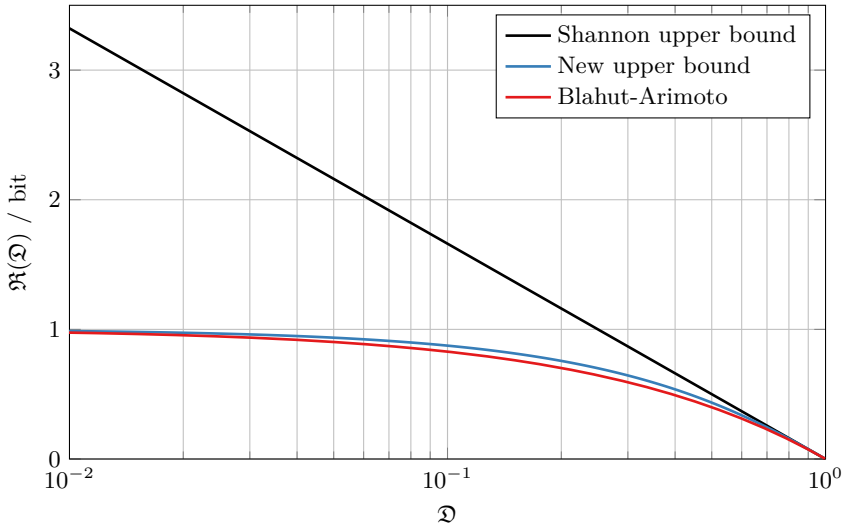

Figure 3.2: Rate-distortion functions and bounds for a bipolar source pdf.

A Matlab tool to calculate the new upper bound can be found on the authors institute website `http://www.ind.rwth-aachen.de`.

3.4 Optimum Performance Theoretically Attainable

The *Optimum Performance Theoretically Attainable* (OPTA) describes the maximum performance in terms of pSNR for a given source pdf for the transmission over a channel with a given quality cSNR and partial or multiple channel uses per source symbol [BT67].

To obtain this bound, three components are combined. First, the corresponding rate-distortion function $\mathfrak{R}(\mathfrak{D})$ for the given source pdf is necessary. This function describes the number of information bits $\mathfrak{R}$ necessary to describe the source symbols with a limited distortion $\mathfrak{D}$. Second, the capacity $C(\text{cSNR})$ of the channel for a given channel quality is required. The capacity states the maximum number of bits C which can be transmitted error-freely with one real-valued (in contrast to complex-valued) channel use. Third, the number N of channel uses for transmitting M source symbols has to be stated:

$$\mathfrak{R}(\mathfrak{D}) \cdot M = C(\text{cSNR}) \cdot N. \tag{3.44}$$

No transmission system, for which the three components from above hold, can obtain a lower $\mathfrak{D}$ than stated in (3.44), thus, OPTA is an upper bound for the end-to-end performance pSNR.

In the following sections, the channel capacity for different channel models are calculated to lay the basis for Section 3.5 where several examples for OPTA are calculated and depicted for different channel models and for different ratios of M and N.

3.4.1 Additive White Gaussian Noise Channel

The capacity in bits per real-valued channel use of an *Additive White Gaussian Noise* (AWGN) channel can be stated as [Sha48]:

$$C_{\text{AWGN}} = \frac{1}{2} \operatorname{ld} (1 + \text{cSNR}) . \tag{3.45}$$

For Gaussian source symbols, the rate-distortion function matches the Shannon upper bound (3.34). With (3.44), for an AWGN channel and Gaussian source symbols, OPTA can be derived as:

$$\frac{1}{2} \operatorname{ld} \left(\frac{\sigma_u^2}{\mathfrak{D}} \right) \cdot M = \frac{1}{2} \operatorname{ld} (1 + \text{cSNR}) \cdot N \tag{3.46}$$

$$\Leftrightarrow \quad \operatorname{ld} \left(\frac{\sigma_u^2}{\mathfrak{D}} \right) = \operatorname{ld} (1 + \text{cSNR}) \cdot \frac{N}{M} \tag{3.47}$$

$$\Leftrightarrow \quad \frac{\sigma_u^2}{\mathfrak{D}} = (1 + \text{cSNR})^{\frac{N}{M}} \tag{3.48}$$

The fraction $\frac{\sigma_u^2}{\mathfrak{D}}$ describes the pSNR which can optimally be achieved for a Gaussian source and an AWGN channel:

$$\text{pSNR}_{\text{OPTA, Gaussian, AWGN}} = (1 + \text{cSNR})^{\frac{N}{M}} . \tag{3.49}$$

The separation theorem [Sha48] states that a transmission system using infinite block sizes and, thus, has an infinite delay, can achieve error-free transmission by separate source and channel coding with an intermediate representation of the source symbols in bits. Interestingly, there are some very few special cases in which OPTA can be reached without infinite delay [Gas02] and, thus, with a limited block size. One example is directly transmitting Gaussian source symbols over an AWGN channel with one channel use per source symbol ($N = M$). With an MMSE estimator at the receiver, which in this case can be realized by a simple linear estimator [Kay93], OPTA is reached at every channel quality even for a fixed transmitter [Gal68, Gas02]. This scheme is optimal also for tiny block sizes such as $N = M = 1$. A derivation of the performance of such a transmission system can be found in Section 3.2.2.

For non-Gaussian source symbols, the pSNR of OPTA is higher than the pSNR of OPTA for Gaussian source symbols, since a lower distortion $\mathfrak{D}$ can be achieved for a given number of information bits (e.g., Figure 3.1a). For the exact derivation

of OPTA for non-Gaussian source symbols the rate-distortion function for this source pdf is necessary. Unfortunately, the new (quite tight) rate-distortion upper bound (Section 3.3.3) cannot be used to calculate OPTA for non-Gaussian source symbols. It upper bounds the distortion and, thus, the pSNR is lower bounded, but OPTA is defined to be an upper bound for the pSNR. However, the Shannon lower bound, can be used to calculate OPTA for non-Gaussian source symbols, since it provides a lower bound for the distortion and, thus, an upper bound of the pSNR.

3.4.2 Binary Symmetric Channel

The *Binary Symmetric Channel* (BSC) assumes a binary input of the channel and a binary output. This is a model for a bipolar modulation scheme such as *Binary Phase Shift Keying* (BPSK) for real-valued channel uses, or *Quadrature Phase Shift Keying* (QPSK) for complex-valued channel uses and *hard decision* demodulation at the receiver.

The capacity in bits per real-valued channel use of a BSC with a probability of error p is given by [Pro95, p. 381]:

$$C_{\mathrm{BSC}} = 1 + p \cdot \mathrm{ld}(p) + (1-p) \cdot \mathrm{ld}(1-p). \tag{3.50}$$

For an AWGN channel with a channel quality cSNR the probability of error for a hard decision decoder can be stated using the Q function as:

$$\begin{aligned} p &= Q\left(\sqrt{\mathrm{cSNR}}\right) \\ &= \frac{1}{\sqrt{2\pi}} \int_{\sqrt{\mathrm{cSNR}}}^{\infty} \exp\left(-\frac{n^2}{2}\right) \mathrm{d}n \\ &= \frac{1}{2} \operatorname{erfc}\left(\sqrt{\frac{\mathrm{cSNR}}{2}}\right). \end{aligned} \tag{3.51}$$

The maximum capacity per channel use of a BSC is 1 bit. For higher modulation schemes, e.g., 8-PSK or 16-QAM, more complex channel models [OL07] with higher maximum capacity have to be employed. These are not considered in this work, since the general concepts and effects can also be described employing a BSC.

3.4.3 Binary-Input Additive White Gaussian Noise Channel

The *Binary-Input Additive White Gaussian Noise* (BIAWGN) channel assumes a binary input transmitted over an AWGN channel. This is a model for a bipolar modulation scheme such as BPSK for real-valued channel uses, or QPSK for complex-valued channel uses and *soft decision* demodulation at the receiver, e.g., using L-values.

The transition probability for an AWGN channel can be stated as

$$\mathrm{p}(z|y) = \frac{1}{\sqrt{2\pi\sigma_n^2}} \cdot \mathrm{e}^{-\frac{(z-y)^2}{2\sigma_n^2}}, \tag{3.52}$$

and the capacity for equiprobable input symbols $y = \pm 1$ and an AWGN channel $z = y + n$ with cSNR $= \frac{1}{\sigma_n^2}$ is [Pro95, p. 385]:

$$\begin{aligned} C_{\mathrm{BIAWGN}} &= I(\mathcal{Y};\mathcal{Z}) = \mathrm{KLD}(\mathrm{p}(y,z)||\mathrm{p}(y)\cdot\mathrm{p}(z)) && (3.53)\\ &= \int_{-\infty}^{\infty} \mathrm{p}(z|1) \cdot \mathrm{ld}\left(\frac{\mathrm{p}(z|1)}{\mathrm{p}(z)}\right) \mathrm{d}z \\ &= \int_{-\infty}^{\infty} \frac{1}{\sqrt{2\pi\sigma_n^2}} \cdot \mathrm{e}^{-\frac{(z-1)^2}{2\sigma_n^2}} \cdot \mathrm{ld}\left(\frac{2}{1+\mathrm{e}^{-\frac{2\cdot z}{\sigma_n^2}}}\right) \mathrm{d}z. && (3.54) \end{aligned}$$

The maximum capacity per channel use of a BIAWGN channel is, as for a BSC 1 bit. Also here, for higher modulation schemes, e.g., 8-PSK or 16-QAM, more complex channel models with higher maximum capacity have to be employed, which are not considered in this work, since the general concepts and effects can also be described employing a BIAWGN channel.

3.4.4 Hybrid Digital-Analog Channel

HDA transmission systems employ D channel uses for discrete transmissions and A channel uses for analog transmissions. For bipolar modulation, the capacity of the transmission channel of HDA systems can, thus, be modeled by the combination of the BSC or BIAWGN channels for the discrete channel uses and the AWGN channel for the analog channel uses.

If *hard decision* decoding is employed for the discrete channel uses, the average capacity of one hybrid channel use can be stated using the BSC:

$$C_{\mathrm{BSC,AWGN}} = \frac{D}{N} \cdot C_{\mathrm{BSC}} + \frac{A}{N} \cdot C_{\mathrm{AWGN}}. \tag{3.55}$$

In case of *soft decision* decoding, the average capacity of one hybrid channel use can be stated using the BIAWGN channel:

$$C_{\mathrm{BIAWGN,AWGN}} = \frac{D}{N} \cdot C_{\mathrm{BIAWGN}} + \frac{A}{N} \cdot C_{\mathrm{AWGN}}. \tag{3.56}$$

3.5 Examples of the Optimum Performance Theoretically Attainable

Figure 3.3 shows *Optimum Performance Theoretically Attainable* (OPTA) for different source pdfs and one channel use $N = 1$ per source symbol $M = 1$. To obtain OPTA, the channel capacity of an AWGN channel (3.45) and the rate-distortion function for the specific source symbol pdf with the ratio between channel uses and source symbols (3.44) has to be evaluated. For Gaussian source symbols, the Shannon upper bound (3.34) gives the exact results. For uniform or Laplacian source distributions, there is no closed form expression, thus, the rate-distortion function is calculated using the numerical iterative Blahut-Arimoto algorithm [Bla72, Ari72]. Figure 3.4 depicts the differences in terms of pSNR between OPTA for non-Gaussian and Gaussian source symbols.

The different behavior of OPTA for different source pdfs can also be observed in the rate-distortion functions in Figures 3.1a and 3.1b. For high distortions (low pSNR), the rate-distortion functions for all source distributions converge. Thus, also OPTA converges to the Gaussian case for all source distributions for bad channel qualities as can be observed in Figure 3.4. For low distortions (high pSNR), the gap between the rate-distortion functions of a specific source distribution and the Gaussian case converge to a constant. E.g., in Figure 3.1a for a uniform source distribution the gap of the distortion at a constant rate in the

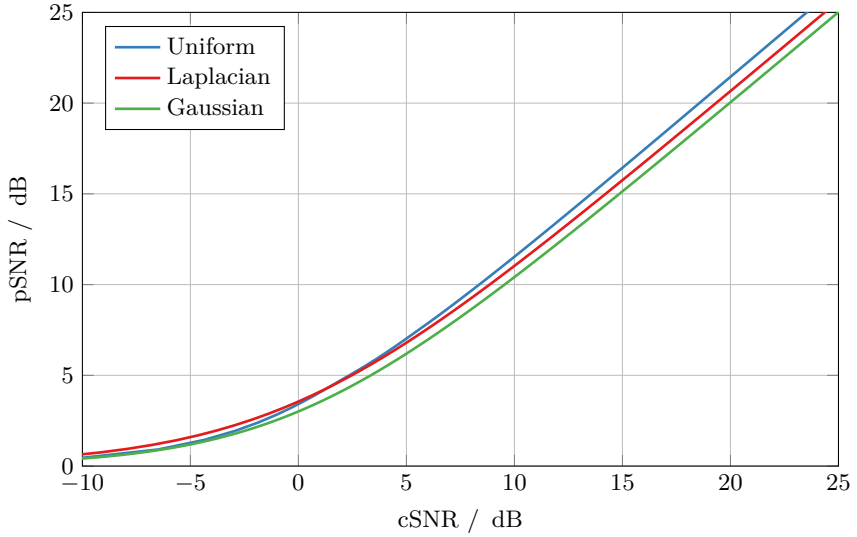

Figure 3.3: OPTA for different source pdfs for $M = 1$ and $N = 1$.

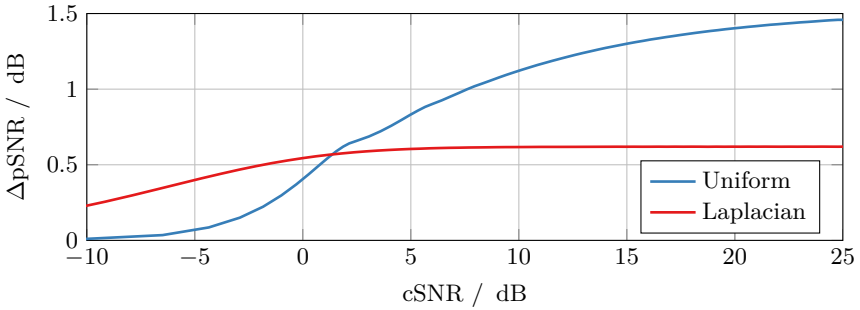

Figure 3.4: Difference of OPTA for different source pdfs to OPTA of Gaussian source.

low distortion region is around 1.5 dB in terms of distortion or pSNR. The same distance $\Delta\text{pSNR}|_{\text{dB}} = 1.5\,\text{dB}$ between OPTA for the uniform source distribution and the Gaussian case can be noted in Figure 3.4 for high channel qualities. For the Laplacian source distribution, OPTA is in between the uniform and the Gaussian case.

Figure 3.5 shows OPTA, calculated for a Gaussian source with the channel capacity for different channel models. Additionally the performance of LABCs with ML and LMMSE estimators is depicted. OPTA is a performance bound, hence, just in very rare constellations (Section 3.4.1) or for infinite block length and delay, this performance can be reached. The depicted performance for the LABCs can be reached by using, e.g., direct unprocessed transmission of the source symbols (Section 3.2) or in case of $r = \frac{M}{N} < 1$ a repetitive transmission of the symbols.

In Figure 3.5a one source symbol ($M = 1$) and two channel symbols ($N = 2$) are employed. The performance bound for the purely digital transmission systems which can be modeled by BSC or BIAWGN channels saturates at $\text{pSNR}|_{\text{dB}} = 12\,\text{dB}$ following the 6 dB-per-bit rule at around $\text{cSNR}|_{\text{dB}} = 10\,\text{dB}$, when the maximum capacity of 1 bit per channel use is reached. Here, for increasing channel qualities, the performance cannot be further improved.

The performance bounds which include soft decision demodulation and therefore are modeled using a BIAWGN channel outperform the bounds for hard decision demodulation with a BSC. This effect is especially prominent for channel qualities where the decoding performance has not yet saturated ($\text{cSNR}|_{\text{dB}} < 10\,\text{dB}$).

For LABCs, the LMMSE estimator surpasses the ML estimator, especially for bad channels. Additionally, the performance of the LMMSE estimator always stays above $\text{pSNR}|_{\text{dB}} = 0\,\text{dB}$. For increasing channel qualities, the performance of both estimators converge as already noted in Section 3.2.2. Above around $\text{cSNR}|_{\text{dB}} = 10\,\text{dB}$, the linear analog block codes outperform the bounds for purely digital transmission.

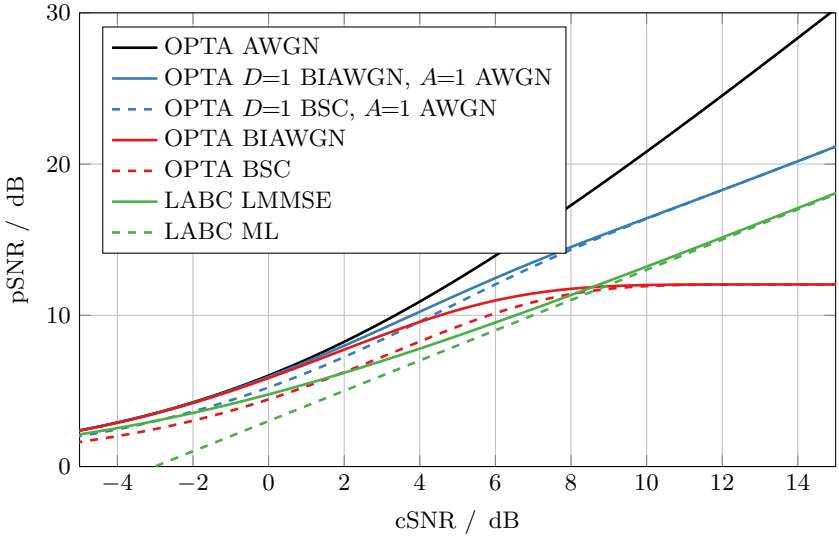

(a) $M = 1$ and $N = 2$.

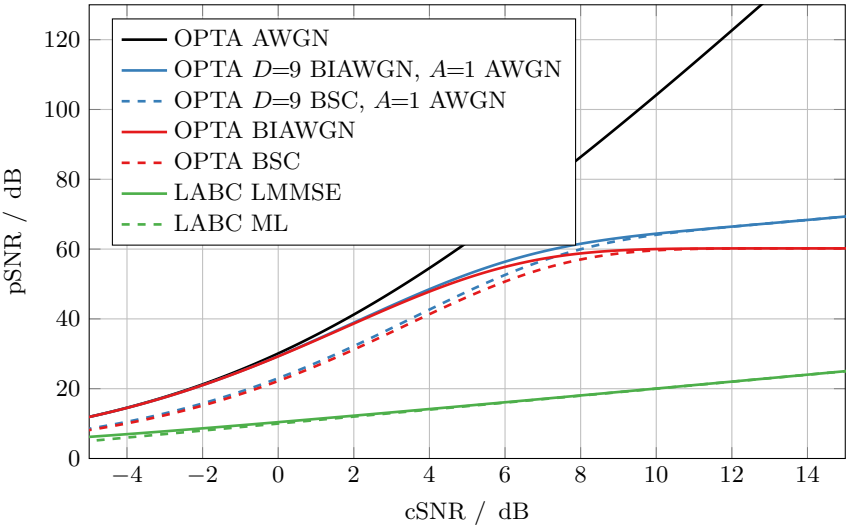

(b) $M = 1$ and $N = 10$.

Figure 3.5: OPTA for Gaussian source symbols and the performance of LABCs.

In Figure 3.5b, ten channel uses ($N = 10$) are employed which yield a significantly increased performance by 48 dB for the bounds employing discrete channel models. The LABCs increase their performance only by around 6 dB.

In both figures, it can be observed that for systems employing non-discrete channel models (AWGN channel in combination with BSC or BIAWGN channel) and for the LABCs, the performance bound improves for an increased channel quality with 1 dB in pSNR for 1 dB in cSNR. Most interestingly, the performance bound of systems employing both, discrete and non-discrete channel models is always higher or equal than for systems employing only discrete channel models. This can be explained by the unbounded capacity increase of the AWGN channel for rising channel qualities which is not given for the discrete channel models which are, for BSC and BIAWGN, bounded by 1 bit per channel use.

In Figure 3.5a for good channels, the difference in terms of pSNR of the systems consisting of both non-discrete and discrete channels to the LABC is only 3 dB. But for $N = 10$ channel uses per source symbol (Figure 3.5b), the difference increases to 44 dB. This shows the potential of systems employing nonlinear operations for encoding.

3.6 Influence of Block Length – The Sphere Packing Bound

For a finite block size, the rate-distortion function and the capacity of a channel can only be reached for a very few special cases [Gas02]. E.g., for the mean-square error distortion (*Mean-Square Error* (MSE)) and a power constrained AWGN channel, only for a Gaussian source with one channel use per source symbol and a LMMSE estimator at the receiver, OPTA can be reached for finite block size and in this case even a block size of 1 [Gal68].

In general, for finite block sizes, the rate-distortion function and the channel capacity cannot be reached.

The aim of channel coding and modulation is to transmit bits with a minimum error rate over a channel. For finite block sizes, the *Sphere Packing Bound* (SPB) gives the maximum achievable performance [Sha59b]. The idea behind the derivation of the SPB is the following: In Section 2.3 it is described that digital channel coding (and modulation) is the art of positioning points (which correspond to the code vectors) in the N-dimensional channel space. The aim is to position as many points, spend as less energy as possible and still maximize the Euclidean distance between the points such, that after adding Gaussian channel noise, the points still can be separated with high probability. Consequently, one important measure is the (squared) Euclidean distance between the points and the energy of the channel noise (i.e., the squared length of the noise vector) in the N-dimensional channel space.

For short block lengths, i.e., few channel dimensions, there are only a few

samples of the channel noise which contribute to the energy of the noise vector. Thus, there are great variations of the energy of the samples from one block to the other around the mean channel noise energy. To achieve a certain error rate after decoding, the distance between the points has to be increased such, that the blocks with higher noise energy still can be decoded. Therefore, less points are possible to position or a certain error rate can only be reached for a sufficiently high channel quality.

For larger block lengths, more samples of the channel noise contribute to the energy of the noise vector and, thus, smaller variations around the mean channel energy occur. In the limit of infinite block lengths, every noise vector has the same energy. In this case, the points can be packed more densely. In the limit of infinite block lengths, the received points all lie on a hypersphere around the sent point and have the same distance to the sent point. One way to derive the channel capacity of an AWGN channel is to take the available volume in the channel space which can be used under a given power constraint and divide it by the volume of the hyperspheres around the points.

Modeling this intuition, the SPB calculates the minimum word error probability which theoretically could be achieved, for finite block sizes, for a given channel coding rate and a given channel quality [Sha59b].

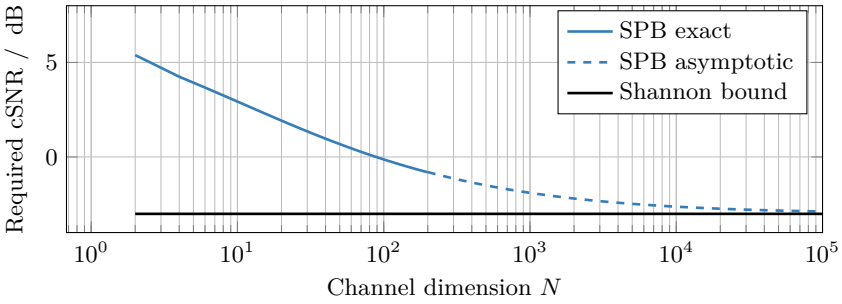

Figure 3.6: The minimum required cSNR according to the SPB for varying channel block sizes for a rate of 1/2 and code word error probability $P_w = 10^{-4}$. Additionally, the limit for infinite block size, the Shannon bound, is depicted.

Figure 3.6 shows the minimum required channel quality for rate-$\frac{1}{2}$ channel coding and modulation system and a target word error rate of $P_w = 10^{-4}$. The solid line is calculated using the exact derivation and the dashed line uses an approximation which holds for larger block lengths [DDP98]. The exact derivation would be too complex to be calculated for large block lengths. Additionally, the limit for infinite block size, i.e., the Shannon bound is depicted.

The SPB proves that codes with short block lengths (i.e., $N = 10$) cannot

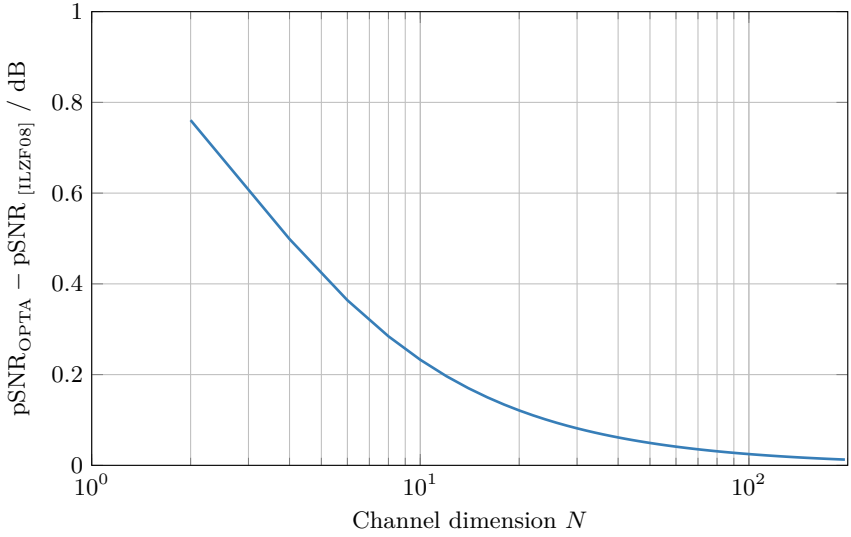

(a) $\frac{N}{M} = \frac{1}{2}$

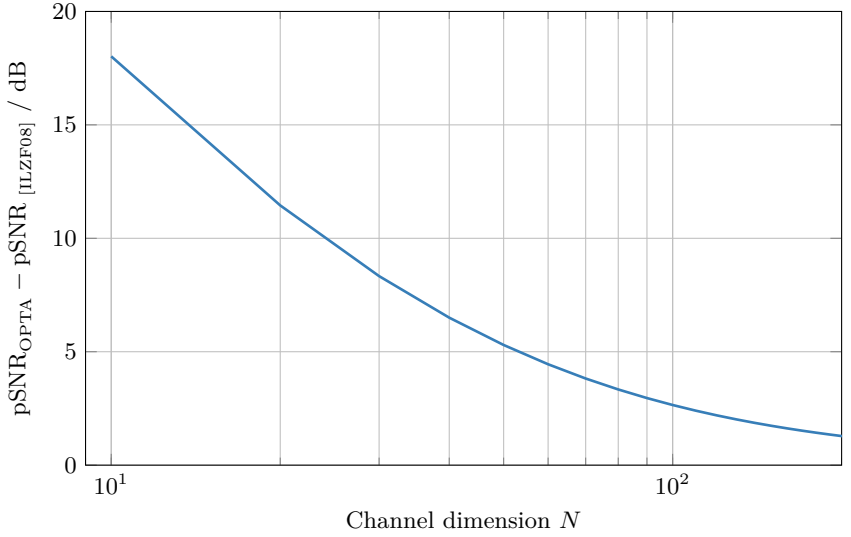

(b) $\frac{N}{M} = \frac{1}{10}$

Figure 3.7: Difference between OPTA and the high-SNR bound in [ILZF08] for a limited channel block size N with different rates for a Gaussian source.

facilitate a transmission at $P_w = 10^{-4}$ below a channel quality of $\text{cSNR}|_{\text{dB}} = 2.9\,\text{dB}$. On the other hand, codes with block lengths of $N = 1000$ could already operate at $\text{cSNR}|_{\text{dB}} = -1.9\,\text{dB}$.

In [DDP98], the performance of several channel codes ranging from very short codes such as Hamming codes to very long codes such as Turbo codes is depicted and compared to the SPB of the corresponding block size. The very interesting result is, that all good codes are very close to the SPB of their block size. The performance gain of, e.g., Turbo codes compared to Hamming codes is not due to the different design, but due the ability to allow decoding at a reasonable complexity and, thus, allow for longer block lengths.

The SPB is a very descriptive method to connect the error rate with the number of input bits, the channel dimension and the channel quality. In [PPV10] a new bound for the capacity of transmission systems with a finite number of channel uses and given channel quality and error rate is proposed. The missing component to construct a block size dependent OPTA is a block size dependent rate-distortion theory, which has not been found, yet.

Another approach is published in [FRW07] where for transmission systems using only continuous-amplitude operations, a similar effect as in the derivation of the SPB is shown, where an increased performance for longer block lengths can be observed.

In [ILZF08] another completely different approach is proposed to calculate OPTA for finite block sizes. Here, a different entropy, namely the Rényi information measure is used, which unlike the "normal" entropy is dependent on the block size. The derivation is only valid for high-SNR channels and high resolution source representations. Figures 3.7a and 3.7b show the difference of OPTA in (3.49) for a Gaussian source transmitted over a power constrained AWGN channel with the squared error distortion measure to the new bound in [ILZF08]. The bounds are calculated for rates of $\frac{M}{N} = \frac{1}{2}$ and $\frac{M}{N} = \frac{1}{10}$ and to meet the high-SNR requirement, a channel quality of $\text{cSNR}|_{\text{dB}} = 100\,\text{dB}$.

Both figures indicate that the bound obtained in [ILZF08] yields lower values as OPTA, especially for small block sizes and low rates (Figure 3.7b). This underlines the effect described by the SPB of Shannon, that an increased block size is necessary to yield a higher potential transmission performance.

Chapter 4

Compander and Space Filling Curves

4.1 Introduction

In this chapter, *compander* and *space filling curves* are considered. A compander consists of a compressor and an expander which usually are nonlinear functions with a scalar input and a scalar output. These functions can be generalized to operate on vectors, also with different input and output dimensions. A space filling curve describes the resulting subspace in the channel space when applying, e.g., a compressor or another (non)-linear function to all admissible source symbols.

In general, any transmission system which operates on continuous-amplitude source symbols and outputs continuous-amplitude channel symbols can be described by a nonlinear function (e.g., a compander), but usually the word "compander" is only used in the 1:1 case (i.e., one channel symbol for one source symbol).

Nonlinear functions with more than one output symbol per input symbol may provide a means of error protection to combat channel noise (Section 2.4.2). One very beautiful example is the Archimedes spiral [FR06, RSV10a] which maps one source symbol to two channel symbols. A variant of the Archimedes spiral which yields, independent of the source *probability density function* (pdf), the same output power as the input power for each symbol, has been used to protect the prediction error in a speech encoder [HV06].

Other systems which provide more than two channel symbols per source symbol are, e.g., curves on a sphere [CTC13, VC03] or orthogonal polynomials [WSR09]. Unfortunately, the gap to *Optimum Performance Theoretically Attainable* (OPTA) grows with an increased number of channel symbols per source symbol.

In this chapter, some examples of nonlinear functions are described and their performance is assessed. First, in Section 4.2 the system model using nonlinear functions as a compressor and an expander is introduced. Then in Section 4.3, the scalar 1:1 case for different source pdfs is investigated using a numerical optimization of the compressor and expander function to maximize the pSNR. In Section 4.4, first, two variants of the Archimedes spiral are compared and then a numerically optimized mapping is generated and assessed.

4.2 System model

A continuous-amplitude mapping of the source symbol u to the channel vector $\boldsymbol{y}$ can also be described by a compressor function. The inverse process, namely the mapping of the noisy received value $\boldsymbol{z}$ to the estimated symbol $\hat{u}$ consequently is an expander. A compander (*comp*ressor and exp*ander*) is typically used in the context of scalar values in which the source and the channel symbols are scalars and hence the compressor function $y = \mathrm{g}(u)$ and the expander function $\hat{u} = \mathrm{h}(z)$ are one-dimensional functions. The case of mappings which add redundancy ($N > M$), e.g., for $N = 2$ and $M = 1$ can also be described by a compander. As the compressor, N one-dimensional compressor functions $y_i = \mathrm{g}_i(u)$, $1 \leq i \leq N$ are used for mapping the source symbol to the entries y_i of the channel vector $\boldsymbol{y}$. The compressor functions can be combined to $\boldsymbol{y} = \mathbf{g}(u)$. The expander is a single function with N input variables and one scalar output variable $\hat{u} = \mathrm{h}(\boldsymbol{z})$. This concept can be easily generalized to higher-dimensional source symbols, but this is not considered here for simplicity. The whole transmission system with a compressor and an expander is depicted in Figure 4.1. Here, the aim of the compander system is achieving the

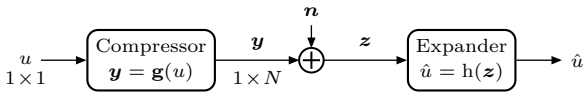

Figure 4.1: General transmission system with compressor and expander function for scalar source symbols.

lowest possible *Mean-Square Error* (MSE) D between the source symbols u and the estimated symbols $\hat{u}$ while using as little average power P for transmission as possible.

The average power P for transmission depends on the compressor function and the source pdf:

$$P(\mathbf{g}) = \frac{1}{N} \cdot \mathrm{E}\{||\boldsymbol{y}||^2\} = \frac{1}{N} \cdot \mathrm{E}\{\boldsymbol{y}\boldsymbol{y}^{\mathrm{T}}\} = \frac{1}{N} \cdot \int \mathbf{g}(u) \cdot \mathbf{g}(u)^{\mathrm{T}} \cdot \mathrm{p}(u)\,\mathrm{d}u. \quad (4.1)$$

The MSE is additionally a function of the expander and the pdf of the noise $\boldsymbol{n}$:

$$\begin{aligned} D(\mathbf{g}, \mathrm{h}) &= \mathrm{E}\{(u - \hat{u})^2\} \\ &= \int_{\mathbb{R}^N} \int (u - \mathrm{h}\left(\mathbf{g}(u) + \boldsymbol{n}\right))^2 \cdot \mathrm{p}(u) \cdot \mathrm{p}(\boldsymbol{n})\,\mathrm{d}u\,\mathrm{d}\boldsymbol{n}. \end{aligned} \quad (4.2)$$

With the power of the source symbols, the pSNR can be stated as:

$$\mathrm{pSNR} = \frac{\mathrm{E}\{u^2\}}{D(\mathbf{g}, \mathrm{h})}. \quad (4.3)$$

4.3 1:1 Mapping

With 1:1 mappings, $M = 1$ source symbol u is mapped to $N = 1$ channel symbol y. Nonlinear mappings may lead to a superior performance than linear mappings. Since closed form expressions are not known for most source distributions, a numerically optimized compressor and expander is presented.

4.3.1 Numerically Optimized Mappings

For most source distributions, an optimal compressor and expander cannot be derived analytically. Therefore a numerical optimization has to be applied. The numerical iterative approach proposed in [Aky11, ARR10] is considered in the following. After an initialization of the compressor, the optimal expander can be stated as the *Minimum Mean-Square Error* (MMSE) estimator. Then, given this expander, the optimal compressor can be calculated using a numerical optimization method. Then again, the first step is repeated to find the optimal expander. This process is repeated until convergence is reached.

In the Appendix A, the expressions needed for this optimization are derived. The optimal expander for a given compressor is stated in Section A.2 as (A.6). To optimize the compressor for a given expander (Appendix A.3.2), the transmission power on the channel and the resulting overall MSE have to be jointly minimized. This joint minimization is facilitated with a Lagrangian cost functional (A.10) using the steepest decent method. Therefore, the derivative of the functional with respect to each discretized point on the compressor function is calculated (A.24) and the minimization of the cost functional is achieved by following the derivative (A.25).

For the case of $M = 1$ and $N = 1$, the minimization of the cost functional is a convex problem [AVRR13], hence, the initialization of the compressor is of minor importance. Here, a linear compressor is used in the first step which is also motivated by the observation that for any source pdf and bad channels, a linear compressor is the optimal compressor anyways [AVRR13].

4.3.2 Simulation Results

In the subsequent sections, the optimal compressor and expander pairs and simulation results for the 1:1 case, the *Additive White Gaussian Noise* (AWGN) channel and for different source pdfs are given. Figure D.1 in the Appendix shows the employed source pdfs for convenience.

Gaussian

One well known and yet surprising result from information theory is that uncoded transmission of Gaussian symbols over an AWGN channel is optimal. Thus, in the case of $M = 1$ and $N = 1$ a linear compressor and a linear estimator which can be derived using the *Linear Minimum Mean-Square Error* (LMMSE) yield

optimal performance. The performance of an LMMSE estimator as the expander for a linear compressor is the same as for a purely linear transmission system such as *Linear Analog Block Codes* (LABCs) which is calculated in (3.29):

$$\mathrm{pSNR}_{\mathrm{LABC,LMMSE,max}} = 1 + \mathrm{cSNR}. \tag{4.4}$$

The same performance is predicted as the OPTA in (3.49). Thus, the optimal compressor and expander pairs for a Gaussian source pdf are well known to be just linear functions.

Uniform

For source samples with a uniform source pdf, no closed form solution is known, therefore, a numerical optimization is applied. Figure 4.2 shows the resulting compressor and expander functions for different channel qualities. Also the linear compressor and expander are shown for comparison. The compressor functions in Figure 4.2a do not deviate significantly from the linear function. For $\mathrm{cSNR}|_{\mathrm{dB}} = 0\,\mathrm{dB}$, the compressor function first bends a little upwards and for higher values downwards. Interestingly, for higher channel qualities ($\mathrm{cSNR}|_{\mathrm{dB}} = 30\,\mathrm{dB}$), this effect is inverted, first the compressor function bends down a little and then tilts up for higher signal values. At around $\mathrm{cSNR}|_{\mathrm{dB}} = 10\,\mathrm{dB}$, the result of the numerically optimized compressor is very close to a linear compressor.

The expander functions in Figure 4.2b show the typical behavior of an MMSE estimator. For low channel qualities, the noise significantly increases the power of the received values and, thus, the range of the received values z is increased. The MMSE estimator reduces the influence of the noise by nonlinearly damping the received values by smoothly limiting the range of $\hat{u}$ to the range of the sent values u. Additionally, the effect of the compressor is inverted.

Figure 4.3a shows the performance of different compander systems. The first two systems employ a linear compressor and either a linear (LMMSE, (3.29)) or a nonlinear (MMSE) expander. The third line depicts the performance of a system using the optimized compressor and expander functions. The theoretical performance limit OPTA for a uniform source distribution (see Section 3.5) is shown for comparison. At first sight, all systems do not differ significantly in performance but exhibit a significant gap to OPTA.

Figure 4.3b shows the gain of the MMSE and the optimized system in comparison to the LMMSE solution. The maximum gain of the MMSE system is around 0.37 dB at $\mathrm{cSNR}|_{\mathrm{dB}} = 9\,\mathrm{dB}$ while the gain approaches 0 dB for lower and higher channel qualities. The effect at lower channel qualities is due to the optimality of linear systems at low channel qualities and at higher channel qualities where the MMSE estimator converges to the linear estimator. The optimized compressor and expander supersede the MMSE solution and show a constant gain at high channel qualities. Here, the gain approaches 0.4 dB which is maintained for rising channel qualities. Interestingly, this gain over the MMSE solution is caused only by the small tilt of

the compressor curve in comparison to the linear compressor (Figure 4.2a). Yet, the gain of this system does not approach OPTA which is around 1.5 dB away from the LMMSE estimator for high channel qualities (Figure 3.4 in Section 3.5).

Laplace

As for source symbols with a uniform pdf, also for Laplacian source symbols a numerical optimization is applied. The pdf of Laplacian source symbols (Figure D.1) contains many symbols with low absolute values and a long tail at larger absolute values. Therefore the range of the source symbols is significantly larger than for source symbols with a uniform pdf. These properties of the Laplacian pdf also impact the optimized compressor in Figure 4.4a. For $\text{cSNR}|_{\text{dB}} \geq 10\,\text{dB}$, small values with high probability of occurrence are stretched apart (small bump for $|u| < 2$) to increase the robustness and larger values are shifted to smaller values to compensate for the higher power needed for the stretched values. The expander in Figure 4.4b inverts this process while considering the different strength of the channel noise. The performance of different compander system is shown in Figure 4.5a. As for the uniform case, the linear system with an LMMSE estimator, the MMSE estimator with a linear compressor and the system with optimized compressor and expander show comparable performance while OPTA for the Laplacian source is not reached. Figure 4.5b shows the gain of the MMSE estimator and the optimized system in comparison to the LMMSE estimator. Also here the MMSE estimator exhibits a peak of the gain at around $\text{cSNR}|_{\text{dB}} = 3\,\text{dB}$ of 0.23 dB. For lower and higher channel qualities the gain converges to 0 dB. Again the numerically optimized compander supersedes the MMSE solution for all channel qualities and achieves a constant gain of around 0.26 dB for rising channel qualities. All in all, the optimized system shows comparable properties as shown in the uniform case, but for a Laplacian source, the achievable gains are even smaller. Yet, the gain of this system also does not approach OPTA which is around 0.6 dB away from the LMMSE estimator for high channel qualities (Figure 3.4 in Section 3.5).

4.4 1:2 Mapping

With 1:2 mappings, $M = 1$ source symbol u is mapped to $N = 2$ channel symbols y_1 and y_2. The motivation is to exploit the potential pSNR improvement enabled by the additional channel use which can be used for additional redundancy. The optimum achievable pSNR for a fixed channel quality cSNR is given by OPTA in Section 3.4 and is significantly higher than using just one channel symbol for one source symbol (1:1). All 1:2 mappings can be described by two 1:1 compressor functions as used in the previous section. There exist an infinite number of continuous-amplitude 1:2 mappings whose performance cannot be predicted without numerical simulations. In the following two different approaches will be described. The first approach uses compressor functions which can be described and parametrized analytically. Two

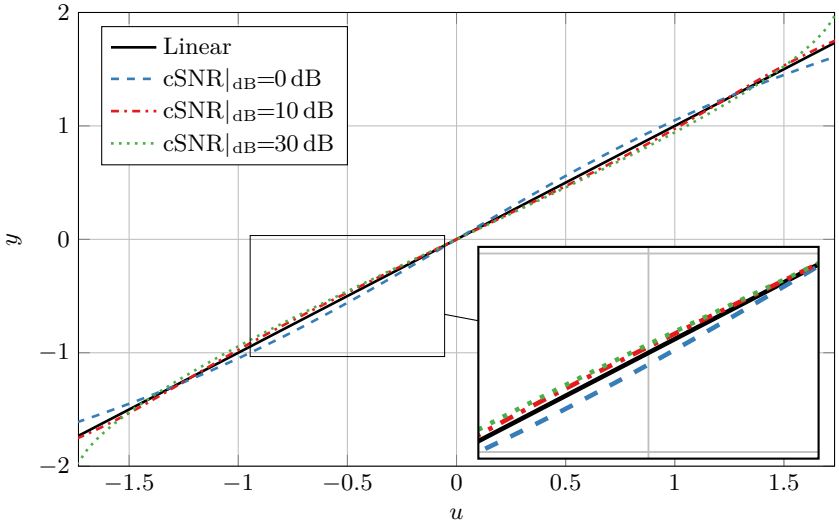

(a) Compressor $y = \mathrm{g}(u)$.

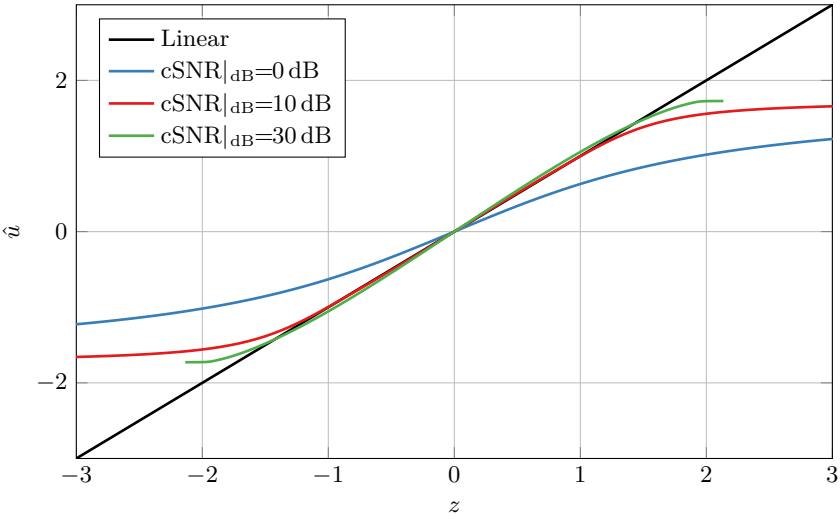

(b) Expander $\hat{u} = \mathrm{h}(z)$.

Figure 4.2: Optimized compressor and expander with $M = 1$ and $N = 1$ for a uniform source pdf for different channel qualities.

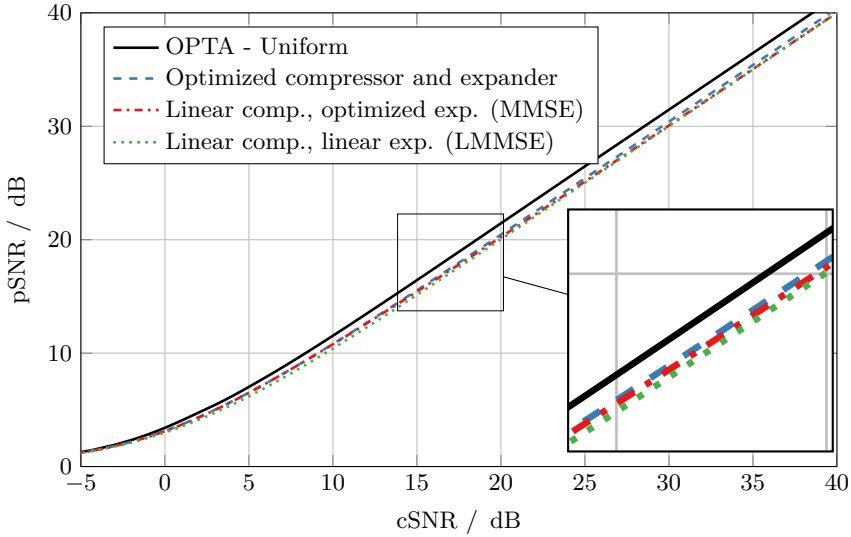

(a) Performance.

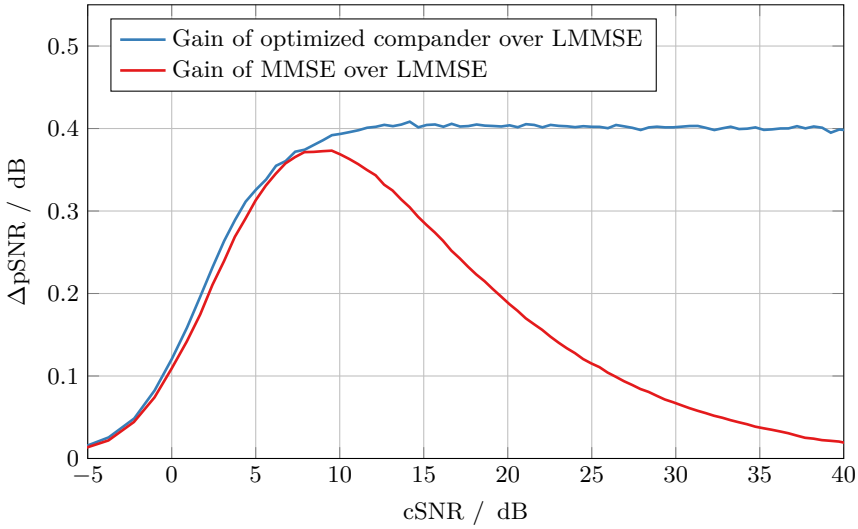

(b) Gains in ΔpSNR in dB.

Figure 4.3: Performance and gains of different compander systems with $M = 1$ and $N = 1$ for a uniform source pdf.

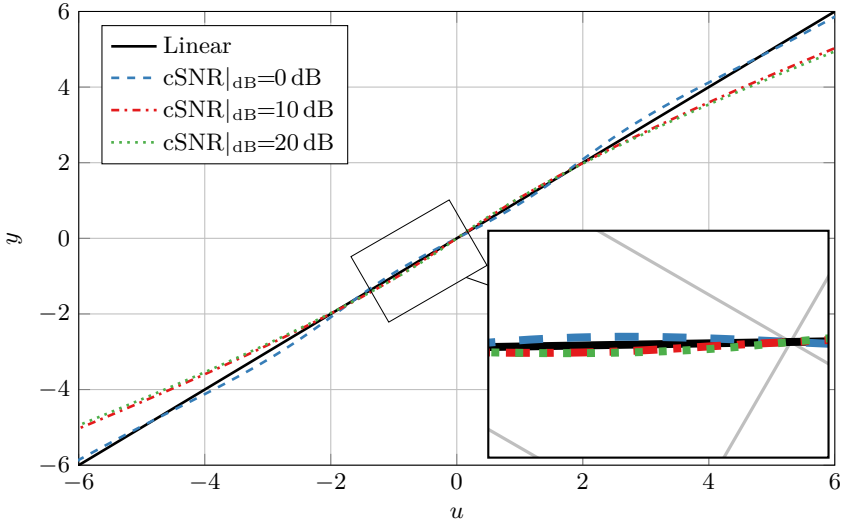

(a) Compressor $y = \mathrm{g}(u)$.

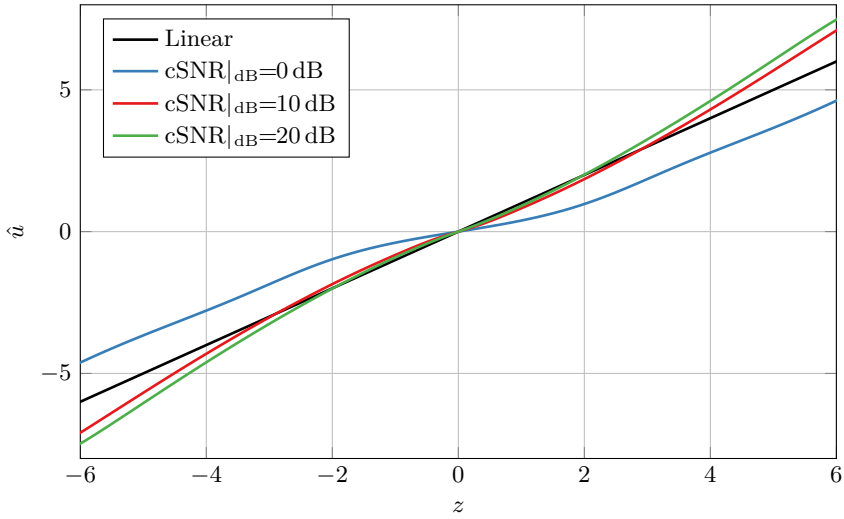

(b) Expander $\hat{u} = \mathrm{h}(z)$.

Figure 4.4: Optimized compressor and expander with $M = 1$ and $N = 1$ for a Laplacian source pdf for different channel qualities.

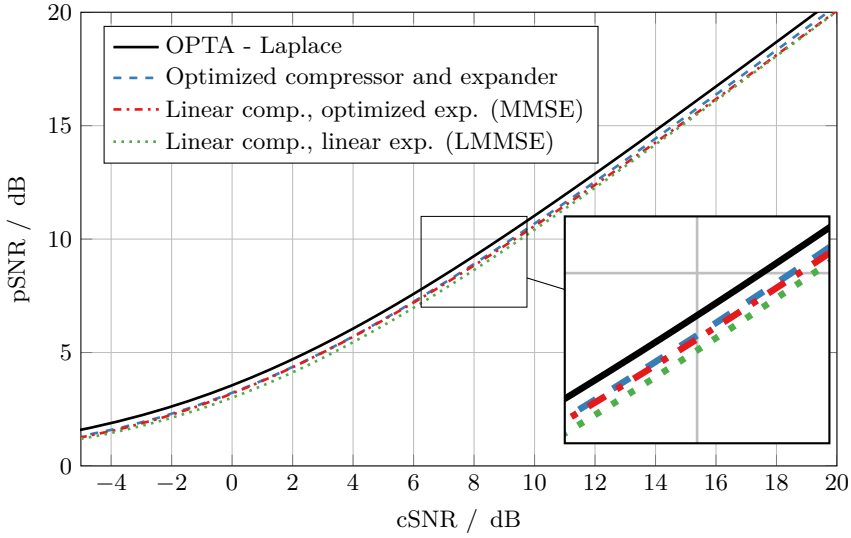

(a) Performance.

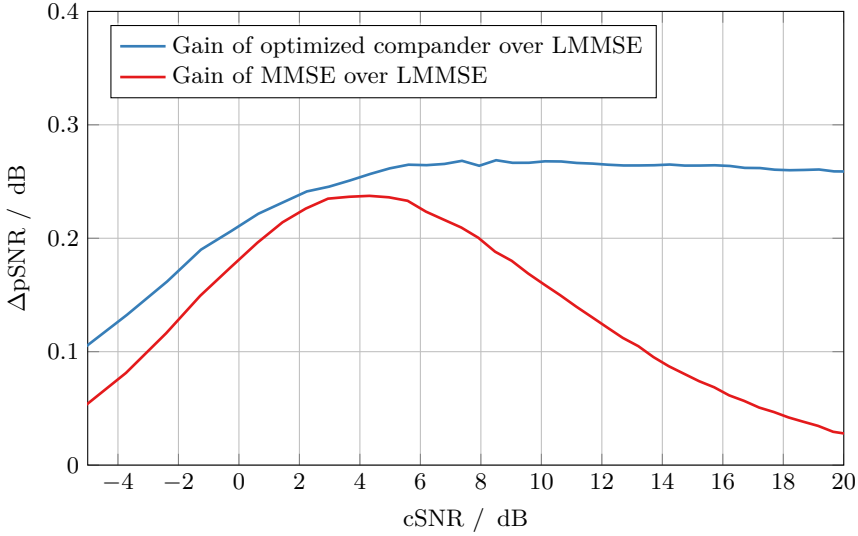

(b) Gains in ΔpSNR in dB.

Figure 4.5: Performance and gains of different compander systems with $M = 1$ and $N = 1$ for a Laplacian source pdf.

variants of spirals are presented. The second approach uses numerically optimized compressor functions.

4.4.1 Archimedes Spirals

This 1:2 mapping is described by two compressor functions g_1 and g_2 as in the previous section for the 1:1 case. The compressor functions can be parametrized and described analytically, but even for a fixed power of the source symbols $E\{u^2\} = 1$, depending on the pdf of the source symbols, the power after the usually nonlinear mapping $\tilde{g}_{1|2}$ cannot be stated analytically. Hence a normalization factor d is used to ensure $E\{y_{1|2}^2\} = 1$:

$$y_1 = g_1(u) = d \cdot \tilde{g}_1(u), \tag{4.5}$$

$$y_2 = g_2(u) = d \cdot \tilde{g}_2(u), \tag{4.6}$$

$$d = \frac{1}{\sqrt{\frac{1}{2} \cdot E\left\{\tilde{g}_1(u)^2 + \tilde{g}_2(u)^2\right\}}}. \tag{4.7}$$

Very common and beautiful 1:2 mappings are spirals. The Archimedes spiral has been introduced in [FR06]. Later, it was shown that spiral-like structures emerge after using a numerical optimization for 1:2 mappings [FRW07]. The Archimedes spiral used here has the property that any two source symbols which have the same Euclidean distance in the source space exhibit the same Euclidean distance in the channel space, walking along the spiral (hence, this type of Archimedes spiral is denoted "equidistant Archimedes spiral" in the following). This is desirable to achieve statistical independence between the channel noise and the source symbols [FR06]. The Archimedes spiral is parametrized with Δ which leads to denser spirals with smaller Δ:

$$\tilde{g}_1(u) = \sqrt{\frac{\Delta \cdot |u|}{0.16 \cdot \pi^2}} \cdot \operatorname{sign}(u) \cdot \cos\left(\sqrt{\frac{|u|}{0.16 \cdot \Delta}}\right), \tag{4.8a}$$

$$\tilde{g}_2(u) = \sqrt{\frac{\Delta \cdot |u|}{0.16 \cdot \pi^2}} \cdot \operatorname{sign}(u) \cdot \sin\left(\sqrt{\frac{|u|}{0.16 \cdot \Delta}}\right). \tag{4.8b}$$

Another variant of the Archimedes spiral is proposed in [HV07]. This 1:2 mapping can be interpreted as a mapping from a real to a complex value while the absolute value is kept constant, but the phase is modified according to the input value. A parameter c varies the density of the spiral with denser spirals for smaller c. Therefore this spiral is called amplitude/phase spiral in this work. The advantage of this mapping compared to the equidistant Archimedes spiral is the independence of the output power from the input pdf. This is especially useful in case of unknown densities with a given power when a normalization after the mapping should be avoided. In [HV07] this spiral is used in the context of a predictive speech codec for the analog transmission of the residual signal.

The definition of the amplitude/phase spiral is as follows with the density parameter c:

$$\tilde{g}_1(u) = u \cdot \cos\left(\frac{|u|}{c}\right), \tag{4.9a}$$

$$\tilde{g}_2(u) = -u \cdot \sin\left(\frac{|u|}{c}\right). \tag{4.9b}$$

In Figure 4.6 the space filling curves of these two approaches are compared. An

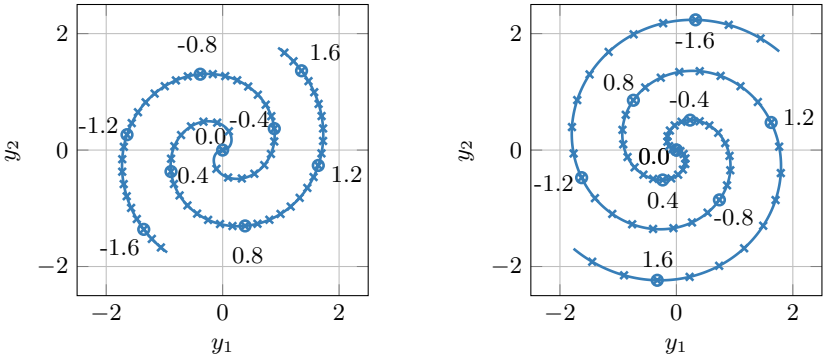

(a) Equidistant Archimedes spiral with $\Delta = 0.2$.

(b) Amplitude/phase spiral with $c = 0.2$.

Figure 4.6: Comparison of the equidistant Archimedes spiral and the amplitude/phase spiral with uniform source pdf.

input signal with uniform pdf with $\mathrm{E}\{u^2\} = 1$ and, thus, $-\sqrt{3} < u < \sqrt{3}$ is encoded and the resulting channel values are depicted. At some channel symbols, their corresponding source value is annotated. In Figure 4.6a, the equidistant Archimedes spiral is depicted. The Euclidean distance between the channel symbols (walking along the spiral) is in accordance to the Euclidean distance of the corresponding source symbols. The amplitude/phase spiral in Figure 4.6b exhibits much denser symbols at low channel values which increase the decoding errors since after transmission over a noisy channel, these symbols are harder to separate.

Figure 4.7 shows the performance of the equidistant Archimedes spiral and the amplitude/phase spiral for uniform and Gaussian source pdfs and different spiral densities. For these simulations, the expander which converts the received noisy channel symbols $\boldsymbol{z}$ to the source estimate $\hat{u}$ is a *Maximum Likelihood* (ML) estimator.

For both pdfs, it can be seen that the equidistant Archimedes spiral exhibits a superior performance. For example, the equidistant Archimedes spiral with $\Delta = 0.2$

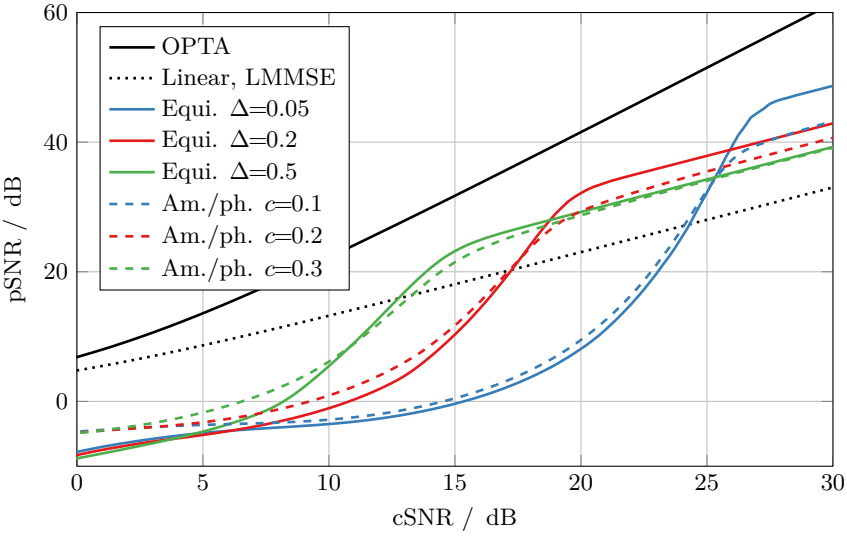

(a) Uniform source pdf.

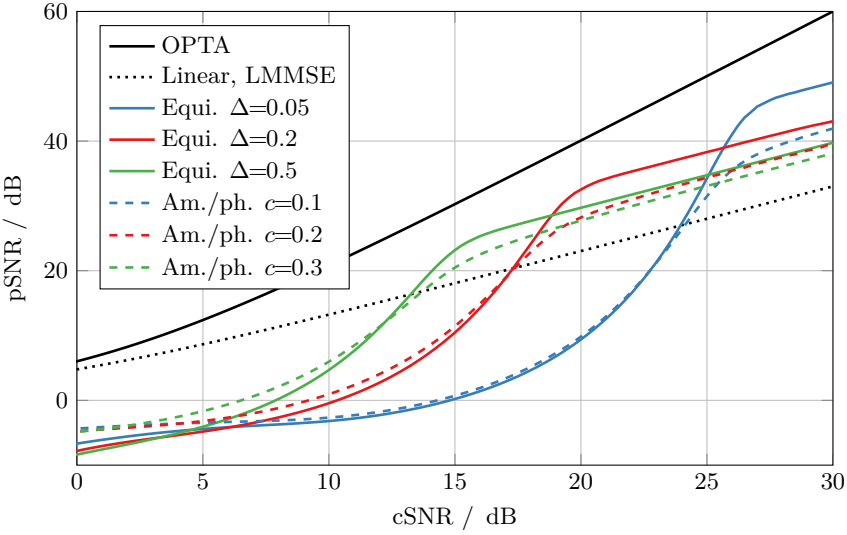

(b) Gaussian source pdf.

Figure 4.7: Performance of equidistant Archimedes spiral and amplitude/phase spiral. Linear mapping with LMMSE estimator for comparison.

shows the same high-cSNR performance as the amplitude/phase spiral with $c = 0.1$, but the waterfall region is at a cSNR which is 5.5 dB lower. The gain in pSNR is especially prominent for dense spirals as, e.g., the ones with $\Delta = 0.05$ and $c = 0.1$. It seems that the equidistance property of the equidistant Archimedes spiral leads to the superior performance compared to the amplitude/phase spiral. For comparison a linear compressor and expander with LMMSE estimation is depicted. For channel qualities above the waterfall region, the performance of all spirals is superior to the linear solution.

The performance of the overall 1:2 compressor and expander system depends not only on the compressor function, but also on the employed expander function. The expander can be designed using different statistical estimators as, e.g., ML, LMMSE or MMSE estimators. The LMMSE estimator is usually just defined for linear systems, but for nonlinear systems a concatenation of the LMMSE (as a preprocessing) and an ML estimator can be used (see Section 6.3.3 and [FVACGF13]). Figure 4.8 shows the performance of the different estimators for an equidistant Archimedes spiral with $\Delta = 0.3$ and a uniform and a Gaussian source pdf. As expected, the performance of the ML estimator is the worst of all employed estimators. Since the source statistics and the channel quality cannot be considered during the estimation, the performance only show marginal differences for both source pdfs. The LMMSE estimator which has knowledge of the cSNR

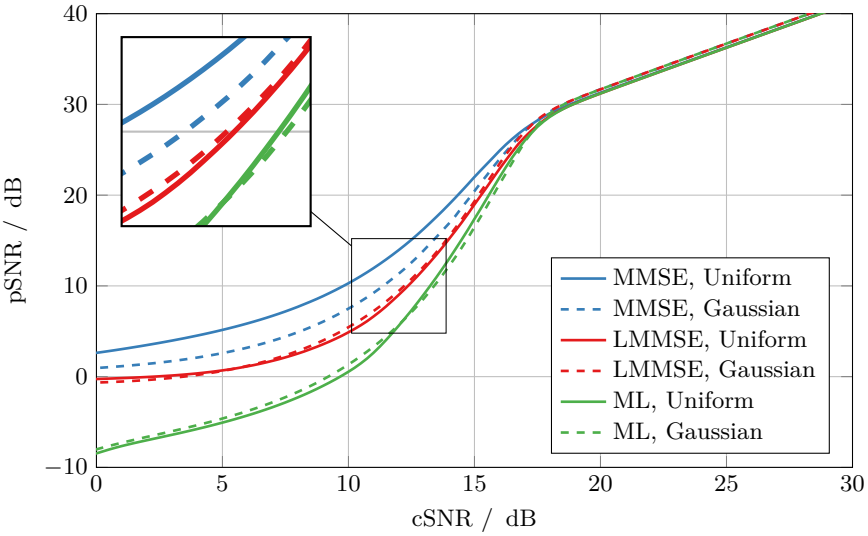

Figure 4.8: Performance of equidistant Archimedes spiral with $\Delta = 0.3$ and different source distributions and different estimators.

increases the performance, especially for low channel qualities and ensures a pSNR which is always higher than 0 dB. Again, the performance is independent of the source statistics. The MMSE estimator achieves a further performance gain, also here particularly for the low channel qualities. This effect for an Archimedes spiral is also shown in [RSV10a]. Since the MMSE estimator also incorporates the source statistics, the performance is different for uniform and Gaussian source pdfs. Since the Gaussian distribution is the hardest to estimate [CT06], the system with a uniform source pdf exhibits a higher performance than the Gaussian system. For high channel qualities, the performance of all estimators converges and in the uniform case, the pSNR is around 0.4 dB higher as for the Gaussian case. Considering the complexity and the performance of the employed estimators the most feasible solution probably is the LMMSE estimator.

4.4.2 Numerically Optimized Mappings

In the previous section different nonlinear 1:2 compressor functions which can be analytically described have been analyzed. In the following, a numerically optimized compressor is proposed which leads to a superior performance.

Problem Formulation

As in the 1:1 case, also in the 1:2 case an optimal compressor and expander pair is not known for any given source distribution. Therefore a numerical optimization has to be applied. The same approach as in Section 4.3 is employed which has been proposed in [Aky11, ARR10].

In the Appendix A, the expressions needed for the optimization are derived. The optimal expander for a given compressor is stated in Section A.2 as (A.7). To optimize the compressor for a given expander (Appendix A.3.1), the transmission power on the channel and the resulting overall MSE have to be jointly minimized. This joint minimization is facilitated with a Lagrangian cost functional (A.10) using the steepest decent method. Thus, the derivative of the functional with respect to each discretized point on the compressor function is calculated ((A.18) and (A.19)) and the minimization of the cost functional is achieved by following the derivatives (A.20) and (A.21).

Challenges

Unlike as in the 1:1 case, the optimization problem is not convex anymore. Thus, the cost functional (A.10) exhibits local minima and the initialization is of crucial importance. If an optimized mapping is sought for several channel qualities, often, a heuristic approach for the initialization is used: The outcome of the optimization for a bad channel quality is used as the initialization for the mapping for a higher channel quality. This “noisy relaxation” is motivated by the observation that the mappings only gradually change for rising channel qualities. The problem of the

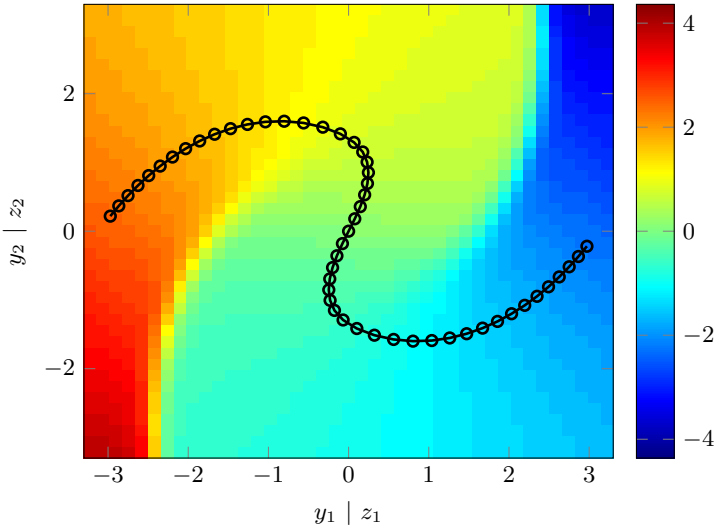

(a) $\mathrm{cSNR}|_{\mathrm{dB}} = 5.5\,\mathrm{dB}$, $\mathrm{pSNR}|_{\mathrm{dB}} = 10.2\,\mathrm{dB}$.

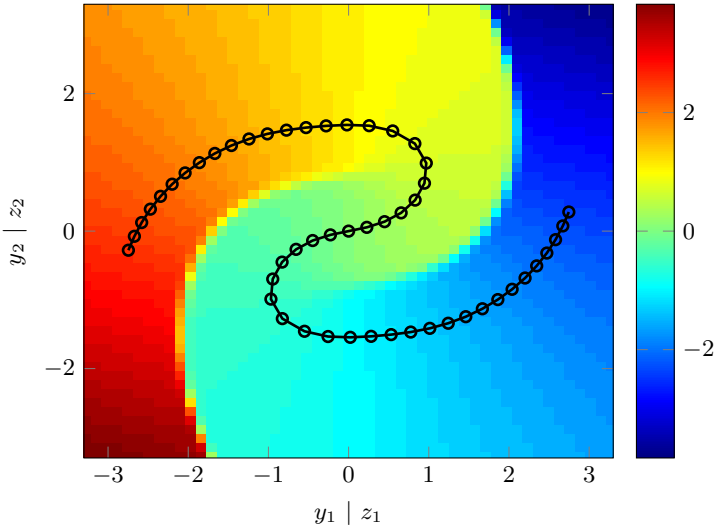

(b) $\mathrm{cSNR}|_{\mathrm{dB}} = 11.6\,\mathrm{dB}$, $\mathrm{pSNR}|_{\mathrm{dB}} = 19\,\mathrm{dB}$.

Figure 4.9: Numerically optimized compressor and expander. The spiral depicts the compressor $y_{1|2} = \mathrm{g}_{1|2}(u)$ for $|u| \leq 2.5$ and the colors depict the expander, which corresponds to the source estimate $\hat{u}$ for received values z_1 and z_2.

initialization for the first channel quality (the worst considered channel quality) remains. In total, even after achieving a seemingly nice and well performing mapping, the question remains if this mapping is a global optimum. Furthermore, the steepest decent method used here is extremely sensitive to the optimization parameters such as the resolution of the discretization of the source and channel symbol range or the thresholds for switching between optimizing the encoder or the decoder.

Simulation Results

In this section the results for a numerically optimized compressor and expander are presented. A Gaussian source is assumed while for the optimization of the compressor, while values above $|u| = 2.5$ are omitted. The optimization is initialized with an Archimedes spiral with $\Delta = 2$ at $\mathrm{cSNR}|_{\mathrm{dB}} = 5.5\,\mathrm{dB}$. The outcome of one optimization is used for the next higher channel quality (noisy relaxation). As the expander an MMSE estimator is employed. To calculated the expander, the compressor function is linearly extrapolated to allow for a larger source range.

Figure 4.9 shows the result of the optimization for two channel qualities

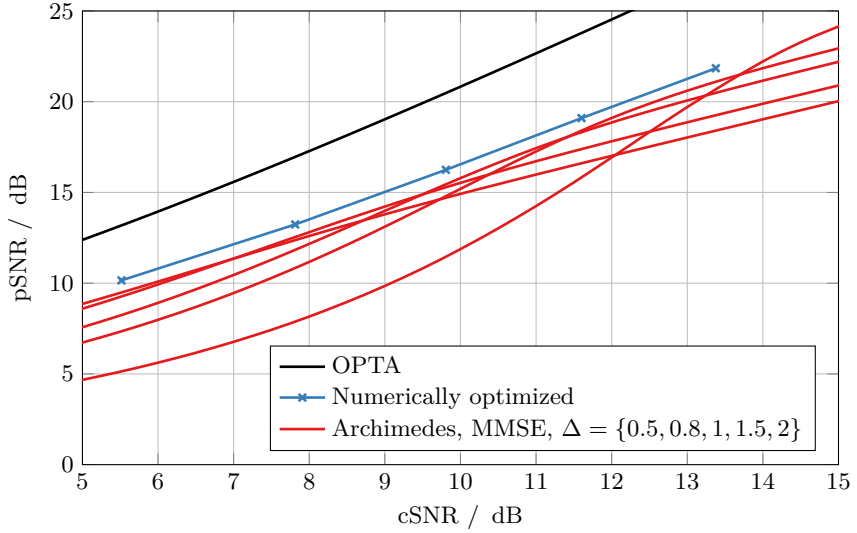

Figure 4.10: Performance of the numerically optimized mapping and an equidistant Archimedes spiral with MMSE estimator and different densities for Gaussian source symbols. Lower Δ correspond to smaller distances between the spiral arms which lead to a better pSNR at high channel qualities.

($\mathrm{cSNR}|_{\mathrm{dB}} = 5.5\,\mathrm{dB}$ and $\mathrm{cSNR}|_{\mathrm{dB}} = 11.6\,\mathrm{dB}$). The black curve is the compressor function, while source symbols above $|u| = 2.5$ are omitted. 50 circles are drawn for each increment of 0.1. It is interesting to note that the equidistance property also holds for the numerically optimized compressor. The curve which emerges after the numerical optimization resembles a spiral, yet its shape is not the same as the Archimedes spiral. The arms of the spiral for the better channel are closer together than the arms of the spiral for the worse channel and the equidistant symbols are further apart which leads to a higher pSNR.

The expander, i.e., the MMSE estimator, is depicted for each symbol z_1 and z_2 which could possibly be received after transmission over an AWGN channel. The value for the estimate $\hat{u}$ of the expander is identified by different colors. Between the arms of the spiral, a transition region between the corresponding values of each arm occurs. For a higher channel quality, the transition is more abrupt, since the estimator relies more on the received symbols than the a-priori known source statistics. This observation has already been made for Archimedes spirals in [RSV10a].

To evaluate the performance of the optimized mapping, Monte Carlo simulations are employed. A Gaussian source is used while values exceeding the range of the compressor are clipped, but the distortion in MSE is still calculated using the original source symbols. The performance of the optimized mapping is depicted in Figure 4.10. For comparison, the performance of several equidistant Archimedes spirals with different densities and MMSE estimators are shown. The numerically optimized compressor and expander exceeds the performance of the all the Archimedes spirals by approximately 0.7 dB in terms of pSNR. The gap to OPTA at $\mathrm{cSNR}|_{\mathrm{dB}} = 10\,\mathrm{dB}$ has shrunk to 2.4 dB in terms of cSNR and 4.28 dB in terms of pSNR.

4.5 Discussion

For several scenarios, nonlinear compander and space filling curves achieve a gain compared to linear mappings. In case of the 1:1 mapping and a uniform source distribution a maximum gain of 0.4 dB in terms of pSNR is achieved. For a Laplacian distribution, the gain is smaller and for a Gaussian source, a linear mapping is already optimal. Closed form solutions for the compressor and expander functions are not known, hence, numerical optimization is necessary. Fortunately, in case of the 1:1 mapping, the problem is convex and therefore optimal solutions are found using, e.g., steepest decent methods.

In case of higher-dimensional mappings (1:2), two variants of the Archimedes spiral are compared which both can be described analytically. The Archimedes spiral with equidistant symbols exhibits a superior performance than the spiral which has the same output and input power for each symbol. Both variants are superior to a linear transmission system. The same numerical optimization as

above is applied to the 1:2 case and here a gain of 0.7 dB in terms of pSNR over the equidistant Archimedes spiral can be achieved. In contrast to the 1:1 case, the numerical optimization algorithm has to solve a non-convex problem which greatly increases the sensitivity to the initialization and other simulation parameters and additionally does not guarantee finding the optimal solution.

The numerically optimized mappings exhibit a slightly higher performance than analytically describable mappings, but the question remains if a gain of 0.4 dB (1:1 case) or 0.7 dB (1:2 case) can justify a complex offline optimization and a higher complexity due to the necessary lookup tables during transmission.

In theory, higher gains are expected for higher-dimensional mappings in which vectors of source symbols are nonlinearly mapped to vectors of channel symbols [FR07]. So far, conventional optimization approaches have lead to unsatisfactory results, e.g., for the 1:3 case in [FRW07]. Therefore, other numerical optimization strategies such as, e.g., deterministic annealing [MAR13] are promising candidates to optimize more complex mappings with longer block lengths.

Chapter 5

Analog Modulo Block Codes

5.1 Introduction

In Section 3.2 and in [RSV09], the performance of *Linear Analog Block Codes* (LABCs) has been derived. A source vector is multiplied with a non-square matrix to generate more channel symbols than source symbols to exploit the available channel uses to increase the performance. As already argued in Section 2.4.2, a purely linear encoding system cannot attain capacity when using redundancy, which is demonstrated by the poor performance of LABCs. The linearity of the LABCs is the limiting factor to achieve a higher performance (Section 2.4.2). In this chapter, a nonlinear modulo operation is appended to the matrix multiplication and the resulting *Analog Modulo Block Codes* (AMBCs) are analyzed.

Continuous amplitude systems employing similar operations such as a modulo operation are known in literature. E.g., in [TK12] systems similar to AMBCs operating with just one source symbol, called shift maps, are proposed. A combination of the shift maps with a spherical mapping are introduced in [VC03]. Another system first quantizes one source symbol and uses the quantized value as a channel symbol. Then it repeatedly quantizes the quantization error from the last quantization to generate more channel symbols. In the end the quantization error itself is transmitted as one channel symbol [KR09].

In this chapter, the approach of multiplying the source vector with a non-square matrix and applying a modulo operation to the result is proposed. It offers more degrees of freedom than the above mentioned systems, since several source symbols can be combined to one code vector to potentially improve the overall performance compared to single symbol systems.

In Section 5.2 the system model of AMBCs is introduced. The analysis in Section 5.3 reveals that after a rotation of the generated code vectors, discrete-valued (discrete part) and continuous-amplitude (analog part) dimensions emerge. The code vectors in the discrete part form a regular lattice which can be exploited for the design of efficient decoders (Section 5.4). The question how to design the new codes is tackled in Section 5.5 while many supporting simulation results are presented.

Most of the results described in this chapter are based on [Sch13] and [SRV15].

5.2 System Model

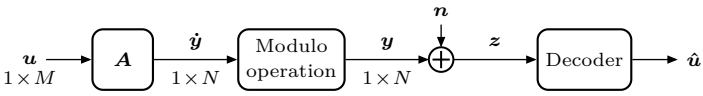

Figure 5.1: System model of an AMBC.

Figure 5.1 shows the system model of AMBCs. A source vector $\boldsymbol{u}$ with dimensions $1 \times M$ is multiplied with a real-valued code (generator) matrix $\boldsymbol{A} \in \mathbb{R}^{M \times N}$ leading to the auxiliary vector $\dot{\boldsymbol{y}}$:

$$\dot{\boldsymbol{y}} = \boldsymbol{u} \cdot \boldsymbol{A}. \tag{5.1}$$

This part of the transmitter strongly resembles an LABC (Section 3.2). The necessity of nonlinear operations to improve the performance compared to purely linear transmissions systems is already stated in Section 2.4.2, thus, the AMBCs employ a modulo operation as the nonlinearity.

A special modulo operation $\mathrm{smod}_m(\cdot)$ is employed which is defined in (5.2) and visualized in Figure 5.2. It is applied to each element of $\dot{\boldsymbol{y}}$ to yield $\boldsymbol{y}$. The modulo operation generates output values in the range of $(-m, m)$ and is symmetric around 0 (hence, "*s*mod"):

$$\mathrm{smod}_m(y) = \big((y + m) \mod 2m\big) - m. \tag{5.2}$$

To ensure unambiguousness, in this work the range of the input values $\boldsymbol{u}$ is limited

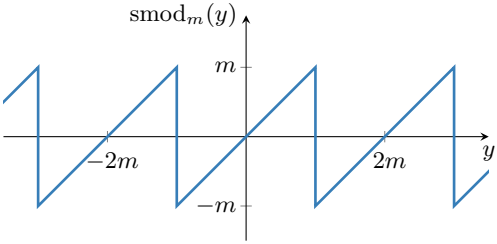

Figure 5.2: Modified (symmetric) modulo function.

to $(-m, m)$ and a systematic coding matrix is used, i.e., part of $\boldsymbol{A}$ is an identity matrix:

$$\boldsymbol{A} = [\mathbb{1} \;\; \tilde{\boldsymbol{A}}]. \tag{5.3}$$

The whole encoding operation can be stated as:

$$\boldsymbol{y} = \mathrm{smod}_m(\dot{\boldsymbol{y}}) = \mathrm{smod}_m(\boldsymbol{u} \cdot \boldsymbol{A})\,. \tag{5.4}$$

The first M entries of $\dot{\boldsymbol{y}}$ are not affected by the modulo operation, since the input values of $\boldsymbol{u}$ are limited to $(-m, m)$ and the first M columns of $\boldsymbol{A}$ are formed by an identity matrix. A transmission with $\boldsymbol{A}_0$ as the code matrix and m_0 as the parameter for the modulo operation is equivalent to employing $\boldsymbol{A} = \frac{1}{m}\boldsymbol{A}_0$ and $m = 1$, since the power of the channel symbols $\boldsymbol{y}$ is considered for evaluating the channel quality cSNR. In the following, without loss of generality,

$$m = 1 \tag{5.5}$$

is employed for simplicity, but in many derivations m is explicitly stated to keep track of its influence.

After encoding, the channel symbols $\boldsymbol{y}$ are transmitted over an *Additive White Gaussian Noise* (AWGN) channel which adds white Gaussian noise $\boldsymbol{n}$ to yield the received vector $\boldsymbol{z}$. A decoder generates an estimate $\hat{\boldsymbol{u}}$ of the initially sent source symbols $\boldsymbol{u}$.

As a quick glance at the effect of encoding AMBCs, two examples are given in the following. Figure 5.3 depicts the valid code vectors of an AMBC with $\boldsymbol{A} = [1 \;\; 2]$, i.e., of a $[1 \;\; 2]$-AMBC. The range of the input values is $(-1, 1)$ and $m = 1$. The first dimension y_1 of the channel vector is equivalent to the scalar source symbol u while $y_2 = \mathrm{smod}_1(2 \cdot u)$ is a scaled version (factor of 2 in u direction) of the modulo function in Figure 5.2. In total, three parallel arms form the channel space of this code. The box which encloses the valid code vectors is called *unit hyper cube*.

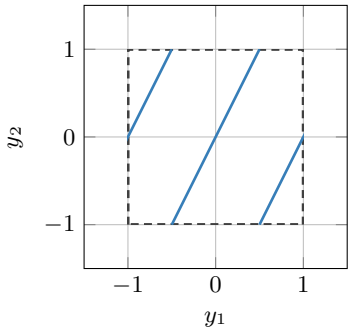

Figure 5.3: Valid code vectors of the $[1 \;\; 2]$-AMBC.

Figure 5.4 visualizes the valid code vectors of the $[1 \;\; 2 \;\; 3]$-AMBC. Here, three channel uses are employed and therefore a 3-dimensional channel space[1] is plotted in Figure 5.4a. The correspondence of the input values u to the channel symbols is visualized by their color. Again, a structure of five parallel arms emerges which

[1] The N-dimensional channel space consists of all points which can be described by an N-dimensional channel vector $\boldsymbol{y}$.

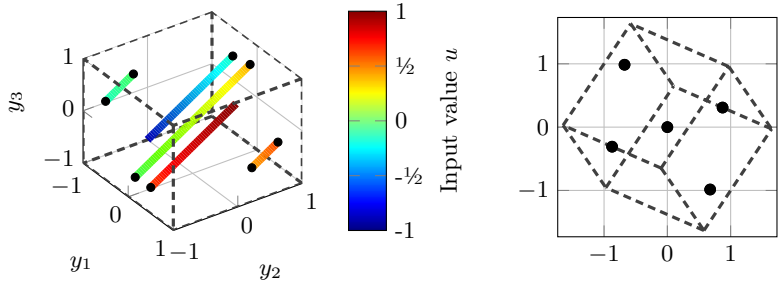

(a) Valid code vectors.

(b) Discrete part.

Figure 5.4: Valid code vectors of the [1 2 3]-AMBC. The color of the points in (a) denotes the corresponding input value u. Subfigure (b) shows a rotated version of the valid code vectors which is referred to as the discrete part.

all fit into the unit hyper cube with a maximum absolute value of $m = 1$ in each dimension. Rotating this structure appropriately yields Figure 5.4b in which the 3-dimensional arms are projected to points in a 2-dimensional plane.

As already stated in Section 2.4, in nonlinear analog transmission systems, discrete and continuous-amplitude dimensions emerge. Here, the discrete dimensions are called "discrete part" of the AMBC and the continuous-amplitude dimensions "analog part". The points observed in Figure 5.4b are be denoted "discrete points" of the AMBC and will play an important role in the analysis of the codes.

5.3 Analysis

In the following sections, systematic AMBCs as defined in (5.3) are analyzed. A rotation matrix $\boldsymbol{G}$ is derived from the code matrix $\boldsymbol{A}$ in Section 5.3.1 which allows to align the arms with the coordinate axis as in Figure 5.4b. This is especially useful as shown in Section 5.3.2 to enable the independent analysis and decoding of the discrete and the analog part of the code vectors. The emerging lattice in the discrete part is described in Section 5.3.3. For high channel qualities (cSNR), the discrete part can be decoded with negligible errors. In Section 5.3.4 it is shown how the high-cSNR performance of an AMBC can directly be derived from the code matrix $\boldsymbol{A}$.

5.3.1 Rotation Matrix

The analysis and also the decoding of AMBC makes use of a rotation matrix, while the rotation is conducted by multiplying the code vectors with the matrix $\boldsymbol{G} \in \mathbb{R}^{N \times N}$. This matrix rotates the arms (Figure 5.4a) forming the valid code vectors such, that they are in parallel to the coordinate axis (Figure 5.4b). Arms in parallel to the coordinate axis are achieved if a multiplication of the code matrix $\boldsymbol{A}$ with the rotation matrix $\boldsymbol{G}$ yields zeros in the last D (5.28) dimensions of the resulting matrix:

$$\boldsymbol{A} \cdot \boldsymbol{G} = \boldsymbol{P} = \begin{bmatrix} \tilde{\boldsymbol{P}} & \mathbb{O}_{M \times D} \end{bmatrix}, \tag{5.6}$$

with the zero matrix $\mathbb{O}$ with dimension $M \times D$.

Since $\boldsymbol{G}$ is a rotation matrix, it is orthogonal ($\boldsymbol{G}^{\mathrm{T}} \cdot \boldsymbol{G} = \mathbb{1} \Leftrightarrow \boldsymbol{G}^{\mathrm{T}} = \boldsymbol{G}^{-1}$) and it holds:

$$\boldsymbol{A} = \boldsymbol{P} \cdot \boldsymbol{G}^{-1} = \boldsymbol{P} \cdot \boldsymbol{G}^{\mathrm{T}} \tag{5.7}$$

$$\Rightarrow \boldsymbol{A}^{\mathrm{T}} = \boldsymbol{G} \cdot \boldsymbol{P}^{\mathrm{T}}. \tag{5.8}$$

The matrices $\boldsymbol{G}$ and $\boldsymbol{P}$ are usually ambiguous for a given matrix $\boldsymbol{A}$. One possibility to obtain a rotation matrix is the QR decomposition[2]of $\boldsymbol{A}^{\mathrm{T}}$ to $\boldsymbol{Q}$ and $\boldsymbol{R}$:

$$\boldsymbol{A}^{\mathrm{T}} = \boldsymbol{Q} \cdot \boldsymbol{R} \quad \Rightarrow \quad \boldsymbol{A} = \boldsymbol{R}^{\mathrm{T}} \cdot \boldsymbol{Q}^{\mathrm{T}}. \tag{5.9}$$

The matrix $\boldsymbol{R} \in \mathbb{R}^{N \times M}$ is an upper right triangle matrix and $\boldsymbol{Q} \in \mathbb{R}^{N \times N}$ is an orthogonal rotation matrix.

The rotation matrix $\boldsymbol{G}$ and the matrix $\boldsymbol{P}$ are defined as follows from the result of the QR decomposition:

$$\boldsymbol{G} = \boldsymbol{Q}, \tag{5.10}$$

$$\boldsymbol{P} = \boldsymbol{R}^{\mathrm{T}}. \tag{5.11}$$

In the following, it is elaborated why a QR decomposition is especially suited for finding an appropriate rotation matrix. It decomposes the matrix $\boldsymbol{A}$ into a rotation matrix with dimension $N \times N$ and a matrix which consists of zeros outside of the leftmost square region with dimension $M \times M$ (Equations (5.9) and (5.6)):

$$\boldsymbol{A} = \boldsymbol{P} \cdot \boldsymbol{G}^{\mathrm{T}} = \begin{bmatrix} \tilde{\boldsymbol{P}}_{M \times M} & \mathbb{O}_{M \times D} \end{bmatrix} \cdot \boldsymbol{G}^{\mathrm{T}}. \tag{5.12}$$

Thus, the effect of multiplying any vector with $\boldsymbol{A}$ is decomposed into two steps. The first step is to multiply the vector with $\tilde{\boldsymbol{P}}$ and add D dimensions which are set to 0. The second step rotates the result with $\boldsymbol{G}^{\mathrm{T}}$.

[2]The *complete* QR decomposition is employed, which yields a $\boldsymbol{Q}$ with dimension $N \times N$.

For analysis or decoding purposes, the last step, i.e., the rotation, can be undone by applying the transposed $\boldsymbol{G}^{\mathrm{T}}$ which again is the original rotation matrix $\boldsymbol{G} = \left(\boldsymbol{G}^{\mathrm{T}}\right)^{\mathrm{T}}$:

$$\boldsymbol{A} \cdot \boldsymbol{G} = \boldsymbol{P} \cdot \boldsymbol{G}^{\mathrm{T}} \cdot \boldsymbol{G} = \boldsymbol{P} = \begin{bmatrix} \tilde{\boldsymbol{P}} & \mathbb{O}_{M \times D} \end{bmatrix}. \tag{5.13}$$

Due to the modulo operation, the source symbols are distributed across parallel arms (Figure 5.3), and the (back) rotation using $\boldsymbol{G}$ aligns them with the coordinate axis.

Thus, any decomposition of $\boldsymbol{A}$ which yields a rotation matrix and a matrix with zeros outside the $M \times M$ square can be used for finding an appropriate rotation matrix for analysis and decoding.

Using the Singular Value Decomposition

Another method to obtain the matrices $\boldsymbol{G}$ and $\boldsymbol{P}$ is the *Singular Value Decomposition* (SVD) [GVL96]:

$$\boldsymbol{A} = \boldsymbol{U} \cdot \boldsymbol{\Sigma} \cdot \boldsymbol{V}^{\mathrm{T}} \tag{5.14}$$

with

$$\boldsymbol{U} \in \mathbb{R}^{M \times M}, \quad \boldsymbol{\Sigma} \in \mathbb{R}^{M \times N}, \quad \boldsymbol{V} \in \mathbb{R}^{N \times N}. \tag{5.15}$$

The matrices $\boldsymbol{U}$ and $\boldsymbol{V}$ are orthogonal and, thus, act as rotation (and/or mirror) matrices. The matrix $\boldsymbol{\Sigma}$ is composed of a diagonal matrix and a zero matrix. The diagonal entries $\gamma_1 \geq \gamma_2 \geq \ldots \gamma_M \geq 0$ are the singular values of $\boldsymbol{A}$:

$$\boldsymbol{\Sigma} = \begin{bmatrix} \tilde{\boldsymbol{\Sigma}} & \mathbb{O}_{M \times D} \end{bmatrix} \quad \text{with} \quad \tilde{\boldsymbol{\Sigma}} = \begin{bmatrix} \gamma_1 & 0 & \ldots & 0 \\ 0 & \gamma_2 & \ldots & 0 \\ \vdots & \vdots & \ddots & \vdots \\ 0 & 0 & \ldots & \gamma_M \end{bmatrix}. \tag{5.16}$$

The rotation matrix $\boldsymbol{G}$ and the matrix $\boldsymbol{P}$ are chosen as follows from the result of the SVD decomposition:

$$\boldsymbol{G} = \boldsymbol{V}, \tag{5.17}$$

$$\boldsymbol{P} = \boldsymbol{U} \cdot \boldsymbol{\Sigma}. \tag{5.18}$$

From (5.16) it can easily be seen that $\boldsymbol{P}$ is zero outside a square region with dimension $M \times M$.

The pseudoinverse

$$\boldsymbol{A}^{+} = \boldsymbol{A}^{\mathrm{T}} \cdot \left(\boldsymbol{A} \cdot \boldsymbol{A}^{\mathrm{T}}\right)^{-1} \quad \text{with} \quad \boldsymbol{A} \cdot \boldsymbol{A}^{+} = \mathbb{1} \tag{5.19}$$

of $\boldsymbol{A} = \boldsymbol{U} \cdot \boldsymbol{\Sigma} \cdot \boldsymbol{V}^{\mathrm{T}}$ can be calculated using the results from the SVD:

$$\boldsymbol{A}^{+} = \boldsymbol{V} \cdot \boldsymbol{\Sigma}^{+} \cdot \boldsymbol{U}^{\mathrm{T}} \quad \text{with} \quad \boldsymbol{\Sigma}^{+} = \begin{bmatrix} \tilde{\boldsymbol{\Sigma}}^{-1} \\ \mathrm{O} \end{bmatrix}. \tag{5.20}$$

5.3.2 Rotated Code Vectors – Discrete and Analog Part

Valid code vectors can be described using the modulo operation (5.4), but also by adding a scaled vector $\boldsymbol{s}$ consisting of integers to the argument of the modulo operation:

$$\boldsymbol{y} = \mathrm{smod}_m(\boldsymbol{u} \cdot \boldsymbol{A}) = \boldsymbol{u} \cdot \boldsymbol{A} + 2m \cdot \boldsymbol{s}, \tag{5.21}$$

with the *jump vector*

$$\boldsymbol{s} = -\left\lceil \frac{\boldsymbol{u} \cdot \boldsymbol{A}}{2m} \right\rfloor \in \mathbb{Z}^{1 \times N}. \tag{5.22}$$

The jump vector $\boldsymbol{s}$ results directly from the modulo operation, while the notation $\lceil \cdot \rfloor$ denotes rounding the argument element-wise to the nearest integer.

After transmission of $\boldsymbol{y}$ over an AWGN channel with additive noise $\boldsymbol{n}$ the received vector $\boldsymbol{z}$ may be described as follows:

$$\boldsymbol{z} = \boldsymbol{y} + \boldsymbol{n} = \mathrm{smod}_m(\boldsymbol{u} \cdot \boldsymbol{A}) + \boldsymbol{n} = \boldsymbol{u} \cdot \boldsymbol{A} + 2m \cdot \boldsymbol{s} + \boldsymbol{n} \tag{5.23}$$

$$\overset{(5.7)}{=} \boldsymbol{u} \cdot \boldsymbol{P} \cdot \boldsymbol{G}^{\mathrm{T}} + 2m \cdot \boldsymbol{s} + \boldsymbol{n}, \tag{5.24}$$

and after rotating with $\boldsymbol{G}$, the vector $\boldsymbol{z}_{\mathrm{rot}}$ is given as:

$$\boldsymbol{z}_{\mathrm{rot}} = \boldsymbol{z} \cdot \boldsymbol{G} = \boldsymbol{u} \cdot \boldsymbol{P} \cdot \boldsymbol{G}^{\mathrm{T}} \cdot \boldsymbol{G} + 2m \cdot \boldsymbol{s} \cdot \boldsymbol{G} + \boldsymbol{n} \cdot \boldsymbol{G} \tag{5.25}$$

$$= \boldsymbol{u} \cdot \boldsymbol{P} + 2m \cdot \boldsymbol{s} \cdot \boldsymbol{G} + \boldsymbol{n}_{\mathrm{rot}}, \tag{5.26}$$

with $\boldsymbol{n}_{\mathrm{rot}} = \boldsymbol{n} \cdot \boldsymbol{G}$.

After the rotation, the arms in the channel space are in parallel to the coordinate axis and therefore the points of the discrete part and the components in parallel to the coordinate axis (analog part) can be analyzed separately. For the further derivations, the rotation matrix $\boldsymbol{G}$ is partitioned into submatrices:

$$\boldsymbol{G} = \big[\underbrace{\boldsymbol{G}_{\mathrm{an}}}_{\in \mathbb{R}^{N \times M}} \quad \underbrace{\boldsymbol{G}_{\mathrm{dis}}}_{\in \mathbb{R}^{N \times D}} \big] \quad \text{and} \quad \boldsymbol{G}_{\mathrm{dis}} = \begin{bmatrix} \boldsymbol{G}_{12} \\ \boldsymbol{B}' \end{bmatrix} \quad \text{with} \quad \boldsymbol{B}' = \frac{\boldsymbol{B}}{2m} \in \mathbb{R}^{D \times D}. \tag{5.27}$$

The submatrix $\boldsymbol{G}_{\mathrm{an}}$ influences only the analog part of the rotated code vectors (see (5.36)) while $\boldsymbol{G}_{\mathrm{dis}}$ influences the discrete part (see (5.38)). The submatrix $\boldsymbol{G}_{\mathrm{dis}}$ is further partitioned to $\boldsymbol{G}_{12}$ and $\boldsymbol{B}'$, a scaled version of the base matrix $\boldsymbol{B}$ which

generates a lattice in the discrete part (see Section 5.3.3). The base matrix $\boldsymbol{B}$ has the dimension $D \times D$ which corresponds to the number of discrete dimensions:

$$D = N - M. \tag{5.28}$$

After partitioning the rotation matrix, the code matrix $\boldsymbol{A}$ may be expressed as:

$$\boldsymbol{A} = \boldsymbol{P} \cdot \boldsymbol{G}^{\mathrm{T}} = \begin{bmatrix} \tilde{\boldsymbol{P}} & \mathbb{O} \end{bmatrix} \cdot \begin{bmatrix} \boldsymbol{G}_{\mathrm{an}}^{\mathrm{T}} \\ \boldsymbol{G}_{\mathrm{dis}}^{\mathrm{T}} \end{bmatrix} = \tilde{\boldsymbol{P}} \cdot \boldsymbol{G}_{\mathrm{an}}^{\mathrm{T}}. \tag{5.29}$$

The rotated received vector $\boldsymbol{z}_{\mathrm{rot}}$ in (5.26) can also be partitioned into an analog part and a discrete part:

$$\begin{aligned} \boldsymbol{z}_{\mathrm{rot}} &= \begin{bmatrix} \boldsymbol{z}_{\mathrm{an}} & \boldsymbol{z}_{\mathrm{dis}} \end{bmatrix} && (5.30) \\ &= \boldsymbol{z} \cdot \boldsymbol{G} && (5.31) \\ &= \boldsymbol{u} \cdot \underbrace{\begin{bmatrix} \tilde{\boldsymbol{P}} & \mathbb{O} \end{bmatrix}}_{\boldsymbol{P}} + 2m \cdot \boldsymbol{s} \cdot \underbrace{\begin{bmatrix} \boldsymbol{G}_{\mathrm{an}} & \boldsymbol{G}_{\mathrm{dis}} \end{bmatrix}}_{\boldsymbol{G}} + \underbrace{\begin{bmatrix} \boldsymbol{n}_{\mathrm{rot,an}} & \boldsymbol{n}_{\mathrm{rot,dis}} \end{bmatrix}}_{\boldsymbol{n} \cdot \boldsymbol{G}}. && (5.32) \end{aligned}$$

The rotated noise vector $\boldsymbol{n}_{\mathrm{rot}}$ can also be partitioned in one part which influences the analog part and one which influences the discrete part[3]. Consequently, also for the rotated valid code vectors, a discrete and an analog part can be defined:

$$\begin{aligned} \boldsymbol{y}_{\mathrm{rot}} &= \begin{bmatrix} \boldsymbol{y}_{\mathrm{an}} & \boldsymbol{y}_{\mathrm{dis}} \end{bmatrix} && (5.33) \\ &= \boldsymbol{y} \cdot \boldsymbol{G} && (5.34) \\ &= \boldsymbol{u} \cdot \underbrace{\begin{bmatrix} \tilde{\boldsymbol{P}} & \mathbb{O} \end{bmatrix}}_{\boldsymbol{P}} + 2m \cdot \boldsymbol{s} \cdot \underbrace{\begin{bmatrix} \boldsymbol{G}_{\mathrm{an}} & \boldsymbol{G}_{\mathrm{dis}} \end{bmatrix}}_{\boldsymbol{G}}. && (5.35) \end{aligned}$$

Analog part The analog part, thus, is:

$$\boldsymbol{z}_{\mathrm{an}} = \boldsymbol{z} \cdot \boldsymbol{G}_{\mathrm{an}} = \boldsymbol{u}\tilde{\boldsymbol{P}} + 2m \cdot \boldsymbol{s} \cdot \boldsymbol{G}_{\mathrm{an}} + \boldsymbol{n}_{\mathrm{rot,an}} \quad \in \mathbb{R}^{1 \times M}, \tag{5.36}$$

$$\boldsymbol{y}_{\mathrm{an}} = \boldsymbol{u} \cdot \tilde{\boldsymbol{P}} + 2m \cdot \boldsymbol{s} \cdot \boldsymbol{G}_{\mathrm{an}} \quad \in \mathbb{R}^{1 \times M}. \tag{5.37}$$

Discrete part For the discrete part it holds:

$$\begin{aligned} \boldsymbol{z}_{\mathrm{dis}} &= \boldsymbol{z} \cdot \boldsymbol{G}_{\mathrm{dis}} = \boldsymbol{u} \cdot \mathbb{O} + 2m \cdot \boldsymbol{s} \cdot \boldsymbol{G}_{\mathrm{dis}} + \boldsymbol{n}_{\mathrm{rot,dis}} \\ &= 2m \cdot \boldsymbol{s} \cdot \boldsymbol{G}_{\mathrm{dis}} + \boldsymbol{n}_{\mathrm{rot,dis}} \quad \in \mathbb{R}^{1 \times D}, && (5.38) \\ \boldsymbol{y}_{\mathrm{dis}} &= 2m \cdot \boldsymbol{s} \cdot \boldsymbol{G}_{\mathrm{dis}} \quad \in \mathbb{R}^{1 \times D}. && (5.39) \end{aligned}$$

Equation (5.38) and (5.39) show that the discrete part of the rotated received vector just depends on the vector $\boldsymbol{s}$ with integer entries and the submatrix $\boldsymbol{G}_{\mathrm{dis}}$ of $\boldsymbol{G}$. The length of the vector is D and the channel noise is expressed as $\boldsymbol{n}_{\mathrm{rot,dis}}$.

[3] Although, the noise has the index $_{\mathrm{dis}}$, the noise itself is not discrete but continuous-amplitude.

5.3.3 Lattice in the Discrete Part

The discrete part of the code is a subspace of all code vectors which are perpendicular to the arms of the code. By rotating the code vectors with $\boldsymbol{G}_{\text{dis}}$, the discrete part is in parallel to the last D dimensions. Thus, the discrete part is obtained by rotating the code vectors and then ignoring the first M dimensions which form the analog part.

The discrete part is crucial for the performance of AMBCs for bad channels. The larger the Euclidean distance between the points, the more robust is the detection of the points against channel noise (Section 2.4.4).

Figure 5.5b shows the discrete part of the code in Figure 5.5a.

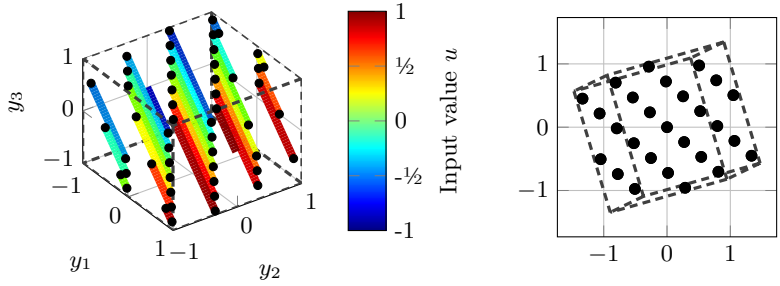

(a) Valid code vectors $\boldsymbol{y}$. **(b)** Discrete part $\boldsymbol{y}\boldsymbol{G}_{\text{dis}}$.

Figure 5.5: Valid code vectors of the $[1 \;\; 6 \;\; -20]$-AMBC. Subfigure (b) shows a rotated version of the valid code vectors which is the discrete part.

The discrete part follows a periodic structure, a lattice. For systematic AMBCs all valid discrete points are integer linear combinations of D base vectors.

Due to the modulo operation and the limited input range, the valid code vectors of the channel symbols $\boldsymbol{y}$ are bordered by the unit hyper cube with an edge length of $2 \cdot m$. After the rotation with $\boldsymbol{G}_{\text{dis}}$, the discrete points are still bordered by the projection of the rotated version of the unit hyper cube (Figure 5.5b).

Since systematic AMBCs ($\boldsymbol{A} = \begin{bmatrix} \mathbb{1} & \tilde{\boldsymbol{A}} \end{bmatrix}$) are employed, for the first M entries of $\dot{\boldsymbol{y}}$ the modulo operation has no effect (for an m greater than the absolute value of u, which is always assumed here). Thus, the first M entries of $\boldsymbol{s} \in \mathbb{Z}^{1 \times N}$ (see (5.21)) are zero, i.e.,

$$\boldsymbol{s} = \begin{bmatrix} \mathbb{O} & \tilde{\boldsymbol{s}} \end{bmatrix}. \tag{5.40}$$

Hence, the discrete part of the valid code vectors can be expressed as

$$\boldsymbol{y}_{\text{dis}} \overset{(5.39)}{=} 2m \cdot \boldsymbol{s} \cdot \boldsymbol{G}_{\text{dis}} \tag{5.41}$$

$$\overset{(5.27)}{=} 2m \cdot \begin{bmatrix} \mathbb{O} & \tilde{\boldsymbol{s}} \end{bmatrix} \cdot \begin{bmatrix} \boldsymbol{G}_{12} \\ \boldsymbol{B}' \end{bmatrix} \tag{5.42}$$

$$= 2m \cdot \tilde{\boldsymbol{s}} \cdot \boldsymbol{B}' \tag{5.43}$$

$$= \tilde{\boldsymbol{s}} \cdot \boldsymbol{B}. \tag{5.44}$$

All discrete points are integer linear combinations of the row vectors of $\boldsymbol{B}$, as long as they are within the projection of the rotated unit hyper cube (Figure 5.5b). Thus, $\boldsymbol{B}$ is the base of the lattice describing the discrete part.

5.3.4 High-cSNR Performance

One figure of merit to compare different transmission systems is their performance for a very good channel quality (high-cSNR). When using AMBCs with very good channels, the power of the noise is sufficiently small to result only in negligible numbers of decoding errors when choosing the lattice point in the discrete part. Thus, (nearly) all arms are selected correctly at the receiver. The performance of the transmission then only depends on the analog part of the AMBC.

Without loss of generality, in the following derivation the central lattice point in the discrete part, i.e., the one in the origin ($\boldsymbol{s} = \mathbb{O}$), is considered. Then, applying the modulo operation to $\dot{\boldsymbol{y}} = \boldsymbol{u}\boldsymbol{A}$ does not have any effect due to $\|\dot{\boldsymbol{y}}\|_\infty < m$ (all entries in $\dot{\boldsymbol{y}}$ have absolute values smaller than m) such that $\boldsymbol{y} = \dot{\boldsymbol{y}}$. Consequently, the AMBC is comparable to an LABC (Section 3.2) and a similar derivation may be employed: For an AWGN channel, a *Least Squares* (LS) estimator achieves the same performance as a *Maximum Likelihood* (ML) estimator [Kay93], which can be realized by a simple multiplication with the pseudoinverse $\boldsymbol{A}^+$ of the code matrix $\boldsymbol{A}$, as shown, e.g., in [RSV09] for LABCs.

When applying the pseudoinverse $\boldsymbol{A}^+$ to the received noisy vector $\boldsymbol{z}$ with a lattice point in the origin ($\boldsymbol{s} = \mathbb{O} \Rightarrow \boldsymbol{y} = \dot{\boldsymbol{y}}$), the estimated source symbol depends on $\boldsymbol{u}$, on the noise vector and the on pseudoinverse $\boldsymbol{A}^+$:

$$\hat{\boldsymbol{u}} = \boldsymbol{z} \cdot \boldsymbol{A}^+ \overset{(\hat{\boldsymbol{s}}=\boldsymbol{s})}{=} (\boldsymbol{u} \cdot \boldsymbol{A} + \boldsymbol{n}) \cdot \boldsymbol{A}^+ = \boldsymbol{u} \cdot \underbrace{\boldsymbol{A} \cdot \boldsymbol{A}^+}_{\mathbb{1}} + \boldsymbol{n} \cdot \boldsymbol{A}^+ = \boldsymbol{u} + \boldsymbol{n} \cdot \boldsymbol{A}^+ \tag{5.45}$$

$$\Rightarrow \quad \hat{\boldsymbol{u}} - \boldsymbol{u} = \boldsymbol{n} \cdot \boldsymbol{A}^+. \tag{5.46}$$

With (5.20), the pseudoinverse can be substituted by the matrices of its SVD:

$$\begin{aligned}
\mathrm{E}\left\{\|\hat{\boldsymbol{u}}-\boldsymbol{u}\|^2\right\} &= \mathrm{E}\left\{\left\|\boldsymbol{n}\cdot\boldsymbol{V}\cdot\begin{bmatrix}\mathbb{1}_M\\ \mathbb{O}_{D\times M}\end{bmatrix}\cdot\tilde{\boldsymbol{\Sigma}}^{-1}\cdot\boldsymbol{U}^{\mathrm{T}}\right\|^2\right\}\\
&= \mathrm{E}\left\{\left\|\boldsymbol{n}\cdot\begin{bmatrix}\mathbb{1}_M\\ \mathbb{O}_{D\times M}\end{bmatrix}\cdot\tilde{\boldsymbol{\Sigma}}^{-1}\right\|^2\right\}\\
&= \sum_{k=1}^{M}\sigma_n^2\cdot\gamma_k^{-2} = \sigma_n^2\cdot\sum_{k=1}^{M}\gamma_k^{-2}. \qquad (5.47)
\end{aligned}$$

The matrices $\boldsymbol{V}$ and $\boldsymbol{U}$ are orthogonal, thus, multiplying $\boldsymbol{n}$ just results in a rotation and no change in the noise power. Thus, they can be omitted in the expectation above. The term $\begin{bmatrix}\mathbb{1}_M\\ \mathbb{O}_{D\times M}\end{bmatrix}$ deletes D out of the N dimensions of $\boldsymbol{n}$ and since the noise power of $\boldsymbol{n}$ is distributed evenly with σ_n^2 per dimension over all dimensions only M entries of $\boldsymbol{n}$ contribute to the sum. The terms γ_k with $1\leq k\leq M$ are the singular values (5.16) of $\boldsymbol{A}$ and are the roots of the positive eigenvalues of $\boldsymbol{A}\cdot\boldsymbol{A}^{\mathrm{T}}$:

$$\gamma_k^2 = |\mathrm{eig}\left(\boldsymbol{A}\cdot\boldsymbol{A}^{\mathrm{T}},k\right)|. \qquad (5.48)$$

The resulting performance of an AMBC for high cSNRs is, thus:

$$\begin{aligned}
\mathrm{pSNR}_{\mathrm{AMBC,high\text{-}CSNR,ML}} &= \frac{\mathrm{E}\left\{\|\boldsymbol{u}\|^2\right\}}{\mathrm{E}\left\{\|\boldsymbol{u}-\hat{\boldsymbol{u}}\|^2\right\}} \qquad (5.49)\\
&= \frac{M\cdot\sigma_u^2}{\sigma_n^2\cdot\sum_{k=1}^{M}\frac{1}{\gamma_k^2}} \qquad (5.50)\\
&\approx \mathrm{cSNR}\cdot\frac{1}{\frac{1}{M}\sum_{k=1}^{M}\frac{1}{\gamma_k^2}}, \qquad \gamma_k^2 = |\mathrm{eig}\left(\boldsymbol{A}\cdot\boldsymbol{A}^{\mathrm{T}},k\right)|, \qquad (5.51)
\end{aligned}$$

with $\mathrm{cSNR}=\frac{\sigma_u^2}{\sigma_n^2}$ for $\frac{\sigma_u^2}{\sigma_y^2}=1$ which holds exactly for integer entries of $\boldsymbol{A}$ and approximately for non-integer entries. The high-cSNR performance can be selected arbitrarily by choosing an $\boldsymbol{A}$ with the appropriate singular values γ_k. However, the performance (5.51) is only attained when the decoder chooses the correct lattice point of the discrete part, which depends on the structure of the discrete part of the code. Thus, the high-cSNR performance may be arbitrarily chosen, but (5.51) only holds for high enough channel qualities.

Equation (5.51) and also its derivation resembles the performance (3.10) and its derivation in Section 3.2.1 of LABC. The difference can be explained as follows. The matrix $\boldsymbol{P}$ in (3.10) is normalized with (3.5) to yield a defined output power after

the matrix multiplication. Due to the type of normalization, the sum of the inverse eigenvalues is constant and the fraction $\frac{N}{M}$ appears in the result. For AMBCs, no normalization occurs (just the modulo operation which can be neglected for the performance in the high-cSNR case), the eigenvalues can be chosen arbitrarily and therefore also the fraction $\frac{N}{M}$ does not appear in (5.51).

5.4 Decoding AMBCs

The aim of the decoder is to find the best estimate $\hat{\boldsymbol{u}}$ of the initially encoded source symbols $\boldsymbol{u}$. In the following sections different types of decoders, tailored for AMBCs, are presented. First a generic *Minimum Mean-Square Error* (MMSE) decoder is briefly introduced in Section 5.4.1 and later the class of rotating decoders, which benefit from the special structure of AMBCs, is presented in Section 5.4.2 with three different variants.

5.4.1 MMSE Decoder

The *Minimum Mean-Square Error* (MMSE) decoder promises the smallest possible mean-square error [Kay93] by considering the statistics of the source symbol vector $\boldsymbol{u}$ and the noise vector $\boldsymbol{n}$.

The MMSE estimator can be stated as the conditional expectation of the source symbols $\boldsymbol{u}$ given the received vector $\boldsymbol{z}$:

$$\begin{aligned}\hat{\boldsymbol{u}} &= \mathrm{E}\left\{\boldsymbol{u}|\boldsymbol{z}\right\} && (5.52)\\ &= \int \boldsymbol{u}\cdot \mathrm{p}\left(\boldsymbol{u}|\boldsymbol{z}\right)\,\mathrm{d}\boldsymbol{u}\\ &= \int \boldsymbol{u}\cdot \frac{\mathrm{p}\left(\boldsymbol{z}|\boldsymbol{u}\right)\cdot \mathrm{p}\left(\boldsymbol{u}\right)}{\mathrm{p}\left(\boldsymbol{z}\right)}\,\mathrm{d}\boldsymbol{u}\\ &= \frac{\int \boldsymbol{u}\cdot \mathrm{p}\left(\boldsymbol{z}|\boldsymbol{u}\right)\cdot \mathrm{p}\left(\boldsymbol{u}\right)\,\mathrm{d}\boldsymbol{u}}{\int \mathrm{p}\left(\boldsymbol{z}|\boldsymbol{u}\right)\cdot \mathrm{p}\left(\boldsymbol{u}\right)\,\mathrm{d}\boldsymbol{u}}. && (5.53)\end{aligned}$$

The complexity of the MMSE decoder is very high, since the integrals in (5.53) have to be evaluated for each dimension M of $\boldsymbol{u}$ and their arguments have to be calculated for each discretized point of $\boldsymbol{u}$. Therefore, this estimator may usually only be used for very small M.

5.4.2 Rotating Decoders

The rotating decoders are motivated by the observation shown in Figure 5.6. The code vectors of AMBCs may be rotated with the matrix $\boldsymbol{G}$ (Section 5.3.1) to align the arms of the code with the coordinate axis. After the rotation, the discrete part can be decoded along the discrete dimensions ($y_{\mathrm{rot},2}$ in Figure 5.6b), which

are orthogonal to the arms, and the analog part along the analog dimensions (in Figure 5.6b $y_{\mathrm{rot},1}$) which are in parallel to the arms.

The two parts of the rotating decoder are visualized in Figure 5.7. The discrete part first rotates the input symbols with a submatrix $\boldsymbol{G}_{\mathrm{dis}}$ of the rotation matrix $\boldsymbol{G}$ (5.38) to obtain a vector $\boldsymbol{z}_{\mathrm{dis}}$ only containing the discrete dimensions:

$$\boldsymbol{z}_{\mathrm{dis}} \overset{(5.38)}{=} \boldsymbol{z} \cdot \boldsymbol{G}_{\mathrm{dis}}.$$

Either the *Discrete Maximum Likelihood* (DML) or the *Zero-Forcing* (ZF) decoder evaluates $\boldsymbol{z}_{\mathrm{dis}}$ and generates an integer estimate $\hat{\tilde{\boldsymbol{s}}}$. This is concatenated with a zero vector yielding an estimate $\hat{\boldsymbol{s}} = \begin{bmatrix} 0 & \hat{\tilde{\boldsymbol{s}}} \end{bmatrix}$ of the jump vector $\boldsymbol{s}$ (5.22).

Starting with (5.23) the estimate $\hat{\boldsymbol{u}}$ may be expressed in dependency of the estimate of the jump vector and the received symbols $\boldsymbol{z}$:

$$\boldsymbol{z} = \hat{\boldsymbol{u}} \cdot \boldsymbol{A} + 2m \cdot \hat{\boldsymbol{s}} \quad \Rightarrow \quad \hat{\boldsymbol{u}} \cdot \boldsymbol{A} = \boldsymbol{z} - 2m \cdot \hat{\boldsymbol{s}}. \tag{5.54}$$

An ML estimate of the analog part can be achieved by using the pseudo inverse of $\boldsymbol{A}$. The pseudo inverse is motivated in Section 3.2.1 in Chapter 3 in the context of linear analog transmission and is given as:

$$\boldsymbol{A}^{+} = \boldsymbol{A}^{\mathrm{T}} \cdot \left(\boldsymbol{A} \cdot \boldsymbol{A}^{\mathrm{T}} \right)^{-1}. \tag{5.55}$$

With $\boldsymbol{A} \cdot \boldsymbol{A}^{+} = \mathbb{1}$, multiplying (5.54) with the pseudo inverse leads to

$$\hat{\boldsymbol{u}} = (\boldsymbol{z} - 2m \cdot \hat{\boldsymbol{s}}) \cdot \boldsymbol{A}^{+}, \tag{5.56}$$

as shown in the analog part of Figure 5.7.

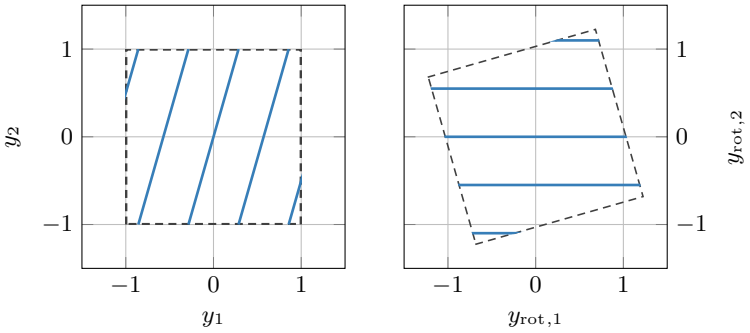

(a) Original code vectors $\boldsymbol{y}$.

(b) Rotated code vectors $\boldsymbol{y}_{\mathrm{rot}} = \boldsymbol{y} \cdot \boldsymbol{G}$.

Figure 5.6: Valid code vectors with $\boldsymbol{A} = \begin{bmatrix} 1 & 3.5 \end{bmatrix}$ and $m = 1$. The box (unit hyper cube) visualizes the limitations by the modulo operation and the limited range of input values.

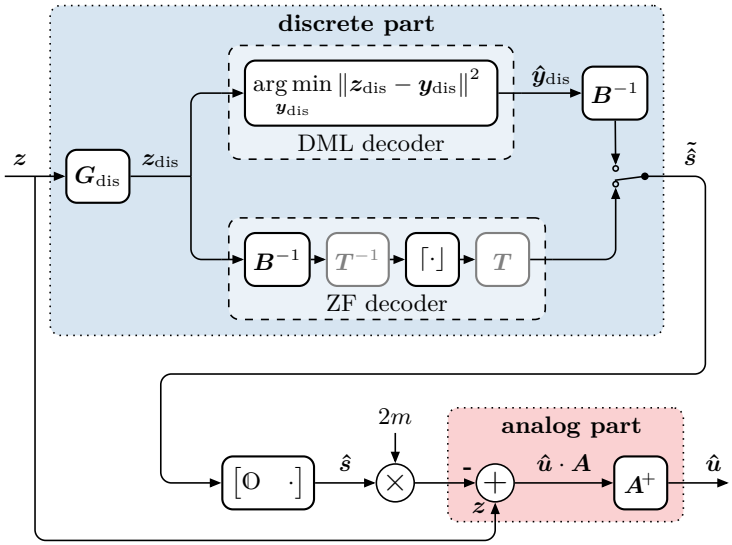

Figure 5.7: Block diagram of rotating decoders. Two options of decoders are depicted: *Discrete Maximum Likelihood* (DML) and *Zero-Forcing* (ZF) decoding.

Discrete Maximum Likelihood Decoder

The aim of the decoders in the discrete part is to obtain the best $\tilde{\hat{\boldsymbol{s}}}$ from a received $\boldsymbol{z}_{\text{dis}}$. The *Discrete Maximum Likelihood* (DML) decoder uses maximum likelihood estimation in the discrete part to estimate $\tilde{\hat{\boldsymbol{s}}}$. The received vector $\boldsymbol{z}_{\text{dis}}$ is compared to all rotated possibly sent code vectors $\boldsymbol{y}_{\text{dis}}$ (5.39) while finding the pair with the smallest Euclidean distance:

$$\hat{\boldsymbol{y}}_{\text{dis}} = \underset{\boldsymbol{y}_{\text{dis}}}{\arg\min} \|\boldsymbol{z}_{\text{dis}} - \boldsymbol{y}_{\text{dis}}\|^2 . \tag{5.57}$$

The found $\hat{\boldsymbol{y}}_{\text{dis}}$ can be reformulated with (5.27), (5.39) and (5.40) to the desired $\tilde{\hat{\boldsymbol{s}}}$ (see also (5.44)):

$$\begin{aligned} \boldsymbol{y}_{\text{dis}} &= \boldsymbol{y} \cdot \boldsymbol{G}_{\text{dis}} = 2m \cdot \begin{bmatrix} \mathbb{O} & \tilde{\boldsymbol{s}} \end{bmatrix} \cdot \begin{bmatrix} \boldsymbol{G}_{12} \\ \boldsymbol{B}' \end{bmatrix} = 2m \cdot \tilde{\boldsymbol{s}} \cdot \boldsymbol{B}' \\ &= \tilde{\boldsymbol{s}} \cdot \boldsymbol{B} \\ \Leftrightarrow \quad \tilde{\boldsymbol{s}} &= \boldsymbol{y}_{\text{dis}} \cdot \boldsymbol{B}^{-1} \qquad (5.58) \\ \Rightarrow \quad \tilde{\hat{\boldsymbol{s}}} &= \hat{\boldsymbol{y}}_{\text{dis}} \cdot \boldsymbol{B}^{-1}. \qquad (5.59) \end{aligned}$$

In total, the DML decoder, including the analog part (5.56) can be stated as (see also Figure 5.7):

$$\hat{\boldsymbol{u}} = \left(\boldsymbol{z} - 2m \cdot \left[\mathbb{0} \quad \left(\underset{\boldsymbol{y}_{\text{dis}}}{\arg\min} \left\| \boldsymbol{z}_{\text{dis}} - \boldsymbol{y}_{\text{dis}} \right\|^2 \right) \cdot \boldsymbol{B}^{-1} \right] \right) \cdot \boldsymbol{A}^{+}. \tag{5.60}$$

This decoder does not require any knowledge about the noise and source statistics and consequently shows a lower performance than the MMSE decoder. It is still quite complex during runtime, since all possible $\boldsymbol{y}_{\text{dis}}$ have to be evaluated, but less complex than the MMSE decoder. A challenge is to find all valid $\boldsymbol{y}_{\text{dis}}$ of the employed AMBC, which fortunately may be done in advance. It may be noted that with the DML decoder, the complete decoder including the analog part, does not achieve an overall ML performance which could be achieved considering both, the discrete and the analog part jointly. This is due to the two stage design of the decoder. It achieves ML performance in the discrete part and then ML performance in the analog part. However, the performance only may differ in the case when the information of the analog part would lead to a different estimate in the discrete part.

Zero-Forcing Decoder

The *Zero-Forcing* (ZF) decoder is motivated by the observation that the discrete part of an AMBC forms a lattice (Section 5.3.3). This periodic structure can be exploited to design a decoder with very low complexity compared to, e.g., the DML or MMSE decoder.

In this work only systematic AMBCs are employed with a leading identity matrix in the code matrix $\boldsymbol{A} = \begin{bmatrix} \mathbb{1} & \tilde{\boldsymbol{A}} \end{bmatrix}$ and input values of $\boldsymbol{u}$ limited to $(-m, m)$. Thus, the modulo operation has no effect on the first $M = N - D$ entries of $\dot{\boldsymbol{y}} = \boldsymbol{u} \cdot \boldsymbol{A}$. Therefore, only the last D entries $\tilde{\boldsymbol{s}}$ of the jump vector $\boldsymbol{s}$ (5.22) are non-zero.

The discrete part $\boldsymbol{z}_{\text{dis}}$ of the received vector $\boldsymbol{z}$ has the same number of entries (D) as the non-zero part of the jump vector $\tilde{\boldsymbol{s}}$, thus, with (5.27), (5.38) and (5.40) $\tilde{\boldsymbol{s}}$ can be estimated as follows:

$$\boldsymbol{z}_{\text{dis}} = \boldsymbol{z} \cdot \boldsymbol{G}_{\text{dis}} = 2m \cdot \begin{bmatrix} \mathbb{0} & \tilde{\boldsymbol{s}} \end{bmatrix} \cdot \begin{bmatrix} \boldsymbol{G}_{12} \\ \boldsymbol{B}' \end{bmatrix} + \boldsymbol{n}_{\text{rot,dis}} \tag{5.61}$$

$$= 2m \cdot \tilde{\boldsymbol{s}} \cdot \boldsymbol{B}' + \boldsymbol{n}_{\text{rot,dis}} \tag{5.62}$$

$$= \tilde{\boldsymbol{s}} \cdot \boldsymbol{B} + \boldsymbol{n}_{\text{rot,dis}}. \tag{5.63}$$

Multiplying with the inverse $\boldsymbol{B}^{-1}$ of $\boldsymbol{B}$ leads to:

$$\begin{aligned} \boldsymbol{z}_{\text{dis}} \cdot \boldsymbol{B}^{-1} &= \tilde{\boldsymbol{s}} \cdot \boldsymbol{B} \cdot \boldsymbol{B}^{-1} + \underbrace{\boldsymbol{n}_{\text{rot,dis}} \cdot \boldsymbol{B}^{-1}}_{\boldsymbol{n}_{\text{ZF}}} \\ &= \tilde{\boldsymbol{s}} + \boldsymbol{n}_{\text{ZF}} \quad \text{with} \quad \boldsymbol{n}_{\text{ZF}} = \boldsymbol{n} \cdot \boldsymbol{G}_{\text{dis}} \cdot \boldsymbol{B}^{-1} \\ \Leftrightarrow \quad \tilde{\boldsymbol{s}} &= \boldsymbol{z}_{\text{dis}} \cdot \boldsymbol{B}^{-1} - \boldsymbol{n}_{\text{ZF}}. \end{aligned} \tag{5.64}$$

Equation (5.64) is very similar to (5.58), if the noise is missing and the sent code vectors are considered instead of the received code vectors:

$$\tilde{\boldsymbol{s}} = \boldsymbol{y} \cdot \boldsymbol{G}_{\text{dis}} \cdot \boldsymbol{B}^{-1} = \boldsymbol{y}_{\text{dis}} \cdot \boldsymbol{B}^{-1}. \tag{5.65}$$

In both equations, it can be noted that, using the base matrix $\boldsymbol{B}$ of the lattice, the discrete part of the code vectors is transformed to integer values in the jump vector. Thus, the zero-forcing decoder rounds the transformed received code vectors $\boldsymbol{z}_{\text{dis}} \cdot \boldsymbol{B}^{-1}$ to the nearest integer to eliminate the channel noise:

$$\begin{aligned}
\tilde{\hat{\boldsymbol{s}}} &= \left\lceil \boldsymbol{z}_{\text{dis}} \cdot \boldsymbol{B}^{-1} \right\rfloor && (5.66)\\
&\overset{(5.38)}{=} \left\lceil \boldsymbol{z} \cdot \boldsymbol{G}_{\text{dis}} \cdot \boldsymbol{B}^{-1} \right\rfloor && (5.67)\\
&\overset{(2.4)}{=} \left\lceil \boldsymbol{y} \cdot \boldsymbol{G}_{\text{dis}} \cdot \boldsymbol{B}^{-1} + \boldsymbol{n}_{\text{ZF}} \right\rfloor && (5.68)\\
&\overset{(5.65)}{=} \lceil \tilde{\boldsymbol{s}} + \boldsymbol{n}_{\text{ZF}} \rfloor && (5.69)\\
&= \lceil \tilde{\boldsymbol{s}} + \lceil \boldsymbol{n}_{\text{ZF}} \rfloor + \underbrace{\text{smod}_{0.5}(\boldsymbol{n}_{\text{ZF}})}_{\|\cdot\|_\infty \leq 0.5} \rfloor = \tilde{\boldsymbol{s}} + \lceil \boldsymbol{n}_{\text{ZF}} \rfloor + \mathbb{O}, && (5.70)
\end{aligned}$$

while it has been used that the noise can be split in to an integer part and a fractional part:

$$\boldsymbol{n}_{\text{ZF}} = \lceil \boldsymbol{n}_{\text{ZF}} \rfloor + \text{smod}_{0.5}(\boldsymbol{n}_{\text{ZF}})\,. \tag{5.71}$$

The estimation error of the jump vector for this decoder is:

$$\tilde{\hat{\boldsymbol{s}}} - \tilde{\boldsymbol{s}} = \lceil \boldsymbol{n}_{\text{ZF}} \rfloor = \left\lceil \boldsymbol{n} \cdot \boldsymbol{G}_{\text{dis}} \cdot \boldsymbol{B}^{-1} \right\rfloor, \tag{5.72}$$

which is $\mathbb{O}$ for transformed noise symbols whose absolute values are smaller than 0.5 ($\|\boldsymbol{n}_{\text{ZF}}\|_\infty = \left\|\boldsymbol{n} \cdot \boldsymbol{G}_{\text{dis}} \cdot \boldsymbol{B}^{-1}\right\|_\infty < 0.5$). Thus, for good channel qualities, the discrete part of AMBCs can be decoded without error and the high-cSNR performance (Section 5.3.4) is reached.

In total, the zero-forcing decoder, including the analog part (5.56) can be stated as (see also Figure 5.7):

$$\hat{\boldsymbol{u}} = \left(\boldsymbol{z} - 2m \cdot \left\lceil \mathbb{O} \quad \left\lceil \boldsymbol{z} \cdot \boldsymbol{G}_{\text{dis}} \cdot \boldsymbol{B}^{-1} \right\rfloor \right\rfloor\right) \cdot \boldsymbol{A}^{+}. \tag{5.73}$$

The decoder does not employ any knowledge of the noise and source statistics and exhibits a very low complexity, since only matrix multiplications and no extensive search operations or integrals are involved.

Zero-Forcing with Lattice Reduction Decoder

The *Zero-Forcing with Lattice Reduction* (ZFLR) decoder operates in the same way as the above zero-forcing decoder but with one additional step. The zero-forcing

decoder is based on the lattice structure in the discrete part of the AMBC. This lattice may be described with different base matrices $\boldsymbol{B}$. The performance of the decoder depends on the lattice, but also on the way it is described by the base matrix.

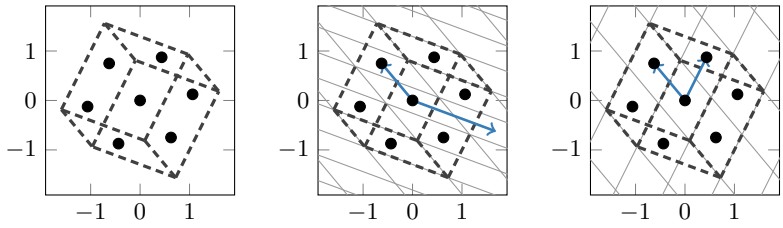

(a) Discrete part.

(b) Decision regions and base vectors without lattice reduction...

(c) ... and with lattice reduction.

Figure 5.8: Discrete part ($\boldsymbol{yG}_{\text{dis}}$) of a [1 2 4]-AMBC: valid code vectors (lattice points) ●, decision borders —— of the zero-forcing decoders, unit hyper cube - - - and base vectors ⟶ are depicted.

Figure 5.8a shows the discrete part of a code with $\boldsymbol{A} = [1 \;\; 2 \;\; 4]$. The dotted lines describe the projection of the unit hyper cube which encloses all valid code vectors. Figure 5.8b additionally depicts the base vectors of the base matrix $\boldsymbol{B}$. It can be seen, that all valid code vectors (lattice points) are integer linear combinations of the base vectors. The borders between the decision regions of the zero-forcing decoder are in parallel to the base vectors and exactly in the middle between the lattice points.

A *lattice reduction* finds an alternative description of the same lattice using another base matrix $\boldsymbol{B}_{\text{red}}$ with base vectors which are as close as possible to orthogonal or exhibit the shortest possible difference in lengths. Here, a very popular algorithm designed for arbitrary lattice dimensions introduced by Lenstra, Lenstra, and Lovász in [LLL82] known as the LLL algorithm [WSJM11] is employed. In Figure 5.8c the base vectors and their decision regions for a base matrix $\boldsymbol{B}_{\text{red}}$ after lattice reduction are shown. The decision regions are a lot closer to the optimal Voronoi region (a circle in two dimensions) than in Figure 5.8b and therefore a better decoding performance is expected.

The transformation of the base matrix $\boldsymbol{B}$ to the reduced base matrix $\boldsymbol{B}_{\text{red}}$ is conducted by multiplying with an integer unimodular matrix[4] $\boldsymbol{T}$ which is derived

[4]The inverse of an integer unimodular matrix also has only integer entries.

by the lattice reduction algorithm. Also the inverse of the reduced base matrix may be expressed with $\boldsymbol{T}$:

$$\begin{aligned}\boldsymbol{B}_{\mathrm{red}} &= \boldsymbol{T} \cdot \boldsymbol{B} \\ \boldsymbol{B}_{\mathrm{red}}^{-1} &= \boldsymbol{B}^{-1} \cdot \boldsymbol{T}^{-1}.\end{aligned} \tag{5.74}$$

In [WSJM11][5] a comprehensive overview about the different algorithms for finding the best $\boldsymbol{T}$ for any base matrix $\boldsymbol{B}$ is given.

The difference between the ZFLR decoder and the ZF decoder is that the base matrix has to be transformed with $\mathbf{T}$ and after rounding the jump vector to the nearest integer, the transformation has to be inverted. Thus, (5.67) and (5.73) can be reformulated as follows (Figure 5.7):

$$\tilde{\hat{\boldsymbol{s}}} = \left\lceil \boldsymbol{z} \cdot \boldsymbol{G}_{\mathrm{dis}} \cdot \boldsymbol{B}^{-1} \cdot \boldsymbol{T}^{-1} \right\rfloor \cdot \boldsymbol{T} \tag{5.75}$$

$$\hat{\boldsymbol{u}} = \left(\boldsymbol{z} - 2m \cdot \begin{bmatrix} \mathrm{O} & \left\lceil \boldsymbol{z} \cdot \boldsymbol{G}_{\mathrm{dis}} \cdot \boldsymbol{B}^{-1} \cdot \boldsymbol{T}^{-1} \right\rfloor \cdot \boldsymbol{T} \end{bmatrix} \right) \cdot \boldsymbol{A}^{+}. \tag{5.76}$$

As the ZF decoder, the ZFLR does not require any knowledge about the statistics of the source and noise. It exhibits the same low complexity as the ZF decoder, just the additional multiplication with $\boldsymbol{T}$ is required. The lattice reduction to obtain the optimal $\boldsymbol{T}$ for a given code matrix $\boldsymbol{A}$ can be conducted in advance.

5.4.3 Performance Comparison

The behavior of the different types of decoders for a [1 2 4]-AMBC are shown in Figure 5.9. A [1 2 4]-AMBC maps $M = 1$ source symbol to $N = 3$ channel symbols. For each possible rotated received vector $\boldsymbol{z} \cdot \boldsymbol{G}$ in the 3-dimensional channel space, a decoder assigns an estimate $\hat{u}$ of the sent scalar source symbol. To obtain a 2-dimensional visualization showing only the discrete part, the 3-dimensional channel space is sliced in parallel to the discrete dimensions. This can be done by, e.g., setting the analog component of the rotated received vector to 0 and then employ the decoder. The color in the figures represents the value of the estimate $\hat{u}$ of the decoder and the black dots correspond to the rotated valid code vectors.

Figure 5.9a shows the behavior of an MMSE decoder. The channel quality is $\mathrm{cSNR}|_{\mathrm{dB}} = 10\,\mathrm{dB}$ which corresponds to a noise standard deviation of $\sigma_n = 0.3$ and a noise variance of $\sigma_n^2 = 0.09$. The standard deviation is depicted as the dotted circle in the figure, while the gray circle encloses 50 % of all noise symbols around the central code vector. The MMSE estimator generates smooth transitions of the estimated symbols between the black dots.

The DML decoder in Figure 5.9b performs ML estimation in the discrete part of the AMBC. Thus, the discrete part of the rotated received vectors is mapped to the valid code vector which has the smallest Euclidean distance and therefore,

[5] In contrast to this work, the base vectors in [WSJM11] are column vectors. Therefore, in some derivations the expressions are transposed.

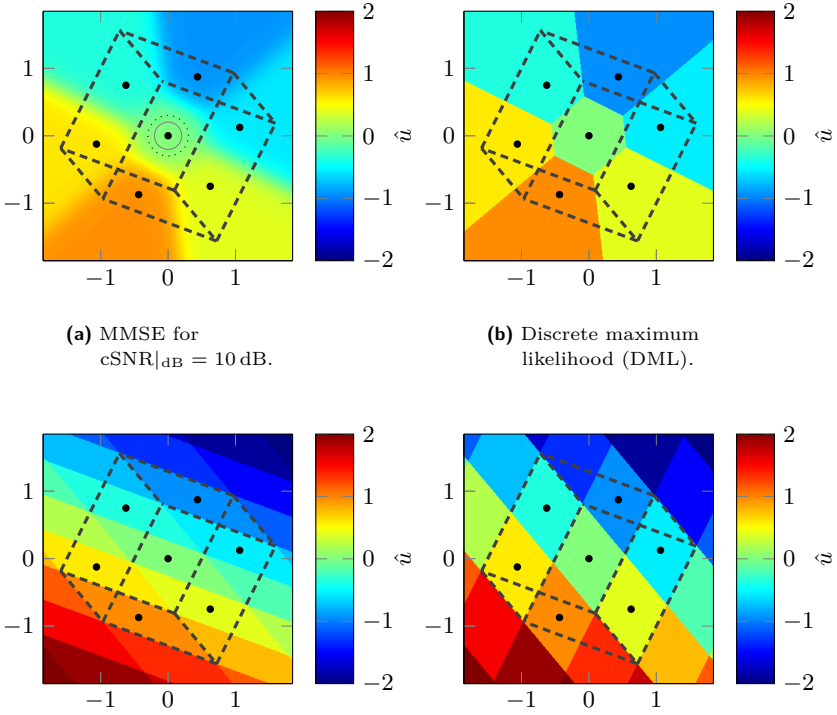

(a) MMSE for $\mathrm{cSNR}|_{\mathrm{dB}} = 10\,\mathrm{dB}$.

(b) Discrete maximum likelihood (DML).

(c) Zero-forcing (ZF).

(d) ZF with lattice reduction.

Figure 5.9: Comparison of different types of decoders for a [1 2 4]-AMBC. The estimate $\hat{u}$ for a wide range of possible received rotated vectors $\boldsymbol{z} \cdot \boldsymbol{G}$ with an an analog part set to 0 is depicted.

many received vectors are assigned to the same code vector. The ensemble of these vectors are denoted "decision region" and the edge between the decision regions "decision borders". For a DML decoder, these decision regions have different and partially very complex shapes, always obeying the rule of the smallest Euclidean distance.

Each decision region of the lattice based ZF decoder (Figure 5.9c) has the same shape, following the base vectors described in $\boldsymbol{B}$. The decision regions are not necessarily very close to the optimum shape obtained by the DML decoder. Here they form a relatively flat parallelogram. In contrast to the MMSE and the DML decoder, the lattice based decoder repeats the decoding pattern beyond the unit hyper cube. Thus, also estimated values beyond the range of the source symbols $|\hat{u}| > 1$ emerge.

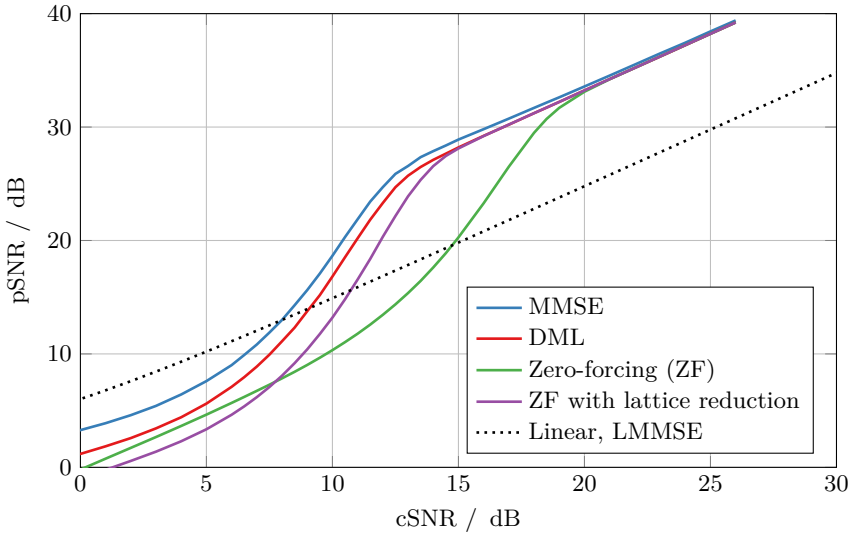

Figure 5.10: Simulation results for different types of decoders for a [1 2 4]-AMBC and source symbols with a uniform *probability density function* (pdf).

The ZFLR decoder in Figure 5.9d draws a similar picture as the ZF decoder, but the parallelograms of the decision regions have a different shape. Here, optimized base vectors are employed which generate parallelograms that are closer to circular decision regions, but describe the same lattice.

Figure 5.10 shows the simulated performance for different types of decoders for a [1 2 4]-AMBC and source symbols following a uniform pdf. As expected, the MMSE decoder achieves the best performance of all decoders for all channel qualities. Its superiority is especially pronounced for lower channel qualities (cSNR $< 15\,\mathrm{dB}$), while for better channels the other decoders nearly reach the MMSE performance.

The DML decoder also achieves very good results with a maximum gap of around 2 dB in terms of pSNR to the MMSE decoder.

The zero-forcing decoder which does not employ lattice reduction exhibits a very poor performance, which for some channel qualities is around 10 dB below the performance of the other decoders. This is due to the shape of the decision regions which is very disadvantageous.

By adding the lattice reduction to the zero-forcing decoder (ZFLR) results can be significantly improved. The same performance as for the DML decoder is achieved for a channel quality which is at most 1 dB better in terms of cSNR. This is a remarkable result for the ZFLR decoder because its complexity is a lot smaller since the full search in the DML decoder is replaced with matrix multiplications.

5.5 Code Design and Simulation Results

The performance of the AMBC transmission systems is, on one hand, dependent on the type of decoder which is employed, but on the other hand, the code matrix $\boldsymbol{A}$ and its dimensions are of paramount importance for the properties and the performance of the code. In this section, approaches for designing codes with different dimensions of $\boldsymbol{A}$ are briefly discussed and their performance is assessed using simulation results with source symbols following a uniform pdf.

5.5.1 1x2 Codes

For systematic AMBCs with $M = 1$ source symbol and $N = 2$ channel symbols, there is just one scalar value (t) which can be chosen to generate different codes:

$$\boldsymbol{A} = \begin{bmatrix} 1 & t \end{bmatrix}. \tag{5.77}$$

With (5.51) and, thus, $\operatorname{eig}\left(\boldsymbol{A} \cdot \boldsymbol{A}^{\mathrm{T}}\right) = 1 + t^2$, the high-cSNR performance of these codes can directly be stated:

$$\mathrm{pSNR}_{\mathrm{AMBC,high\text{-}CSNR,ML}} \approx \mathrm{cSNR} \cdot \left(1 + t^2\right). \tag{5.78}$$

Higher values of t lead to codes with more arms (Figure 5.3) and therefore a higher cSNR is needed for successful decoding. Since also the source symbols are distributed on more arms, the high-cSNR performance is also increased.

Figure 5.11 shows the performance of different 1x2 AMBCs. The tradeoff between the high-cSNR performance and the channel quality needed for successful decoding can be observed.

5.5.2 1x3 Codes

For codes which map $M = 1$ source symbol to $N = 3$ channel symbols, a 2-dimensional ($D = 2$) lattice (5.28) in the discrete part emerges. This lattice influences the performance of the decoders for the discrete part as shown in Figures 5.9 and 5.10. A good lattice enables successful decoding at lower channel qualities than permitted by a bad lattice. A good lattice positions the discrete points as far as possible from each other on a given area to reduce the effect of the channel noise on selecting the correct discrete point during decoding. For the two-dimensional case this is achieved by a hexagonal lattice with base vectors of equal length and an angle of 60°.

In [Sch13] it is derived how for given base vectors the corresponding code matrix $\boldsymbol{A}$ can be derived. As described in the context of lattice reduction (Section 5.4.2), the same lattice can be generated with different base vectors. This is achieved by applying a unimodular matrix $\boldsymbol{T}$, which consists of integers, to the chosen base vectors (5.74) ("reversed reduction"). The 5 missing coefficients to

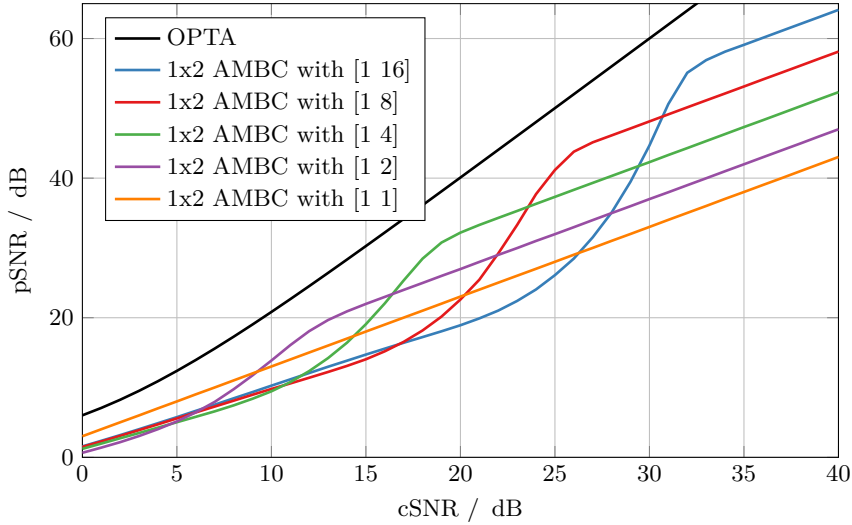

Figure 5.11: Simulation results for different 1x2 codes with DML decoding and source symbols with a uniform pdf. The AMBC with [1 1] yields the same performance as a LABC.

extend this 2x2 matrix to the 3x3 rotation matrix $\boldsymbol{G}$ (5.27) are selected such that $\boldsymbol{G}$ is orthogonal and, thus, is a rotation matrix. With the triangular matrix $\boldsymbol{P}$ where just one entry is non-zero which can be derived from $\boldsymbol{G}$, the code matrix $\boldsymbol{A}$ can directly be stated (5.7). Interestingly, for the 1x3 code, the high-cSNR performance cannot be chosen arbitrarily for any given lattice. Depending on the unimodular matrix used for the reversed reduction, different AMBCs with the desired lattice structure may be designed, but only with discrete high-cSNR performances.

Figure 5.12 shows the simulation results for 1x3 codes which exhibit approximately the same high-cSNR performance but use different base matrices. The base vectors of the codes with an angle of $\delta = 60°$ and $90°$ have equal lengths. With another approach, a code is designed which has base vectors with unequal lengths and a base angle of $\delta \approx 66°$. The codes with $\delta = 90°$ and $\delta \approx 66°$ have approximately the same performance, although the lengths and the angles between the base vectors are different. The code with the hexagonal lattice ($\delta = 60°$) exhibits a superior performance compared to the other codes. Thus, for codes with just one source symbol, choosing a good lattice for the discrete dimensions and generating the corresponding code matrix leads to good codes for the given code rate and high-cSNR performance.

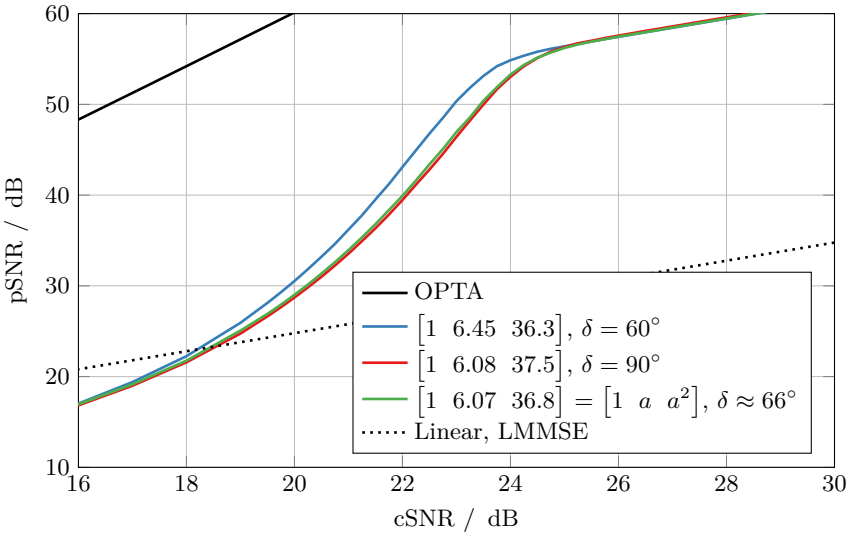

Figure 5.12: Simulation results for different designed 1x3 codes with DML decoding. All codes except for the code with $\delta \approx 66°$ exhibit equal lengths for the base vectors. Source symbols with a uniform pdf are employed.

5.5.3 2x4 Codes

In this section systematic AMBCs with $M = 2$ input symbols and $N = 4$ channel symbols are considered. Also here, the discrete part is 2-dimensional ($D = 2$), thus, the same considerations as in the previous section for 1x3 codes for designing a good lattice will be taken. Also here, two base vectors with equal length and a given angle lead to a matrix $\boldsymbol{B}$ with dimension 2x2. This matrix is reversed (inverse lattice reduction) with a unimodular $\boldsymbol{T}$. Since for the expansion to the rotation matrix $\boldsymbol{G}$ with dimension 4x4, more entries of $\boldsymbol{G}$ have to be chosen. Thus, more degrees of freedom are available. E.g., for the 2x4 codes, the high-cSNR performance can arbitrarily be chosen for any given base vectors and unimodular matrix $\boldsymbol{T}$. The details of the design of 2x4 codes are derived in [Sch13].

Figure 5.13 shows the simulation results for different 2x4 codes and one 1x2 code, all with $r = \frac{1}{2}$ and the same high-cSNR performance. The base vectors of the lattice of the 2x4 codes exhibit angles of 20°, 60° and 90°. DML decoding is employed. The code with 20° shows a very poor performance and successful decoding is only possible at high channel qualities (cSNR $> 29\,\mathrm{dB}$). The 2x4 code with 90° shows exactly the same performance as the 1x2 code. This can be easily explained with the code matrix of one 2x4 code with 90° ($\boldsymbol{A} = \left[\begin{smallmatrix} 1 & 0 & 4.29 & 0 \\ 0 & 1 & 0 & 4.29 \end{smallmatrix}\right]$), which

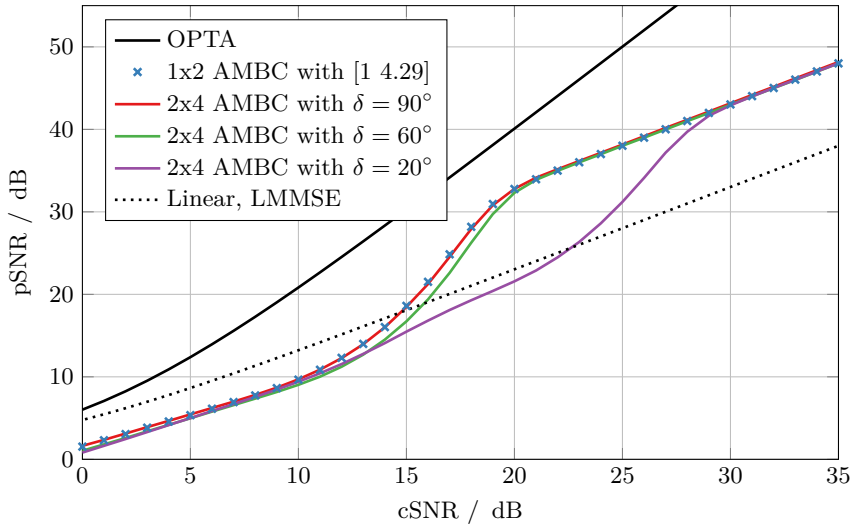

Figure 5.13: Simulation results for different designed $r = \frac{1}{2}$ codes with DML decoding, i.e., designed 2x4 codes with different angles between the base vectors of the lattice and a 1x2 code with the same high-cSNR performance are shown. Source symbols with a uniform pdf are employed.

is just a repetition of the 1x2 code with the code matrix $\boldsymbol{A} = [1 \;\; 4.29]$. Thus, for a 2x4 code with 90°, the shorter 1x2 code has the same performance with less complexity and delay.

Interestingly, the code with 60°, which employs the (expected to be) optimal hexagonal lattice for the discrete part, shows a poorer performance than the code with 90° and consequently also a poorer performance than the shorter 1x2 code. The hexagonal lattice should lead to a superior performance when decoding the lattice points, but there is another dominating effect.

Figure 5.14 shows a very promising hint for the effect of the superior performance of the code with 90°. The three subfigures correspond to three 2x4 codes with different angles between the base vectors of the lattice. Here, not the discrete lattice, but the 2-dimensional source space covered by all possible source vectors $\boldsymbol{u}$ is shown. The areas (i.e., slices) cut by the lines correspond to all source vectors which are mapped to one discrete point. The points on the slices are stretched by the influence of $\boldsymbol{A}$ and are transmitted as the analog part in the channel space. For a 20° code in Subfigure 5.14a it is shown how the source space is partitioned into 91 slices which are very pointy and narrow. For the 60° code in Subfigure 5.14b only

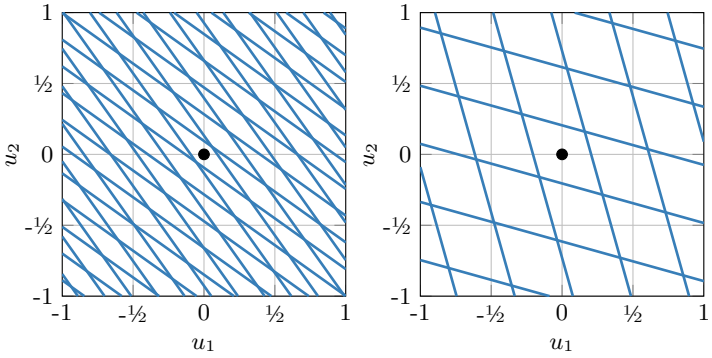

(a) 20°code, 91 slices.
$\boldsymbol{A} = \begin{bmatrix} 1 & 0 & 1.36 & -4.88 \\ 0 & 1 & 4.88 & -1.37 \end{bmatrix}$

(b) 60°code, 35 slices.
$\boldsymbol{A} = \begin{bmatrix} 1 & 0 & 7.58 & -10.6 \\ 0 & 1 & 10.6 & -7.55 \end{bmatrix}$

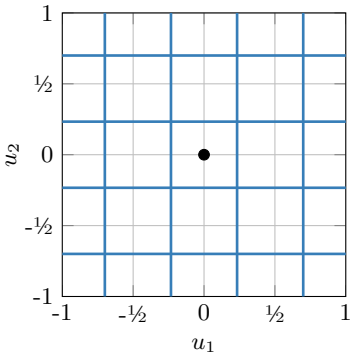

(c) 90°code, 25 slices.
$\boldsymbol{A} = \begin{bmatrix} 1 & 0 & 4.29 & 0 \\ 0 & 1 & 0 & 4.29 \end{bmatrix}$

Figure 5.14: Distribution of the source symbols for 2x4 codes to the discrete points for varying angles between the base vectors of the underlying lattice. Each slice describes the source symbols which are mapped to one common discrete point. The black dot describes the origin $u_1 = u_2 = 0$.

35 slices are needed and 25 slices for the 90° code in Subfigure 5.14c are depicted. It can be observed, that the angle between the base vectors of the lattice in the discrete part influences the number and the shape of the slices in which the source space is partitioned.

This has two effects. First, if for an angle lower than 90° more slices and, thus, more discrete lattice points are needed to achieve the same high-cSNR performance, these points have to be closer together in the discrete part. Therefore, a higher channel quality is needed for successful decoding (Figure 5.13). It may be noted that the base vectors of the lattice exhibit equal lengths, but their absolute length is not given during the design and is derived from the required high-cSNR performance. The second effect comes from the shape of the slices. An AMBC may be interpreted as a concatenation of a vector quantizer, a mapping of the quantizer indices to lattice points, and a transmission of the resulting quantization error as the analog part, while the lattice points and the analog part are additionally rotated in space. Here, each slice can be regarded as the Voronoi region of the vector quantizer. From quantizer theory it is known that spherical Voronoi regions are optimal [LG89] [Krü10] since the symbols in the "spikes" of the slices contribute significantly to the quantizer distortion, i.e., to the required transmission power in this context. Thus, the slice which is closest to a sphere is the square of the 90° code. The other codes, including the one with the hexagonal lattice (60°), need a higher transmission power in the analog part which is equivalent to the need of a higher channel quality for operation.

Both effects lead to the observation that for all angles between base vectors of equal length for the lattice in the discrete part the 2x4 code with 90° achieves the best performance. As observed above, a 1x2 code can reach the same performance as a 2x4 code with 90° at a lower delay and complexity.

5.6 Discussion

In this chapter, AMBCs, which are composed of a multiplication with a non-square matrix and a subsequent modulo operation, are introduced and analyzed. In contrast to the purely linear LABCs, which just consist of the matrix multiplication, additional channel uses can be exploited to significantly improve the performance of the transmission system. Thus, the idea of adding a modulo operation as a nonlinearity to the LABCs resulting in the AMBCs is fruitful.

In Section 5.2, the system model is proposed, and in Section 5.3 the resulting codes are analyzed. A rotation matrix can be found to facilitate the analysis and to enable the special type of rotating decoders. Also, the high-cSNR performance can directly be stated for any given code matrix and the analysis of the resulting lattice is given.

Section 5.4 gives an overview of different decoder techniques including rotating decoders, which decompose the received code vectors to a discrete and analog part

in the first step to facilitate independent analysis of both parts. Discrete maximum likelihood decoding and zero-forcing decoding with or without lattice reduction is applied to the discrete part.

In Section 5.5, the crucial question of finding appropriate code matrices is tackled. For codes operating on just one source symbol at a time, a guideline for designing good codes can be given which is mainly finding a good lattice for the discrete part. For codes which combine several source symbols, e.g., 2x4 codes, surprising effects come into play which question applying the same guidelines also for these codes. The choice of the lattice of the discrete part influences which source vectors are jointly mapped to one common lattice points. The shape and number of the resulting slices significantly impacts the performance of the transmission system which motivates further studies. The crucial question is whether the shape and number of slices can independently be designed from the lattice of the discrete part, or if there are ways to combine good lattices and a favorable slicing for AMBCs.

As shown in [Sch13], for codes combining even more source symbols, more degrees of freedom emerge for the design. Longer block lengths are crucial for an increased performance (Section 3.6) and may provide the necessary flexibility in the design of AMBCs to decouple the lattice in the discrete part and the slicing of the source vectors. Another open question is how to transmit symbols following source distributions without a limited range. Here, compressor functions which map the source symbols to a limited range could be employed which will lead to some loss in terms of pSNR compared to the case of uniform pdfs [Sak70].

As observed in Section 3.2.1, the performance of LABCs can be improved for bad channel qualities using *Linear Minimum Mean-Square Error* (LMMSE) instead of ML estimation. This is a promising enhancement for the analog part of LABCs.

Chapter 6

Hybrid Digital-Analog Transmission

6.1 Introduction

In 2002, Skoglund et al [SPA02] answered the following question: "Can transmission systems involving continuous-amplitude processing outperform purely digital transmission systems?". They combined a numerically optimized digital transmission system with analog transmission of the quantization error to a *Hybrid Digital-Analog* (HDA) transmission system. For the digital and analog branch, orthogonal channels are used. In the digital branch, the quantizer, the generic channel code and the modulation are numerically optimized jointly. The benchmark is a purely digital system with a *Linde, Buzo and Gray* (LBG) quantizer and a generic numerically optimized channel code which is realized as a mapper between the quantization indices and the higher-dimensional code vectors. The HDA transmission system outperforms the digital system for all channel qualities.

Although the performance of the HDA system is remarkable, the design is very complex and unfeasible for long block lengths. The generic channel coding requires lookup tables at the encoder as well as at the decoder whose complexity is prohibitively high.

In this chapter a similar question is addressed: "Can HDA codes using conventional digital codes outperform conventional purely digital codes?". The design of conventional digital codes is widely known and their complexity during operation is manageable in real life systems.

In Section 6.2, purely digital and HDA transmission systems are introduced. In the subsequent Section 6.3, the performance and design of HDA systems is derived. After introducing different estimators for the digital (Section 6.3.2) and analog branch (Section 6.3.3), the properties of a joint estimator of both branches are elaborated (Section 6.3.4). In Section 6.3.5 it is shown that for every purely digital transmission system, a corresponding HDA system can be designed which shows superior performance for all channel qualities. Also the design guidelines for such a system are given ([RV13a] and [RBV14]).

The design of HDA transmission systems offers several new degrees of freedom in comparison to purely digital transmission. The effects and benefits of these new design parameters are derived in Section 6.4. Most interestingly, if the digital branch

cannot be altered in an HDA system, the analog branch can still exploit additional channel uses increasing the overall performance significantly (Section 6.4.4).

In purely digital transmission the *Iterative Source-Channel Decoding* (ISCD) transmission has been shown to achieve close-to-capacity performance [Adr03]. In Section 6.5 the benefits of HDA transmission and ISCD are combined which leads to the surprising observation that the performance of the digital channel decoder may benefit from the analog branch.

6.2 System Model

6.2.1 Purely Digital Transmission

Figure 6.1 shows a conventional digital transmission system. Also here, A/D and D/A converters are necessary, but they exhibit a sufficiently high precision so the quantization error introduced here can be neglected (Section 2.2). The source emits continuous-amplitude, discrete-time symbols which are combined to an M-dimensional source vector $\boldsymbol{u}$ following the *probability density function* (pdf) $\mathrm{p}_{\boldsymbol{u}}$. The source symbols are quantized (Q) with 2^{F_D} quantization levels. A bitmapper (BM) transforms the quantized values to $\ell_{\boldsymbol{v}_\mathrm{D}}$ *source bits* forming the bit vector $\boldsymbol{v}_\mathrm{D}$ with on average F_D bits per source symbol. The rate $r_\mathrm{D}^\mathrm{src} = \frac{M}{\ell_{\boldsymbol{v}_\mathrm{D}}}$ describes the ratio between the source dimension and the number of source bits. For non-redundant bitmapping, the rate of the quantizer and bitmapper consequently is $r_\mathrm{D}^\mathrm{src} = \frac{1}{F_\mathrm{D}}$. Subsequently, a digital channel code followed by digital modulation transforms the source bits into N real-valued channel symbols forming the vector $\boldsymbol{y}_\mathrm{D}$. The channel vector has an average power of $\mathrm{E}\{||\boldsymbol{y}_\mathrm{D}||^2\}/N = 1$. Modulation schemes using complex-valued symbols (QPSK, 8PSK) are also considered by noting the equivalence between one complex-valued symbol and two real-valued symbols. Since channel coding and modulation is combined in one step (ccm), the ratio between the number of bits $\ell_{\boldsymbol{v}_\mathrm{D}}$ and the number of real symbols N is denoted as the coding-modulation rate

$$r_\mathrm{D}^\mathrm{ccm} = \frac{\ell_{\boldsymbol{v}_\mathrm{D}}}{N}. \tag{6.1}$$

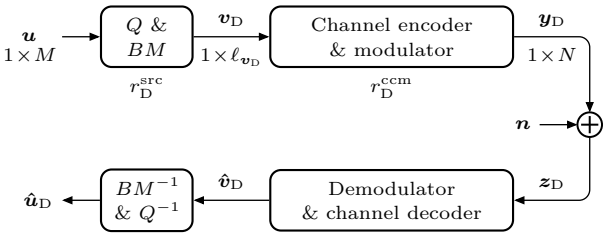

Figure 6.1: Conventional purely digital transmission.

Moreover, the ratio between the number of real source symbols and real channel symbols is given by the source-channel rate $r = M/N$. Additive white Gaussian noise $\boldsymbol{n}$ with variance σ_n^2 per dimension disturbs the channel symbols, thereby yielding the received symbols $\boldsymbol{z}_\mathrm{D}$. After demodulation, channel decoding and reconstruction of quantized values, $\hat{\boldsymbol{u}}_\mathrm{D}$ gives an estimate of the initial source symbols.

6.2.2 Hybrid Digital-Analog Transmission

Figure 6.2 illustrates the proposed HDA transmission system [RV13a]. Again, A/D and D/A converters are necessary, but their sufficiently high precision allows to neglect the introduced quantization error (Section 2.2). The general idea is to use a conventional digital transmission system for $\boldsymbol{u}$ and additionally transmit the quantization error $\boldsymbol{u}_\mathrm{H}^\mathrm{a}$ using continuous-amplitude (pseudo-analog) discrete-time processing. The upper branch of the hybrid encoder and decoder is referred to as the *digital* branch and the lower branch as the *analog* branch. All operations, also in the "analog" branch, are conducted by digital signal processing. The continuous-amplitude symbols are floating or fixed point variables with a precision depending on the digital processor. In a real-world system, only the source samples and the symbols on the transmission channel are "truly" analog. The digital branch is

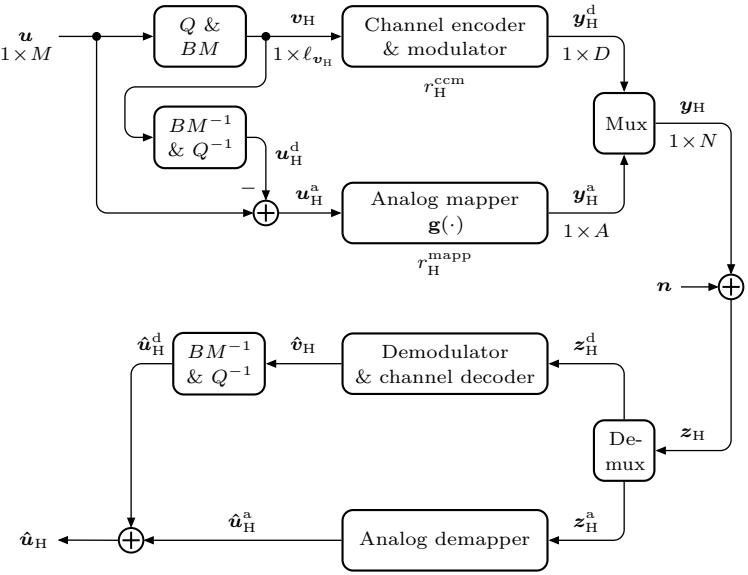

Figure 6.2: Hybrid Digital-Analog transmission.

a purely digital transmission system; per frame of M source symbols $\boldsymbol{u}$, D real channel dimensions are used by the digital branch. The analog branch takes $A > 0$ channel uses. Thus, the total number of channel uses per HDA frame is

$$N = D + A, \tag{6.2}$$

with $D < N$ and the coding-modulation rate in the digital branch is

$$r_{\mathrm{H}}^{\mathrm{ccm}} = \frac{\ell_{\boldsymbol{v}_{\mathrm{H}}}}{N - A} = \frac{\ell_{\boldsymbol{v}_{\mathrm{H}}}}{D}. \tag{6.3}$$

In order to compare both systems, the respective numbers of channel uses (N) in the digital system and in the HDA system are kept equal.

In the hybrid encoder, scalar quantization Q is applied to the elements of frame $\boldsymbol{u}$ of length M. Alternatively a vector quantizer might be applied to the complete frame or parts of the frame. Then a bit-mapper (BM) generates the bit vector $\boldsymbol{v}_{\mathrm{H}}$ with on average F_{H} bits per source symbol. The quantized source representation $\boldsymbol{u}_{\mathrm{H}}^{\mathrm{d}}$ is decoded locally in the transmitter. The quantization error $\boldsymbol{u}_{\mathrm{H}}^{\mathrm{a}} = \boldsymbol{u} - \boldsymbol{u}_{\mathrm{H}}^{\mathrm{d}}$ is processed in the analog branch. The analog mapper uses the continuous-amplitude function $\mathbf{g}(\cdot)$ to map the M entries of the vector $\boldsymbol{u}_{\mathrm{H}}^{\mathrm{a}}$ to the A entries of $\boldsymbol{y}_{\mathrm{H}}^{\mathrm{a}}$ with average power $\frac{1}{A}\,\mathrm{E}\{||\boldsymbol{y}_{\mathrm{H}}^{\mathrm{a}}||^2\} = 1$. The function $\mathbf{g}(\cdot)$ is achieved by normalizing a given mapping function $\tilde{\mathbf{g}}(\cdot)$:

$$\boldsymbol{y}_{\mathrm{H}}^{\mathrm{a}} = \sqrt{\frac{1}{\mathrm{E}\{(\tilde{\mathbf{g}}(\boldsymbol{u}_{\mathrm{H}}^{\mathrm{a}}))^2\}}} \cdot \tilde{\mathbf{g}}(\boldsymbol{u}_{\mathrm{H}}^{\mathrm{a}}) = \mathbf{g}(\boldsymbol{u}_{\mathrm{H}}^{\mathrm{a}}). \tag{6.4}$$

The function $\mathbf{g}(\cdot)$ can also be defined to work on several entries of $\boldsymbol{u}_{\mathrm{H}}^{\mathrm{a}}$ in one step and also output multiple entries of $\boldsymbol{y}_{\mathrm{H}}^{\mathrm{a}}$. The ratio between the input and the output dimensions of the block is

$$r_{\mathrm{H}}^{\mathrm{mapp}} = \frac{M}{N - D} = \frac{M}{A}. \tag{6.5}$$

This mapping $\mathbf{g}(\cdot)$ could, in case of $A = M$, e.g., be a linear amplification (with $\tilde{\mathbf{g}}(\boldsymbol{u}_{\mathrm{H}}^{\mathrm{a}}) = \boldsymbol{u}_{\mathrm{H}}^{\mathrm{a}}$) or a nonlinear function (Chapter 4) with a rate of $r_{\mathrm{H}}^{\mathrm{mapp}} = 1$ or in case of $A = 2 \cdot M$ an Archimedes spiral (Section 4.4.1, [FR06, RSV10a]) which maps one symbol onto two symbols ($r_{\mathrm{H}}^{\mathrm{mapp}} = 1/2$).

After multiplexing the symbols from the digital and analog branch and transmitting over the AWGN channel, the symbols are demultiplexed and conveyed to the digital and analog decoding branches. The analog demapper then gives $\hat{\boldsymbol{u}}_{\mathrm{H}}^{\mathrm{a}}$ as the estimate of the quantization error which can be facilitated using several methods such as *Maximum Likelihood* (ML), *Linear Minimum Mean-Square Error* (LMMSE) and *Minimum Mean-Square Error* (MMSE) estimators. The outputs of the analog and digital branches are added, whereby $\hat{\boldsymbol{u}}_{\mathrm{H}}$ gives an estimate of the initial source symbols.

Additionally to the channel quality cSNR and the end-to-end parameters SNR pSNR, the branch SNR (bSNR) is introduced for the HDA system. The bSNR describes the signal to noise ratio between the symbols sent in each branch and the corresponding estimates:

$$\mathrm{bSNR}^{\mathrm{d}} = \frac{\mathrm{E}\left\{||\boldsymbol{u}_{\mathrm{H}}^{\mathrm{d}}||^2\right\}}{\mathrm{E}\left\{||\boldsymbol{u}_{\mathrm{H}}^{\mathrm{d}} - \hat{\boldsymbol{u}}_{\mathrm{H}}^{\mathrm{d}}||^2\right\}}, \tag{6.6}$$

$$\mathrm{bSNR}^{\mathrm{a}} = \frac{\mathrm{E}\left\{||\boldsymbol{u}_{\mathrm{H}}^{\mathrm{a}}||^2\right\}}{\mathrm{E}\left\{||\boldsymbol{u}_{\mathrm{H}}^{\mathrm{a}} - \hat{\boldsymbol{u}}_{\mathrm{H}}^{\mathrm{a}}||^2\right\}}. \tag{6.7}$$

6.3 Performance and Design

In this section the performance and design of the HDA transmission system is discussed. First, a quick glance at the main difference of the performance of purely digital and hybrid transmission is given in Section 6.3.1 After introducing different estimators for the digital (Section 6.3.2) and analog branch (Section 6.3.3), the properties of a joint estimation of both branches are elaborated (Section 6.3.4) and visualized with simulation results. In Section 6.3.5 it is shown that for every purely digital transmission system, a corresponding HDA system can be designed which shows superior performance for all channel qualities. Also the design guidelines for such a system are given and their effectiveness is supported by simulation results.

6.3.1 Quick Glance at the Performance of HDA Transmission

For a first impression, Figure 6.3 shows a comparison between purely digital and HDA transmission.

Scalar ($M = 1$) source symbols following a uniform pdf are uniformly quantized with either 5 or 6 bits per symbol. A natural binary bitmapping is applied and the resulting bits are transmitted without further channel coding using *Binary Phase Shift Keying* (BPSK) modulation.

The solid red curve shows the performance of purely digital transmission using $F_{\mathrm{D}} = 6$ bits per source symbol and hence $N = 6$ channel symbols. At a certain channel quality (around $\mathrm{cSNR}|_{\mathrm{dB}} \geq 13\,\mathrm{dB}$) all bits are transmitted with negligible error probability and, thus, the performance saturates at $\mathrm{pSNR}|_{\mathrm{dB}} = 36\,\mathrm{dB}$. This saturation effect is due to the unrecoverable distortion introduced by the quantizer.

The dashed red curve shows the same purely digital system using just $F_{\mathrm{D}} = 5$ quantization bits and, thus, $N = 5$ channel symbols. Here, the performance saturates at $\mathrm{pSNR}|_{\mathrm{dB}} = 30\,\mathrm{dB}$ which is 6 dB lower due to the coarser quantization.

The solid blue curve shows the performance of HDA transmission which combines the purely digital transmission with $F_{\mathrm{H}} = 5$ quantization bits per source symbol and additional transmission of the quantization error leading to a total of $N = D + A = 5 + 1 = 6$ channel uses. This system employs the same number

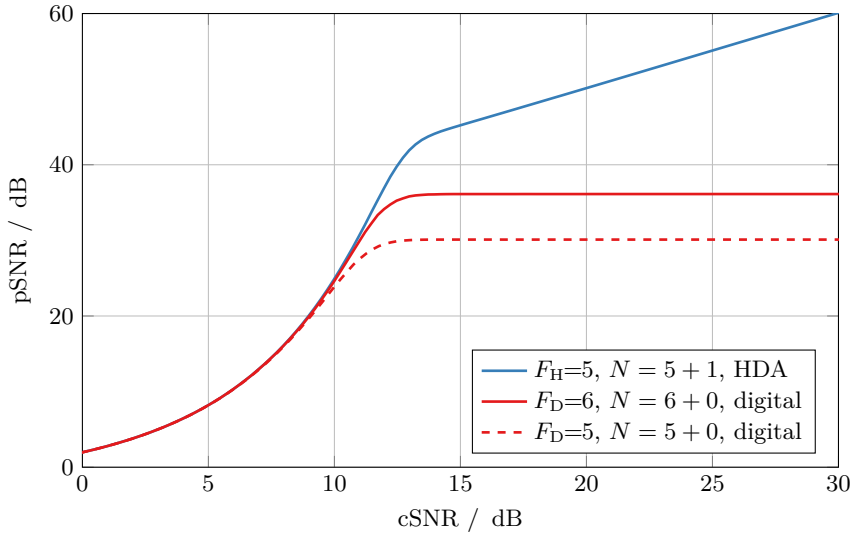

Figure 6.3: HDA and digital transmission without digital channel coding. Uniform source pdf. $M = 1$. HDA: $A = 1$, $D = 5$, $N = 6$, LMMSE estimator in analog branch. Digital: $N \in \{5, 6\}$.

of channel uses and the same transmission power as the purely digital system with the black solid curve. First of all, it can be observed, that the HDA system does not show a saturation, but improves its performance for increasing channel qualities. Second, the loss due to a coarser quantization in the HDA system is overcompensated by the analog transmission of the quantization error. Thus, the purely digital transmission is outperformed by the HDA transmission.

6.3.2 Estimators for the Digital Branch

The decoding and estimation techniques which can be applied in the purely digital system and the digital branch of the HDA system are essentially the same. For a fair comparison of a purely digital and an HDA system, the techniques should, of course, be of the same type. For demodulation, channel decoding and reconstruction of the quantized values, either hard or soft decision techniques can be applied. In case of soft decision, the inverse bit mapper BM^{-1} obtains the probability of occurrence $\mathrm{p}(\hat{\boldsymbol{v}}|Q(\boldsymbol{u}))$ for each quantization level $Q(\boldsymbol{u})$ for the soft output $\hat{\boldsymbol{v}}$ by the channel decoder. The function $Q(\boldsymbol{u})$ refers to all possible quantization levels of the source symbols. In the HDA case, the quantized values are denoted as $\boldsymbol{u}_{\mathrm{H}}^{\mathrm{d}}$, which replaces $Q(\boldsymbol{u})$ in equations related to the HDA case.

There are different estimators which convert these probabilities to an estimate

$\hat{\boldsymbol{u}}$ for $\boldsymbol{u}$. The simplest estimator is the ML estimator which just takes the most probable quantization level. The estimator is shown for the purely digital ($\hat{\boldsymbol{u}}_{\mathrm{D}}$) and the hybrid case ($\hat{\boldsymbol{u}}_{\mathrm{H}}^{\mathrm{d}}$):

$$\begin{aligned}\hat{\boldsymbol{u}}_{\mathrm{D,ML}} &= \underset{Q(\boldsymbol{u})}{\operatorname{argmax}}\, \mathrm{p}(\hat{\boldsymbol{v}}_{\mathrm{D}}|Q(\boldsymbol{u})),\\ \hat{\boldsymbol{u}}_{\mathrm{H,ML}}^{\mathrm{d}} &= \underset{\boldsymbol{u}_{\mathrm{H}}^{\mathrm{d}}}{\operatorname{argmax}}\, \mathrm{p}(\hat{\boldsymbol{v}}_{\mathrm{H}}|\boldsymbol{u}_{\mathrm{H}}^{\mathrm{d}})).\end{aligned} \tag{6.8}$$

The *Maximum a Posteriori* (MAP) estimator takes into account the a-priori known probability of occurrence of each quantization level:

$$\begin{aligned}\hat{\boldsymbol{u}}_{\mathrm{D,MAP}} &= \underset{Q(\boldsymbol{u})}{\operatorname{argmax}}\, \mathrm{p}(Q(\boldsymbol{u})|\hat{\boldsymbol{v}}_{\mathrm{D}}) = \underset{Q(\boldsymbol{u})}{\operatorname{argmax}}\, \mathrm{p}(\hat{\boldsymbol{v}}_{\mathrm{D}}|Q(\boldsymbol{u})) \cdot \mathrm{p}(Q(\boldsymbol{u})),\\ \hat{\boldsymbol{u}}_{\mathrm{H,MAP}}^{\mathrm{d}} &= \underset{\boldsymbol{u}_{\mathrm{H}}^{\mathrm{d}}}{\operatorname{argmax}}\, \mathrm{p}(\boldsymbol{u}_{\mathrm{H}}^{\mathrm{d}}|\hat{\boldsymbol{v}}_{\mathrm{H}}) = \underset{\boldsymbol{u}_{\mathrm{H}}^{\mathrm{d}}}{\operatorname{argmax}}\, \mathrm{p}(\hat{\boldsymbol{v}}_{\mathrm{H}}|\boldsymbol{u}_{\mathrm{H}}^{\mathrm{d}}) \cdot \mathrm{p}(\boldsymbol{u}_{\mathrm{H}}^{\mathrm{d}}).\end{aligned} \tag{6.9}$$

The estimator leading to the smallest *Mean-Square Error* (MSE) is the MMSE estimator which weights the reconstruction points of all possible quantization levels with their a-posteriori probability of occurrence:

$$\begin{aligned}\hat{\boldsymbol{u}}_{\mathrm{D,MMSE}} &= \mathrm{E}\left\{Q(\boldsymbol{u})|\hat{\boldsymbol{v}}_{\mathrm{D}}\right\} = \sum_{Q(\boldsymbol{u})} Q(\boldsymbol{u}) \cdot \mathrm{p}(Q(\boldsymbol{u})|\hat{\boldsymbol{v}}_{\mathrm{D}}),\\ \hat{\boldsymbol{u}}_{\mathrm{H,MMSE}}^{\mathrm{d}} &= \mathrm{E}\left\{\boldsymbol{u}_{\mathrm{H}}^{\mathrm{d}}|\hat{\boldsymbol{v}}_{\mathrm{D}}\right\} = \sum_{\boldsymbol{u}_{\mathrm{H}}^{\mathrm{d}}} \boldsymbol{u}_{\mathrm{H}}^{\mathrm{d}} \cdot \mathrm{p}(\boldsymbol{u}_{\mathrm{H}}^{\mathrm{d}}|\hat{\boldsymbol{v}}_{\mathrm{H}}).\end{aligned} \tag{6.10}$$

6.3.3 Estimators for the Analog Branch

In the analog branch, several different estimators can be applied. The performance of the estimators can be assessed independently of the digital branch by considering the branch SNR (bSNR$^{\mathrm{a}}$) of the analog branch (6.7), i.e., the SNR between the quantization error $\boldsymbol{u}_{\mathrm{H}}^{\mathrm{a}}$ and the estimate $\hat{\boldsymbol{u}}_{\mathrm{H}}^{\mathrm{a}}$ of the same in the receiver.

Maximum Likelihood Estimator

The least complex estimator, which is considered here, is the *Maximum Likelihood* (ML) estimator:

$$\begin{aligned}\hat{\boldsymbol{u}}_{\mathrm{H,ML}}^{\mathrm{a}} &= \underset{\boldsymbol{u}_{\mathrm{H}}^{\mathrm{a}}}{\operatorname{argmax}}\, \mathrm{p}(\boldsymbol{z}_{\mathrm{H}}^{\mathrm{a}}|\boldsymbol{u}_{\mathrm{H}}^{\mathrm{a}}) = \underset{\boldsymbol{u}_{\mathrm{H}}^{\mathrm{a}}}{\operatorname{argmax}}\, \mathrm{p}(\boldsymbol{z}_{\mathrm{H}}^{\mathrm{a}}|\boldsymbol{y}_{\mathrm{H}}^{\mathrm{a}})\\ &= \underset{\boldsymbol{u}_{\mathrm{H}}^{\mathrm{a}}}{\operatorname{argmax}}\, \mathrm{p}(\boldsymbol{z}_{\mathrm{H}}^{\mathrm{a}}|\, \mathbf{g}(\boldsymbol{u}_{\mathrm{H}}^{\mathrm{a}}))\\ &= \underset{\boldsymbol{u}_{\mathrm{H}}^{\mathrm{a}}}{\operatorname{argmax}}\, \mathrm{p}_{\boldsymbol{\mathcal{N}}}(\boldsymbol{z}_{\mathrm{H}}^{\mathrm{a}} - \mathbf{g}(\boldsymbol{u}_{\mathrm{H}}^{\mathrm{a}})),\end{aligned} \tag{6.11}$$

while $\mathrm{p}_{\boldsymbol{\mathcal{N}}}(\cdot)$ is the pdf of the additive noise vector. In case of additive Gaussian noise, or any other additive noise which has its maximum probability at $\boldsymbol{n} = 0$, the optimum $\hat{\boldsymbol{u}}_{\mathrm{H}}^{\mathrm{a}}$ is found when the argument of $\mathrm{p}_{\boldsymbol{\mathcal{N}}}(\cdot)$ is 0:

$$\begin{aligned} & \boldsymbol{z}_{\mathrm{H}}^{\mathrm{a}} - \mathbf{g}(\hat{\boldsymbol{u}}_{\mathrm{H,ML}}^{\mathrm{a}}) = 0 \\ \Leftrightarrow \quad & \boldsymbol{z}_{\mathrm{H}}^{\mathrm{a}} = \mathbf{g}(\hat{\boldsymbol{u}}_{\mathrm{H,ML}}^{\mathrm{a}}) \\ \Leftrightarrow \quad & \hat{\boldsymbol{u}}_{\mathrm{H,ML}}^{\mathrm{a}} = \mathbf{g}^{-1}(\boldsymbol{z}_{\mathrm{H}}^{\mathrm{a}}). \end{aligned} \tag{6.12}$$

Thus, $\hat{\boldsymbol{u}}_{\mathrm{H,ML}}^{\mathrm{a}}$ is found by applying the inverted analog mapper function $\mathbf{g}^{-1}(\cdot)$ to the received value $\boldsymbol{z}_{\mathrm{H}}^{\mathrm{a}}$. The ML estimator does not require any knowledge about the channel quality (cSNR) or the pdf of the quantization error $\mathrm{p}(\boldsymbol{u}_{\mathrm{H}}^{\mathrm{a}})$. For a linear analog mapper ($\tilde{\mathbf{g}}(\boldsymbol{u}_{\mathrm{H}}^{\mathrm{a}}) = \boldsymbol{u}_{\mathrm{H}}^{\mathrm{a}}$) with $r_{\mathrm{H}}^{\mathrm{mapp}} = 1$ the performance is derived in 3.2.1 and is

$$\mathrm{bSNR}_{\mathrm{ML}}^{\mathrm{a}} = \mathrm{cSNR}. \tag{6.13}$$

Minimum Mean Square Error Estimator

The *Minimum Mean-Square Error* (MMSE) estimator is, in general, a nonlinear estimator which minimizes the MSE. The MMSE estimate $\hat{\boldsymbol{u}}_{\mathrm{H,MMSE}}^{\mathrm{a}}$ can be stated as the conditional expectation of $\boldsymbol{u}_{\mathrm{H}}^{\mathrm{a}}$ given the received value $\boldsymbol{z}_{\mathrm{H}}^{\mathrm{a}}$:

$$\begin{aligned} \hat{\boldsymbol{u}}_{\mathrm{H,MMSE}}^{\mathrm{a}} = \mathrm{E}\left\{\boldsymbol{u}_{\mathrm{H}}^{\mathrm{a}} | \boldsymbol{z}_{\mathrm{H}}^{\mathrm{a}}\right\} &= \int \boldsymbol{u}_{\mathrm{H}}^{\mathrm{a}} \cdot \mathrm{p}(\boldsymbol{u}_{\mathrm{H}}^{\mathrm{a}} | \boldsymbol{z}_{\mathrm{H}}^{\mathrm{a}}) \, \mathrm{d}\boldsymbol{u}_{\mathrm{H}}^{\mathrm{a}} \\ &= \int \boldsymbol{u}_{\mathrm{H}}^{\mathrm{a}} \cdot \frac{\mathrm{p}(\boldsymbol{z}_{\mathrm{H}}^{\mathrm{a}} | \boldsymbol{u}_{\mathrm{H}}^{\mathrm{a}}) \cdot \mathrm{p}(\boldsymbol{u}_{\mathrm{H}}^{\mathrm{a}})}{\mathrm{p}(\boldsymbol{z}_{\mathrm{H}}^{\mathrm{a}})} \, \mathrm{d}\boldsymbol{u}_{\mathrm{H}}^{\mathrm{a}} \\ &= \frac{1}{\mathrm{p}(\boldsymbol{z}_{\mathrm{H}}^{\mathrm{a}})} \cdot \int \boldsymbol{u}_{\mathrm{H}}^{\mathrm{a}} \cdot \mathrm{p}_{\boldsymbol{\mathcal{N}}}(\boldsymbol{z}_{\mathrm{H}}^{\mathrm{a}} - \mathbf{g}(\boldsymbol{u}_{\mathrm{H}}^{\mathrm{a}})) \cdot \mathrm{p}(\boldsymbol{u}_{\mathrm{H}}^{\mathrm{a}}) \, \mathrm{d}\boldsymbol{u}_{\mathrm{H}}^{\mathrm{a}} \\ &= \frac{1}{C} \cdot \int \boldsymbol{u}_{\mathrm{H}}^{\mathrm{a}} \cdot \mathrm{p}_{\boldsymbol{\mathcal{N}}}(\boldsymbol{z}_{\mathrm{H}}^{\mathrm{a}} - \mathbf{g}(\boldsymbol{u}_{\mathrm{H}}^{\mathrm{a}})) \cdot \mathrm{p}(\boldsymbol{u}_{\mathrm{H}}^{\mathrm{a}}) \, \mathrm{d}\boldsymbol{u}_{\mathrm{H}}^{\mathrm{a}}, \end{aligned} \tag{6.14}$$

with $C = \mathrm{p}(\boldsymbol{z}_{\mathrm{H}}^{\mathrm{a}}) = \int \mathrm{p}_{\boldsymbol{\mathcal{N}}}(\boldsymbol{z}_{\mathrm{H}}^{\mathrm{a}} - \mathbf{g}(\boldsymbol{u}_{\mathrm{H}}^{\mathrm{a}})) \cdot \mathrm{p}(\boldsymbol{u}_{\mathrm{H}}^{\mathrm{a}}) \, \mathrm{d}\boldsymbol{u}_{\mathrm{H}}^{\mathrm{a}}$ as a normalization, so the integral $\int \mathrm{p}(\boldsymbol{u}_{\mathrm{H}}^{\mathrm{a}} | \boldsymbol{z}_{\mathrm{H}}^{\mathrm{a}}) \, \mathrm{d}\boldsymbol{u}_{\mathrm{H}}^{\mathrm{a}}$ is 1. The potentially nonlinear effects of the analog mapper $\mathbf{g}(\cdot)$, the pdf of the quantization error $\mathrm{p}(\boldsymbol{u}_{\mathrm{H}}^{\mathrm{a}})$ and the pdf of the additive noise are incorporated in the estimation and have to be available to the estimator. This estimator shows the highest complexity, since, in general, an M-dimensional integration has to be performed. It also shows the highest performance in terms of pSNR which cannot be stated in closed form and has to be obtained by simulations.

Linear Minimum Mean Square Error Estimator

A less complex estimator which minimizes the MSE using only linear operations is the *Linear Minimum Mean-Square Error* (LMMSE) estimator. This estimator just

depends on the mean and variance of the quantization error and the noise. Since only linear operations are permitted, the LMMSE estimator can just be used for a linear analog mapper $\mathbf{g}(\cdot)$. The LMMSE estimator can be derived using (3.13) with an identity matrix as a mapper ($\boldsymbol{P} = \mathbb{1}$) and the same dimensions before and after the mapping ($A = M$):

$$\hat{\boldsymbol{u}}^{\mathrm{a}}_{\mathrm{H,LMMSE}} = \boldsymbol{z}^{\mathrm{a}}_{\mathrm{H}} \cdot \boldsymbol{Q} = \frac{\mathrm{cSNR}}{1 + \mathrm{cSNR}} \cdot \boldsymbol{z}^{\mathrm{a}}_{\mathrm{H}}. \tag{6.15}$$

In case of a linear analog mapper, the performance can directly be stated as (3.29):

$$\mathrm{bSNR}^{\mathrm{a}}_{\mathrm{LMMSE}} = \mathrm{cSNR} + 1. \tag{6.16}$$

For a nonlinear analog mapper, it is also possible to concatenate the LMMSE estimator and the ML estimator [FVACGF13]. The LMMSE estimator normalizes the channel output variance and the ML estimator inverts the nonlinear mapping leading to the following estimator:

$$\hat{\boldsymbol{u}}^{\mathrm{a}}_{\mathrm{H,LMMSE+ML}} = \mathbf{g}^{-1}\left(\frac{\mathrm{cSNR}}{1 + \mathrm{cSNR}} \cdot \boldsymbol{z}^{\mathrm{a}}_{\mathrm{H}}\right). \tag{6.17}$$

As in the nonlinear ML estimator case above, the performance cannot be stated directly.

For very good channels, the ML estimator performs as good as the LMMSE estimator, but for bad channels, the LMMSE estimator is superior. For a Gaussian source and an AWGN channel, the LMMSE performance reaches the MMSE performance, while in any other case, the MMSE estimator outperforms all other estimators [Kay93].

6.3.4 Joint and Independent Estimation

In Figure 6.2 two independent estimators for the digital and the analog branch are used and their estimates are added up. In the following section, a joint estimator which considers both, the digital and the analog branch, is derived [RV13a, RBV14]. In the subsequent section, the optimality of the initially presented independent estimation is derived for statistically independent quantized values and quantization errors. Simulation results are provided to visualize the performance difference of both estimation techniques.

Optimal Joint Estimation

In the following, a joint MMSE estimator is considered, which incorporates the information of both, the digital and the analog branch, to form one estimate. Figure 6.4 shows the modified HDA transmission system with the joint estimator, which replaces the analog demapper, the inverse bitmapping (BM^{-1}), and the summation in Figure 6.2. It is assumed that $\hat{\boldsymbol{v}}_{\mathrm{H}}$ is a *sufficient statistics* [Kay93] of

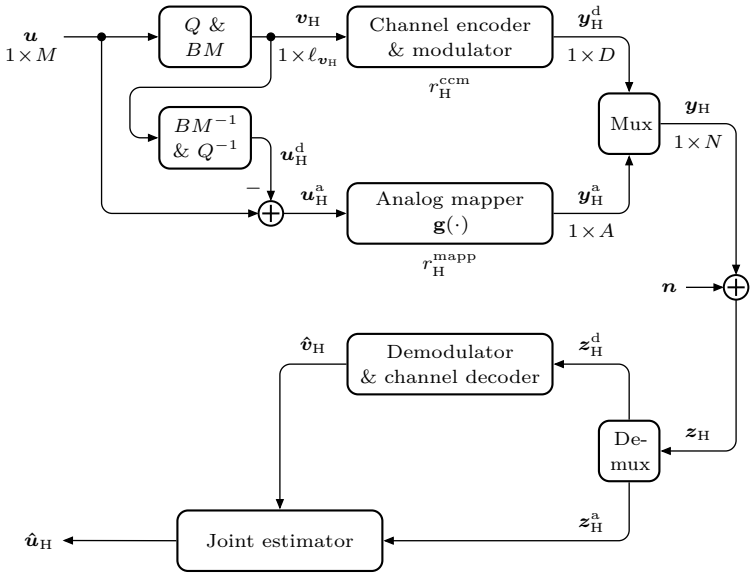

Figure 6.4: Hybrid Digital-Analog transmission with joint estimation.

$\boldsymbol{z}_\mathrm{H}^\mathrm{d}$, thus, the demodulator and channel decoder convert the received values to soft values without losing information. Therefore, in the evaluation of probabilities, $\hat{\boldsymbol{v}}_\mathrm{H}$ and $\boldsymbol{z}_\mathrm{H}^\mathrm{d}$ may be interchanged without changing the result. The effect of channel coding, modulation, transmission over an AWGN channel, demodulation and channel decoding is contained in the soft information of $\hat{\boldsymbol{v}}_\mathrm{H}$. The same holds for $\boldsymbol{z}_\mathrm{D}$ and $\hat{\boldsymbol{v}}_\mathrm{D}$ for purely digital transmission. The joint MMSE estimate of $\boldsymbol{u}$ for the received values $\boldsymbol{z}_\mathrm{H}^\mathrm{d}$ and $\boldsymbol{z}_\mathrm{H}^\mathrm{a}$ in the digital and the analog branch, respectively, can be stated follows (see Section B.1 in the appendix for complete derivation):

$$\begin{aligned}\hat{\boldsymbol{u}}_\mathrm{H} &= \mathrm{E}\{\boldsymbol{u}|\boldsymbol{z}_\mathrm{H}^\mathrm{a}, \boldsymbol{z}_\mathrm{H}^\mathrm{d}\} && (6.18)\\ &= \frac{1}{C}\cdot\int \boldsymbol{u}_\mathrm{H}^\mathrm{a}\cdot \mathrm{p}(\boldsymbol{z}_\mathrm{H}^\mathrm{a}|\boldsymbol{u}_\mathrm{H}^\mathrm{a})\cdot \mathrm{p}(\boldsymbol{z}_\mathrm{H}^\mathrm{d}|\boldsymbol{u}_\mathrm{H}^\mathrm{a})\cdot \mathrm{p}(\boldsymbol{u}_\mathrm{H}^\mathrm{a})\,\mathrm{d}\boldsymbol{u}_\mathrm{H}^\mathrm{a}\\ &\quad + \frac{1}{C}\cdot\sum_{\boldsymbol{u}_\mathrm{H}^\mathrm{d}} \boldsymbol{u}_\mathrm{H}^\mathrm{d}\cdot \mathrm{p}(\boldsymbol{z}_\mathrm{H}^\mathrm{d}|\boldsymbol{u}_\mathrm{H}^\mathrm{d})\cdot \mathrm{p}(\boldsymbol{z}_\mathrm{H}^\mathrm{a}|\boldsymbol{u}_\mathrm{H}^\mathrm{d})\cdot \mathrm{P}(\boldsymbol{u}_\mathrm{H}^\mathrm{d}). && (6.19)\end{aligned}$$

The constant C is $C = \mathrm{p}(\boldsymbol{z}_\mathrm{H}^\mathrm{a}, \boldsymbol{z}_\mathrm{H}^\mathrm{d})$.

The formula shows that the joint estimator can be split up into two estimators. The estimator for the digital branch (second line in (6.19)) incorporates knowledge about the statistics of the quantization error $\mathrm{p}\left(\boldsymbol{z}_\mathrm{H}^\mathrm{a}|\boldsymbol{u}_\mathrm{H}^\mathrm{d}\right)$ as does the estimator for the analog branch (first line in (6.19)) about the quantized values $\mathrm{p}\left(\boldsymbol{z}_\mathrm{H}^\mathrm{a}|\boldsymbol{u}_\mathrm{H}^\mathrm{a}\right)$.

The cross terms $\mathrm{p}(\boldsymbol{z}_{\mathrm{H}}^{\mathrm{d}}|\boldsymbol{u}_{\mathrm{H}}^{\mathrm{a}})$ and $\mathrm{p}(\boldsymbol{z}_{\mathrm{H}}^{\mathrm{a}}|\boldsymbol{u}_{\mathrm{H}}^{\mathrm{d}})$ in (6.19) indicate that the general MMSE estimator cannot be calculated using separate estimators for the digital and analog branches.

More details and insight about the derivation of the joint estimator can be found in [Bun12].

Optimality of Independent Estimation

In several scenarios, the quantized values $\boldsymbol{u}_{\mathrm{H}}^{\mathrm{d}}$ in the digital and the quantization error $\boldsymbol{u}_{\mathrm{H}}^{\mathrm{a}}$ in the analog branch are statistically independent. This holds, e.g., for a uniform source pdf with a uniform quantizer and is approximately given in most practical cases.

In case of statistical independence, the following relation holds:

$$\mathrm{p}(\boldsymbol{u}_{\mathrm{H}}^{\mathrm{a}}, \boldsymbol{u}_{\mathrm{H}}^{\mathrm{d}}) = \mathrm{p}(\boldsymbol{u}_{\mathrm{H}}^{\mathrm{a}}) \cdot \mathrm{p}(\boldsymbol{u}_{\mathrm{H}}^{\mathrm{d}}). \tag{6.20}$$

Using the statistical independence, the MMSE estimator can be stated as follows (see Section B.2 in the appendix) while $\hat{\boldsymbol{u}}_{\mathrm{H}}^{\mathrm{a}}$ and $\hat{\boldsymbol{u}}_{\mathrm{H}}^{\mathrm{d}}$ are the independent MMSE estimates in the analog and the digital branch respectively:

$$\hat{\boldsymbol{u}}_{\mathrm{H}} = \hat{\boldsymbol{u}}_{\mathrm{H}}^{\mathrm{a}} + \hat{\boldsymbol{u}}_{\mathrm{H}}^{\mathrm{d}}. \tag{6.21}$$

Equation (6.21) shows that, given statistical independence (6.20), independent MMSE estimation in the digital and analog branches and adding up the results yields the optimal MMSE estimation.

Simulation Results

In this section, the performance of joint and independent estimation will be compared. The 80-dimensional ($M = 80$) source vector is quantized with varying fidelity from $F_{\mathrm{H}} = 1$ to $F_{\mathrm{H}} = 4$ bits per source symbol. A rate-$\frac{1}{2}$ recursive systematic convolutional code with the generator polynomial $\{1, 15/13\}_8$ – the same code which is used as a component code in UMTS-LTE [3GP11] – is employed with a BPSK modulation. Since no puncturing is used, the number of channel uses varies from $N = 160$ to $N = 640$ and therefore just simulations with the same quantizer fidelity can be compared. In case of independent estimation (Figure 6.2) an MMSE estimator is used in both, the digital and the analog branch. The joint estimator employs a joint MMSE estimator (6.19).

Figure 6.5 shows the performance for a uniform source pdf. For this source pdf, the used uniform quantizer generates statistically independent quantized values and quantization errors. In accordance with (6.21), the performance of the independent and the joint estimator is the same for all quantization fidelities.

A different result is depicted in Figure 6.6. For a Gaussian source pdf, the employed *Lloyd-Max Quantizer* (LMQ) generates statistically dependent quantized

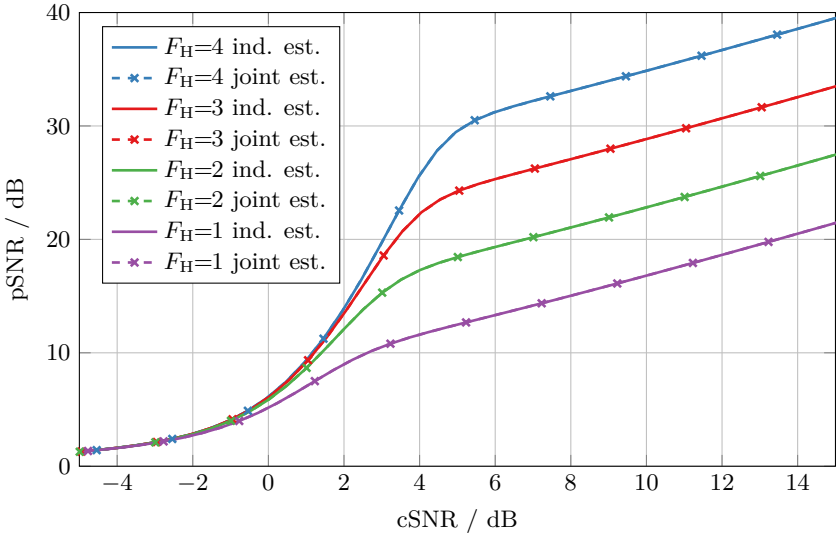

Figure 6.5: Independent and joint estimator for source symbols with a uniform pdf for different quantizer fidelities.

values $\boldsymbol{u}_{\mathrm{H}}^{\mathrm{d}}$ and quantization errors $\boldsymbol{u}_{\mathrm{H}}^{\mathrm{a}}$. For all quantization fidelities, the joint estimator exhibits a superior performance to the independent estimator. The gain vanishes for very low channel qualities, but as soon as the channel quality is high enough for the digital branch to transmit with low error probability, a gain in pSNR of up to 0.4 dB can be achieved.

6.3.5 Theoretical System Performance

In this section, the performance of HDA and purely digital transmission is assessed [RV13a, RBV14] while it is assumed that both systems employ the same type of digital quantization, coding, and modulation concepts. Since the overall performance of the HDA system depends on the transmission errors in the digital branch and the noise in the analog branch, different cases depending on the channel quality can be distinguished. In the following the range of possible channel qualities is partitioned into several regions (Fig 6.7). In the high-cSNR region, the "Good channel conditions", the digital branch transmits with negligible error probability (starting at $\mathrm{cSNR}_D^{\mathrm{sat.}}$). Here, the performance of the transmission system is governed by the analog branch. In the low-cSNR region region, the "Bad channel conditions", many bit errors in the digital branch occur. The channel quality at which an ideal capacity achieving code would transmit without bit errors is $\mathrm{cSNR}_{\mathrm{ideal},P_e=0}$. The

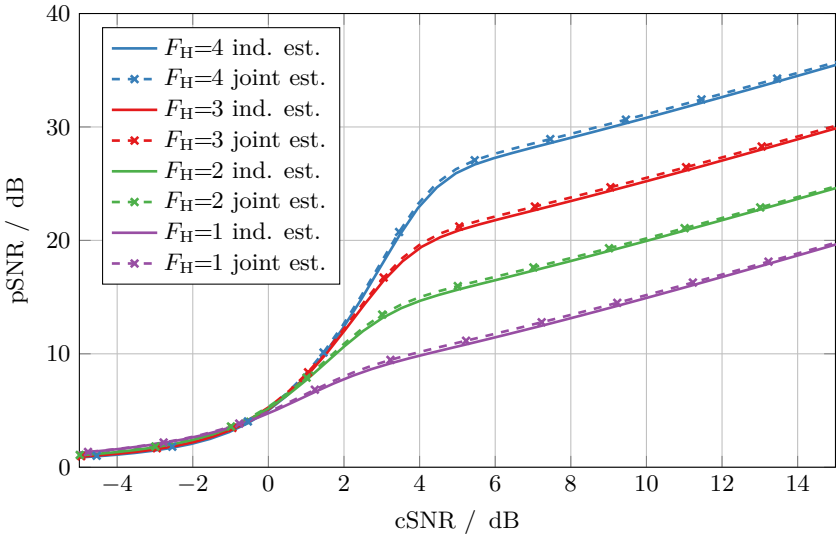

Figure 6.6: Independent and joint estimator for source symbols with a Gaussian pdf for different quantizer fidelities.

gap interval, here in dB,

$$\Delta_{\mathrm{ideal}}|_{\mathrm{dB}} = \mathrm{cSNR}_{\mathrm{ideal},P_e=0}|_{\mathrm{dB}} - \mathrm{cSNR}_D^{\mathrm{sat.}}|_{\mathrm{dB}} \tag{6.22}$$

between the ideal code and the practical code is also depicted in Fig. 6.7.

Good Channel Conditions

The region of "Good channel conditions" comprises the cSNR above a certain channel quality ($\mathrm{cSNR}_D^{\mathrm{sat.}}$) in which almost error-free transmission in the digital branch is achieved. This channel quality assuring error-free transmission in the digital branch can be lower bounded using the Shannon capacity. First, a source encoder which yields equiprobable output bits and an ideal channel code is assumed. This assumption facilitates error-free decoding employing $r_{\mathrm{D}}^{\mathrm{ccm}} = \frac{\ell_{\boldsymbol{v}_{\mathrm{D}}}}{N} \leq C$ bits per channel use at $\mathrm{cSNR}_D^{\mathrm{sat.}}$:

$$r_{\mathrm{D}}^{\mathrm{ccm}} \leq C = \frac{1}{2}\,\mathrm{ld}\left(1 + \mathrm{cSNR}_D^{\mathrm{sat.}}\right) \tag{6.23}$$

$$\Rightarrow \quad \mathrm{cSNR}_D^{\mathrm{sat.}} \geq 4^{r_{\mathrm{D}}^{\mathrm{ccm}}} - 1 \tag{6.24}$$

$$\Rightarrow \quad \mathrm{cSNR}_D^{\mathrm{sat.}} \cdot \Delta_{\mathrm{ideal}} = 4^{r_{\mathrm{D}}^{\mathrm{ccm}}} - 1. \tag{6.25}$$

The factor Δ_{ideal} equals 1 for ideal digital channel codes, and $0 < \Delta_{\mathrm{ideal}} < 1$ holds for codes in practice. Thus, for $\mathrm{cSNR} \geq \mathrm{cSNR}_D^{\mathrm{sat.}} = \frac{4^{r_{\mathrm{D}}^{\mathrm{ccm}}} - 1}{\Delta_{\mathrm{ideal}}}$ error-free decoding in

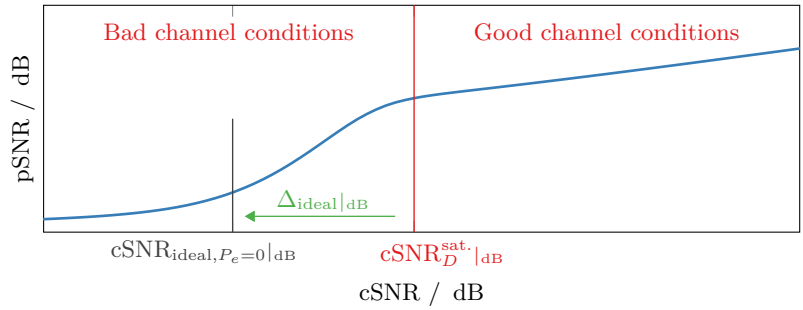

Figure 6.7: Illustration of different channel quality regions.

the digital branch can be achieved.

Digital codes show a waterfall behavior from erroneous to error-free transmission. Comparing the same type of codes, the channel quality at which the waterfall occurs depends on the coding rate r^{ccm}. To design an HDA transmission system with the waterfall at the same or lower cSNR, the coding rate of the HDA system $r_{\text{H}}^{\text{ccm}}$ (6.3) has to be equal or better (lower) than that of the purely digital system $r_{\text{D}}^{\text{ccm}}$ (6.1) :

$$r_{\text{H}}^{\text{ccm}} \leq r_{\text{D}}^{\text{ccm}} \tag{6.26}$$

$$\Rightarrow \quad r_{\text{H}}^{\text{ccm}} = r_{\text{D}}^{\text{ccm}} - \Delta r, \qquad \Delta r \geq 0. \tag{6.27}$$

Since the HDA system needs equal or lower coding rates for the digital branch and A additional channel uses for the analog branch, the same number of channel uses (N) in both systems can only be achieved by changing another parameter: the number of bits ($\ell_{\boldsymbol{v}_{\text{H}}}$) generated by quantizer and bit-mapper. This number of bits can be decreased by reducing the fidelity of the quantizer in the HDA system.

The quantizer in the purely digital transmission system utilizes

$$F_{\text{D}} = \ell_{\boldsymbol{v}_{\text{D}}}/M = r_{\text{D}}^{\text{ccm}} \cdot N/M \tag{6.28}$$

bits per source dimension while the quantizer in the HDA system utilizes

$$F_{\text{H}} = \ell_{\boldsymbol{v}_{\text{H}}}/M = r_{\text{H}}^{\text{ccm}} \cdot (N-A)/M \tag{6.29}$$

bits per source dimension.

Starting with (6.27), and using (6.28) and (6.29), the required difference $\Delta F =$

$F_\mathrm{D} - F_\mathrm{H}$ in bits per dimension can be calculated as follows:

$$
\begin{aligned}
& r_\mathrm{H}^\mathrm{ccm} = r_\mathrm{D}^\mathrm{ccm} - \Delta r \\
\Leftrightarrow \quad & \frac{F_\mathrm{H} \cdot M}{N - A} = r_\mathrm{D}^\mathrm{ccm} - \Delta r \\
\Leftrightarrow \quad & F_\mathrm{H} = \frac{N - A}{M} \cdot (r_\mathrm{D}^\mathrm{ccm} - \Delta r) \\
\Rightarrow \quad & \Delta F := F_\mathrm{D} - F_\mathrm{H} \qquad (6.30) \\
& \quad = r_\mathrm{D}^\mathrm{ccm} \cdot \frac{N}{M} - r_\mathrm{D}^\mathrm{ccm} \cdot \frac{N - A}{M} + \Delta r \cdot \frac{N - A}{M} \\
& \quad = r_\mathrm{D}^\mathrm{ccm} \cdot \frac{A}{M} + \Delta r \cdot \left(\frac{N}{M} - \frac{A}{M} \right) \\
& \Delta F = \frac{r_\mathrm{D}^\mathrm{ccm}}{r_\mathrm{H}^\mathrm{mapp}} + \Delta r \cdot \left(\frac{N}{M} - \frac{1}{r_\mathrm{H}^\mathrm{mapp}} \right). \qquad (6.31)
\end{aligned}
$$

Thus, given a match of the digital channel coding rates ($\Delta r = 0$) and an analog branch with $r_\mathrm{H}^\mathrm{mapp} = 1$ ($A = M$), the difference in quantization fidelity only depends on the given channel coding rate of the purely digital system $r_\mathrm{D}^\mathrm{ccm}$.

The influence on the MSE of this lower fidelity of the quantization in the HDA system is derived in the following. Since the channel quality is considered to be high enough ($\mathrm{cSNR} \geq \mathrm{cSNR}_D^{\mathrm{sat.}}$) to facilitate error-free transmission in the digital branch, the distortion in the digital branch is zero $\mathrm{E}\{||\boldsymbol{u}_\mathrm{H}^\mathrm{d} - \hat{\boldsymbol{u}}_\mathrm{H}^\mathrm{d}||^2\} = 0$.

Therefore, it can be shown that the end-to-end MSE of the HDA system just depends on the performance of the analog branch:

$$
\begin{aligned}
\mathrm{E}\left\{||\boldsymbol{u} - \hat{\boldsymbol{u}}_\mathrm{H}||^2\right\} &= \mathrm{E}\left\{||(\boldsymbol{u}_\mathrm{H}^\mathrm{d} + \boldsymbol{u}_\mathrm{H}^\mathrm{a}) - (\hat{\boldsymbol{u}}_\mathrm{H}^\mathrm{d} + \hat{\boldsymbol{u}}_\mathrm{H}^\mathrm{a})||^2\right\} \\
&= \mathrm{E}\left\{||\boldsymbol{u}_\mathrm{H}^\mathrm{d} - \hat{\boldsymbol{u}}_\mathrm{H}^\mathrm{d}||^2\right\} + \mathrm{E}\left\{||\boldsymbol{u}_\mathrm{H}^\mathrm{a} - \hat{\boldsymbol{u}}_\mathrm{H}^\mathrm{a}||^2\right\} \\
&\quad + 2\,\mathrm{E}\left\{\boldsymbol{u}_\mathrm{H}^\mathrm{d} \cdot \boldsymbol{u}_\mathrm{H}^{\mathrm{a}\,\mathrm{T}}\right\} - 2\,\mathrm{E}\left\{\boldsymbol{u}_\mathrm{H}^\mathrm{d} \cdot \hat{\boldsymbol{u}}_\mathrm{H}^{\mathrm{a}\,\mathrm{T}}\right\} \\
&\quad - 2\,\mathrm{E}\left\{\boldsymbol{u}_\mathrm{H}^\mathrm{a} \cdot \hat{\boldsymbol{u}}_\mathrm{H}^{\mathrm{d}\,\mathrm{T}}\right\} + 2\,\mathrm{E}\left\{\hat{\boldsymbol{u}}_\mathrm{H}^\mathrm{d} \cdot \hat{\boldsymbol{u}}_\mathrm{H}^{\mathrm{a}\,\mathrm{T}}\right\} \\
&\overset{\hat{\boldsymbol{u}}_\mathrm{H}^\mathrm{d} = \boldsymbol{u}_\mathrm{H}^\mathrm{d}}{=} \mathrm{E}\left\{||\boldsymbol{u}_\mathrm{H}^\mathrm{a} - \hat{\boldsymbol{u}}_\mathrm{H}^\mathrm{a}||^2\right\}. \qquad (6.32)
\end{aligned}
$$

With (6.32) and the SNR of the analog branch (6.7), the pSNR of the HDA transmission system

$$
\mathrm{pSNR}_\mathrm{H} = \frac{\mathrm{E}\{||\boldsymbol{u}||^2\}}{\mathrm{E}\{||\boldsymbol{u} - \hat{\boldsymbol{u}}_\mathrm{H}||^2\}} \qquad (6.33)
$$

can be reformulated for good channel qualities ($\mathrm{cSNR} > \mathrm{cSNR}_D^{\mathrm{sat.}}$) to the following:

$$
\begin{aligned}
\mathrm{pSNR}_\mathrm{H}^{\mathrm{sat.}}(\mathrm{cSNR}) &= \frac{\mathrm{E}\{||\boldsymbol{u}||^2\}}{\mathrm{E}\{||\boldsymbol{u}_\mathrm{H}^\mathrm{a} - \hat{\boldsymbol{u}}_\mathrm{H}^\mathrm{a}||^2\}} \\
&= \frac{\mathrm{E}\{||\boldsymbol{u}||^2\}}{\mathrm{E}\{||\boldsymbol{u}_\mathrm{H}^\mathrm{a}||^2\}} \cdot \mathrm{bSNR}^\mathrm{a}(\mathrm{cSNR}). \qquad (6.34)
\end{aligned}
$$

The fraction $\mathrm{E}\{||\boldsymbol{u}||^2\}/\mathrm{E}\{||\boldsymbol{u}_{\mathrm{H}}^{\mathrm{a}}||^2\}$ in (6.34) refers to the pSNR of the quantizer (i.e., quantization noise) and $\mathrm{bSNR}^{\mathrm{a}}$ (6.7) refers to the SNR of just the analog branch which is dependent on the current cSNR. Hence, for channels with no transmission errors in the digital branch, the overall performance only depends on the analog branch and the fidelity of the quantizer. Since fewer bits are spent for the quantization in the HDA transmission system (6.31), the variance of the quantization noise is higher than that of the purely digital system. This loss has to be compensated by the analog branch of the HDA system and can be quantified using the rate-distortion function.

The rate-distortion function $\mathfrak{R}(\mathfrak{D})$ is the minimum information rate in bits per symbol which is needed to describe source symbols following a certain pdf with a maximum distortion $\mathfrak{D}$ (MSE) [CT06]. Here, the quantizers which operate in the purely digital system and in the digital branch of the HDA system are regarded. The quantizer in the purely digital system uses an information rate of R_D bits per symbol while the quantizer of the HDA system employs a lower fidelity, namely an information rate of R_H bits per symbol. The rate-distortion function can be stated in closed form for Gaussian sources (3.34), but for other source pdfs and to account for quantizer imperfection, a rate loss is introduced, $R_{\mathrm{H,imp}}$ and $R_{\mathrm{D,imp}}$ for the HDA and purely digital system, respectively. Since both quantizers are of the same type and operate on symbols with the same pdf and the same dimension, they have the same space filling advantage and same shape advantage [LG89]. Furthermore, the differences in quantizer fidelity are relatively small (< 1bit, (6.31)), thus, the rate losses are approximately equal ($R_{\mathrm{H,imp}} = R_{\mathrm{D,imp}}$). The difference of the information rates of the quantizers $R_D - R_H$ is then equal to the difference of the bit rates of the quantizers ΔF (6.30).

The $\mathrm{bSNR}^{\mathrm{a}}$ which needs to be achieved in the analog branch to compensate for the quantizer with lower fidelity, is derived using (6.33) and employing the rate-distortion function, which resembles the 6 dB-per-bit rule:

$$
\begin{aligned}
& \mathrm{pSNR}_{\mathrm{H}}^{\mathrm{sat.}}(\mathrm{cSNR}) \geq \mathrm{pSNR}_{\mathrm{D}}^{\mathrm{sat.}}(\mathrm{cSNR}) \\
\Rightarrow \quad & 2^{2\cdot(R_H - R_{\mathrm{H,imp}})} \cdot \mathrm{bSNR}^{\mathrm{a}}(\mathrm{cSNR}) \geq 2^{2\cdot(R_D - R_{\mathrm{D,imp}})} \\
\Rightarrow \quad & \mathrm{bSNR}^{\mathrm{a}}(\mathrm{cSNR}) \geq 4^{R_D - R_H} = 4^{\Delta F} \qquad (6.35) \\
\Rightarrow \quad & \mathrm{bSNR}^{\mathrm{a}}(\mathrm{cSNR})|_{\mathrm{dB}} \geq \Delta F \cdot 6\,\mathrm{dB}, \qquad (6.36)
\end{aligned}
$$

while $\mathrm{bSNR}^{\mathrm{a}}(\mathrm{cSNR})|_{\mathrm{dB}}$ is denoting $10\log_{10}(\mathrm{bSNR}^{\mathrm{a}}(\mathrm{cSNR}))$.

Combining Eqs. (6.25), (6.31), and (6.35) yields:

$$\begin{aligned}\mathrm{bSNR}^{\mathrm{a}}(\mathrm{cSNR}) \geq & 4^{\frac{r_{\mathrm{D}}^{\mathrm{ccm}}}{r_{\mathrm{H}}^{\mathrm{mapp}}}+\Delta r\cdot\left(\frac{N}{M}-\frac{1}{r_{\mathrm{H}}^{\mathrm{mapp}}}\right)} \\ &= \left(4^{r_{\mathrm{D}}^{\mathrm{ccm}}}\right)^{\frac{1}{r_{\mathrm{H}}^{\mathrm{mapp}}}} \cdot 4^{\Delta r\cdot\left(\frac{N}{M}-\frac{1}{r_{\mathrm{H}}^{\mathrm{mapp}}}\right)} \\ &= \left(\mathrm{cSNR}_D^{\mathrm{sat.}}\cdot\Delta_{\mathrm{ideal}}+1\right)^{\frac{1}{r_{\mathrm{H}}^{\mathrm{mapp}}}} \cdot 4^{\Delta r\cdot\left(\frac{N}{M}-\frac{1}{r_{\mathrm{H}}^{\mathrm{mapp}}}\right)}. \end{aligned} \tag{6.37}$$

Equation (6.37) describes the required performance of the analog branch for $\mathrm{cSNR} \geq \mathrm{cSNR}_D^{\mathrm{sat.}}$ for channel codes with a given performance (Δ_{ideal}) and a given rate difference Δr to yield a superior HDA system.

Ideal Channel Coding In case of ideal channel codes, the Shannon capacity is achieved and, thus, $\Delta_{\mathrm{ideal}} = 1$. For the same channel coding rate ($\Delta r = 0$) in the digital branch and the purely digital system, there is an analog transmission system known to reach the required performance (6.37) for finite block lengths: A linear encoder ($\tilde{\boldsymbol{g}}(\boldsymbol{u}_{\mathrm{H}}^{\mathrm{a}}) = \boldsymbol{u}_{\mathrm{H}}^{\mathrm{a}}$) with no additional redundancy ($r_{\mathrm{H}}^{\mathrm{mapp}} = 1$) and an LMMSE estimator at the receiver.

The performance of the LMMSE estimator is [Kay93]

$$\mathrm{bSNR}^{\mathrm{a}}(\mathrm{cSNR}) = \mathrm{cSNR} + 1. \tag{6.38}$$

Using this estimator, the required performance (6.37) for $\mathrm{cSNR} \geq \mathrm{cSNR}_D^{\mathrm{sat.}}$ of the analog branch is achieved at $\mathrm{cSNR} = \mathrm{cSNR}_D^{\mathrm{sat.}}$. Thus, (6.37) holds with equality at $\mathrm{cSNR} = \mathrm{cSNR}_D^{\mathrm{sat.}}$. Consequently, using a quantizer which follows the 6 dB-per-bit rule and channel codes with the same coding rate ($\Delta r = 0$) in the purely digital system and in the digital branch and an LMMSE estimator in the analog branch, even for ideal channel coding ($\Delta_{\mathrm{ideal}} = 1$), an HDA system can be built which outperforms purely digital transmission.

Practical Channel Coding In the case of practical non-ideal digital codes, due to $0 < \Delta_{\mathrm{ideal}} < 1$, (6.37) holds with inequality for $\mathrm{cSNR} \geq \mathrm{cSNR}_D^{\mathrm{sat.}}$ and the above mentioned requirements can be relaxed. The rates of the channel coding in the digital branch may be chosen to be higher than in the purely digital system and equality of the rates is not required anymore ($\Delta r \geq 0$).

The design of the analog branch is of great importance for the performance of the HDA system: The maximum $\mathrm{bSNR}^{\mathrm{a}}$ which can be achieved is described by the *optimum performance theoretically attainable* (OPTA) (Section 3.4). OPTA can be evaluated equating the channel capacity and the rate-distortion function considering multiple or partial channel uses per source symbol. For transmitting M Gaussian source symbols employing $A = M/r_{\mathrm{H}}^{\mathrm{mapp}}$ channel uses, OPTA can be

stated as follows and cannot be exceeded by the analog branch (see (3.49)):

$$\mathrm{OPTA}(\mathrm{cSNR}) := (\mathrm{cSNR}+1)^{\frac{1}{r_{\mathrm{H}}^{\mathrm{mapp}}}} \geq \mathrm{bSNR}^{\mathrm{a}}(\mathrm{cSNR}). \tag{6.39}$$

In case of ideal channel codes ($\Delta_{\mathrm{ideal}} = 1$) and $\Delta r = 0$, the analog branch needs to achieve OPTA since then (6.37) is equal to OPTA (6.39) at $\mathrm{cSNR} = \mathrm{cSNR}_D^{\mathrm{sat.}}$. The LMMSE estimator used above reaches this performance for all source symbol pdfs and $r_{\mathrm{H}}^{\mathrm{mapp}} = 1$. For $r_{\mathrm{H}}^{\mathrm{mapp}} \neq 1$, no transmission system using finite block lengths (A) achieves OPTA [Gas02], but with the relaxed requirement on the performance due to practical channel codes ($0 < \Delta_{\mathrm{ideal}} < 1$), other analog transmission systems with $r_{\mathrm{H}}^{\mathrm{mapp}} \neq 1$ exhibiting other desired properties can be employed (Section 6.4).

However, it has to be assured that $\mathrm{bSNR}^{\mathrm{a}}$ is large enough for $\mathrm{cSNR} \geq \mathrm{cSNR}_D^{\mathrm{sat.}}$ to compensate for the loss in quantizer fidelity (ΔF) to still design an HDA system which outperforms purely digital transmission.

If the design requirements for the HDA system cannot be met to ensure superior performance at $\mathrm{cSNR} = \mathrm{cSNR}_D^{\mathrm{sat.}}$, nonetheless, the performance of the HDA system improves with better channels and eventually surpasses that of the purely digital system.

Bad Channel Conditions

In this section, the case of channel conditions worse than in the former section is considered ($\mathrm{cSNR} < \mathrm{cSNR}_D^{\mathrm{sat.}}$). In the digital branch, transmission errors occur and, thus, the bit error probability is non-zero. For simplicity of the analysis, uniform quantization is assumed. Also source symbols with a uniform pdf are considered for clarity, other pdfs are covered by introducing loss factors. The influence of bit errors on the *Mean-Square Error* (MSE) after uniformly quantizing source symbols with a uniform pdf with variance 1, can be stated [OL07, p. 294] as

$$\mathrm{MSE}(P_e, F) = 4 \cdot P_e \cdot (1 - 4^{-F}) \tag{6.40}$$

with the bit error rate $P_e < 0.5$ after channel decoding and a number of quantizer bits F per source symbol.

For statistically independent quantized values and quantization errors, according to (6.20) the MSE of the two branches can be added. Thus, the performance of a purely digital transmission system with F_{D} quantization bits per source symbol is given by the quantization noise ($4^{-F_{\mathrm{D}}}$) and the $\mathrm{MSE}(P_e, F_{\mathrm{D}})$ caused by bit errors:

$$\mathrm{pSNR}_{\mathrm{D}} = \frac{\frac{1}{M}\,\mathrm{E}\{||\boldsymbol{u}||^2\}}{4^{-F_{\mathrm{D}}} + 4 \cdot P_e \cdot (1 - 4^{-F_{\mathrm{D}}})}. \tag{6.41}$$

In the HDA system, the analog branch additionally transmits the quantization error. The MSE of the quantization error is then lowered by the $\mathrm{bSNR}^{\mathrm{a}}$ of the analog branch (6.34). With an LMMSE estimator (6.38) the MSE of the quantization

error 4^{-F_H} with F_H quantization bits per source symbol is attenuated by a factor of $\frac{1}{\mathrm{bSNR}^\mathrm{a}} = \frac{1}{1+\mathrm{cSNR}}$:

$$\mathrm{pSNR}_\mathrm{H} = \frac{\frac{1}{M}\,\mathrm{E}\{||\boldsymbol{u}||^2\}}{4^{-F_\mathrm{H}} \cdot \frac{1}{1+\mathrm{cSNR}} + 4P_e \cdot (1 - 4^{-F_\mathrm{H}})}. \tag{6.42}$$

Since the HDA performance pSNR_H improves with rising channel quality cSNR, the lowest channel quality at which the HDA system outperforms a purely digital system is of interest. If the difference in quantization fidelity $\Delta F = F_\mathrm{D} - F_\mathrm{H}$ is given as well as the bit error rate P_e at which both systems operate ($\Delta r = 0$), this channel quality is derived as follows:

$$\begin{aligned}
&\mathrm{pSNR}_\mathrm{H} \geq \mathrm{pSNR}_\mathrm{D} \\
\Leftrightarrow \quad & 4^{-F_\mathrm{D}} + 4P_e(1 - 4^{-F_\mathrm{D}}) \geq \frac{4^{-F_\mathrm{H}}}{1+\mathrm{cSNR}} + 4P_e \cdot (1 - 4^{-F_\mathrm{H}}) \\
\Leftrightarrow \quad & 4^{-F_\mathrm{D}}\,(1 - 4P_e) + 4P_e \geq 4^{-F_\mathrm{H}} \cdot \left(\frac{1}{1+\mathrm{cSNR}} - 4P_e\right) + 4P_e \\
\Leftrightarrow \quad & 4^{-F_\mathrm{D}}\,(1 - 4P_e) \geq 4^{-F_\mathrm{H}} \cdot \left(\frac{1}{1+\mathrm{cSNR}} - 4P_e\right) \\
\Leftrightarrow \quad & 4^{-F_\mathrm{D}+F_\mathrm{H}}\,(1 - 4P_e) \geq \frac{1}{1+\mathrm{cSNR}} - 4P_e \\
\Leftrightarrow \quad & 4^{-\Delta F}\,(1 - 4P_e) + 4P_e \geq \frac{1}{1+\mathrm{cSNR}} \\
\Leftrightarrow \quad & \mathrm{cSNR} \geq \frac{1}{4^{-\Delta F} \cdot (1 - 4P_e) + 4P_e} - 1 \\
\Leftrightarrow \quad & \mathrm{cSNR} \geq \frac{1}{4^{-\Delta F} + 4P_e \cdot (1 - 4^{-\Delta F})} - 1\,.
\end{aligned} \tag{6.43}$$

In case of a given channel quality and ΔF, the minimum required P_e for a superior HDA system (more bit errors lead to superior HDA system) can be obtained by reformulating (6.43) accordingly. This bit error rate is denoted $P_{e,\mathrm{limit}}$:

$$P_e \geq \frac{\frac{1}{\mathrm{cSNR}+1} - 4^{-\Delta F}}{4 \cdot (1 - 4^{-\Delta F})} := P_{e,\mathrm{limit}}. \tag{6.44}$$

For error-free transmission in the digital branch, $P_e = 0$ holds and the minimum cSNR at which the HDA system outperforms the purely digital system can be obtained using (6.43) as $\mathrm{cSNR} \geq 4^{\Delta F} - 1 = \mathrm{cSNR}_{\mathrm{ideal},P_e=0}$. With results from the previous section, it can be shown that $\mathrm{cSNR}_{\mathrm{ideal},P_e=0}$ is at the same time the minimum theoretically required channel quality for all possible digital transmission systems to facilitate error-free transmission. For this, the same channel coding rates in the HDA and digital system ($\Delta r = 0$) and $r_\mathrm{H}^\mathrm{mapp} = 1$ is considered and, thus, $\Delta F = r_\mathrm{D}^\mathrm{ccm}$ (6.31). Using (6.25), the same minimum channel quality ($\mathrm{cSNR}_{\mathrm{ideal},P_e=0}$) at which a channel code reaching Shannon capacity ($\Delta_\mathrm{ideal} = 0$) leads to error-free transmission, can be calculated.

Thus, no digital transmission system achieves error-free transmission below $\mathrm{cSNR}_{\mathrm{ideal},P_e=0}$. Practical systems achieve error-free transmission at a higher channel quality ($\mathrm{cSNR}_D^{\mathrm{sat.}}$, see Figure 6.7). Since $\mathrm{cSNR}_D^{\mathrm{sat.}} \geq \mathrm{cSNR}_{\mathrm{ideal},P_e=0}$ and HDA transmission outperforms purely digital transmission for all channel qualities greater than $\mathrm{cSNR}_{\mathrm{ideal},P_e=0}$, all practical HDA systems outperform purely digital transmission. Furthermore, the HDA system further benefits from the analog branch (6.34) and the gain to purely digital transmission further increases.

Ideal channel codes reaching the Shannon capacity, exhibit a "rectangular" waterfall. Transmission at a channel quality below the design channel quality leads to an abrupt breakdown of the code and consequently to a bit error rate of 50%. Evaluating (6.43) with an even smaller bit error rate ($P_e = 0.25 < 0.5$) leads to a minimum $\mathrm{cSNR} = 0 \mathrel{\hat{=}} \mathrm{cSNR}|_{\mathrm{dB}} = -\infty\,\mathrm{dB}$ at which the HDA system outperforms the purely digital system. Thus, for ideal channel coding, the HDA system outperforms the purely digital transmission for all channel qualities.

Figures 6.8a and 6.8b show the bit error rate P_e after channel decoding for a given cSNR for $\Delta F = 1$ and $\Delta F = \frac{1}{3}$ respectively. If after digital channel decoding more bit errors than $P_{e,\mathrm{limit}}$ given in (6.44) occur, the HDA system outperforms purely digital transmission. The performance of ideal codes reaching the Shannon capacity (with a "rectangular" waterfall) shows more errors than $P_{e,\mathrm{limit}}$ for all channel qualities as discussed above.

In case of transmission below capacity, error-free transmission is not possible anymore. But for a given capacity, which minimum error probability for a given coding rate is still possible?

If the source bits are protected using lossy channel coding, so that each bit of the lossy encoded bits matches the original bit with probability $1 - P_e$ after channel decoding, then the source can be described as follows: according to the rate-distortion theory, this leads to a source with rate $1 - H(P_e)$ per source bit with $H(P_e)$ as the entropy of a binary source with P_e as the probability of occurrence of, e.g., "1". If due to channel coding $r_{\mathrm{D}}^{\mathrm{ccm}} = \Delta F$ (6.31) information bits per channel use are transmitted over, e.g., an AWGN channel, then it holds (e.g., [Moo05, p. 51])

$$\Delta F \cdot (1 - H(P_e)) \leq C_{\mathrm{AWGN}}(\mathrm{cSNR}). \tag{6.45}$$

The performance of an optimal (in the sense of a lowest possible error rate) lossy coding system is also shown in Figs. 6.8a and 6.8b. For most channel qualities, the curve labeled "Lossy coding" is above $P_{e,\mathrm{limit}}$. However, for a small range of channel qualities, the lossy coding system curve is below $P_{e,\mathrm{limit}}$. For the employed LMMSE estimator, this gap for $\Delta F = \frac{1}{3}$ is equivalent to a maximum of 0.096 dB in terms of pSNR.

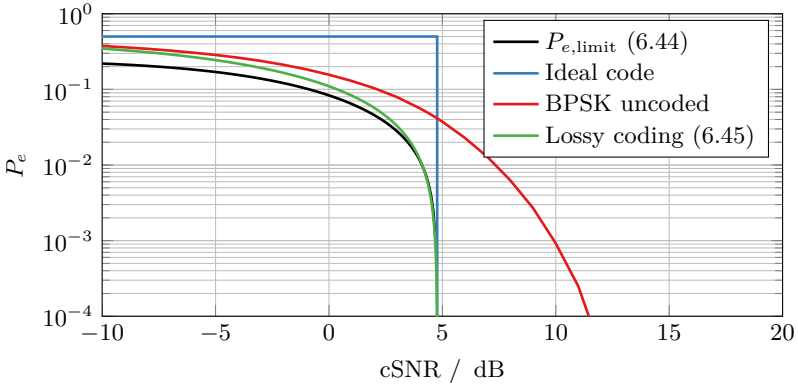

(a) Quantizer fidelity difference: $\Delta F = 1$. Codes reaching the Shannon limit, lossy coding and transmission with BPSK without a channel code lead to superior HDA system, since their P_e is higher than $P_{e,\text{limit}}$.

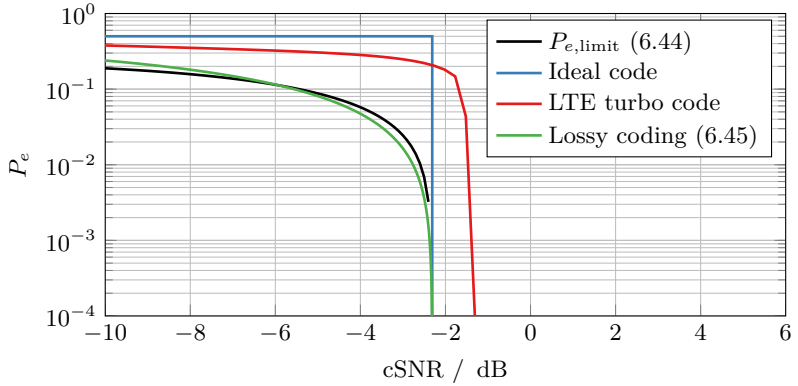

(b) Quantizer fidelity difference: $\Delta F = \frac{1}{3}$. Codes reaching the Shannon limit and LTE turbo coding lead to superior HDA system. For ideal lossy coding, at some cSNR digital coding may be superior.

Figure 6.8: Bit error rate P_e after digital channel decoding for given cSNR and $r_{\text{H}}^{\text{ccm}} = r_{\text{D}}^{\text{ccm}}$. For systems with a higher P_e than $P_{e,\text{limit}}$ (6.44), the HDA system is superior to purely digital transmission.

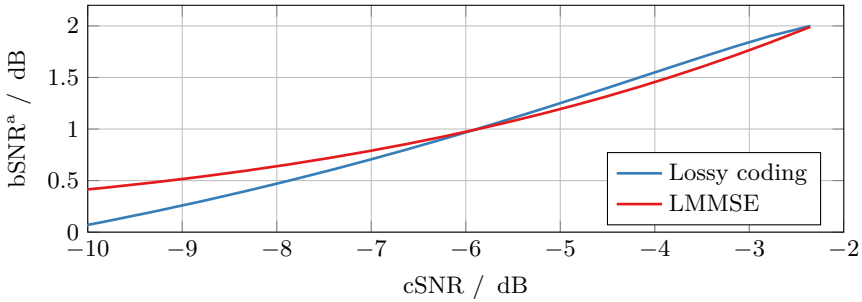

(a) Quantizer fidelity difference: $\Delta F = \frac{1}{3}$. Performance $\mathrm{bSNR}^{\mathrm{a}}$ in the analog branch required by lossy coding to yield superior HDA system and performance achieved by LMMSE estimation.

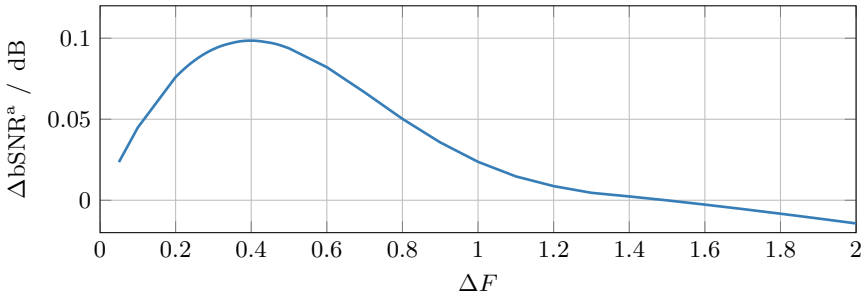

(b) Maximum difference between required performance in analog branch for lossy coding and performance of LMMSE estimation for varying ΔF

Figure 6.9: Influence of lossy coding on required performance in analog branch.

Converting the gap in P_e to a gap in terms of pSNR can be done as follows: Equation (6.44) is derived using the LMMSE performance (6.38) in the analog branch. Instead, the performance $\mathrm{bSNR}^{\mathrm{a}}$ in the analog branch can directly be considered:

$$P_e \geq \frac{\frac{1}{\mathrm{bSNR}^{\mathrm{a}}} - 4^{-\Delta F}}{4 \cdot (1 - 4^{-\Delta F})} := P_{e,\mathrm{limit}}. \tag{6.46}$$

With (6.45) it can be derived at which cSNR a lossy coding system achieves $P_{e,\mathrm{limit}}$. Furthermore, with (6.46), the $\mathrm{bSNR}^{\mathrm{a}}$ which is at least required to build a superior HDA system with this given $P_{e,\mathrm{limit}}$ can be calculated. This required performance in the analog branch for a lossy coding system for a given channel quality is depicted in Figure 6.9a for $\Delta F = \frac{1}{3}$. For comparison, the performance which LMMSE estimation in the analog branch achieves is also stated. It can be seen that for building a superior HDA system, the lossy coding system requires a performance

in the analog branch which is by 0.096 dB higher than by LMMSE estimation. Figure 6.9b shows that a maximum gap of 0.099 dB is achieved for $\Delta F = 0.4$. For smaller and greater ΔF, the gap is tinier.

Still, the depicted performance of an optimal lossy coding system can only be achieved for the design channel quality and only asymptotically in block length and complexity. Thus, for any practical system in which a code would be optimized for error-free transmission and not for lossy coding, the gap will vanish. Furthermore, replacing the LMMSE estimator by an MMSE estimator could also directly compensate this gap (Section 4.3).

In Figure 6.8, two reference systems are also depicted. For $r_{\mathrm{D}}^{\mathrm{ccm}} = \Delta F = 1$, the performance of an uncoded BPSK transmission is shown. For $r_{\mathrm{D}}^{\mathrm{ccm}} = \Delta F = \frac{1}{3}$ an LTE Turbo code with information block length 10^4 using a random interleaver and BPSK modulation with 20 decoding iterations is plotted. For both codes, an HDA transmission system outperforms purely digital transmission for all channel qualities.

Design Guidelines

The following design guidelines for an HDA system ensure superior performance also for digital channel codes reaching the Shannon limit ($\Delta_{\mathrm{ideal}} = 1$) for all channel qualities: For the analog branch, $A = M$ channel uses are employed ($r_{\mathrm{H}}^{\mathrm{mapp}} = 1$). A simple linear analog mapper with an LMMSE estimator at the receiver achieves (6.37). Other systems with $r_{\mathrm{H}}^{\mathrm{mapp}} \neq 1$ and finite block lengths are not known to achieve this performance. Thus, in general it is best to use a system with $r_{\mathrm{H}}^{\mathrm{mapp}} = 1$. The fidelity of the quantizer in the HDA system is lowered by $\Delta F = r_{\mathrm{D}}^{\mathrm{ccm}}$ to ensure the same coding rate $r_{\mathrm{H}}^{\mathrm{ccm}}$ in the digital branch as well as in the purely digital system ($r_{\mathrm{D}}^{\mathrm{ccm}}$), hence $\Delta r = 0$ and $r_{\mathrm{H}}^{\mathrm{ccm}} = r_{\mathrm{D}}^{\mathrm{ccm}}$. For a non-ideal practical channel code ($0 < \Delta_{\mathrm{ideal}} < 1$), the above requirements still lead to superior HDA transmission, but the requirements can also be relaxed as long as the performance of the analog branch $\mathrm{bSNR}^{\mathrm{a}}$ ensures (6.37). Hence, in the analog branch, other systems not reaching OPTA can be employed which may have other desired properties and use $r_{\mathrm{H}}^{\mathrm{mapp}} \neq 1$ (Section 6.4). Also the fidelity of the quantizer in the HDA system can be chosen with more flexibility as long as $\Delta F \geq \frac{r_{\mathrm{D}}^{\mathrm{ccm}}}{r_{\mathrm{H}}^{\mathrm{mapp}}}$, i.e., (6.26) and (6.31) hold.

Simulation Results

Figure 6.10 shows simulation results for a Gaussian source with scalar LMQ employing a rate-$\frac{1}{2}$ recursive systematic convolutional code with the generator polynomial $\{1, 15/13\}_8$ — the same code which is used as a component code in UMTS-LTE. The different rates for different quantizer fidelities are achieved by puncturing only the parity bits, thereby with BPSK modulation always yielding $N = 560$. The decoder uses soft information from the channel and the inverse bit-mapper uses ML estimation. Since the scalar quantizer uses the same quantization

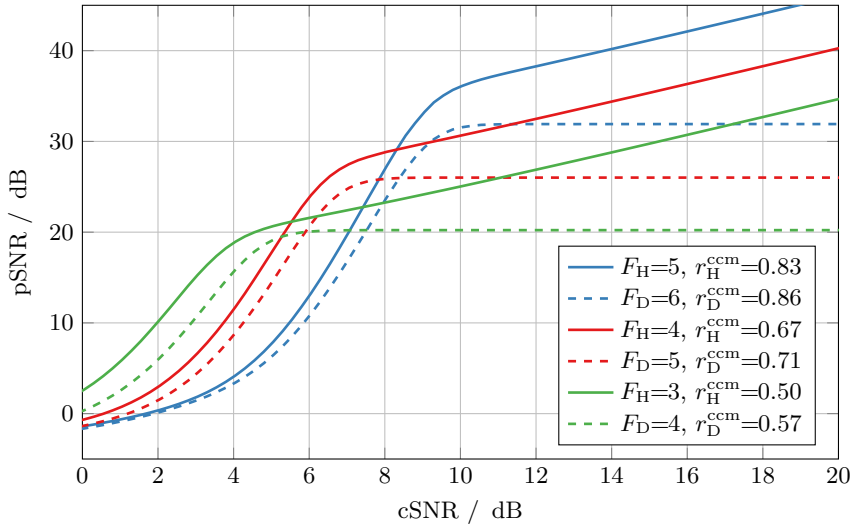

Figure 6.10: HDA and digital transmission using convolutional codes. Gaussian source pdf and scalar Lloyd-Max quantization. $M = 80$, $N = 560$. HDA: $A = 80$, $D = 480$.

fidelity for all symbols, F_D and F_H can only be integers. According to (6.31), the digital coding rates are not equal in the purely digital system and the digital branch of the HDA system. The convolutional codes are not capacity achieving and hence the gap to OPTA is quite large. For instance the $F_D = 4$ simulation with $\mathrm{cSNR}_D^{\mathrm{sat.}}|_{\mathrm{dB}} \approx 5\,\mathrm{dB}$ yields $\Delta_{\mathrm{ideal}} \approx 0.38 \mathrel{\hat{=}} -4.2\,\mathrm{dB}$ (6.25). Linear analog mapping ($\tilde{\mathbf{g}}(\boldsymbol{u}_{\mathrm{H}}^{\mathrm{a}}) = \boldsymbol{u}_{\mathrm{H}}^{\mathrm{a}}$) and an LMMSE estimator are used in the analog branch. This results in a $\mathrm{bSNR}^{\mathrm{a}}$ at $\mathrm{cSNR}_D^{\mathrm{sat.}}$ which is greater than the loss due to the coarser quantizer. Most interestingly, due to the different lower rate $r_{\mathrm{H}}^{\mathrm{ccm}}$ of the digital branch than the rate $r_{\mathrm{D}}^{\mathrm{ccm}}$ of the purely digital system, the waterfall of the HDA system is shifted to lower channel qualities. E.g., with the $F_H = 3$ simulation, a gain in cSNR of 1 dB can be achieved while the pSNR of the HDA system is also improved. This is due to the lower channel coding rate $r_{\mathrm{H}}^{\mathrm{ccm}}$ in the digital branch as in the purely digital system ($r_{\mathrm{D}}^{\mathrm{ccm}}$) while the analog branch overcompensates the resulting higher loss due to the even coarser quantizer.

Figure 6.11 shows simulation results for Gaussian and uniform distributed source symbols with dimension $M = 714$ which are quantized with either scalar Lloyd-Max quantization or uniform quantization, respectively. A rate-$\frac{1}{3}$ Turbo code, the same code which is used in UMTS-LTE, is employed using an interleaver size of $D = 4284$ or $N = 4998$ bits for the HDA or purely digital system respectively. In all simulations, 20 decoding iterations are conducted. The different rates for

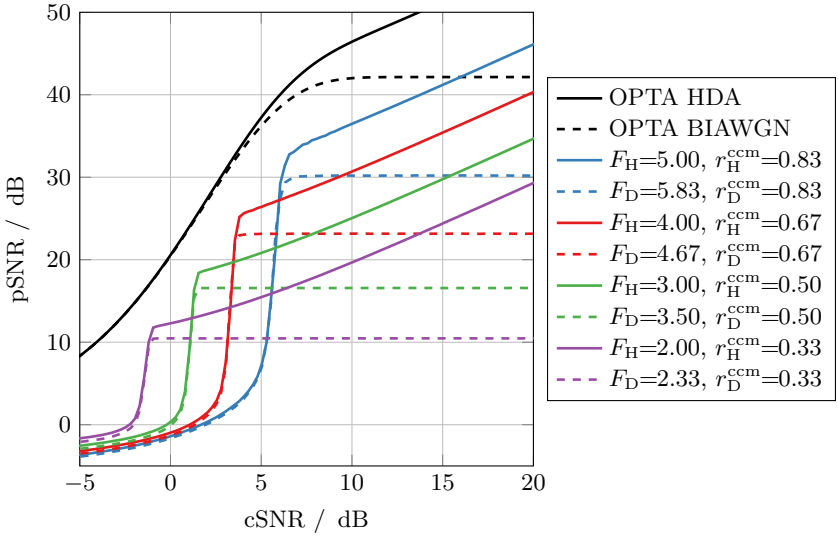

(a) Gaussian source pdf and scalar Lloyd-Max quantization.

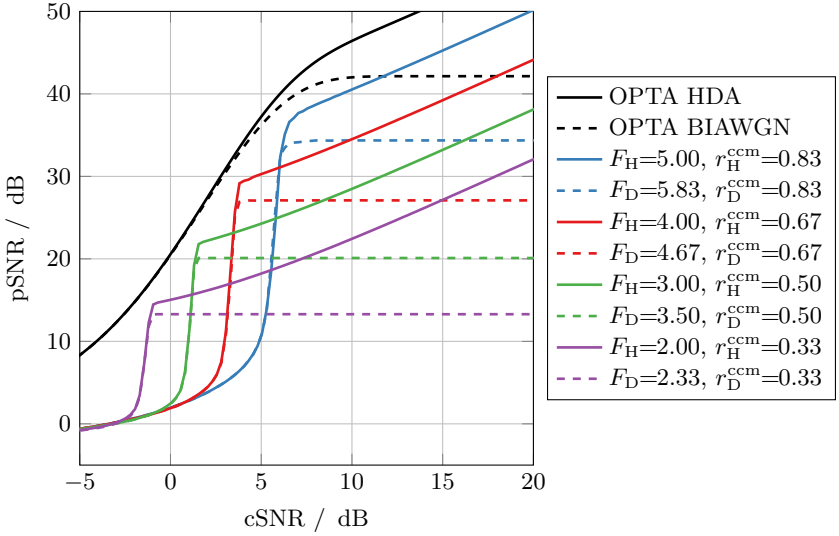

(b) Uniform source pdf and scalar uniform quantization.

Figure 6.11: HDA and digital transmission using Turbo codes. $M = 714$, $N = 4998$. HDA: $A = 714$, $D = 4284$.

different quantizer fidelities are achieved by puncturing only the parity bits, thereby with BPSK modulation always yielding $N = 4998$. To benefit from the good performance of the Turbo code, the size of the interleaver is chosen to be around 5000. For purely digital and HDA simulations which exhibit the same coding rates, the interleaver size cannot be chosen arbitrarily while still obtaining integer vector lengths (Appendix C). For an overall rate of $\frac{M}{N} = \frac{1}{7}$, M has to be an integer multiple of 42 (Table C.1). Therefore, therefore the number of channel symbols N has to be an integer multiple of $42/r = 42 \cdot 7 = 294$. To achieve an interleaver size of around 5000, the vector lengths are multiplied by a factor of $\frac{5000}{294} \approx 17$ which yield $M = 42 \cdot 17 = 714$ and $N = 294 \cdot 17 = 4998$. In the simulation, an integer number of quantization bits F_{H} per source symbol is chosen for the HDA simulation which yields a non-integer F_{D} for the purely digital case. Non-integer quantization bits are achieved by averaging over several symbols, e.g., 2.33 bits can be achieved by quantizing the first symbol with 3 bits and the next two symbols with 2 bits.

In the figures, also the *Optimum Performance Theoretically Attainable* (OPTA) (Section 3.4.3) for the purely digital case with a *Binary-Input Additive White Gaussian Noise* (BIAWGN) channel using $\frac{N}{M} = 7$ channel uses per source symbol is depicted. Since BPSK modulation with soft decoding is used, the BIAWGN channel is a valid model for calculating the capacity. For the HDA case (Section 3.4.4) a BIAWGN channel with $\frac{D}{M} = 6$ channel uses per source symbol for the digital branch and an *Additive White Gaussian Noise* (AWGN) channel with $\frac{A}{M} = 1$ channel use per source symbol for the analog branch is calculated. It can be observed that all transmission systems do not achieve capacity, but attain the performance limits quite closely (e.g., in Figure 6.11b only 1.14 dB in terms of cSNR for $F_{\mathrm{H}} = 2$).

The superior performance of the Turbo code in comparison to the convolutional code above is expressed in $\Delta_{\mathrm{ideal}} \approx 0.73 \mathrel{\hat{=}} -1.36\,\mathrm{dB}$. This Δ_{ideal} can be obtained with (6.25) for the $F_{\mathrm{D}} = 2.33$ simulation with $r_{\mathrm{D}}^{\mathrm{ccm}} = 1/3$ where the channel code saturates at $\mathrm{cSNR}_{D}^{\mathrm{sat.}}|_{\mathrm{dB}} \approx -0.95\,\mathrm{dB}$ (Figure 6.11a and 6.11b). Also for this good channel code, the linear analog mapping ($\tilde{\mathbf{g}}(\boldsymbol{u}_{\mathrm{H}}^{\mathrm{a}}) = \boldsymbol{u}_{\mathrm{H}}^{\mathrm{a}}$) and an LMMSE estimator in the analog branch achieve a $\mathrm{bSNR}^{\mathrm{a}}$ at $\mathrm{cSNR}_{D}^{\mathrm{sat.}}$ which is greater than the loss due to the coarser quantizer. Thus, also here the HDA transmission outperforms purely digital transmission at all channel qualities.

6.4 New Degrees of Freedom

HDA transmission offers new degrees of freedom in the design which are not available in purely digital transmission. While keeping the overall transmission power constant, the available transmission power can be unevenly distributed to the analog and digital channel symbols. The effects and benefits of this power distribution are described in Section 6.4.1. In the previous sections, the analog mapper usually consists of just a scalar factor to achieve power normalization of the quantization error. Nonlinear mappings and also mappings leading to more analog

channel uses (A) than source dimensions (M) can be employed (Section 6.4.2). For a given number of channel uses, the optimal assignment of these to the analog and the digital branch is not obvious. This aspect is discussed in Section 6.4.3. If the design of the digital branch is fixed and additional channel uses are available just for the analog branch, the design of the analog branch provides several options to exploit these additional analog channel uses (Section 6.4.4).

6.4.1 Optimal Power Distribution

With HDA transmission, the distribution of the power between the digital and analog channel symbols is a new degree of freedom. The overall transmission power is, of course, kept constant while, e.g., for good channels more power can be assigned to the analog symbols, while the digital channel symbols are attenuated. In this case, the "experienced" channel quality of the digital branch is lower, since symbols with less transmission power are disturbed with a constant noise power. If the digital code is still in the saturation region, an improved overall performance can be achieved, since the higher "experienced" channel quality in the analog branch can be exploited.

There are different scenarios in which an optimized power distribution is of interest. Usually the design of the digital branch is not very flexible, e.g., when the quantizer fidelity can only be chosen in integer steps. If at a given channel quality, the digital branch has already saturated for the coarser quantizer but still cannot decode without error for the finer quantizer (with the resulting weaker channel coding and modulation), the pSNR can still be improved by choosing a better power distribution. If in a system, the quantization and coding parameters of the digital branch cannot be adapted to a varying channel quality, still, a variation of the power distribution can, in a certain range, adapt the transmitter to the channel quality.

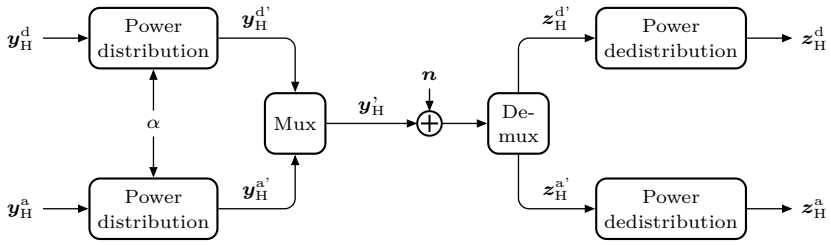

Figure 6.12: Additional processing for power distribution.

Figure 6.12 shows the additional processing blocks which are necessary for choosing an optimal power distribution. The output of the digital and analog branch at the transmitter ($\boldsymbol{y}_{\mathrm{H}}^{\mathrm{d}}$ and $\boldsymbol{y}_{\mathrm{H}}^{\mathrm{a}}$) and the input to the branches at the receiver ($\boldsymbol{z}_{\mathrm{H}}^{\mathrm{d}}$ and $\boldsymbol{z}_{\mathrm{H}}^{\mathrm{a}}$) are the same as in Figure 6.2.

Before transmission over the AWGN channel, it is assured that the average power is 1 for all channel symbols. This leads to the following average energy (see footnote 1 on page 8) of the vector $\boldsymbol{y}_{\mathrm{H}}^{\text{'}}$:

$$\mathrm{E}\left\{||\boldsymbol{y}_{\mathrm{H}}^{\text{'}}||^2\right\} = N. \tag{6.47}$$

A new factor $0 < \alpha < 1$ controls the power of the analog and the digital channel symbols. It describes the ratio between the energy of the analog transmission vector $\boldsymbol{y}_{\mathrm{H}}^{\mathrm{a'}}$ and the energy of the whole transmission vector $\boldsymbol{y}_{\mathrm{H}}^{\text{'}}$:

$$\mathrm{E}\left\{||\boldsymbol{y}_{\mathrm{H}}^{\mathrm{a'}}||^2\right\} = \alpha \cdot N. \tag{6.48}$$

Consequently, the energy of the digital transmission vector is

$$\mathrm{E}\left\{||\boldsymbol{y}_{\mathrm{H}}^{\mathrm{d'}}||^2\right\} = (1-\alpha) \cdot N. \tag{6.49}$$

Thus, a "neutral" power distribution as in the above sections and in Figure 6.2 can be achieved by choosing $\alpha = \frac{A}{N}$.

The energy before of the digital symbol vector before the power distribution is $\mathrm{E}\left\{||\boldsymbol{y}_{\mathrm{H}}^{\mathrm{d}}||^2\right\} = D$ and for the analog symbol vector it holds $\mathrm{E}\left\{||\boldsymbol{y}_{\mathrm{H}}^{\mathrm{a}}||^2\right\} = A$. Therefore, the scaling of the corresponding symbols can be described by:

$$\boldsymbol{y}_{\mathrm{H}}^{\mathrm{a'}} = \boldsymbol{y}_{\mathrm{H}}^{\mathrm{a}} \cdot \sqrt{\alpha \cdot \frac{N}{A}}\,, \tag{6.50}$$

$$\boldsymbol{y}_{\mathrm{H}}^{\mathrm{d'}} = \boldsymbol{y}_{\mathrm{H}}^{\mathrm{d}} \cdot \sqrt{(1-\alpha) \cdot \frac{N}{D}}. \tag{6.51}$$

The "experienced" channel quality $\mathrm{cSNR}^{\mathrm{a}}$ of the analog branch is as follows:

$$\begin{aligned}
\mathrm{cSNR}^{\mathrm{a}} &= \frac{\mathrm{E}\left\{(y_{\mathrm{H}}^{\mathrm{a'}})^2\right\}}{\mathrm{E}\left\{n^2\right\}} = \frac{\mathrm{E}\left\{||\boldsymbol{y}_{\mathrm{H}}^{\mathrm{a'}}||^2\right\}}{\mathrm{E}\left\{||\boldsymbol{n}||^2\right\} \cdot \frac{A}{N}} \\
&\overset{(6.48)}{=} \frac{N \cdot \alpha}{\mathrm{E}\left\{||\boldsymbol{n}||^2\right\}} \cdot \frac{N}{A} \\
&\overset{(6.47)}{=} \frac{\mathrm{E}\left\{||\boldsymbol{y}_{\mathrm{H}}^{\text{'}}||^2\right\}}{\mathrm{E}\left\{||\boldsymbol{n}||^2\right\}} \cdot \alpha \cdot \frac{N}{A} \\
&= \mathrm{cSNR} \cdot \alpha \cdot \frac{N}{A}.
\end{aligned} \tag{6.52}$$

The channel quality $\mathrm{cSNR}^{\mathrm{d}}$ of the digital branch is:

$$\mathrm{cSNR}^{\mathrm{d}} = \mathrm{cSNR} \cdot (1-\alpha) \cdot \frac{N}{D}. \tag{6.53}$$

The overall performance of an HDA transmission system with an arbitrary power distribution α can also be derived analytically. For this, the individual performances

of the digital and the analog branch have to be available for all channel qualities, for an arbitrary reference power distribution α_0. In the following, the dependency of the overall pSNR on the branch SNR is calculated and then the influence of α is derived.

With (6.21) the MSE and, thus, the pSNR of an HDA system can be stated as a function of the SNR of both branches (bSNR):

$$\begin{aligned} \mathrm{E}\left\{||\boldsymbol{u}-\hat{\boldsymbol{u}}||^2\right\} &= \mathrm{E}\left\{||\boldsymbol{u}_{\mathrm{H}}^{\mathrm{d}}-\hat{\boldsymbol{u}}_{\mathrm{H}}^{\mathrm{d}}||^2\right\}+\mathrm{E}\left\{||\boldsymbol{u}_{\mathrm{H}}^{\mathrm{a}}-\hat{\boldsymbol{u}}_{\mathrm{H}}^{\mathrm{a}}||^2\right\} \\ &\overset{(6.6),(6.7)}{=} \frac{\mathrm{E}\left\{||\boldsymbol{u}_{\mathrm{H}}^{\mathrm{d}}||^2\right\}}{\mathrm{bSNR}^{\mathrm{d}}}+\frac{\mathrm{E}\left\{||\boldsymbol{u}_{\mathrm{H}}^{\mathrm{a}}||^2\right\}}{\mathrm{bSNR}^{\mathrm{a}}}, \end{aligned} \tag{6.54}$$

leading to

$$\mathrm{pSNR} \overset{(2.2),(6.54)}{=} \frac{\mathrm{E}\left\{||\boldsymbol{u}||^2\right\}}{\frac{\mathrm{E}\left\{||\boldsymbol{u}_{\mathrm{H}}^{\mathrm{d}}||^2\right\}}{\mathrm{bSNR}^{\mathrm{d}}}+\frac{\mathrm{E}\left\{||\boldsymbol{u}_{\mathrm{H}}^{\mathrm{a}}||^2\right\}}{\mathrm{bSNR}^{\mathrm{a}}}}. \tag{6.55}$$

For any HDA system and the reference α_0, the SNR of each branch at the channel quality cSNR_{α_0} can be stated as $\mathrm{bSNR}^{\mathrm{a}}_{\alpha_0}(\mathrm{cSNR}_{\alpha_0})$ and $\mathrm{bSNR}^{\mathrm{d}}_{\alpha_0}(\mathrm{cSNR}_{\alpha_0})$. Using (6.52) and (6.53), the channel qualities which are experienced by the individual branches during the simulation are

$$\mathrm{cSNR}^{\mathrm{a}} = \mathrm{cSNR}_{\alpha_0}\cdot\alpha_0\cdot\frac{N}{A}, \tag{6.56}$$

$$\mathrm{cSNR}^{\mathrm{d}} = \mathrm{cSNR}_{\alpha_0}\cdot(1-\alpha_0)\cdot\frac{N}{D}. \tag{6.57}$$

The experienced channel quality of each branch for a chosen α can be stated in dependency of the channel quality cSNR_{α}, analogously as above:

$$\mathrm{cSNR}^{\mathrm{a}} = \mathrm{cSNR}_{\alpha}\cdot\alpha\cdot\frac{N}{A}, \tag{6.58}$$

$$\mathrm{cSNR}^{\mathrm{d}} = \mathrm{cSNR}_{\alpha}\cdot(1-\alpha)\cdot\frac{N}{D}. \tag{6.59}$$

Equation (6.58) and (6.56) for the analog branch and (6.59) and (6.57) for the digital branch, lead to a relation between the desired channel quality cSNR_{α} for the chosen α and the reference channel quality cSNR_{α_0} at which the corresponding bSNR is looked up. For the analog branch, it holds:

$$\mathrm{cSNR}_{\alpha_0} = \mathrm{cSNR}_{\alpha}\cdot\frac{\alpha}{\alpha_0}, \tag{6.60}$$

and for the digital branch

$$\mathrm{cSNR}_{\alpha_0} = \mathrm{cSNR}_{\alpha}\cdot\frac{1-\alpha}{1-\alpha_0}. \tag{6.61}$$

Thus, given the simulation results for just one reference α_0, the performance of an HDA system with an arbitrary α can be stated analytically as follows:

$$\mathrm{pSNR}(\alpha, \mathrm{cSNR}) \overset{(6.55),(6.60),(6.61)}{=} \frac{\mathrm{E}\left\{||\boldsymbol{u}||^2\right\}}{\frac{\mathrm{E}\left\{||\boldsymbol{u}_{\mathrm{H}}^{\mathrm{d}}||^2\right\}}{\mathrm{bSNR}_{\alpha_0}^{\mathrm{d}}\left(\mathrm{cSNR}\cdot\frac{1-\alpha}{1-\alpha_0}\right)} + \frac{\mathrm{E}\left\{||\boldsymbol{u}_{\mathrm{H}}^{\mathrm{a}}||^2\right\}}{\mathrm{bSNR}_{\alpha_0}^{\mathrm{a}}\left(\mathrm{cSNR}\cdot\frac{\alpha}{\alpha_0}\right)}}. \tag{6.62}$$

Figure 6.13 shows the performance of three different HDA systems with varying power distribution α. All systems use 100-dimensional ($M = 100$) source symbols with a uniform pdf. Different scalar uniform quantizers with fidelities between $F_{\mathrm{H}} = 2$ and $F_{\mathrm{H}} = 4$ bit per symbol are employed. A rate-$\frac{1}{2}$ convolutional code with puncturing and BPSK modulation leading to $N = 400$ channel uses is utilized. In the analog branch an LMMSE estimator is employed.

The solid lines correspond to simulations with a neutral power distribution ($\alpha = \frac{A}{N}$). The dashed lines and the solid black line depict simulation results with the same $F_{\mathrm{H}} = 3$ and varying α. In Figure 6.13a, the dashed lines and the solid black line correspond to simulations with an $\alpha \in \{0.05, 0.1, 0.2, 0.4, 0.8\}$ in which the power in the analog branch is doubled from one curve to the other. This leads to 3 dB gains of the pSNR in the high-cSNR region. In Figure 6.13b, the dashed lines and the black solid line correspond to simulations with an $\alpha \in \{0.9, 0.8, 0.6, 0.2\}$ in which the power in the digital branch is doubled from one curve to the other leading to 3 dB left shifts of the waterfall.

Especially interesting for this setup are the simulations with $F_{\mathrm{H}} = 3$ and $\alpha \in \{0.4, 0.6\}$. Without varying the fidelity of the quantizer ($F_{\mathrm{H}} = 3$), these simulations achieve optimal operating points which lie in between the simulations with $F_{\mathrm{H}} = 3$ and $F_{\mathrm{H}} = 4$ with $\alpha = \frac{A}{N}$. Thus, the power distribution with $\alpha \geq \frac{A}{N}$ provides a simple method to gradually adapt the performance of an HDA system.

Figure 6.14 shows the performance of the same system as above for Gaussian sources and a fixed fidelity $F_{\mathrm{H}} = 3$ with $\alpha \in \{0.05, 0.2, 0.8\}$. The solid lines show the simulated performance while the crosses depict the performance obtained with (6.62) using the simulation result with $\alpha_0 = 0.2$ as a reference for the branch SNR of the digital and analog branch. The simulated and the theoretical performance match perfectly.

6.4.2 Variants of the Analog Branch

The inherent difference of HDA transmission systems compared to purely digital transmission is the additional analog branch which transmits the quantization error. Many designs of an analog branch are possible while still ensuring a fair comparison between HDA and purely digital transmission. In the previous sections only linear analog mapper and demapper are employed. In Figure 6.15 nonlinear mapper and demapper are compared and also mappings with two analog output symbols per

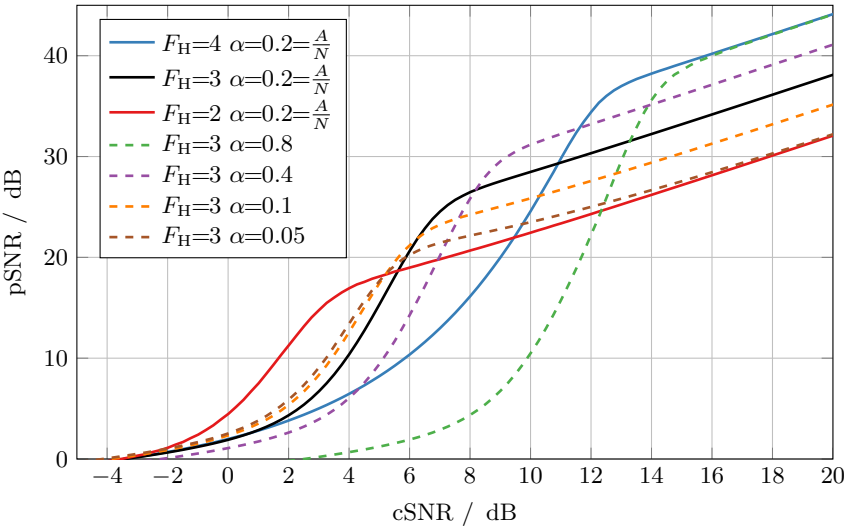

(a) For $F_{\mathrm{H}} = 3$, from one curve to the other, the power in the analog branch is doubled by varying α.

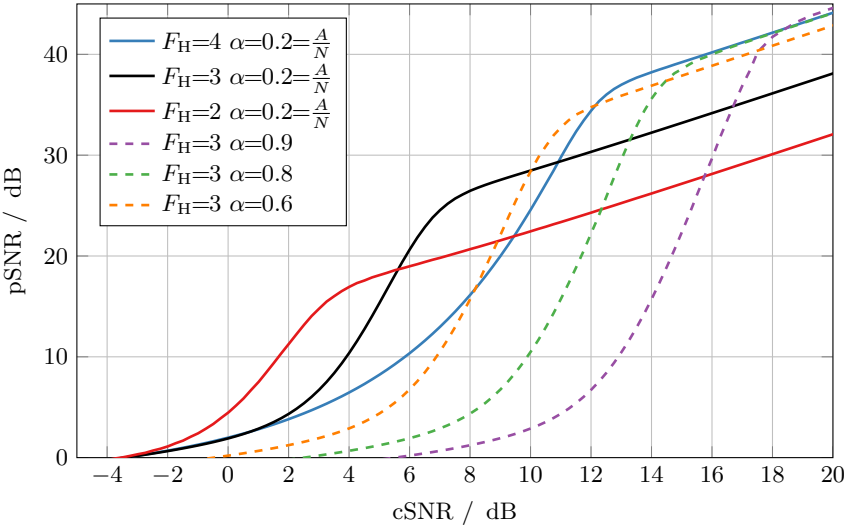

(b) For $F_{\mathrm{H}} = 3$, from one curve to the other, the power in the digital branch is doubled by varying α.

Figure 6.13: HDA transmission using convolutional codes with a uniform source pdf and scalar uniform quantization. $M = 100$, $A = 100$, $D = 400$, $N = 500$. The fidelity of the quantizer and also the power distribution α are varied.

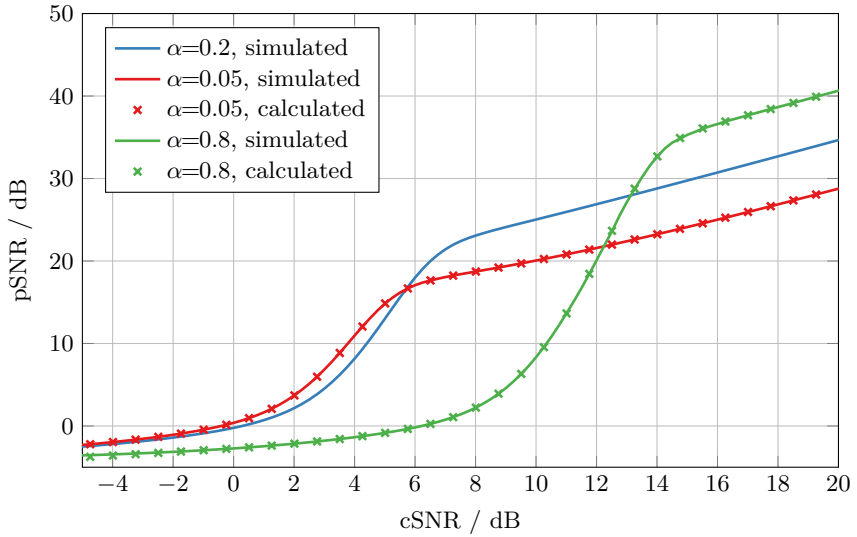

Figure 6.14: HDA transmission using convolutional codes with a Gaussian source pdf and scalar Lloyd-Max quantization. $M = 100$, $A = 100$, $D = 400$, $N = 500$, $F_{\mathrm{H}} = 3$. Solid lines are obtained with simulations and the crosses are calculated using (6.62) with $\alpha_0 = 0.2$.

analog input symbol are shown. Puncturing in the digital branch facilitates the same overall number of channel uses $N = 56$ for $M = 8$ source symbols for all simulations.

In all simulations, source symbols with a uniform pdf are employed with different scalar uniform quantizers with fidelities between $F = 3$ and $F = 5$ bit per symbol. A rate-$\frac{1}{2}$ convolutional code with puncturing and BPSK modulation is utilized. First, a purely digital transmission system with $F_{\mathrm{D}} = 4$ is depicted for comparison which is superseded by an HDA system with $F_{\mathrm{H}} = 3$ and a linear analog mapper with an LMMSE estimator as the analog demapper. Instead of the LMMSE estimator, also an MMSE estimator can be employed which slightly increases the performance for around $5\,\mathrm{dB} < \mathrm{cSNR}|_{\mathrm{dB}} < 25\,\mathrm{dB}$. The convergence of the MMSE estimator to the LLMSE estimator for increasing channel qualities has already been observed in Section 4.3. In the analog branch of an HDA transmission system, also a numerically optimized compander system, as described in Chapter 4, can be utilized. Again, the performance is slightly increased and in contrast to the MMSE estimator, for increasing channel qualities a constant performance improvement of the pSNR of 0.4 dB can be observed. The improvement is exactly the same as already observed in Section 4.3.2 for a uniform source distribution, since the quantization error in this simulation also has a uniform pdf.

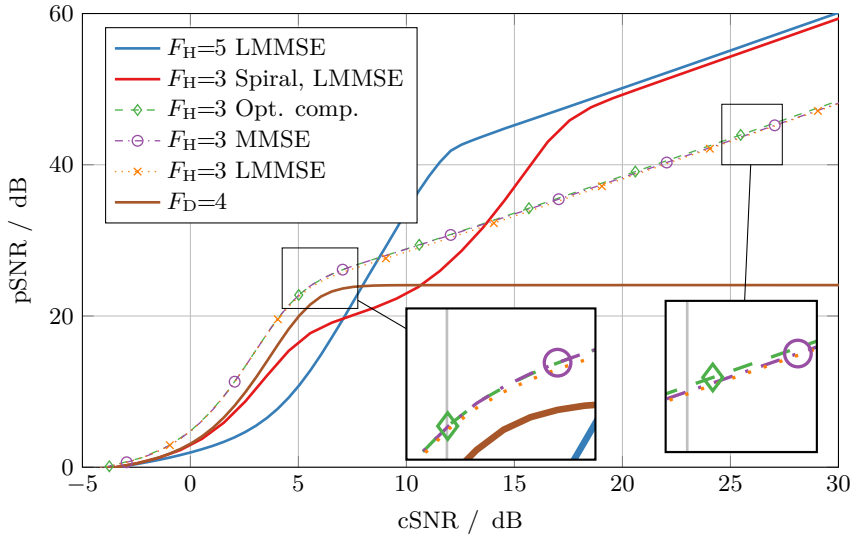

Figure 6.15: Purely digital and HDA transmission using a convolutional code with a uniform source pdf and uniform scalar quantization with $M = 8$ and $N = 56$ for all simulations. Different quantizers and analog mappings are compared.

A very interesting configuration is the use of a nonlinear analog mapping with two output symbols per source symbol. If well designed, this nonlinearity leads to an improved performance in the high-cSNR region. The downside is the larger number of channel uses for the analog branch which decreases the performance of the digital channel code, since puncturing is employed. One simulation ($F_{\mathrm{H}} = 3$ Spiral, LMMSE) shows an HDA system with $F_{\mathrm{H}} = 3$ and an Archimedes spiral (Section 4.4.1) with $\Delta = 0.3$ and LMMSE estimation. LMMSE estimation for nonlinear mappings can be facilitated using a concatenation of LMMSE and ML estimation (Section 6.3.3). The performance at high channel qualities is thereby improved by 12 dB compared to a linear mapping with the same quantization fidelity. Using a higher fidelity of $F_{\mathrm{H}} = 5$ and a linear mapper with LMMSE estimation results in about the same high-cSNR performance, but the HDA system with a linear mapper outperforms the one with Archimedes spiral at lower channel qualities.

6.4.3 Optimal Partition of Channel Uses

The partition of a given (fixed) number of channel uses N to digital and analog channel uses (D and A) is a new degree of freedom, which is introduced by the

HDA concept. At first sight, it is not obvious, how many channel uses should be given to the analog branch. The overall performance of an HDA system is governed by the performance of both, the digital and the analog branch. Thus, it is most favorable if both branches exploit the assigned channel uses in the most effective way. In the analog branch, there exists just one analog mapper which achieves the best possible performance per channel use. For Gaussian input $\boldsymbol{u}_{\mathrm{H}}^{\mathrm{a}}$, a linear analog mapper ($\tilde{\mathbf{g}}(\boldsymbol{u}_{\mathrm{H}}^{\mathrm{a}}) = \boldsymbol{u}_{\mathrm{H}}^{\mathrm{a}}$) with the same number of channel uses A as source dimensions M and an LMMSE estimator achieves OPTA (Section 3.4). For any mapping with $r_{\mathrm{H}}^{\mathrm{mapp}} = \frac{M}{A} \neq 1$ and finite block lengths, the available analog channel uses are not exploited efficiently, since OPTA cannot be reached anymore [Gas02].

In case of $A < M$ channel uses for the analog branch (a compressing analog mapper is used with $r_{\mathrm{H}}^{\mathrm{mapp}} > 1$), more channel uses are available for the digital branch. Unfortunately, since also the digital branch cannot reach OPTA for finite dimensions, these additional dimensions are not used as effectively as they could be with an analog system.

For $A > M$ channel uses in the analog branch, a system has to apply nonlinear elements in the analog branch (Section 2.4.2) in order to approach OPTA. As already shown in Section 2.4.3 this analog mapper can be understood as another HDA system. A system which uses a "small" HDA system as the analog mapper for another "big" HDA system would have two digital branches: a digital branch with a small block length and a digital branch with a long block length. Due to the effects described by the *Sphere Packing Bound* (SPB) (Section 3.6) long block lengths are favorable. Thus, these two digital branches should be combined to jointly achieve a better performance due to the longer (combined) block length. The resulting system with one digital branch and the remaining analog branch from the "small" HDA system is equivalent to the above described HDA system with an analog mapper with $r_{\mathrm{H}}^{\mathrm{mapp}} = 1$.

In total, for a given fixed number of channel uses N, when no constraints on the design of the HDA system are given, it is best to use an analog mapper with $r_{\mathrm{H}}^{\mathrm{mapp}} = 1$. It should use $A = M$ dimensions for the analog branch and the remaining $D = N - A$ dimensions for the digital branch.

6.4.4 Exploiting Additional Analog Channel Uses

In the previous sections, a strong emphasis is placed on a fair comparison between purely digital and HDA transmission. This is ensured by the same number of source dimensions M and channel uses N in simulations. HDA codes may also be used in a different scenario: If a digital transmission system is given and cannot be adapted to exploit additional available channel uses, this digital system can be taken as the digital branch of an HDA system and the additional channel uses can be utilized by the analog branch. The analog branch acts as an enhancement layer to the purely digital system.

At the channel qualities at which the performance of the digital branch has

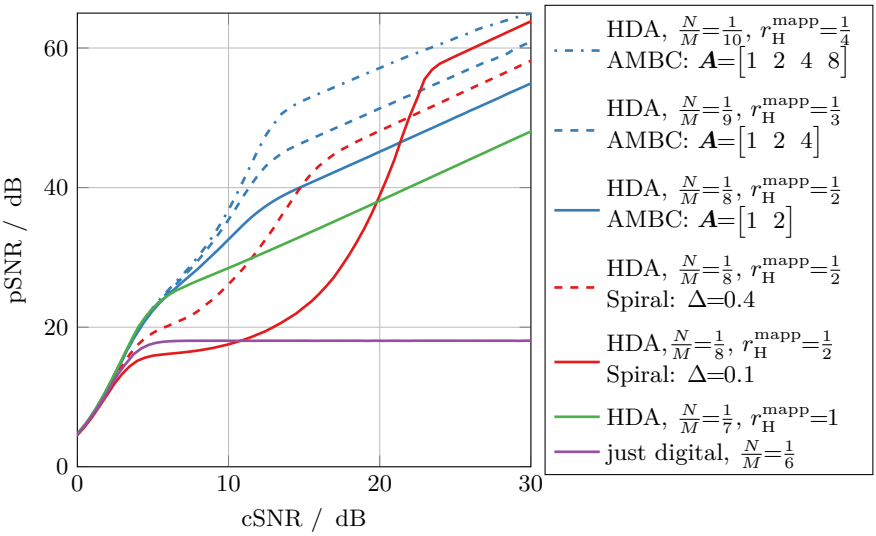

Figure 6.16: Purely digital transmission using a convolutional code with a uniform source pdf and uniform scalar quantization with $F_{\mathrm{D}} = 3$. $M = 10$, $N = 60$. Hybrid systems use the same digital branch with $F_{\mathrm{H}} = 3$, $D = 60$ and additional channel uses, either with a linear mapping, Archimedes spirals or *Analog Modulo Block Codes* (AMBCs).

saturated, the performance gain due to the additional analog branch can easily be stated as the sum of the $\mathrm{cSNR}_D^{\mathrm{sat.}}$ of the digital branch and the $\mathrm{bSNR}^{\mathrm{a}}$ of the analog branch (6.34).

Figure 6.16 shows the performance of a purely digital transmission system and HDA systems with additional channel uses for the analog branch. Symbols following a uniform source pdf with $M = 10$ dimensions are quantized using $F_{\mathrm{D}} = F_{\mathrm{H}} = 3$ bits per symbol. A rate-$\frac{1}{2}$ convolutional code and BPSK modulation leads to $N = 60$ channel uses in the purely digital system and $D = 60$ channel uses in the digital branch of the HDA system. The HDA systems use the same parameters in the digital branch as in the purely digital transmission system but with additional channel uses to improve transmission quality. The HDA system with $r_{\mathrm{H}}^{\mathrm{mapp}} = 1$ uses a linear mapping with LMMSE estimation ($N = 70$). Two HDA systems with Archimedes spirals are depicted with $r_{\mathrm{H}}^{\mathrm{mapp}} = \frac{1}{2}$ and different densities of the spiral ($\Delta = 0.1$ and $\Delta = 0.4$) using an LMMSE estimator and a total of $N = 80$ channel uses. Another variant of the analog branch are AMBCs as introduced in Chapter 5. Here three different AMBCs with rates $r_{\mathrm{H}}^{\mathrm{mapp}} \in \left\{\frac{1}{2}, \frac{1}{3}, \frac{1}{4}\right\}$ are employed with $N \in \{80, 90, 100\}$.

The overall performance of the transmission system is significantly increased due to the additional analog branch. Depending on the amount of available additional channel uses, the pSNR at, e.g., $\text{cSNR}|_{\text{dB}} = 20\,\text{dB}$ can be improved by 20 dB, 30 dB, 33 dB or even 40 dB.

Thus, also in the case of a given digital branch, additional channel uses can be exploited by HDA transmission providing powerful means to still improve the overall transmission quality.

6.5 Iterative Source-Channel Decoding

In Section 6.3.4 the statistical dependency of the quantization error u_{H}^{a} and the quantized values u_{H}^{d} has already been introduced. For uniform source pdfs and uniform quantizers these variables are statistically independent, but, e.g., for a Gaussian source with an LMQ, statistical dependency can be exploited, e.g., by a joint MMSE estimation at the receiver (Figure 6.4).

In, e.g., [Adr03, SACV11], a *Iterative Source-Channel Decoding* (ISCD) system is introduced which consists of serial turbo-like decoding which exchanges extrinsic information about the information bits between the *Soft Decision Source Decoder* (SDSD) and the soft decision channel decoder. The SDSD exploits a-priori information about the source statistics, e.g., the source pdf or correlation in time or space to improve the reliability of the information received by the channel decoder. The improved information is fed back to the channel decoder and enhances the reliability even further by exploiting the structure of the channel code. The information exchange is usually facilitated by L-values which represent the probability of a bit being one or zero.

To design a powerful ISCD transmission system, usually a rate-1 convolutional encoder and redundant bitmapping is used. Both are connected by an interleaver.

In the context of HDA transmission, the idea of ISCD can be developed even further. In case of statistical dependency of the quantization error and the quantized values, the received symbols in the analog branch carry information about the received bits in the digital branch. Thus, they can be used as a-priori information in the SDSD. As an intermediate step in the SDSD, the a-posteriori probability of each quantization level is calculated using the L-values from the channel decoder and a-priori information from the source statistics. If, e.g., an LMQ is used which has very narrow quantization intervals at small values and very wide quantization intervals at the tail of the pdf, a received analog symbol with a very high value will most probably correspond to a quantization interval at the tail of the pdf. This information is additionally combined in the SDSD to alter the probabilities of the quantized values. The reliability of the analog received symbols, i.e., the influence of the AWGN channel is considered, too.

Figure 6.17 shows the structure of an HDA system with ISCD. At the transmitter, an interleaver (π) is inserted between the source encoder (quantization and

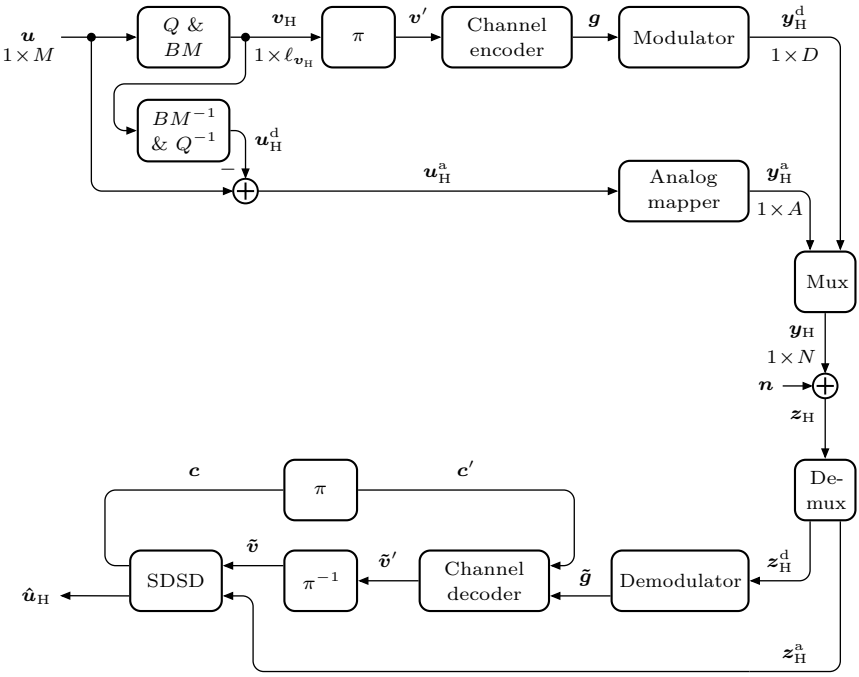

Figure 6.17: *Hybrid Digital-Analog* (HDA) transmission system with *Iterative Source-Channel Decoding* (ISCD).

redundant bitmapping) and the channel encoder. At the receiver, a de-interleaver (π^{-1}) is needed between the channel decoder and the SDSD. Furthermore, a feedback loop for the extrinsic information gained in the SDSD with an interleaver is introduced. The received symbols from the analog branch are fed directly to the SDSD.

Figure 6.18 shows simulation results for an 800-dimensional ($M = 800$) Gaussian source which is quantized using a $F_\mathrm{H} = 4$ bit LMQ. Redundant bitmapping is used which adds another 4 bits per source symbol by bit repetition. A rate-1 recursive non-systematic convolutional code with the generator polynomial $\{1, 10/17\}_8$ and BPSK modulation is employed. Thus, the coding rate of the system is $r_\mathrm{H}^\mathrm{ccm} = \frac{1}{2}$ and including the analog branch the channel dimension is $N = 7200$. A maximum of 20 iterations is allowed for decoding. The employed interleaver is an S-random interleaver with a minimum distance of 8 which is the number of bits after the redundant bitmapping. The green curve shows the performance of an HDA decoding system (Figure 6.2) with two independent MMSE estimators, one for the analog

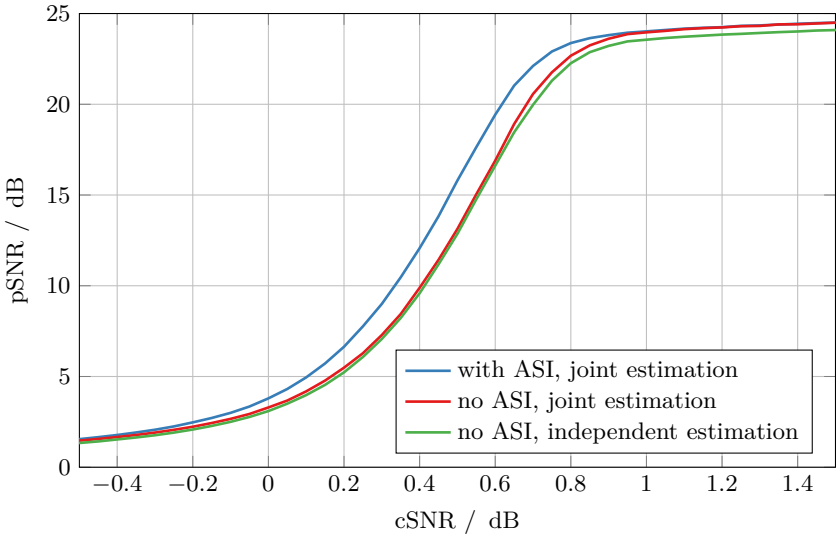

Figure 6.18: Performance of HDA with ISCD. The green curve shows the performance of independent MMSE estimation in both branches. The red curve uses joint estimation of both branches. The blue curve additionally uses the *Analog Side Information* (ASI) from the analog branch to improve the performance.

branch and one for the digital branch. Here, in the digital branch a ISCD decoder is used. The red curve shows the improved performance by using a joint MMSE estimator for both branches as described in Section 6.3.4. Here, the statistical dependency between the quantized values and the quantization error is exploited.

The blue line shows the best performance obtained by the system in Figure 6.17. Here, the information of the analog branch (*Analog Side Information* (ASI)) is used in the SDSD to improve the reliability of the quantized values and additionally this extrinsic information is fed back to the channel decoder. Consequently, the decoding performance of the channel decoder is also slightly improved, which results in a shift of the waterfall to the left. Hence, exploiting the ASI, which is provided by the analog branch of the HDA system in the context of ISCD, improves the overall system performance.

More details, the complete derivations and also the influence of the ASI on the so called *Extrinsic Information Transfer* (EXIT) chart are described in [Bun12].

6.6 Discussion

In this chapter, the following question has been considered: "Can HDA codes using conventional digital codes outperform conventional purely digital codes?"

This question can be answered positively. HDA transmission systems which use conventional digital codes are introduced in Section 6.2. It has been shown in Section 6.3.5 that for every purely digital transmission system, a corresponding HDA transmission system can be designed which exhibits superior performance while using the same number of channel uses and the same transmission power. Furthermore, for channel codes not achieving capacity, the HDA system can be configured with a lower channel coding rate in the digital branch as in the purely digital system. This moves the waterfall to lower channel qualities. Thus, without increasing the complexity or using more powerful digital channel codes, the waterfall region can be shifted to lower channel qualities while the pSNR is still superior. Furthermore, the pSNR is superior for all channel qualities.

Explicit design guidelines have been presented with supporting simulation results for AWGN channels. For fading channels, similar results are given in [RBV14]. The complexity of an HDA transmission system compared to purely digital transmission is only moderately increased since the analog branch just applies a scalar factor (LMMSE estimator) and one additional summation per source symbol. Depending on the implementation, the complexity of the HDA system may even decrease. This is due to the fewer quantization bits and hence fewer bits which need to be encoded and decoded in the digital branch.

Both, the analog and the digital branch of the system use independent estimators which is suboptimal in some cases (Section 6.3.4). Using joint estimation leads to an improved pSNR performance. However, the achievable gains are relatively small. The reason is that quantizers generate only small statistical dependencies between the quantized values and the quantization error. But, precisely these dependencies are exploited by a joint estimator. Also a combination of HDA and ISCD which exploit the statistical dependencies between the digital and the analog branch leads to an even superior performance (Section 6.5). Interestingly, the information of the analog branch can be used to improve the performance of the digital channel decoder, thus, leading to successful decoding at smaller cSNRs. Though, the gains are relatively small and may probably not justify the complexity increase.

A nice feature of HDA transmission systems is that they offer new degrees of freedom (Section 6.4). The power between the digital and analog channel symbols can be distributed unevenly. This provides a means to easily adapt the performance of a system to a given channel quality. Furthermore, other analog mappers besides simply a scalar factor, can be employed to increase the performance or create other desired properties. Most interestingly, if the design of a purely digital transmission system cannot be adapted to additionally available channel uses, the overall performance can be significantly increased by adding an analog branch, thus, designing an HDA system!

Chapter 7

Application Example: Hybrid Digital-Analog Transform Coding

7.1 Introduction

In the context of a combined digital and analog transmission, there are, in general, several methods which could be employed to exploit correlation in source signals. In [HV06, HV07] a system optimized for speech signals is proposed. Predictive source coding is employed, while the spectral envelope is transmitted digitally, and the prediction error is transmitted using continuous-amplitude processing.

Skoglund et al. [SPA02] published an HDA system for sources with and without correlation by using vector quantization and a redundant mapping of quantization indices to channel vectors as the digital branch and uncoded transmission of the quantization errors as the analog branch. The digital and analog channel symbols are multiplexed and transmitted over an additive white Gaussian noise (AWGN) channel. The vector quantizer, the decoder codebook at the transmitter side (to calculate the quantization error), the decoder codebook at the receiver side, the redundant mapping and normalization factors for the analog branch are optimized jointly using numerical methods. For an 8-dimensional Gaussian vector source whose symbols are transmitted with 16 channel symbols, Monte Carlo simulations show [SPA02] the superiority of the HDA system over a purely digital system which uses the same numerical optimization strategy.

Nonetheless, the aforementioned system has drawbacks: the design of the HDA codes is complex and, thus, infeasible for long block lengths. Additionally, exhaustive search in the decoding algorithms is required for the general vector quantization and the redundant mapping (look-up table decoding).

In the following sections, the use of transform coding to exploit correlation of the source in the context of HDA transmission is described [RV13b]. The ideas of the design of HDA codes for *independent identically distributed* (i.i.d.) sources as in Chapter 6 inspire a new Hybrid Digital-Analog transform coding system. It is based on a block transform to exploit source correlation and a simplified HDA

design employing well-known digital codes and potentially long block lengths with analog transmission of the quantization error.

First, the purely digital transmission system with block transform is briefly discussed in Section 7.2 as well as block transform and bit allocation techniques are reviewed in Section 7.3. Section 7.4 introduces the Hybrid Digital-Analog extension for block transform coding with its simulation results in Section 7.5. The chapter is concluded with a short discussion (Section 7.6).

7.2 Purely Digital Transmission System

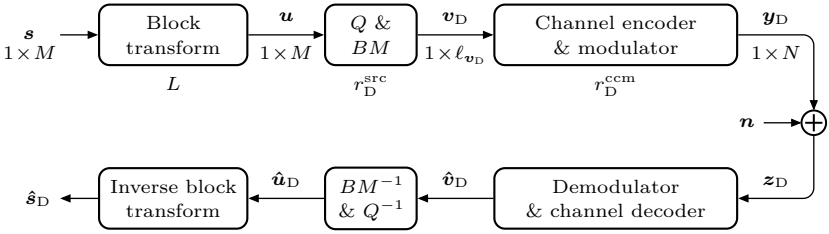

Figure 7.1: Purely digital transmission system with transform coding.

Figure 7.1 shows a conventional digital transmission system with transform coding. The system is very similar to the purely digital transmission system described in Section 6.2.1. Additional functionality is added by a block transform which performs a decorrelation of the source symbols. The source emits continuous-amplitude and discrete-time source symbols $\boldsymbol{s}$ with dimension $1\times M$ following the *probability density function* (pdf) $\mathrm{p}_{\boldsymbol{S}}$ and correlation ρ of successive symbols. At the receiver, after reconstruction of the quantized values, the inverse block transform gives an estimate $\hat{\boldsymbol{s}}_{\mathrm{D}}$ of the initial source symbols $\boldsymbol{s}$.

The end-to-end symbol SNR for the purely digital and the *Hybrid Digital-Analog* (HDA) systems are described by the sSNR defined in (2.1).

7.3 Block Transform and Bit Allocation

The block transform can be described by a matrix multiplication:

$$(u_{j\cdot L},...,u_{j\cdot L+L-1})^{\mathrm{T}} = \boldsymbol{T}\cdot(s_{j\cdot L},...,s_{j\cdot L+L-1})^{\mathrm{T}} \quad \forall j\in\mathbb{N}. \tag{7.1}$$

The matrix $\boldsymbol{T}$ has the dimension $L\times L$. If $M>L$, the vector $\boldsymbol{s}$ is partitioned to an integer number of blocks of the length L, $\boldsymbol{T}$ is applied to each block and the results are concatenated to yield $\boldsymbol{u}$ with length M. If the transform matrix $\boldsymbol{T}$ is orthogonal (i.e., unitary, but real-valued), then the subsequent bit allocation works best and

the matrix used for the inverse block transform is $\boldsymbol{T}^{\mathrm{T}}$. A well known orthogonal transform yielding optimal results is the *Karhunen-Loève Transform* (KLT). Here, the transform matrix is adapted to the source statistics and has to be send to the receiver as side information. To avoid sending this additional information, a fixed transform is sought. The *Discrete Cosine Transform* (DCT) is a good approximation of the KLT and yields reasonable performance without transmitting any side information. Unfortunately, also for a source without correlation the first coefficient of the DCT transform has twice the variance of the other coefficients. Thus, this transform is not orthogonal. But with a normalization by $1/\sqrt{2}$ of the first coefficient ensures orthogonality. Here, this *normalized* DCT (DCTN) will be employed to use a orthogonal transform and to avoid sending the source specific KLT matrix as side information.

For the bit allocation, the well known water filling technique is used. First, the variance of each vector entry is computed. Then single bits are repetitively assigned to the quantizer of the vector entry with the highest variance. Then, the corresponding variance is lowered by 6 dB and the assignment is repeated until all bits are spent [JN84]. The maximum gain in dB which can be expected exploiting a source correlation with the correlation factor ρ is given by $10 \cdot \log_{10}\left((1-\rho^2)^{-1}\right)$ [JN84].

7.4 Hybrid Digital-Analog Transmission System

Figure 7.2 illustrates the HDA transmission system (Section 6.2.2) which is extended by transform coding. Here, a block transform and the inverse block transform are added.

Due to the bit allocation and the resulting different quantizers for different entries of $\boldsymbol{u}$, the power of the quantization error $y_{\mathrm{H}}^{\mathrm{a}}$ is not the same for all entries. Therefore, for each entry $y_{\mathrm{H},i}^{\mathrm{a}}$, a different normalization has to be applied:

$$y_{\mathrm{H},i}^{\mathrm{a}} = \sqrt{\frac{1}{\mathrm{E}\{(\tilde{\mathrm{g}}_i(u_{\mathrm{H},i}^{\mathrm{a}})^2\}}} \cdot \tilde{\mathrm{g}}_i(u_{\mathrm{H},i}^{\mathrm{a}}) = \mathrm{g}_i(u_{\mathrm{H},i}^{\mathrm{a}}) \qquad \forall\ 0 \leq i < M. \tag{7.2}$$

In case of a very small power or too few bits, the bit allocation may choose to allocate zero bits to one entry. Then no information about this entry is transmitted using the digital branch and the original entry is send using only the analog branch.

After adding the outputs of the analog and digital branches and after the inverse block transformation, $\hat{\boldsymbol{s}}_{\mathrm{H}}$ gives an estimate of the initial source symbols.

7.5 Simulation Results

Figure 7.3a shows the performance of several HDA and purely digital transmission systems. A Gaussian source with correlation $\rho = 0.8$ and dimension $M = 120$ is

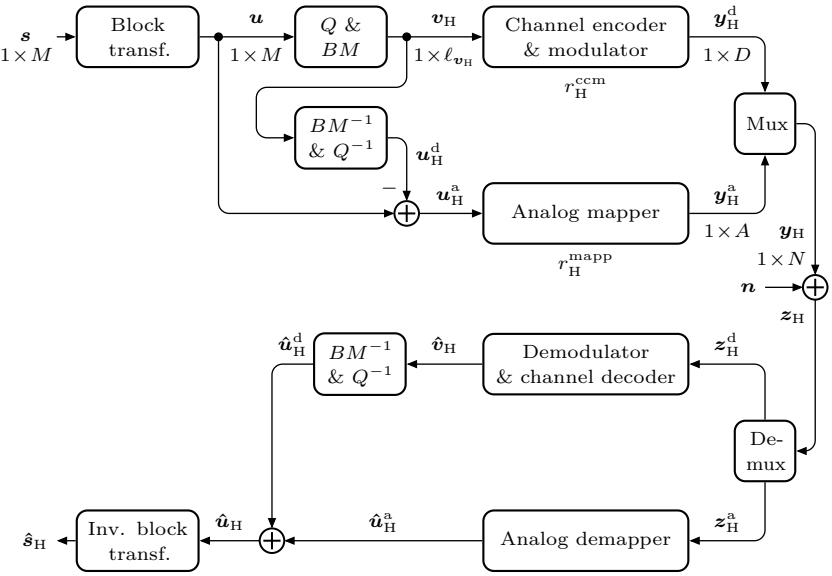

Figure 7.2: HDA transmission system with transform coding.

transformed by a DCTN with $L = 120$ and quantized using a scalar *Lloyd-Max Quantizer* (LMQ) whose fidelity is assigned by water filling. In both systems, a parallel concatenated Turbo code using convolutional component codes with the generator polynomial $\{1, 15/13\}_8$ and random interleaving is used with 20 decoding iterations. The Turbo code is the same code which is used in UMTS-LTE [3GP11], though the input block length is $\ell_{\boldsymbol{v}}$. The modulation is chosen to be BPSK. All simulations employ $N = 720$ channel uses, while the HDA system utilizes a linear mapper ($\tilde{\mathbf{g}}(\boldsymbol{u}_{\mathrm{H}}^{\mathrm{a}}) = \boldsymbol{u}_{\mathrm{H}}^{\mathrm{a}}$) with $A = M = 120$ dimensions for the analog branch and $D = N - A = 600$ dimensions for the digital branch. Puncturing of parity bits facilitates the adaptation of the channel code rate of the digital branch for the HDA ($r_{\mathrm{H}}^{\mathrm{ccm}}$) and the purely digital ($r_{\mathrm{D}}^{\mathrm{ccm}}$) system. The analog demapper is a LMMSE estimator. For each shown purely digital system, a corresponding HDA system is designed transmitting on average fewer quantization bits per source dimension $F_{\mathrm{H}} < F_{\mathrm{D}}$ to ensure the same channel coding rate $r_{\mathrm{H}}^{\mathrm{ccm}} = r_{\mathrm{D}}^{\mathrm{ccm}}$ (design guidelines in Section 6.3.5). In contrast to the simulations using the same scalar quantizer for each symbol (e.g., Figure 6.10), the water filling employed here facilitates the use of, on average, fractional bits per source dimension to ensure the same channel coding rate for HDA and purely digital systems. Most interestingly, all HDA systems surpass the corresponding purely digital system for all channel qualities and additionally improve the sSNR for increasing channel qualities cSNR.

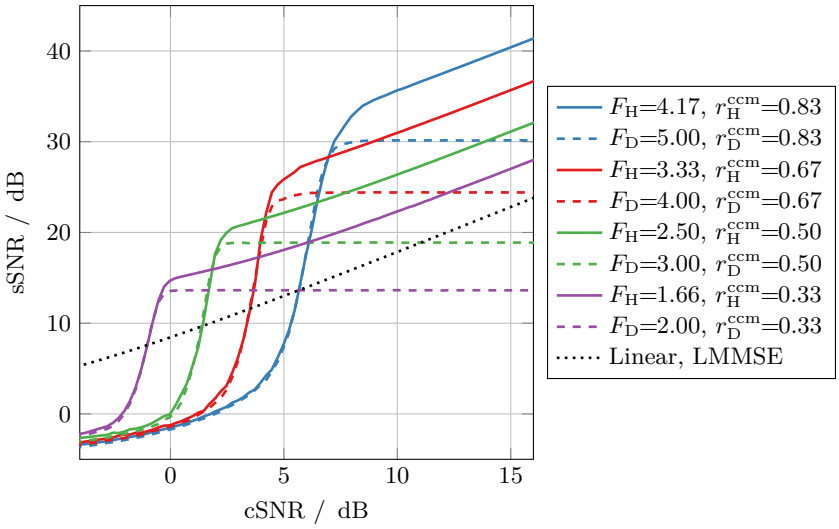

(a) DCTN transform and Turbo coding.

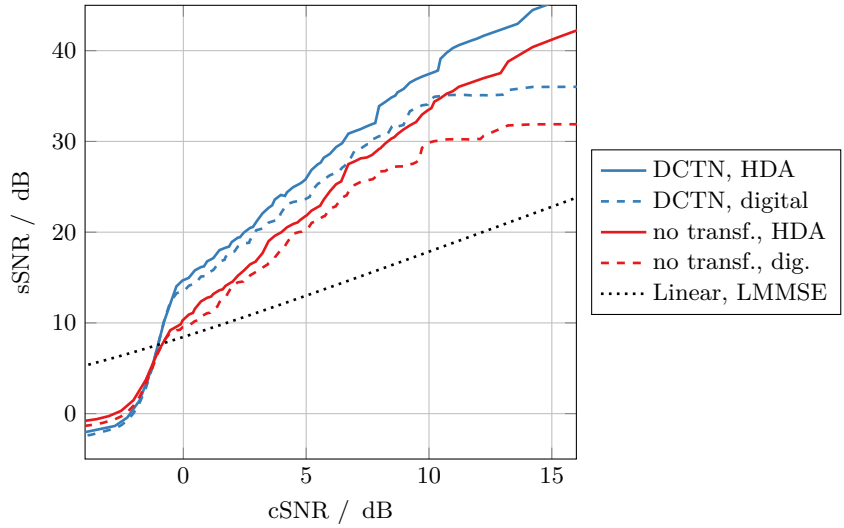

(b) Envelopes for simulations with and without DCTN transform.

Figure 7.3: HDA and digital transmission for a Gaussian source with correlation $\rho = 0.8$ and Turbo coding. $M = 120$, $L = 120$, $N = 720$. F_H and F_D are the number of quantization bits per source symbol for the HDA and purely digital system, respectively. Purely analog transmission system for comparison.

In Figure 7.3b, the same simulation parameters are used as above, but here, only the upper envelope of the curve array for varying quantizer fidelities is shown. Two experiments use the DCTN and two are conducted without transform coding. For comparison, a purely analog transmission system is depicted in which the source vector is transmitted $N/M = 6$ times and at the receiver a LMMSE estimator combines the received symbols (Section 3.2.2). Again all simulations use the same source and channel dimensions.

Transform coding using the DCTN improves the sSNR of the transmission system. For both, the purely digital and the HDA transmission system, the performance increases by around 4.2 dB which is quite close to the theoretical limit of $10 \cdot \log_{10}\left((1-\rho^2)^{-1}\right) = 4.4\,\text{dB}$ [JN84]. All envelopes of HDA systems surpass the envelopes of their corresponding purely digital transmission systems for all channel qualities.

7.6 Discussion

In this chapter, a new Hybrid Digital-Analog (HDA) transmission system for sources with correlation is proposed. A block transform is used to perform a decorrelation of the source symbols to exploit its potential to improve the overall end-to-end fidelity. In addition to the digital representation of the transform coefficients, the HDA system also transmits the quantization error in the transform domain using continuous-amplitude methods. Thus, the inherent error introduced by the quantizer is compensated by additional analog transmission. With improving channel qualities, thereby, the saturation of the transmission fidelity is eliminated as in the HDA system described in Chapter 6.

In comparison to a purely digital system, the transmission fidelity of the HDA system is superior for all channel qualities while the overall number of channel uses is kept constant. Moreover, since well-known, excellent digital codes are employed, long block lengths can be supported.

Simulations comparing purely digital and HDA transmission systems employing Gaussian source pdfs with correlation, an orthogonal transform with water filling as the bit allocation technique and Turbo codes show the superiority of HDA codes over purely digital codes for all channel qualities. These simulations also indicate that the performance of HDA codes additionally rises for increasing channel qualities (*graceful improvement*). Ultimately, the proposed HDA transmission system surpasses the purely digital transmission system at all channel qualities.

Chapter 8

Comparison of Proposed Systems

8.1 Introduction

In the preceding chapters, several transmission systems employing continuous-amplitude techniques are analyzed. Each of these systems has its specific strengths and weaknesses in its specific fields of application. The properties of the proposed systems are summed up in Section 8.2.

For one common very specific field of application, all proposed systems may be parametrized accordingly. In Section 8.3 simulation results are given to enable a performance comparison.

8.2 Properties of Proposed Systems

8.2.1 Linear Analog Block Codes

Linear Analog Block Codes (LABCs) (Section 3.2 and [RSV09]) employ only linear operations to transmit a source vector and to decode the received vector. This very low complexity scheme just employs one matrix multiplication at the transmitter. It has been shown that even this multiplication can be omitted, since appropriately repeating the input vector is already optimal. Decoding may be conducted using again just a matrix multiplication, or in case of repetition simple averaging is sufficient. The scheme supports single letter codes ($M = 1$). For a rate of $r = \frac{M}{N} = 1$ and Gaussian input symbols, LABCs achieve capacity.

For rates $r < 1$, LABCs cannot exploit the additional channel uses to significantly improve the transmission quality. Doubling the number of channel uses just leads to an improvement of 3 dB in terms of pSNR (3.11).

8.2.2 Compander and Space Filling Curves

In Chapter 4 compander and space filling curves are analyzed. Here, a compressor function $\boldsymbol{y} = \mathbf{g}(u)$ (non)-linearly maps the source symbols u to (several) channel symbols $\boldsymbol{y}$. The received symbols $\boldsymbol{z}$ are (non)-linearly mapped to the estimate $\hat{u}$ by an expander $\hat{u} = \mathrm{h}(\boldsymbol{z})$. The scheme supports single letter codes ($M = 1$). For a

1:1 system ($N = M = 1$) and input symbols which are not Gaussian, a nonlinear mapping improves the overall performance. For Gaussian symbols, again a linear mapping is optimal as in the case of LABCs. For a 1:2 mapping which nonlinearly maps one source symbol to two channel symbols, significant gains compared to linear systems can be observed. Especially mappings with closed form expressions such as the Archimedes spiral are well suited.

The compressor and expander may be further optimized using iterative numerical methods. This helps to further improve the performance compared to, e.g., a linear mapping in the 1:1 case or the Archimedes spiral in the 1:2 case, but is computationally very complex during design time. During runtime these optimized mappings and estimators have to be realized with lookup tables which is infeasible for longer block lengths. Also, there are no mappings known in literature for longer block lengths exhibiting a good performance.

8.2.3 Analog Modulo Block Codes

In Chapter 5 *Analog Modulo Block Codes* (AMBCs) are introduced. They are inspired by LABCs with an additional modulo operation as a nonlinearity. Single letter codes are supported and systematic AMBCs exhibit the nice property that the source symbols are sent unchanged as the first channel symbols. Different types of decoders may be employed including *Zero-Forcing with Lattice Reduction* (ZFLR) decoding which nearly achieves *Maximum Likelihood* (ML) performance, but with significantly lower complexity. The idea of adding the modulo operation as a nonlinearity to the LABCs is very fruitful, since the performance of AMBCs is significantly higher than the performance of purely linear systems.

So far, only for very specific rates and block lengths, a good design strategy is proposed, e.g., for $M > 1$ the optimal design is still to be found. Thus, AMBCs are not yet suited for longer block lengths but with an appropriate design strategy longer block lengths are feasible with, e.g., ZFLR decoding. Additionally, so far, only uniform source *probability density function*s (pdfs) are considered. For other source distributions, compressor functions would have to be employed [Sak70] to map the source symbols to a limited range.

8.2.4 Hybrid Digital-Analog Transmission

Hybrid Digital-Analog (HDA) transmission is analyzed in Chapter 6. These systems exploit the insight that the channel space of any nonlinear continuous-amplitude transmission system can be decomposed into a subspace in which only discrete values occur and a subspace with continuous values (Section 2.4.3). In HDA transmission systems, this insight is transformed to the design rule. A purely digital transmission system (digital branch) occupies part of the channel uses and the quantization error occurring in the digital branch is additionally transmitted using continuous-amplitude means (analog branch).

HDA systems benefit from the advantages of purely digital transmission systems. It can be selected from a huge variety of channel codes, each with its specific properties. Long block lengths with capacity approaching performance are supported. In Section 6.3.5 it has been shown that HDA systems achieve the same or superior performance as purely digital systems, with the additional advantage that the end-to-end SNR increases for rising channel qualities and does not saturate as in any purely digital system. In the analog branch, the above mentioned transmission systems such as Archimedes spirals or AMBCs can be employed to add even more flexibility. Single letter codes are supported by HDA systems, but there are only very few possible variants and not an infinite number of setups as in case of Archimedes spirals or AMBCs.

The complexity of HDA systems is only marginally higher than of purely digital systems. Therefore all block lengths and performance limits reached by purely digital transmission systems in practice can also be reached with HDA transmissions with the additional benefit of an increased performance for rising channel qualities.

8.3 Simulation Results

It is not trivial to compare the different transmission systems described in the previous chapters, since all of them have their individual strengths and weaknesses. For the special case of a uniform source pdf with $M = 1$ source symbol and $N = 2$ channel symbols, all systems can be designed. In Section 8.3.1 all systems are compared for the rate $r = \frac{M}{N} = \frac{1}{2}$. First, systems with the shortest possible block length ($M = 1$) are considered. Later, HDA system which offer a much higher flexibility, since they can be designed with long block lengths with, e.g., $M = 5000$ source symbols. With these systems, the gap to capacity is reduced.

Thanks to their flexibility, HDA systems may be designed for such rates. But, since these rates are rather unusual, further HDA transmission systems are evaluated in Section 8.3.2 and compared to purely digital transmission.

8.3.1 Two channel symbols per source symbol ($r = 1/2$)

Very Small Block Length ($M = 1$)

In Figure 2.3 in Chapter 2, different examples of 1:2 systems are depicted. Here, each system is parametrized to yield the same high-cSNR performance. In Figure 8.1 their performances are compared. Additionally, the upper performance bound *Optimum Performance Theoretically Attainable* (OPTA) for a uniform source pdf (Section 3.4) is shown.

The performance of a purely linear system, i.e., an LABC is given in (3.11). Also, the equidistant Archimedes spiral (Section 4.4.1) with $\Delta = 0.25$ and an AMBC (Chapter 5) with $\boldsymbol{A} = [1 \;\; 3.9]$ is depicted. As HDA system, a uniform quantizer with $F_{\mathrm{H}} = 2$ bits per symbol, no channel coding and 4-ASK modulation is chosen.

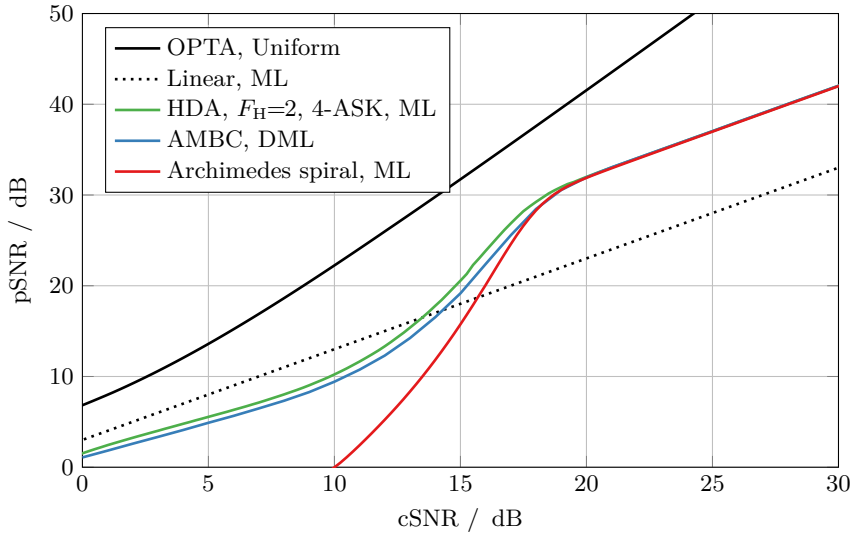

Figure 8.1: Performance comparison of the systems shown in Figure 2.3, with ML decoding. Scalar source symbols ($M = 1$) with a uniform pdf are transmitted using $N = 2$ channel uses with a linear system, an equidistant Archimedes spiral with $\Delta = 0.25$, an AMBC with $\boldsymbol{A} = [1 \;\; 3.9]$ and an HDA system with $F_H = 2$ quantization bits, no channel coding and 4-ASK modulation.

In the HDA system, an ML estimator is used as analog demapper. All systems use $N = 2$ channel symbols for $M = 1$ source symbol and ML estimation. The AMBC uses the *Discrete Maximum Likelihood* (DML) estimator. For the Archimedes spiral and the AMBC, the high-cSNR performance can be arbitrarily chosen. For the HDA system with such a small block length, the high-cSNR performance can only be parametrized by the resolution of the scalar quantizer. For this small block length, the strengths of HDA transmission systems cannot be fully exploited.

The purely linear system cannot be parametrized at all and shows the poorest performance at high channel qualities. The HDA and AMBC transmission systems achieve a similar performance, while the HDA system is marginally better. The performance of the Archimedes spiral decreases more heavily for lower channel qualities than the other transmission systems.

The similar performance of the HDA transmission and the AMBC can be explained by the similar structure of the valid code vectors in the channel space (Figure 2.3). Both systems exhibit parallel arms while a rotation of the code vectors of the AMBC (nearly) yields the same code vectors as the HDA system. This interesting property is exploited by several types of decoders of AMBCs

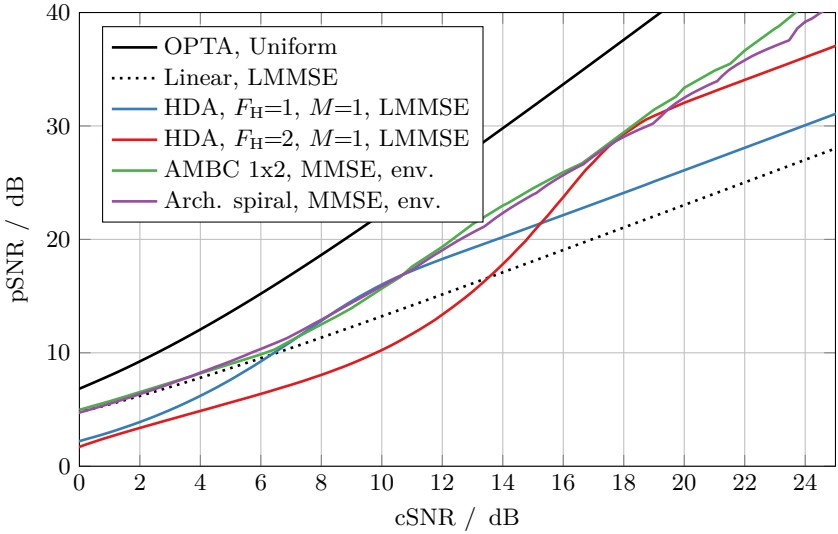

Figure 8.2: Performance comparison of several systems for source symbols with a uniform pdf with $M = 1$ source symbol and $N = 2$ channel symbols. HDA systems with $F_H = \{1, 2\}$ quantization bits, BPSK or 4-ASK modulation are given. Also, the envelope of all 1x2 AMBCs and of all equidistant Archimedes spirals is shown.

(Section 5.4.2).

In Figure 8.2 a similar comparison is conducted as above. Still, just $N = 2$ channel symbols are employed for ($M = 1$) source symbol. Compared to the above figure, better estimators are employed in all systems. In detail, for the linear system, a *Linear Minimum Mean-Square Error* (LMMSE) estimator is used. For the AMBC system and the equidistant Archimedes spiral, the envelope of the performance of all possible variants with $M = 1$ and $N = 2$ with *Minimum Mean-Square Error* (MMSE) estimator is shown. Here, the envelopes of the Archimedes spiral and the AMBCs are very similar while it seems that again the AMBC is slightly better.

Two HDA systems with $M = 1$ are shown which both use LMMSE estimation in the analog branch. One uses a quantizer with $F_H = 1$ bit per source symbol and BPSK modulation and the other uses $F_H = 2$ bits with 4-ASK modulation. Both do not employ any channel coding. The HDA system with the higher quantizer resolution exhibits a high-cSNR performance which is 6 dB better, but a successful decoding is not attained until higher channel qualities compared to the case of $F_H = 1$. These HDA systems achieve the envelope of the performance of the Archimedes spiral and the AMBC. All in all, in terms of flexibility and complexity,

for a uniform source pdf, the AMBC is the best choice for such a small block length.

The Benefit of Long Block Lengths

In Figure 8.3 a similar comparison is conducted as above. The overall code rate $r = \frac{M}{N} = \frac{1}{2}$ is the same for all systems, while the number of source symbols M is varied. Again, the source symbols follow a uniform pdf.

The two HDA systems with $M = 1$ are the same as shown in Figure 8.2. One uses a quantizer with $F_{\mathrm{H}} = 1$ bit per source symbol and BPSK modulation and the other uses $F_{\mathrm{H}} = 2$ bits with 4-ASK modulation. Both do not employ any channel coding. In their analog branch, LMMSE estimation is applied.

To give a glance at the flexibility and potentially better performance of HDA codes, two other systems which with a longer block length are evaluated.

These HDA systems combine $M = 5000$ source symbols, employ scalar uniform quantization, and use higher order modulation, namely 16-QAM and 256-QAM with gray mapping. Redundant bitmapping which simply repeats the output bits of the quantizer and a rate-1 recursive non-systematic convolutional code with the generator polynomial $\{1, 10/17\}_8$ and Iterative Source-Channel Decoding (ISCD) is used (Section 6.5). Here, MMSE estimation is chosen. The redundant bit mapping

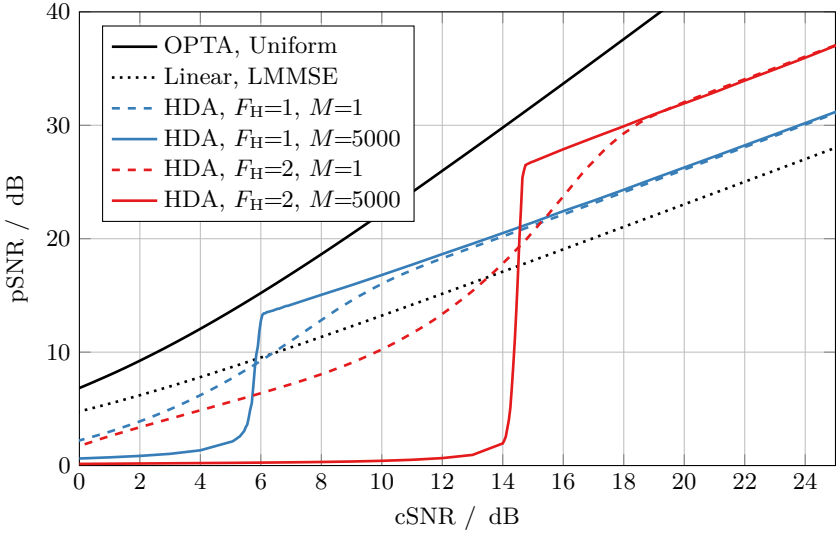

Figure 8.3: Performance comparison of several systems for source symbols with a uniform pdf. HDA systems with a rate of $r = \frac{1}{2}$ with $F_{\mathrm{H}} = \{1, 2\}$ quantization bits per source symbol are shown. The block length of the systems are varied for comparison.

and channel encoding converts, e.g., in the $F_{\mathrm{H}} = 2$ case, the 10000 quantization bits to 20000 bits which are fed to the modulator. The 256-QAM mapping generates 2500 complex channel symbols which is equivalent to $D = 5000$ real channel symbols. With $A = M = 5000$ quantization error symbols, $N = D + A = 10000$ channel uses are employed in total, leading to a code rate of $r = \frac{1}{2}$.

The system achieves the same high-cSNR performance as the HDA system with just $M = 1$ source symbol, but thanks to the greater block length and the employed channel coding, successful decoding is possible at lower channel qualities and yields a steep waterfall.

The HDA system with $F_{\mathrm{H}} = 1$ just exhibits a gap of just 1.18 dB in terms of cSNR to OPTA. This gap could be further reduced by optimizing the bitmapping, the interleaver or by employing a vector quantizer instead of a scalar quantizer. This flexibility and the usage of known techniques employed in digital systems is the strength of HDA transmission systems.

8.3.2 Hybrid Digital-Analog Transmission Outperforming Purely Digital Transmission

In the following, two examples from Chapter 6 are recapitulated which outline the key benefits of HDA transmission over purely digital transmission.

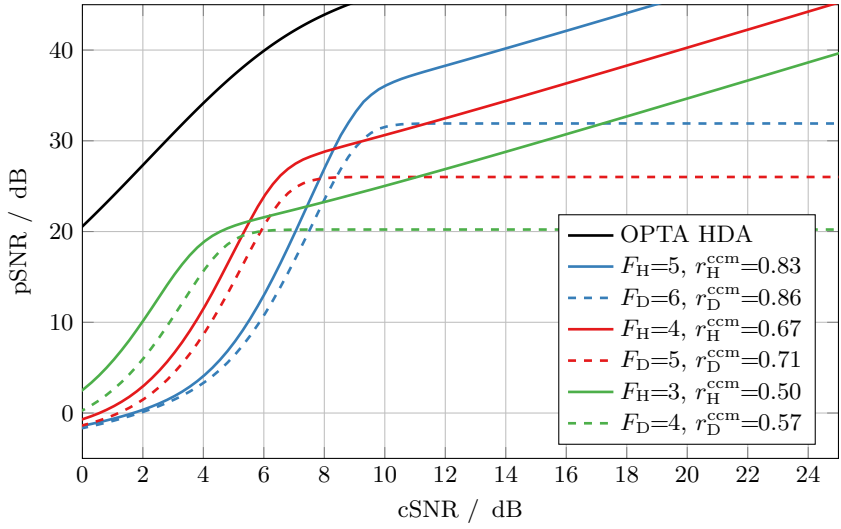

Figure 8.4: HDA and digital transmission using convolutional codes. Gaussian source pdf and scalar Lloyd-Max quantization. $M = 80$, $N = 560$, $r = \frac{1}{7}$. HDA: $A = 80$, $D = 480$.

The first example (Figure 8.4, more details on page 106) uses an 80-dimensional ($M = 80$) Gaussian source with scalar *Lloyd-Max Quantizer* (LMQ) employing a rate-$\frac{1}{2}$ convolutional code. The different rates for different quantizer fidelities are achieved by puncturing only the parity bits, thereby with BPSK modulation always yielding $N = 560$. The overall rate is $r = \frac{M}{N} = \frac{1}{7}$ to demonstrate an HDA system which may operate at lower channel qualities than in the example above. Linear analog mapping and an LMMSE estimator are used in the analog branch. Several modes are considered which differ in the fidelity of the scalar quantizer. Since the fidelity of the quantizer can only be varied in integer steps, the channel coding rates of the HDA ($r_{\mathrm{H}}^{\mathrm{ccm}}$) and the purely digital system ($r_{\mathrm{D}}^{\mathrm{ccm}}$) are not equal. The channel coding of the HDA system is stronger and, thus, leads to decodability at lower channel qualities, improving the waterfall region by up to 1 dB! Additionally, the HDA systems always exhibit a superior end-to-end transmission quality plus an increasing performance for rising channel qualities.

In the second example (Figure 8.5, more details on page 107), the convolutional encoder is replaced by rate-$\frac{1}{3}$ Turbo coding and the block length is increased to $N = 4998$. The overall rate is unchanged ($r = \frac{1}{7}$). Again, only parity bits are punctured, BPSK modulation is employed and the analog branch consists of linear analog mapping and an LMMSE estimator. For the uniformly distributed source symbols, alternating quantizers with different fidelities are employed enabling a

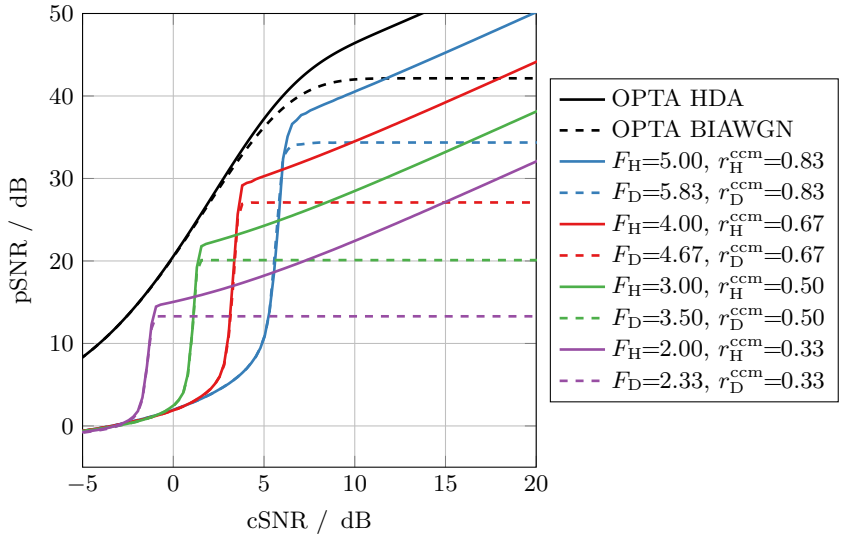

Figure 8.5: HDA and digital transmission using Turbo codes. Uniform source pdf and scalar uniform quantization. $M = 714$, $N = 4998$, $r = \frac{1}{7}$. HDA: $A = 714$, $D = 4284$.

fractional average number of quantization bits per source symbol. Thus, the rates of the channel coding in the HDA ($r_{\mathrm{H}}^{\mathrm{ccm}}$) and the purely digital system ($r_{\mathrm{D}}^{\mathrm{ccm}}$) can be chosen to be equal. The waterfall region of the HDA and the purely digital system is, thus, at the same channel quality. In comparison to the convolution code above, the Turbo code greatly improves the coding performance, such that, e.g., the HDA system with $F_{\mathrm{H}} = 2$ just exhibits a gap of only 1.14 dB in terms of cSNR to OPTA. As above, for the relevant channel qualities, all HDA systems are superior to purely linear transmission with LMMSE decoding.

It can be seen that for all fidelities, the HDA system achieves a superior performance compared to the purely digital system and additionally continuously improves the end-to-end transmission quality for rising channel qualities.

Chapter 9

Summary

During the last 25 years, most of the communication systems have been converted to purely digital technology, while the transmitted content is, to a large extent, analog by nature. The quantizer inside the source encoder limits the resolution of the reproduction of the content in the receiver due to the inevitable quantization noise. Depending on the available resources for transmission – channel bandwidth, transmission power, and channel quality – a compromise has to be found between the resolution, i.e., the bit rate of the source encoder, and the strength of the channel coding. Digital systems are usually designed for worst case channel conditions. However, often the channel quality is much better, which is not reflected in an improved end-to-end transmission quality due to inevitable quantization noise produced by the source encoder.

Adaptive Multi Rate (AMR) systems have been developed to tackle this problem. They open up the possibility to choose the best setup for source, channel coding, and modulation to benefit from better channel conditions to improve the reproduction quality. However, the AMR systems rely on the availability of a feedback channel for channel quality measurement which is often not given. For this reason, alternative concepts which improve their end-to-end transmission quality with increasing channel qualities also for non-adaptive transmitters are of interest.

In this thesis, the focus is set on systems with a fixed transmitter which still benefit from an increased channel quality and circumvent the saturation effect of the end-to-end transmission quality. Purely analog (discrete-time and continuous-amplitude) transmission systems are considered, both with linear and nonlinear components. The performance of linear systems is derived analytically. *Linear Analog Block Codes* (LABCs) are considered as one representative. Computer simulations assess the performance of *Companding Systems* and *Space Filling Curves* including the famous *Archimedes spiral*, showing the performance gain due to the employed nonlinearities. Based on the conducted studies, a new class of nonlinear analog codes, i.e., the *Analog Modulo Block Codes* (AMBCs) is proposed. Their structure enables a rich variety of analyses and decoder concepts while performing competitively with a lower complexity as, e.g., Archimedes spirals. Still, all considered systems operate on very short block lengths and exhibit a considerable gap to capacity.

Besides avoiding the saturation effect, the design flexibility of the transmission systems and the overall performance is of major importance. A very promising approach with a flexible design and high performance is *Hybrid Digital-Analog* (HDA) transmission. Here, sophisticated conventional digital transmission systems are combined with analog transmission techniques for continuously improving performance for rising channel qualities. In contrast to other systems employing continuous-amplitude processing, also long block lengths are supported enabling a performance approaching capacity. In an HDA system with a not capacity achieving digital branch, e.g., due to complexity or delay constraints, the analog branch of the HDA system partially compensates the imperfectness of the digital branch and leads to decodability at lower channel qualities. Furthermore, HDA transmission can even be combined successfully with the AMR concept.

General Aspects and Performance Bounds

The general properties, differences and similarities of purely digital and analog transmission systems are outlined. A focus is set on the consequences of nonlinearities in analog transmission systems which lead to discrete-valued and continuous-amplitude dimensions in the channel space. It could be shown that these nonlinearities are essential for a superior performance compared to purely linear analog transmission systems. The performance of linear analog transmission is developed analytically for several types of estimators at the receiver.

To bound the performance of different transmission systems, the *Optimum Performance Theoretically Attainable* (OPTA) for digital and analog channel models is derived. By combining the models for digital and analog channels, OPTA can also be derived for HDA transmission. Interestingly, OPTA for HDA channel models is higher than for purely digital channel models. This effect comes from the limitation of the capacity of digital channel models while analog channel models experience an increased capacity for rising channel qualities.

A key aspect for achieving an improved performance up to capacity is the block size of a transmission system. One way to grasp its influence is given by Shannon with the *Sphere Packing Bound* [Sha59b] for digital transmission systems. Here, this intuition is adopted to nonlinear analog or HDA transmission and the need for long block lengths is justified.

In the context of source encoding, the rate-distortion function states the minimum information rate (number of bits) necessary to encode source symbols with a given *probability density function* (pdf) at a certain mean-square error distortion. The usually applied method to obtain the rate-distortion function is the very costly *Blahut-Arimoto algorithm* which relies on a numerical optimization. In this thesis a new upper bound for the rate-distortion function is proposed. The new bound can be calculated at very low complexity and results to be quite tight.

Continuous-Amplitude Transmission

The simplest modulation schemes for continuous-amplitude transmission systems are companding and space filling curves. They usually map just one source symbol via (non)-linear functions to one or more channel symbols and hence operate with very small block lengths. In this thesis, the companding functions for a system mapping one source symbol to one channel symbol (1:1 mapping) are considered and numerically optimized for non-Gaussian source symbols to assess the potential performance improvements in comparison to linear transmission.

Also 1:2 systems are considered which transmit one additional redundancy symbol and hence employ two channel uses per source symbol. The use of nonlinear mappings, such as the Archimedes spiral leads to significant performance gains compared to linear transmission systems. Also here, numerical optimization of this mapping is conducted to achieve further performance improvements. Unfortunately, the corresponding optimization problem is non-convex and, thus, finding a good maximum is not trivial.

Motivated by the insights in the previous chapters, a new class of continuous-amplitude transmission systems, the *Analog Modulo Block Codes* (AMBCs) is proposed. A real-valued matrix multiplication and a modulo operation are concatenated, where the former creates the necessary redundancy and the latter the essential nonlinearity. The analysis reveals that after a rotation of the generated code vectors, discrete-valued (discrete part) and continuous-amplitude (analog part) dimensions emerge. The code vectors in the discrete part form a regular lattice which can be exploited in the design of efficient decoders. *Zero-forcing decoding with lattice reduction* in the discrete part and separate estimation in the analog part leads to near *Maximum Likelihood* (ML) performance with a very low complexity. AMBCs slightly supersede the performance of, e.g., Archimedes spirals and are a promising candidate for high performing continuous-amplitude transmission systems with low complexity and very small block lengths.

Hybrid Digital-Analog Transmission

HDA transmission turns the necessity of nonlinear transmission and the emergence of discrete-valued and continuous-amplitude dimensions into a design principle. It benefits from the advantages of both, the digital and the analog world. In the digital branch, digital transmission is employed, while the inevitable quantization error is additionally transmitted using continuous-amplitude methods in the analog branch.

A new design method is introduced which uses conventional digital transmission systems with its flexibility and potentially capacity achieving performance. Thus, HDA transmission systems can be designed for the same scenarios for which purely digital transmission is employed, as long as the source content and the channel exhibit a continuous-amplitude nature. Needless to say, when comparing

purely digital and HDA transmission, the same resources – channel bandwidth, transmission power, and channel quality – are assumed. The investigation results in design guidelines for competitive HDA systems: The key is to employ, in comparison to a purely digital transmission system, a coarser quantizer. This leads to fewer bits to be transmitted and hence fewer channel uses in the digital branch. The channel uses which are, thus, saved in the digital branch, are then utilized for additional transmissions in the analog branch.

It is shown that for every purely digital transmission system, a superior HDA system can be found. Furthermore, constructive design guidelines are formulated.

These guidelines are turned into practice by implementing several HDA transmission systems which are thoroughly assessed. In one example Turbo coding is considered: At the worst channel quality at which the purely digital transmission system still can operate, the corresponding HDA system improves the transmission fidelity (pSNR) by 3 dB. Moreover, unlimited gains are theoretically possible for rising channel qualities. Depending on the quantization fidelity, at $\mathrm{cSNR}|_{\mathrm{dB}} = 10\,\mathrm{dB}$ gains of 6.2 to 9.2 dB in terms of pSNR are measured. At $\mathrm{cSNR}|_{\mathrm{dB}} = 20\,\mathrm{dB}$, the gains increase up to $16.2 - 19.2\,\mathrm{dB}$.

Furthermore, different types of receivers are considered: Joint *Minimum Mean-Square Error* (MMSE) estimation using symbols from both branches is proposed while usually separate estimation in both branches is employed. It is shown that, for statistically independent quantization levels and quantization errors, separate MMSE estimation yields the same performance as joint MMSE estimation. Even very sophisticated transmission concepts, such as iterative source-channel decoding for digital transmission systems can be extended to HDA transmission by using the received analog symbols as additional side information in the iterative decoding process.

In HDA transmission, the separation into a digital and an analog branch offers several new degrees of freedom in the design: The transmission power of both branches can be distributed optimally to yield more flexibility in the design. Also continuous-amplitude systems adding redundancy, such as Archimedes spirals or AMBCs lead to further gains in terms of pSNR, if the additional channel uses cannot be utilized by the digital branch. Combining a purely digital system with a 1:2 Archimedes spiral yields, e.g., a gain of 29 dB in terms of pSNR at $\mathrm{cSNR}|_{\mathrm{dB}} = 20\,\mathrm{dB}$, adding a 1:4 AMBC in the analog branch yields a gain of even 37 dB.

When using digital transmission systems with channel codes which are not capacity achieving, e.g., due to short block lengths, the HDA system can be designed with a lower channel coding rate in the digital branch compared to the purely digital system yielding a “waterfall” at lower channel qualities. Thus, without increasing the complexity or using an enhanced design of the digital channel code, the waterfall region can be shifted to lower channel qualities while the pSNR is still superior. Using, e.g., a convolutional code, the HDA system lowers the channel quality for successful transmission by 1 dB in terms of cSNR.

Initially, HDA transmission has been intended for scenarios without feedback of the current channel quality measured at the receiver. But, as HDA transmission outperforms purely digital systems, the concept is also an interesting candidate for AMR transmission with feedback. Different quantizer resolutions are considered leading to different "modes" which could compose a potential AMR system. For the turbo coding example, it is shown that the overall performance of an AMR system using HDA transmission is improved by, e.g., up to 3 dB in terms of pSNR.

The comparisons demonstrate the superiority of HDA transmission systems for all channel qualities with the advantage of an improved performance for rising channel qualities.

Furthermore, the application of the HDA concept to the transmission of correlated source symbols is evaluated. A block transform performs a decorrelation while the transform coefficients are transmitted the HDA concept. As in a purely digital system, the correlation can be exploited with the additional benefits of HDA transmission showing a superior performance at all channel qualities.

Comparison of Different Systems

For the comparison of the different transmission systems discussed in this thesis, one common scenario has been specified. The Archimedes spirals can only be employed for transmitting one source symbol employing two channel symbols, while the AMBCs just operate on uniform source distributions. Linear analog transmission and HDA systems can be parametrized accordingly. Thus, a scenario with a uniform source pdf and two channel uses and source symbol is employed. As expected, the by far worst performance is obtained with the linear system. The nonlinear candidates show a significantly better performance, while the HDA and AMBC system are slightly better than the Archimedes spiral. If long block lengths are permitted, the HDA system increases its performance and outperforms all other systems. The Archimedes spiral cannot be designed for longer block lengths and different rates, while the AMBC system still has the potential for finding appropriate designs. Here, its flexibility makes HDA transmission the superior choice.

By combining both worlds – digital and analog transmission systems – new concepts emerge which fuse the advantages of both systems. These *Hybrid Digital-Analog* (HDA) transmission systems supersede purely digital concepts and are an attractive solution for wireless systems such as microphones, loudspeakers or distributed sensors.

Appendix A

Numerical Optimization Method for Compressor and Expander

A.1 System model

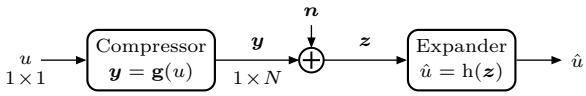

Figure A.1: General transmission system with compressor and expander function for scalar source symbols.

Figure A.1 shows the general transmission system with compressor $\boldsymbol{y} = \mathbf{g}(u)$ and expander $\hat{u} = \mathrm{h}(\boldsymbol{z})$. In [Aky11] an approach for a numerical optimization of the compressor and expander function has been proposed which alternates between optimizing the expander for a given compressor and then optimizing the compressor for the given expander until convergence is reached.

Here, the steps of the optimization are elaborated in more detail. The special cases of $M = 1$ with $N = 1$ and $N = 2$ are explicitly considered and the discretized versions of the formulas are given.

A.2 Optimal Expander h for a Given Compressor g

For a given compressor function $\mathbf{g}$, the best expander function h in terms of *Mean-Square Error* (MSE) is a function which facilitates *Minimum Mean-Square Error* (MMSE) estimation. The MMSE estimator is the conditional expectation of the received values:

$$\hat{u} = \mathrm{h}(\boldsymbol{z}) = \mathrm{E}\{u|\boldsymbol{z}\} \tag{A.1}$$

$$= \int u \cdot \mathrm{p}_{\mathcal{U}|\boldsymbol{\mathcal{Z}}}(u|\boldsymbol{z})\,\mathrm{d}u. \tag{A.2}$$

Bayes' rule yields:

$$\mathrm{p}_{\mathcal{U}|\boldsymbol{\mathcal{Z}}}(u|\boldsymbol{z}) = \frac{\mathrm{p}_{\boldsymbol{\mathcal{Z}}|\mathcal{U}}(\boldsymbol{z}|u) \cdot \mathrm{p}_{\mathcal{U}}(u)}{\mathrm{p}_{\boldsymbol{\mathcal{Z}}}(\boldsymbol{z})} = \frac{\mathrm{p}_{\boldsymbol{\mathcal{Z}}|\mathcal{U}}(\boldsymbol{z}|u) \cdot \mathrm{p}_{\mathcal{U}}(u)}{\int \mathrm{p}_{\boldsymbol{\mathcal{Z}}|\mathcal{U}}(\boldsymbol{z}|u) \cdot \mathrm{p}_{\mathcal{U}}(u)\,\mathrm{d}u}. \tag{A.3}$$

Since additive noise is used, the channel transition probability can be easily stated in terms of the noise *probability density function* (pdf):

$$\mathrm{p}_{\boldsymbol{\mathcal{Z}}|\mathcal{U}}(\boldsymbol{z}|u) = \mathrm{p}_{\boldsymbol{\mathcal{N}}}(\boldsymbol{z} - \boldsymbol{y}) = \mathrm{p}_{\boldsymbol{\mathcal{N}}}(\boldsymbol{z} - \mathbf{g}(u)). \tag{A.4}$$

Plugging everything together yields the expander function for any received vector $\boldsymbol{z}$:

$$\mathrm{h}(\boldsymbol{z}) = \frac{\int u \cdot \mathrm{p}_{\boldsymbol{\mathcal{N}}}(\boldsymbol{z} - \mathbf{g}(u)) \cdot \mathrm{p}_{\mathcal{U}}(u)\,\mathrm{d}u}{\int \mathrm{p}_{\boldsymbol{\mathcal{N}}}(\boldsymbol{z} - \mathbf{g}(u)) \cdot \mathrm{p}_{\mathcal{U}}(u)\,\mathrm{d}u}. \tag{A.5}$$

In a practical implementation the above integrals have to be discretized using sums. One possibility is an approximation which sums over rectangles with the width Δ_γ at discrete points γ_i, if it is integrated over γ. The width of the rectangles and the range of values γ_i over which the sum is taken has to be carefully chosen to avoid large numerical errors and hence significant differences to a description with integrals.

In case of a compander with $M = 1$ and $N = 1$, the optimal expander for a given compressor can be calculated as:

$$\mathrm{h}(z) = \frac{\sum_i u_i \cdot \mathrm{p}_{\mathcal{N}}(z - \mathrm{g}(u_i)) \cdot \mathrm{p}_{\mathcal{U}}(u_i) \cdot \Delta_u}{\sum_i \mathrm{p}_{\mathcal{N}}(z - \mathrm{g}(u_i)) \cdot \mathrm{p}_{\mathcal{U}}(u_i) \cdot \Delta_u} = \frac{\sum_i u_i \cdot \mathrm{p}_{\mathcal{N}}(z - \mathrm{g}(u_i)) \cdot \mathrm{p}_{\mathcal{U}}(u_i)}{\sum_i \mathrm{p}_{\mathcal{N}}(z - \mathrm{g}(u_i)) \cdot \mathrm{p}_{\mathcal{U}}(u_i)}. \tag{A.6}$$

In case of using $M = 1$ and $N = 2$, two compressor functions, namely g_1 and g_2 are employed which yield the following expression as the optimal expander:

$$\mathrm{h}(z_1, z_2) = \frac{\sum_i u_i \cdot \mathrm{p}_{\mathcal{N}}(z_1 - \mathrm{g}_1(u_i)) \cdot \mathrm{p}_{\mathcal{N}}(z_2 - \mathrm{g}_2(u_i)) \cdot \mathrm{p}_{\mathcal{U}}(u_i)}{\sum_i \mathrm{p}_{\mathcal{N}}(z_1 - \mathrm{g}_1(u_i)) \cdot \mathrm{p}_{\mathcal{N}}(z_2 - \mathrm{g}_2(u_i)) \cdot \mathrm{p}_{\mathcal{U}}(u_i)}. \tag{A.7}$$

A.3 Optimal Compressor g for a Given Expander h

For a given expander function h, the best compressor function $\mathbf{g}$ in terms of MSE cannot be stated in a closed form expression as in the section above. Instead, a different approach is used which allows for a successive approximation of the optimal compressor function.

The aim is to find the best compressor function $\mathbf{g}$ for a given expander function h while the optimization criterion is the MSE:

$$\begin{aligned} D(\mathbf{g}, \mathrm{h}) &= \mathrm{E}\{(u - \hat{u})^2\} \\ &= \int_{\mathbb{R}^N} \int (u - \mathrm{h}\left(\mathbf{g}(u) + \boldsymbol{n}\right))^2 \cdot \mathrm{p}(u) \cdot \mathrm{p}(\boldsymbol{n})\,\mathrm{d}u\,\mathrm{d}\boldsymbol{n}. \end{aligned} \tag{A.8}$$

A second figure of merit is the power used for transmission which shall be as small as possible:

$$P(\mathbf{g}) = \frac{1}{N} \cdot \mathrm{E}\{||\boldsymbol{y}||^2\} = \frac{1}{N} \cdot \mathrm{E}\{\boldsymbol{y}\boldsymbol{y}^{\mathrm{T}}\} = \frac{1}{N} \cdot \int \mathbf{g}(u) \cdot \mathbf{g}(u)^{\mathrm{T}} \cdot \mathrm{p}(u)\,\mathrm{d}u. \quad \text{(A.9)}$$

Since the MSE and the power depend on each other, a compromise has to be found which can be facilitated using a Lagrangian cost functional. The variable P_T defines the power which should be achieved by $P(\mathbf{g})$, but P_T will vanish after deriving $J(\mathbf{g})$ anyway:

$$J(\mathbf{g}) = D(\mathbf{g}) + \lambda \cdot (P(\mathbf{g}) - P_T)\,. \quad \text{(A.10)}$$

Instead of optimizing the MSE and the transmission power independently, now, $J(\mathbf{g})$ can be minimized in order to optimize both figures of merit jointly. For that, the noise variance of n is set to 1 and, thus, the channel quality is governed by the transmission power P. The variable λ weights the importance between the transmission power and the MSE which leads to different operating points and, thus, different channel qualities of the transmission system. A small λ gives the MSE a high importance and hence decreases the MSE with the cost of a higher transmission power and therefore a higher channel quality. A high λ weights the transmission power higher and, thus, decreases the same which results in an increased MSE at a lower channel quality.

For a fixed λ, the channel quality can also be varied by choosing a noise pdf with a higher variance. A higher noise variance then yields a higher MSE at a lower channel quality.

A.3.1 1:2 Dimensional Expander

For $M = 1$ and $N = 2$, the terms for the transmission power and the MSE can be stated explicitly without vector integrals as follows:

$$P(\mathbf{g}) = \frac{1}{2} \cdot \int \left(\mathrm{g}_1(u)^2 + \mathrm{g}_2(u)^2\right) \cdot \mathrm{p}(u)\,\mathrm{d}u, \quad \text{(A.11)}$$

$$D(\mathbf{g}) = \iiint \left(u - \mathrm{h}\left(\mathrm{g}_1(u) + n_1, \mathrm{g}_2(u) + n_2\right)\right)^2 \cdot \mathrm{p}(u) \cdot \mathrm{p}(n_1) \cdot \mathrm{p}(n_2)\,\mathrm{d}u\,\mathrm{d}n_1\,\mathrm{d}n_2. \quad \text{(A.12)}$$

As in Section A.2, the integrals can be discretized with Δ_n and Δ_u as the width of the integration rectangles of the integration over n and u:

$$P(\mathbf{g}) = \frac{1}{2} \cdot \sum_i \left(\mathrm{g}_1(u_i)^2 + \mathrm{g}_2(u_i)^2\right) \cdot \mathrm{p}(u_i) \cdot \Delta_u, \quad \text{(A.13)}$$

$$D(\mathbf{g}) = \sum_{j_1} \sum_{j_2} \sum_i \left(u_i - \mathrm{h}\left(\mathrm{g}_1(u_i) + n_{j_1}, \mathrm{g}_2(u_i) + n_{j_2}\right)\right)^2 \cdot \mathrm{p}(u_i) \cdot \mathrm{p}(n_{j_1}) \cdot \mathrm{p}(n_{j_2}) \cdot \Delta_u \cdot \Delta_n^2. \quad \text{(A.14)}$$

One possibility to minimize $J(\mathbf{g})$ in (A.10) is using the steepest decent method [ARR10, BV04] which requires the derivative with respect of each variable which can be varied to find the optimum solution. After the above discretization, the compressor function $\mathbf{g}$ is defined at the discrete points u_k. At each point, the compressor function for each of the two channel dimensions can be optimized and, thus, the derivative is taken with respect to all points u_k. The derivative of $J(\mathbf{g})$ with respect to the points of the first compressor function g_1 is:

$$\begin{aligned}\frac{\partial J(\mathbf{g})}{\partial \mathrm{g}_1(u_k)} =& \frac{\partial}{\partial \mathrm{g}_1(u_k)} \Bigg[\sum_{j_1} \sum_{j_2} \sum_{i} \left(u_i - \mathrm{h}\left(\mathrm{g}_1(u_i) + n_{j_1}, \mathrm{g}_2(u_i) + n_{j_2}\right)\right)^2 \\ & \qquad \cdot \mathrm{p}(u_i) \cdot \mathrm{p}(n_{j_1}) \cdot \mathrm{p}(n_{j_2}) \cdot \Delta_u \cdot \Delta_n^2 \Bigg] \\ & + \lambda \frac{\partial}{\partial \mathrm{g}_1(u_k)} \left[\frac{1}{2} \cdot \sum_i \left(\mathrm{g}_1(u_i)^2 + \mathrm{g}_2(u_i)^2\right) \cdot \mathrm{p}(u_i) \cdot \Delta_u - P_T \right] \end{aligned} \tag{A.15}$$

$$\begin{aligned} =& \sum_{j_1} \sum_{j_2} \sum_{i} \Bigg[2 \cdot \left(u_i - \mathrm{h}\left(\mathrm{g}_1(u_i) + n_{j_1}, \mathrm{g}_2(u_i) + n_{j_2}\right)\right) \cdot (-1) \\ & \qquad \cdot \mathrm{h}^{'(1)}\left(\mathrm{g}_1(u_i) + n_{j_1}, \mathrm{g}_2(u_i) + n_{j_2}\right) \cdot \frac{\partial \mathrm{g}_1(u_i)}{\partial \mathrm{g}_1(u_k)} \\ & \qquad \cdot \mathrm{p}(u_i) \cdot \mathrm{p}(n_{j_1}) \cdot \mathrm{p}(n_{j_2}) \cdot \Delta_u \cdot \Delta_n^2 \Bigg] \\ & + \lambda \cdot \frac{1}{2} \cdot \sum_i 2 \cdot \mathrm{g}_1(u_i) \cdot \frac{\partial \mathrm{g}_1(u_i)}{\partial \mathrm{g}_1(u_k)} \cdot \mathrm{p}(u_i) \cdot \Delta_u. \end{aligned} \tag{A.16}$$

The term $\mathrm{h}^{'(1)}$ is the derivative of h with respect to the first argument. Since

$$\frac{\partial \mathrm{g}_1(u_i)}{\partial \mathrm{g}_1(u_k)} = \begin{cases} 1 & \text{for } i = k \\ 0 & \text{for } i \neq k \end{cases}, \tag{A.17}$$

the above equation can be simplified as:

$$\begin{aligned}\frac{\partial J(\mathbf{g})}{\partial \mathrm{g}_1(u_k)} =& \sum_{j_1} \sum_{j_2} \Bigg[-2 \cdot \left(u_k - \mathrm{h}\left(\mathrm{g}_1(u_k) + n_{j_1}, \mathrm{g}_2(u_k) + n_{j_2}\right)\right) \\ & \qquad \cdot \mathrm{h}^{'(1)}\left(\mathrm{g}_1(u_k) + n_{j_1}, \mathrm{g}_2(u_k) + n_{j_2}\right) \\ & \qquad \cdot \mathrm{p}(u_k) \cdot \mathrm{p}(n_{j_1}) \cdot \mathrm{p}(n_{j_2}) \cdot \Delta_u \cdot \Delta_n^2 \Bigg] \\ & + \lambda \cdot \mathrm{g}_1(u_k) \cdot \mathrm{p}(u_k) \cdot \Delta_u. \end{aligned} \tag{A.18}$$

With $\mathrm{h}^{'(2)}$ as the derivative of h with respect to the second argument, the derivative of the derivative of $J(\mathbf{g})$ with respect to the points of the second compressor function g_2 is:

$$\begin{aligned}\frac{\partial J(\mathbf{g})}{\partial\, \mathrm{g}_2(u_k)} = \sum_{j_1}\sum_{j_2} \Big[& -2 \cdot (u_k - \mathrm{h}\,(\mathrm{g}_1(u_k) + n_{j_1}, \mathrm{g}_2(u_k) + n_{j_2})) \\ & \cdot \mathrm{h}^{'(2)}\,(\mathrm{g}_1(u_k) + n_{j_1}, \mathrm{g}_2(u_k) + n_{j_2}) \\ & \cdot \mathrm{p}(u_k) \cdot \mathrm{p}(n_{j_1}) \cdot \mathrm{p}(n_{j_2}) \cdot \Delta_u \cdot \Delta_n^2 \Big] \\ & + \lambda \cdot \mathrm{g}_2(u_k) \cdot \mathrm{p}(u_k) \cdot \Delta_u. \end{aligned} \tag{A.19}$$

The steepest decent method updates each variable successively. In each step, the derivative of the target function with respect to one variable is calculated, weighted with the step size μ and subtracted from the current variable to yield the updated variable. For both compressor functions, this can be stated as follows:

$$\mathrm{g}_1^{\text{updated}}(u_k) = \mathrm{g}_1^{\text{current}}(u_k) - \mu \cdot \frac{\partial J(\mathbf{g}^{\text{current}})}{\partial\, \mathrm{g}_1(u_k)}, \tag{A.20}$$

$$\mathrm{g}_2^{\text{updated}}(u_k) = \mathrm{g}_2^{\text{current}}(u_k) - \mu \cdot \frac{\partial J(\mathbf{g}^{\text{current}})}{\partial\, \mathrm{g}_2(u_k)}. \tag{A.21}$$

A.3.2 1:1 Dimensional Expander

The above formulas can also be stated for the case of $M = 1$ and $N = 1$. The transmission power and the MSE can be stated in their discretized form as:

$$P(\mathrm{g}) = \sum_i \mathrm{g}(u_i)^2 \cdot \mathrm{p}(u_i) \cdot \Delta_u, \tag{A.22}$$

$$D(\mathrm{g}) = \sum_j \sum_i (u_i - \mathrm{h}\,(\mathrm{g}(u_i) + n_j))^2 \cdot \mathrm{p}(u_i) \cdot \mathrm{p}(n_j) \cdot \Delta_u \cdot \Delta_n. \tag{A.23}$$

The derivative of $J(\mathrm{g})$ with respect to the points of the first compressor function g is:

$$\begin{aligned}\frac{\partial J(\mathrm{g})}{\partial\, \mathrm{g}(u_k)} = \sum_j [& -2 \cdot (u_k - \mathrm{h}\,(\mathrm{g}(u_k) + n_j)) \cdot \mathrm{h}^{'}\,(\mathrm{g}(u_k) + n_j) \\ & \cdot \mathrm{p}(u_k) \cdot \mathrm{p}(n_j) \cdot \Delta_u \cdot \Delta_n\ ] \\ & + 2 \cdot \lambda \cdot \mathrm{g}(u_k) \cdot \mathrm{p}(u_k) \cdot \Delta_u. \end{aligned} \tag{A.24}$$

The function $\mathrm{h}^{'}$ is again the derivative of h with respect to the argument. The update formula for the steepest decent method is then:

$$\mathrm{g}^{\text{updated}}(u_k) = \mathrm{g}^{\text{current}}(u_k) - \mu \frac{\partial J(\mathrm{g}^{\text{current}})}{\partial\, \mathrm{g}(u_k)}. \tag{A.25}$$

Appendix B

Joint MMSE Estimator for HDA transmission

B.1 Derivation of Joint Estimator

The joint MMSE estimator (6.19) of $\boldsymbol{u}$ for the received values $\boldsymbol{z}^{\mathrm{d}}$ and $\boldsymbol{z}^{\mathrm{a}}$ in the digital and the analog branch, respectively, is derived. The constant C is $C = \mathrm{p}(\boldsymbol{z}^{\mathrm{a}}, \boldsymbol{z}^{\mathrm{d}})$ and the step from (B.3) to (B.4) is detailed below[1].

$$
\begin{aligned}
\hat{\boldsymbol{u}} &= \mathrm{E}\{\boldsymbol{u}|\boldsymbol{z}^{\mathrm{a}}, \boldsymbol{z}^{\mathrm{d}}\} && \text{(B.1)}\\
&= \int \boldsymbol{u} \cdot \mathrm{p}(\boldsymbol{u}|\boldsymbol{z}^{\mathrm{a}}, \boldsymbol{z}^{\mathrm{d}})\,\mathrm{d}\boldsymbol{u}\\
&= \iint (\boldsymbol{u}^{\mathrm{d}} + \boldsymbol{u}^{\mathrm{a}}) \cdot \mathrm{p}(\boldsymbol{u}^{\mathrm{a}}, \boldsymbol{u}^{\mathrm{d}}|\boldsymbol{z}^{\mathrm{a}}, \boldsymbol{z}^{\mathrm{d}})\,\mathrm{d}\boldsymbol{u}^{\mathrm{d}}\,\mathrm{d}\boldsymbol{u}^{\mathrm{a}} && \text{(B.2)}\\
&= \int \boldsymbol{u}^{\mathrm{a}} \int \mathrm{p}(\boldsymbol{u}^{\mathrm{a}}, \boldsymbol{u}^{\mathrm{d}}|\boldsymbol{z}^{\mathrm{a}}, \boldsymbol{z}^{\mathrm{d}})\,\mathrm{d}\boldsymbol{u}^{\mathrm{d}}\,\mathrm{d}\boldsymbol{u}^{\mathrm{a}} + \int \boldsymbol{u}^{\mathrm{d}} \int \mathrm{p}(\boldsymbol{u}^{\mathrm{a}}, \boldsymbol{u}^{\mathrm{d}}|\boldsymbol{z}^{\mathrm{a}}, \boldsymbol{z}^{\mathrm{d}})\,\mathrm{d}\boldsymbol{u}^{\mathrm{a}}\,\mathrm{d}\boldsymbol{u}^{\mathrm{d}}\\
&= \int \boldsymbol{u}^{\mathrm{a}} \cdot \mathrm{p}(\boldsymbol{u}^{\mathrm{a}}|\boldsymbol{z}^{\mathrm{a}}, \boldsymbol{z}^{\mathrm{d}})\,\mathrm{d}\boldsymbol{u}^{\mathrm{a}} + \int \boldsymbol{u}^{\mathrm{d}} \cdot \mathrm{p}(\boldsymbol{u}^{\mathrm{d}}|\boldsymbol{z}^{\mathrm{a}}, \boldsymbol{z}^{\mathrm{d}})\,\mathrm{d}\boldsymbol{u}^{\mathrm{d}}\\
&= \frac{1}{C} \int \boldsymbol{u}^{\mathrm{a}} \cdot \mathrm{p}(\boldsymbol{z}^{\mathrm{a}}, \boldsymbol{z}^{\mathrm{d}}, \boldsymbol{u}^{\mathrm{a}})\,\mathrm{d}\boldsymbol{u}^{\mathrm{a}} + \frac{1}{C} \int \boldsymbol{u}^{\mathrm{d}} \cdot \mathrm{p}(\boldsymbol{z}^{\mathrm{d}}, \boldsymbol{z}^{\mathrm{a}}, \boldsymbol{u}^{\mathrm{d}})\,\mathrm{d}\boldsymbol{u}^{\mathrm{d}}\\
&= \frac{1}{C} \int \boldsymbol{u}^{\mathrm{a}} \cdot \mathrm{p}(\boldsymbol{z}^{\mathrm{a}}|\boldsymbol{z}^{\mathrm{d}}, \boldsymbol{u}^{\mathrm{a}}) \cdot \mathrm{p}(\boldsymbol{z}^{\mathrm{d}}|\boldsymbol{u}^{\mathrm{a}}) \cdot \mathrm{p}(\boldsymbol{u}^{\mathrm{a}})\,\mathrm{d}\boldsymbol{u}^{\mathrm{a}}\\
&\quad + \frac{1}{C} \int \boldsymbol{u}^{\mathrm{d}} \cdot \mathrm{p}(\boldsymbol{z}^{\mathrm{d}}|\boldsymbol{z}^{\mathrm{a}}, \boldsymbol{u}^{\mathrm{d}}) \cdot \mathrm{p}(\boldsymbol{z}^{\mathrm{a}}|\boldsymbol{u}^{\mathrm{d}}) \cdot \mathrm{p}(\boldsymbol{u}^{\mathrm{d}})\,\mathrm{d}\boldsymbol{u}^{\mathrm{d}} && \text{(B.3)}\\
&= \frac{1}{C} \int \boldsymbol{u}^{\mathrm{a}} \cdot \mathrm{p}(\boldsymbol{z}^{\mathrm{a}}|\boldsymbol{u}^{\mathrm{a}}) \cdot \mathrm{p}(\boldsymbol{z}^{\mathrm{d}}|\boldsymbol{u}^{\mathrm{a}}) \cdot \mathrm{p}(\boldsymbol{u}^{\mathrm{a}})\,\mathrm{d}\boldsymbol{u}^{\mathrm{a}}\\
&\quad + \frac{1}{C} \sum_{\boldsymbol{u}^{\mathrm{d}}} \boldsymbol{u}^{\mathrm{d}} \cdot \mathrm{p}(\boldsymbol{z}^{\mathrm{d}}|\boldsymbol{u}^{\mathrm{d}}) \cdot \mathrm{p}(\boldsymbol{z}^{\mathrm{a}}|\boldsymbol{u}^{\mathrm{d}}) \cdot \mathrm{P}(\boldsymbol{u}^{\mathrm{d}}). && \text{(B.4)}
\end{aligned}
$$

[1] To improve readability, the index H is omitted in this Appendix.

Changing the integral to the sum from (B.3) to (B.4) is possible, since $\mathrm{p}(\boldsymbol{u}^{\mathrm{d}})$ is composed of a series of diracs weighted by the probability of occurrence of the quantization levels $\mathrm{P}(\tilde{\boldsymbol{u}}^{\mathrm{d}})$:

$$\mathrm{p}(\boldsymbol{u}^{\mathrm{d}}) = \sum_{\tilde{\boldsymbol{u}}^{\mathrm{d}}} \delta(\tilde{\boldsymbol{u}}^{\mathrm{d}} - \boldsymbol{u}^{\mathrm{d}}) \mathrm{P}(\tilde{\boldsymbol{u}}^{\mathrm{d}}). \tag{B.5}$$

The fact that $\boldsymbol{z}^{\mathrm{a}}$ is independent from $\boldsymbol{z}^{\mathrm{d}}$ if $\boldsymbol{u}^{\mathrm{a}}$ is given ((B.3) to (B.4)), is detailed below. The step from (B.6) to (B.7) can be derived using the observation that some variables are connected by two Markov chains: $\boldsymbol{u} \to \boldsymbol{u}^{\mathrm{d}} \to \boldsymbol{z}^{\mathrm{d}}$ and $\boldsymbol{u} \to \boldsymbol{u}^{\mathrm{a}} \to \boldsymbol{z}^{\mathrm{a}}$. Then, the local Markov property is satisfied: each variable is conditionally independent of its non-descendants given its parent variables [NI03].

$$\begin{aligned}
\mathrm{p}(\boldsymbol{z}^{\mathrm{a}}|\boldsymbol{z}^{\mathrm{d}}, \boldsymbol{u}^{\mathrm{a}}) &= \frac{\mathrm{p}(\boldsymbol{z}^{\mathrm{a}}, \boldsymbol{z}^{\mathrm{d}}, \boldsymbol{u}^{\mathrm{a}})}{\mathrm{p}(\boldsymbol{z}^{\mathrm{d}}, \boldsymbol{u}^{\mathrm{a}})} \\
&= \frac{\iint \mathrm{p}(\boldsymbol{z}^{\mathrm{d}}, \boldsymbol{z}^{\mathrm{a}}, \boldsymbol{u}^{\mathrm{d}}, \boldsymbol{u}^{\mathrm{a}}, \boldsymbol{u}) \,\mathrm{d}\boldsymbol{u}\,\mathrm{d}\boldsymbol{u}^{\mathrm{d}}}{\iiint \mathrm{p}(\boldsymbol{z}^{\mathrm{d}}, \boldsymbol{z}^{\mathrm{a}}, \boldsymbol{u}^{\mathrm{d}}, \boldsymbol{u}^{\mathrm{a}}, \boldsymbol{u}) \,\mathrm{d}\boldsymbol{u}\,\mathrm{d}\boldsymbol{u}^{\mathrm{d}}\,\mathrm{d}\boldsymbol{z}^{\mathrm{a}}} \qquad \text{(B.6)} \\
&= \frac{\iint \mathrm{p}(\boldsymbol{u}) \cdot \mathrm{p}(\boldsymbol{u}^{\mathrm{a}}|\boldsymbol{u}) \cdot \mathrm{p}(\boldsymbol{u}^{\mathrm{d}}|\boldsymbol{u}) \cdot \mathrm{p}(\boldsymbol{z}^{\mathrm{a}}|\boldsymbol{u}^{\mathrm{a}}) \cdot \mathrm{p}(\boldsymbol{z}^{\mathrm{d}}|\boldsymbol{u}^{\mathrm{d}}) \,\mathrm{d}\boldsymbol{u}\,\mathrm{d}\boldsymbol{u}^{\mathrm{d}}}{\iiint \mathrm{p}(\boldsymbol{u}) \cdot \mathrm{p}(\boldsymbol{u}^{\mathrm{a}}|\boldsymbol{u}) \cdot \mathrm{p}(\boldsymbol{u}^{\mathrm{d}}|\boldsymbol{u}) \cdot \mathrm{p}(\boldsymbol{z}^{\mathrm{a}}|\boldsymbol{u}^{\mathrm{a}}) \cdot \mathrm{p}(\boldsymbol{z}^{\mathrm{d}}|\boldsymbol{u}^{\mathrm{d}}) \,\mathrm{d}\boldsymbol{u}\,\mathrm{d}\boldsymbol{u}^{\mathrm{d}}\,\mathrm{d}\boldsymbol{z}^{\mathrm{a}}} \qquad \text{(B.7)} \\
&= \frac{\iint \mathrm{p}(\boldsymbol{u}) \cdot \mathrm{p}(\boldsymbol{u}^{\mathrm{a}}|\boldsymbol{u}) \cdot \mathrm{p}(\boldsymbol{u}^{\mathrm{d}}|\boldsymbol{u}) \cdot \mathrm{p}(\boldsymbol{z}^{\mathrm{d}}|\boldsymbol{u}^{\mathrm{d}}) \,\mathrm{d}\boldsymbol{u}\,\mathrm{d}\boldsymbol{u}^{\mathrm{d}} \cdot \mathrm{p}(\boldsymbol{z}^{\mathrm{a}}|\boldsymbol{u}^{\mathrm{a}})}{\int \iint \mathrm{p}(\boldsymbol{u}) \cdot \mathrm{p}(\boldsymbol{u}^{\mathrm{a}}|\boldsymbol{u}) \cdot \mathrm{p}(\boldsymbol{u}^{\mathrm{d}}|\boldsymbol{u}) \cdot \mathrm{p}(\boldsymbol{z}^{\mathrm{d}}|\boldsymbol{u}^{\mathrm{d}}) \,\mathrm{d}\boldsymbol{u}\,\mathrm{d}\boldsymbol{u}^{\mathrm{d}} \cdot \mathrm{p}(\boldsymbol{z}^{\mathrm{a}}|\boldsymbol{u}^{\mathrm{a}}) \,\mathrm{d}\boldsymbol{z}^{\mathrm{a}}} \\
&= \frac{\mathrm{p}(\boldsymbol{z}^{\mathrm{a}}|\boldsymbol{u}^{\mathrm{a}})}{\int \mathrm{p}(\boldsymbol{z}^{\mathrm{a}}|\boldsymbol{u}^{\mathrm{a}}) \,\mathrm{d}\boldsymbol{z}^{\mathrm{a}}} \\
&= \mathrm{p}(\boldsymbol{z}^{\mathrm{a}}|\boldsymbol{u}^{\mathrm{a}}). \qquad \text{(B.8)}
\end{aligned}$$

The same can be stated for:

$$\mathrm{p}(\boldsymbol{z}^{\mathrm{d}}|\boldsymbol{z}^{\mathrm{a}}, \boldsymbol{u}^{\mathrm{d}}) = \ldots = \mathrm{p}(\boldsymbol{z}^{\mathrm{d}}|\boldsymbol{u}^{\mathrm{d}}). \tag{B.9}$$

B.2 Estimator for Statistical Independence

For statistical independence between quantized values $\boldsymbol{u}^{\mathrm{d}}$ and the quantization error $\boldsymbol{u}^{\mathrm{a}}$ the following relation holds (6.20):

$$\mathrm{p}(\boldsymbol{u}^{\mathrm{a}}, \boldsymbol{u}^{\mathrm{d}}) = \mathrm{p}(\boldsymbol{u}^{\mathrm{a}}) \cdot \mathrm{p}(\boldsymbol{u}^{\mathrm{d}}). \tag{B.10}$$

Then, the cross terms $\mathrm{p}(\boldsymbol{z}^{\mathrm{d}}|\boldsymbol{u}^{\mathrm{a}})$ and $\mathrm{p}(\boldsymbol{z}^{\mathrm{a}}|\boldsymbol{u}^{\mathrm{d}})$ in (B.4) simplify to

$$\begin{aligned}
\mathrm{p}(\boldsymbol{z}^{\mathrm{d}}|\boldsymbol{u}^{\mathrm{a}}) &= \frac{\mathrm{p}(\boldsymbol{z}^{\mathrm{d}}, \boldsymbol{u}^{\mathrm{a}})}{\mathrm{p}(\boldsymbol{u}^{\mathrm{a}})} \\
&= \frac{\iint \mathrm{p}(\boldsymbol{z}^{\mathrm{d}}, \boldsymbol{u}^{\mathrm{a}}, \boldsymbol{u}^{\mathrm{d}}, \boldsymbol{u})\,\mathrm{d}\boldsymbol{u}\,\mathrm{d}\boldsymbol{u}^{\mathrm{d}}}{\iiint \mathrm{p}(\boldsymbol{z}^{\mathrm{d}}, \boldsymbol{u}^{\mathrm{a}}, \boldsymbol{u}^{\mathrm{d}}, \boldsymbol{u})\,\mathrm{d}\boldsymbol{u}\,\mathrm{d}\boldsymbol{u}^{\mathrm{d}}\,\mathrm{d}\boldsymbol{z}^{\mathrm{d}}} \\
&= \frac{\iint \mathrm{p}(\boldsymbol{u}) \cdot \mathrm{p}(\boldsymbol{u}^{\mathrm{d}}|\boldsymbol{u}) \cdot \mathrm{p}(\boldsymbol{u}^{\mathrm{a}}|\boldsymbol{u}) \cdot \mathrm{p}(\boldsymbol{z}^{\mathrm{d}}|\boldsymbol{u}^{\mathrm{d}})\,\mathrm{d}\boldsymbol{u}\,\mathrm{d}\boldsymbol{u}^{\mathrm{d}}}{\iiint \mathrm{p}(\boldsymbol{u}) \cdot \mathrm{p}(\boldsymbol{u}^{\mathrm{d}}|\boldsymbol{u}) \cdot \mathrm{p}(\boldsymbol{u}^{\mathrm{a}}|\boldsymbol{u}) \cdot \mathrm{p}(\boldsymbol{z}^{\mathrm{d}}|\boldsymbol{u}^{\mathrm{d}})\,\mathrm{d}\boldsymbol{u}\,\mathrm{d}\boldsymbol{u}^{\mathrm{d}}\,\mathrm{d}\boldsymbol{z}^{\mathrm{d}}} \\
&= \frac{\iint \mathrm{p}(\boldsymbol{u}, \boldsymbol{u}^{\mathrm{d}}, \boldsymbol{u}^{\mathrm{a}}) \cdot \mathrm{p}(\boldsymbol{z}^{\mathrm{d}}|\boldsymbol{u}^{\mathrm{d}})\,\mathrm{d}\boldsymbol{u}\,\mathrm{d}\boldsymbol{u}^{\mathrm{d}}}{\iiint \mathrm{p}(\boldsymbol{u}, \boldsymbol{u}^{\mathrm{d}}, \boldsymbol{u}^{\mathrm{a}}) \cdot \mathrm{p}(\boldsymbol{z}^{\mathrm{d}}|\boldsymbol{u}^{\mathrm{d}})\,\mathrm{d}\boldsymbol{u}\,\mathrm{d}\boldsymbol{u}^{\mathrm{d}}\,\mathrm{d}\boldsymbol{z}^{\mathrm{d}}} \\
&= \frac{\int \mathrm{p}(\boldsymbol{u}^{\mathrm{d}}, \boldsymbol{u}^{\mathrm{a}}) \cdot \mathrm{p}(\boldsymbol{z}^{\mathrm{d}}|\boldsymbol{u}^{\mathrm{d}})\,\mathrm{d}\boldsymbol{u}^{\mathrm{d}}}{\iint \mathrm{p}(\boldsymbol{u}^{\mathrm{d}}, \boldsymbol{u}^{\mathrm{a}}) \cdot \mathrm{p}(\boldsymbol{z}^{\mathrm{d}}|\boldsymbol{u}^{\mathrm{d}})\,\mathrm{d}\boldsymbol{u}^{\mathrm{d}}\,\mathrm{d}\boldsymbol{z}^{\mathrm{d}}} \\
&\overset{\text{(B.10)}}{=} \frac{\mathrm{p}(\boldsymbol{u}^{\mathrm{a}}) \int \mathrm{p}(\boldsymbol{z}^{\mathrm{d}}, \boldsymbol{u}^{\mathrm{d}})\,\mathrm{d}\boldsymbol{u}^{\mathrm{d}}}{\mathrm{p}(\boldsymbol{u}^{\mathrm{a}}) \iint \mathrm{p}(\boldsymbol{z}^{\mathrm{d}}, \boldsymbol{u}^{\mathrm{d}})\,\mathrm{d}\boldsymbol{u}^{\mathrm{d}}\,\mathrm{d}\boldsymbol{z}^{\mathrm{d}}} \\
&= \mathrm{p}(\boldsymbol{z}^{\mathrm{d}}), \qquad \text{(B.11)}
\end{aligned}$$

and

$$\mathrm{p}(\boldsymbol{z}^{\mathrm{a}}|\boldsymbol{u}^{\mathrm{d}}) = \ldots = \mathrm{p}(\boldsymbol{z}^{\mathrm{a}}). \qquad \text{(B.12)}$$

Due to the independence of $\boldsymbol{u}^{\mathrm{a}}$ and $\boldsymbol{u}^{\mathrm{d}}$, the constant C can be split up into two terms:

$$C = \mathrm{p}(\boldsymbol{z}^{\mathrm{a}}, \boldsymbol{z}^{\mathrm{d}}) = \mathrm{p}(\boldsymbol{z}^{\mathrm{a}}) \cdot \mathrm{p}(\boldsymbol{z}^{\mathrm{d}}). \qquad \text{(B.13)}$$

With (B.11), (B.12) and (B.13), (B.4) can be simplified to:

$$\begin{aligned}
\hat{\boldsymbol{u}} =& \frac{1}{\mathrm{p}(\boldsymbol{z}^{\mathrm{a}}) \cdot \mathrm{p}(\boldsymbol{z}^{\mathrm{d}})} \int \boldsymbol{u}^{\mathrm{a}} \cdot \mathrm{p}(\boldsymbol{z}^{\mathrm{a}}|\boldsymbol{u}^{\mathrm{a}}) \cdot \mathrm{p}(\boldsymbol{z}^{\mathrm{d}}) \cdot \mathrm{p}(\boldsymbol{u}^{\mathrm{a}})\,\mathrm{d}\boldsymbol{u}^{\mathrm{a}} \\
&+ \frac{1}{\mathrm{p}(\boldsymbol{z}^{\mathrm{a}}) \cdot \mathrm{p}(\boldsymbol{z}^{\mathrm{d}})} \sum_{\boldsymbol{u}^{\mathrm{d}}} \boldsymbol{u}^{\mathrm{d}} \cdot \mathrm{p}(\boldsymbol{z}^{\mathrm{d}}|\boldsymbol{u}^{\mathrm{d}}) \cdot \mathrm{p}(\boldsymbol{z}^{\mathrm{a}}) \cdot \mathrm{p}(\boldsymbol{u}^{\mathrm{d}}) \\
=& \int \boldsymbol{u}^{\mathrm{a}} \cdot \mathrm{p}(\boldsymbol{u}^{\mathrm{a}}|\boldsymbol{z}^{\mathrm{a}})\,\mathrm{d}\boldsymbol{u}^{\mathrm{a}} + \sum_{\boldsymbol{u}^{\mathrm{d}}} \boldsymbol{u}^{\mathrm{d}} \cdot \mathrm{p}(\boldsymbol{u}^{\mathrm{d}}|\boldsymbol{z}^{\mathrm{d}}) \\
=& \mathrm{E}\{\boldsymbol{u}^{\mathrm{a}}|\boldsymbol{z}^{\mathrm{a}}\} + \mathrm{E}\{\boldsymbol{u}^{\mathrm{d}}|\boldsymbol{z}^{\mathrm{d}}\} \\
=& \hat{\boldsymbol{u}}^{\mathrm{a}} + \hat{\boldsymbol{u}}^{\mathrm{d}}. \qquad \text{(B.14)}
\end{aligned}$$

Thus, $\hat{\boldsymbol{u}}$ can be obtained by calculating the MMSE estimates of both branches independently and adding up the results for statistical independence between quantized values $\boldsymbol{u}^{\mathrm{d}}$ and the quantization error $\boldsymbol{u}^{\mathrm{a}}$.

Appendix C

Selection of Parameters for HDA and Purely Digital Simulations

C.1 Prerequisites

In Section 6.3.5 and in the Design Guidelines on page 105 it is derived how to construct a superior *Hybrid Digital-Analog* (HDA) transmission system for every purely digital transmission system. The key is to lower the quantization fidelity in the HDA system in order to achieve the same channel coding and modulation rates r^{ccm} and r^{ccm} in the HDA and in the digital system, respectively ($\Delta r = r^{\mathrm{ccm}} - r^{\mathrm{ccm}} = 0$).

The difference in fidelity is defined in (6.30) as

$$\Delta F = F - F, \tag{C.1}$$

and for $\Delta r = 0$ it holds:

$$\Delta F = \frac{r^{\mathrm{ccm}}}{r^{\mathrm{mapp}}} = \frac{r^{\mathrm{ccm}}}{r^{\mathrm{mapp}}}. \tag{C.2}$$

It can be seen that frequently fractional bits per symbol are needed in the quantizer which can be achieved by vector quantization or by mixing scalar quantizers with different fidelities. In any case it has to be assured that the right number of input symbols M is available to yield an *integer* number of output bits $\ell_{\boldsymbol{v}} = M \cdot F$. In some settings, the total number of quantization bits in the purely digital system is an integer. But also the case in which the total number of quantization bits in the HDA system is an integer and the corresponding purely digital system should be designed.

The transmission system is defined by the overall rate (2.3)

$$r = \frac{M}{N}, \tag{C.3}$$

and the rate of the analog mapper (6.5) in the analog branch of the HDA system:

$$r^{\mathrm{mapp}} = \frac{M}{N - D} = \frac{M}{A}. \tag{C.4}$$

The rate of the channel coding and modulation r^{ccm} is of minor importance for the following derivation. It just has to be assured that for the chosen rate and a given quantization fidelity the overall rate r can be achieved.

To choose the right M, three requirements can be found:

1. The number of channel symbols N has to be an integer.
2. The number of output bits $\ell_{\boldsymbol{v}}$ of the quantizer in the HDA system has to be an integer for a given integer number of quantization bits per symbol F in the digital system.
3. The number of output bits $\ell_{\boldsymbol{v}}$ of the quantizer in the digital system has to be an integer for a given integer number of quantization bits per symbol F in the HDA system.

The first requirement always has to be met. Depending on the design, one of the other two requirements may suffice, but for a maximum flexibility in the design all three requirements should hold.

In any case, a larger M can be chosen to meet further requirements, as, e.g., long block lengths for Turbo coding, as long as M is an integer multiple of the minimum M found here.

C.2 Integer Number of Channel Uses N

The number of channel uses is defined as follows (2.3):

$$N = M \cdot \frac{1}{r}. \tag{C.5}$$

To obtain an integer N, the denominator of the reduced fraction $\frac{1}{r}$ has to be a divider of M. Thus:

$$\frac{a_1}{b_1} = \frac{1}{r} \tag{C.6}$$

with integers a_1 and b_1. The greatest common divisor is $\gcd(a_1, b_1) = 1$. Then

$$b_1 \mid M, \tag{C.7}$$

i.e., b_1 is a divider of M.

C.3 Integer Total Number of Quantization Bits in HDA System for Integer F

The channel coding and modulation rate in the purely digital system is (6.28):

$$r^{\mathrm{ccm}} = F \cdot r. \tag{C.8}$$

The number of quantized bits in the purely digital system $\ell_{\boldsymbol{v}}$ is an integer anyways, since M and F are integer values.

For $\Delta r = r^{\mathrm{ccm}} - r^{\mathrm{ccm}} = 0$ the number of quantized bits in the HDA system is:

$$\begin{aligned}\ell_{\boldsymbol{v}} &= M \cdot F \\ &= M \cdot (F - \Delta F) \\ &= M \cdot \left(F - \frac{F \cdot r}{r^{\mathrm{mapp}}}\right) \\ &= M \cdot F \cdot \left(1 - \frac{r}{r^{\mathrm{mapp}}}\right). \end{aligned} \tag{C.9}$$

Thus, to obtain an integer $\ell_{\boldsymbol{v}}$, the denominator of the reduced fraction $\frac{r}{r^{\mathrm{mapp}}}$ has to be a divider of M. Therefore:

$$\frac{a_2}{b_2} = \frac{r}{r^{\mathrm{mapp}}} \tag{C.10}$$

with integers a_2 and b_2. The greatest common divisor is $\gcd(a_2, b_1) = 2$. Then

$$b_2 \mid M, \tag{C.11}$$

i.e., b_2 is a divider of M.

C.4 Integer Total Number of Quantization Bits in Digital System for Integer F

The channel coding and modulation rate in the purely digital system is (6.29):

$$\begin{aligned} r^{\mathrm{ccm}} &= \frac{M \cdot F}{N - A} \\ &= \frac{F}{\frac{N}{M} - \frac{A}{M}} \\ &= \frac{F}{\frac{1}{r} - \frac{1}{r^{\mathrm{mapp}}}}. \end{aligned} \tag{C.12}$$

The number of quantized bits in the HDA system $\ell_{\boldsymbol{v}}$ is an integer anyways, since M and F are integer values.

For $\Delta r = r^{\mathrm{ccm}} - r^{\mathrm{ccm}} = 0$ the number of quantized bits in the purely digital

system is:

$$\begin{aligned}
\ell_{\boldsymbol{v}} &= M \cdot F \\
&= M \cdot (F + \Delta F) \\
&= M \cdot \left(F + \frac{r^{\mathrm{ccm}}}{r^{\mathrm{mapp}}} \right) \\
&= M \cdot F \cdot \left(1 + \frac{1}{r^{\mathrm{mapp}} \cdot \left(\frac{1}{r} - \frac{1}{r^{\mathrm{mapp}}} \right)} \right) \\
&= M \cdot F \cdot \left(1 + \frac{1}{\frac{r^{\mathrm{mapp}}}{r} - 1} \right) \\
&= M \cdot F \cdot \left(1 + \frac{r}{r^{\mathrm{mapp}} - r} \right) \\
&= M \cdot F \cdot \frac{r^{\mathrm{mapp}}}{r^{\mathrm{mapp}} - r}.
\end{aligned} \tag{C.13}$$

Thus, to obtain an integer $\ell_{\boldsymbol{v}}$, the denominator of the reduced fraction $\frac{r^{\mathrm{mapp}}}{r^{\mathrm{mapp}}-r}$ has to be a divider of M. Therefore:

$$\frac{a_3}{b_3} = \frac{r^{\mathrm{mapp}}}{r^{\mathrm{mapp}} - r} \tag{C.14}$$

with integers a_3 and b_3. The greatest common divisor is $\gcd(a_3, b_1) = 3$. Then

$$b_3 \mid M, \tag{C.15}$$

i.e., b_3 is a divider of M.

C.5 Example

For different r, the requirements can be found in Table C.1 with lcm denoting the least common multiple. Thus, for the simulations in Figures 6.11a and 6.11b with a rate of $r = 1/7$ and integer number of bits in both, the digital and the HDA system, M has to be an integer multiple of 42.

					M is multiple of the lcm of		
r	r^{mapp}	b_1	b_2	b_3	b_1 & b_2	b_1 & b_3	b_1 & b_2 & b_3
1/2	1	2	2	1	2	2	2
1/3	1	3	3	2	3	6	6
1/4	1	4	4	3	4	12	12
1/5	1	5	5	4	5	20	20
1/6	1	6	6	5	6	30	30
1/7	1	7	7	6	7	42	42
1/8	1	8	8	7	8	56	56
1/9	1	9	9	8	9	72	72
1/10	1	10	10	9	10	90	90
1/11	1	11	11	10	11	110	110
1/12	1	12	12	11	12	132	132
1/13	1	13	13	12	13	156	156
1/14	1	14	14	13	14	182	182
1/15	1	15	15	14	15	210	210
1/16	1	16	16	15	16	240	240
1/17	1	17	17	16	17	272	272
1/18	1	18	18	17	18	306	306
1/19	1	19	19	18	19	342	342
1/20	1	20	20	19	20	380	380
2/3	1	2	3	1	6	2	6
1/3	1/2	3	3	1	3	3	3
1/4	1/2	4	2	1	4	4	4
1/5	1/2	5	5	3	5	15	15
1/6	1/2	6	3	2	6	6	6
1/7	1/2	7	7	5	7	35	35
1/8	1/2	8	4	3	8	24	24
1/9	1/2	9	9	7	9	63	63
1/10	1/2	10	5	4	10	20	20

Table C.1: Choosing M for different rates r and different requirements.

Appendix D

Properties of Selected Probability Density Functions

In Chapter 4, some properties of the different employed *probability density functions* (pdfs) are needed. They are listed here for convenience.

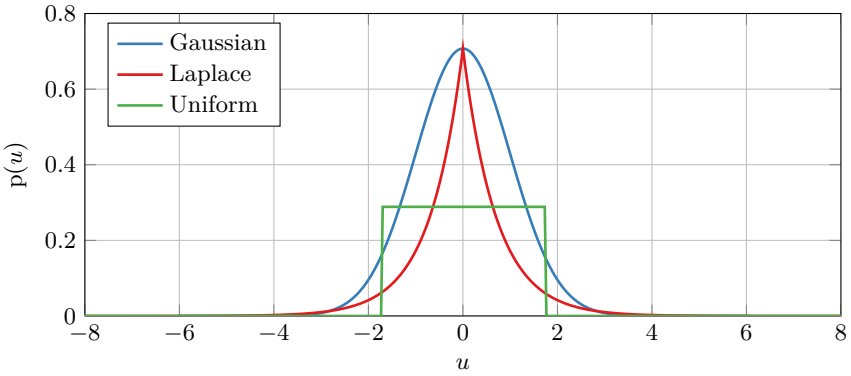

Figure D.1: Different source pdfs with $\mathrm{E}\{u^2\} = 1$.

Figure D.1 shows the pdf for uniform, Gaussian and Laplacian source symbols with a variance of $\mathrm{E}\{u^2\} = 1$. The following table shows the definitions of the pdfs:

Uniform distribution:	$\mathrm{p}(u) = \begin{cases} \frac{1}{2a} & \text{for } -a < u < a \\ 0 & \text{else} \end{cases}$	with $a = \sqrt{3\sigma^2}$,
Gaussian distribution:	$\mathrm{p}(u) = \frac{1}{\sqrt{2\pi\sigma^2}} \mathrm{e}^{-\frac{u^2}{2\sigma^2}}$,	
Laplacian distribution:	$\mathrm{p}(u) = \frac{1}{2\lambda} \mathrm{e}^{-\frac{\lvert u \rvert}{\lambda}}$	with $\lambda = \sqrt{\frac{\sigma^2}{2}}$.

List of Abbreviations

AMBC	*Analog Modulo Block Code*
AMR	*Adaptive Multi Rate*
ASI	*Analog Side Information*
ASK	*Amplitude Shift Keying*
AWGN	*Additive White Gaussian Noise*
BIAWGN	*Binary-Input Additive White Gaussian Noise*
BPSK	*Binary Phase Shift Keying*
BSC	*Binary Symmetric Channel*
DCT	*Discrete Cosine Transform*
DCTN	*Normalized Discrete Cosine Transform*
DML	*Discrete Maximum Likelihood*
EXIT	*Extrinsic Information Transfer*
GSV	*Guo-Shamai-Verdú*
HDA	*Hybrid Digital-Analog*
i.i.d.	*independent identically distributed*
ISCD	*Iterative Source-Channel Decoding*
KLD	*Kullback-Leibler distance*
KLT	*Karhunen-Loève Transform*
LABC	*Linear Analog Block Code*
LBG	*Linde, Buzo and Gray*
LMMSE	*Linear Minimum Mean-Square Error*
LMQ	*Lloyd-Max Quantizer*
LS	*Least Squares*

MAP	*Maximum a Posteriori*
ML	*Maximum Likelihood*
MMSE	*Minimum Mean-Square Error*
MSE	*Mean-Square Error*
OPTA	*Optimum Performance Theoretically Attainable*
pdf	*probability density function*
QPSK	*Quadrature Phase Shift Keying*
SDSD	*Soft Decision Source Decoder*
SNR	*Signal to Noise Ratio*
SPB	*Sphere Packing Bound*
SVD	*Singular Value Decomposition*
ZF	*Zero-Forcing*
ZFLR	*Zero-Forcing with Lattice Reduction*

List of Symbols

The following list enumerates the most important symbols in this thesis. First the format, additional indices and labeling which specifies the variables more precisely is listed. Then special matrices, common variables and at the end signal to noise ratios are listed.

x	scalar symbol
$\boldsymbol{x}$	vector of with elements
$\hat{x}$	estimated symbol
$\hat{\boldsymbol{x}}$	estimated vector
$\mathcal{X}$	random variable
$\boldsymbol{\mathcal{X}}$	random vector
$\boldsymbol{X}$	matrix
x	variable in purely digital system
x	variable in Hybrid Digital-Analog system
x^{d}	variable in digital branch of Hybrid Digital-Analog system
x^{a}	variable in analog branch of Hybrid Digital-Analog system
$\ell_{\boldsymbol{x}}$	length of the vector $\boldsymbol{x}$
x_{rot}	rotated variable in AMBC system
x_{dis}	discrete part of variable in AMBC system
x_{an}	analog part of variable in AMBC system
$\boldsymbol{X}_{\mathrm{dis}}$	discrete part of matrix in AMBC system
$\boldsymbol{X}_{\mathrm{an}}$	analog part of matrix in AMBC system
$\mathbb{O}$	zero matrix
$\mathbf{0}$	zero vector
$\mathbb{1}$	unity matrix
$\boldsymbol{A}$	coding matrix in AMBCs
$\tilde{\boldsymbol{A}}$	non-identity part of coding matrix in AMBCs
$\boldsymbol{B}$	base matrix of lattice in discrete part of AMBC
$\boldsymbol{B}_{\mathrm{red}}$	reduced base matrix of lattice in discrete part of AMBC
$\boldsymbol{C}$	covariance matrix in the context of linear analog block codes
$\boldsymbol{G}$	rotation matrix in AMBCs
$\boldsymbol{P}$	encoding matrix for linear analog block codes

$\boldsymbol{P}$	upper triangle matrix in AMBCs
$\tilde{\boldsymbol{P}}$	non-zero part of upper triangle matrix in AMBCs
$\boldsymbol{Q}$	decoding matrix for linear analog block codes
$\boldsymbol{Q}$	Q-matrix of QR decomposition
$\boldsymbol{R}$	R-matrix of QR decomposition
$\boldsymbol{\Sigma}$	sigma-matrix of singular value decomposition
$\tilde{\boldsymbol{\Sigma}}$	non-zero part of sigma-matrix of singular value decomposition
$\boldsymbol{T}$	transform matrix for block transform coding
$\boldsymbol{T}$	unimodular matrix to reduced base matrix of lattice in discrete part of AMBC
$\boldsymbol{U}$	U-matrix of singular value decomposition
$\boldsymbol{V}$	V-matrix of singular value decomposition
A	dimension of analog part of channel vector
α	factor for power distribution between analog and digital branch in HDA system
BM	bitmapper function
c	parameter of amplitude/phase Archimedes spiral
D	dimension of digital part of channel vector
$\mathfrak{D}$	mean-square error distortion in the context of rate-distortion theory
d	parameter of equidistant Archimedes spiral
Δ_{ideal}	gap in channel quality between system with negligible bit error probability and capacity achieving system
e	Euler's number
F	number of quantization bits per source symbol
F	number of quantization bits per source symbol in purely digital system
F	number of quantization bits per source symbol in HDA system
ΔF	difference between number of quantization bits per symbol of digital and HDA system
g	compressor function and analog mapper in analog branch of HDA system
$\tilde{\text{g}}$	compressor function and analog mapper without normalization
h	expander function and analog demapper in analog branch of HDA system
L	dimension of block transform coder
M	dimension of source vector
m	parameter for symmetric modulo operation parameter for AMBCs
N	dimension of channel vector
n	noise symbol

P	probability density function of discrete valued variable
p	probability density function of continuous-amplitude variable
P_e	bit error rate
π	interleaver function
Q	quantizer function
$\mathfrak{R}$	information rate in the context of rate-distortion theory
r	overall rate of transmission system
r^{ccm}	rate of channel coding and modulation
r^{ccm}	rate of channel coding and modulation in purely digital system
r^{ccm}	rate of channel coding and modulation in digital branch of HDA system
Δr	rate difference of channel coding and modulation in purely digital system and HDA system
r^{mapp}	rate of the analog mapper in HDA system
r^{src}	rate of source encoder
ρ	correlation factor of correlated source symbols
s	symbol of real life, e.g., correlated, source symbols
$\boldsymbol{s}$	jump vector in AMBCs
$\tilde{\boldsymbol{s}}$	non-zero part of jump vector in AMBCs
σ	standard deviation
u	parameter source symbol
u^{a}	quantization error in HDA system
u^{d}	quantized parameter source symbol in HDA system
v	quantization bits
v	quantization bits in digital system
v	quantization bits in HDA system
y	channel symbol
y	channel symbol in digital system
y	channel symbol in HDA system
y^{a}	channel symbol of analog branch in HDA system
$y^{\mathrm{a'}}$	channel symbol in analog branch after power distribution
y^{d}	channel symbol of digital branch in HDA system
$y^{\mathrm{d'}}$	channel symbol in digital branch after power distribution
$\dot{y}$	channel symbol before modulo operation in AMBCs
z	received symbol
z	received symbol in digital system
z	received symbol in HDA system
z^{a}	received symbol of analog branch in HDA system
$z^{\mathrm{a'}}$	received symbol in analog branch before power dedistribution
z^{d}	received symbol of digital branch in HDA system
$z^{\mathrm{d'}}$	received symbol in digital branch before power dedistribution

cSNR	channel signal to noise ratio
$\mathrm{cSNR}^{\mathrm{a}}$	channel signal to noise ratio in analog branch
$\mathrm{cSNR}^{\mathrm{d}}$	channel signal to noise ratio in digital branch
$\mathrm{cSNR}_{\mathrm{ideal},P_e=0}$	minimum channel quality at which error-free transmission for capacity achieving code is possible
$\mathrm{cSNR}_{D}^{\mathrm{sat.}}$	minimum channel quality at which transmission with negligible bit error probability is possible in purely digital system
$\mathrm{cSNR}_{H}^{\mathrm{sat.}}$	minimum channel quality at which transmission with negligible bit error probability is possible in HDA system
pSNR	parameter signal to noise ratio - parameters generated in source encoder
$\mathrm{bSNR}^{\mathrm{a}}$	parameter signal to noise ratio of symbols in analog branch
$\mathrm{bSNR}^{\mathrm{d}}$	parameter signal to noise ratio of symbols in digital branch
$\mathrm{pSNR}_{\mathrm{D}}^{\mathrm{sat.}}$	parameter signal to noise ratio at which purely digital system saturates
$\mathrm{pSNR}_{\mathrm{H}}^{\mathrm{sat.}}$	parameter signal to noise ratio at which digital branch in HDA system saturates
sSNR	symbol signal to noise ratio - for real life source symbols

Bibliography

[3GP11] 3GPP TS 36.212. "Evolved Terrestrial Radio Access (E-UTRA); Multiplexing and Channel Coding". 3GPP Technical Specification Group Radio Access Network, April 2011.

[Adr03] M. Adrat. *Iterative Source-Channel Decoding for Digital Mobile Communications*. Phd thesis, Institute of Communication Systems and Data Processing (IND), RWTH Aachen University, July 2003.

[Aky11] E. Akyol. *Complexity and Delay Constrained Compression and Transmission of Information*. PhD thesis, University of California, 2011.

[Ari72] S. Arimoto. "An Algorithm for Computing the Capacity of Arbitrary Discrete Memoryless Channels". *IEEE Transactions on Information Theory*, vol. 18, no. 1, pp. 14–20, January 1972.

[ARR10] E. Akyol, K. Rose, and T. Ramstad. "Optimal Mappings for Joint Source Channel Coding". *2010 IEEE Information Theory Workshop (ITW)*, pp. 1–5, 2010.

[AVRR13] E. Akyol, K. Viswanatha, K. Rose, and T. A. Ramstad. "On Zero Delay Source-Channel Coding". *CoRR*, vol. abs/1302.3660, 2013.

[BGT93] C. Berrou, A. Glavieux, and P. Thitimajshima. "near shannon limit error-correcting coding and decoding: Turbo-codes. 1". *Communications, 1993. ICC 93. Geneva. Technical Program, Conference Record, IEEE International Conference on*, vol. 2, pp. 1064 –1070 vol.2, May 1993.

[Bla72] R. Blahut. "Computation of channel capacity and rate-distortion functions". *IEEE Transactions on Information Theory*, vol. 18, no. 4, pp. 460–473, July 1972.

[BSGF13] G. Brante, R. Souza, and J. Garcia-Frias. "Spatial Diversity Using Analog Joint Source Channel Coding in Wireless Channels". *IEEE Transactions on Communications*, vol. 61, no. 1, pp. 301–311, 2013.

[BT67] T. Berger and D. Tufts. “Optimum Pulse Amplitude Modulation - I: Transmitter-Receiver Design and Bounds from Information Theory”. *IEEE Transactions on Information Theory*, vol. 13, no. 2, pp. 196–208, April 1967.

[Bun12] J. Bunte. “Iterative Source Channel Decoding (ISCD) for Hybrid Digital Analog (HDA) Codes”. Diplomarbeit, Institute of Communication Systems and Data Processing (IND), RWTH Aachen University, December 2012.

[BV04] S. Boyd and L. Vandenberghe. *Convex Optimization*. Cambridge University Press, 2004.

[CFRU01] S.-Y. Chung, G. Forney, T. Richardson, and R. Urbanke. “On the Design of Low-Density Parity-Check Codes Within 0.0045 dB of the Shannon Limit”. *IEEE Communications Letters*, vol. 5, no. 2, pp. 58–60, February 2001.

[Cle06] T. Clevorn. *Turbo DeCodulation: Iterative Joint Source-Channel Decoding and Demodulation*. Phd thesis, Institute of Communication Systems and Data Processing (IND), RWTH Aachen University, Templergraben 55, 52056 Aachen, November 2006.

[CT06] T. Cover and J. Thomas. *Elements of Information Theory*. Wiley-Interscience New York, 2006.

[CTC13] A. Campello, C. Torezzan, and S. Costa. “Curves on Flat Tori and Analog Source-Channel Codes”. *IEEE Transactions on Information Theory*, vol. 59, no. 10, pp. 6646–6654, 2013.

[CW98] B. Chen and G. Wornell. “Analog Error-Correcting Codes Based on Chaotic Dynamical Systems”. *IEEE Transactions on Communications*, vol. 46, no. 7, pp. 881–890, July 1998.

[DDP98] S. Dolinar, D. Divsalar, and F. Pollara. “Code Performance as a Function of Block Size”. *Telecommunications and Mission Operations Progress Report*, vol. 133, pp. 1–23, 1998.

[DRM12] M. Dörpinghaus, M. Rüngeler, and R. Mathar. “Upper-Bounding Rate Distortion Functions based on the Minimum Mean-Square Error”. *International Zurich Seminar on Communications*. IEEE, February 2012.

[ERHV10a] T. Esch, M. Rüngeler, F. Heese, and P. Vary. “A Modified Minimum Statistics Algorithm for Reducing Time Varying Harmonic Noise”. *ITG-Fachtagung Sprachkommunikation*, Bochum, Germany, October 2010. VDE Verlag GmbH.

[ERHV10b] T. Esch, M. Rüngeler, F. Heese, and P. Vary. "Combined Reduction of Time Varying Harmonic and Stationary Noise Using Frequency Warping". *2010 Conference Record of the Forty-Fourth Asilomar Conference on Signals, Systems and Computers*, pp. 533–537. IEEE, November 2010.

[ERHV12] T. Esch, M. Rüngeler, F. Heese, and P. Vary. "Estimation of Rapidly Time-Varying Harmonic Noise for Speech Enhancement". *IEEE Signal Processing Letters*, vol. 19, no. 10, pp. 659 –662, October 2012.

[ETS98] ETSI Rec. GSM 06.90. "Digital Cellular Telecommunication System; Adaptive Multi-Rate (AMR) Speech Transcoding", 1998.

[FR06] P. Floor and T. Ramstad. "Noise Analysis for Dimension Expanding Mappings in Source-Channel Coding". *IEEE 7th Workshop on Signal Processing Advances in Wireless Communications, 2006. SPAWC 2006.*, pp. 1–5, July 2006.

[FR07] P. Floor and T. Ramstad. "Optimality of Dimension Expanding Shannon-Kotel'nikov Mappings". *IEEE Information Theory Workshop, 2007. ITW '07.*, pp. 289–294, September 2007.

[FRW07] P. Floor, T. Ramstad, and N. Wernersson. "Power Constrained Channel Optimized Vector Quantizers used for Bandwidth Expansion". *4th International Symposium on Wireless Communication Systems, 2007. ISWCS 2007.*, pp. 667–671, October 2007.

[FVACGF13] O. Fresnedo, F. Vazquez-Araujo, L. Castedo, and J. Garcia-Frias. "Low-Complexity Near-Optimal Decoding for Analog Joint Source Channel Coding Using Space-Filling Curves". *IEEE Communications Letters*, vol. 17, no. 4, pp. 745–748, 2013.

[Gal68] R. Gallager. *Information Theory and Reliable Communication*. John Wiley & Sons, Inc. New York, NY, USA, 1968.

[Gas02] M. Gastpar. *To Code, or not to Code*. PhD thesis, École Polytechnique Fédérale de Lausanne, Lausanne, Switzerland, December 2002.

[GSV04] D. Guo, S. Shamai, and S. Verdú. "Mutual Information and MMSE in Gaussian Channels". *IEEE International Symposium on Information Theory, 2004. ISIT 2004. Proceedings.*, pp. 349–349, 2004.

[GSV05] D. Guo, S. Shamai, and S. Verdú. "Mutual Information and Minimum Mean-Square Error in Gaussian Channels". *IEEE Transactions on Information Theory*, vol. 51, no. 4, pp. 1261–1282, April 2005.

[GVL96] G. Golub and C. Van Loan. *Matrix Computations*, vol. 3. Johns Hopkins Univ Pr, 1996.

[HGFL11] Y. Hu, J. Garcia-Frias, and M. Lamarca. "Analog Joint Source-Channel Coding Using Non-Linear Curves and MMSE Decoding". *IEEE Transactions on Communications*, vol. PP, no. 99, pp. 1 –11, 2011.

[HV06] C. Hoelper and P. Vary. "Bandwidth Efficient Mixed Pseudo Analogue - Digital Speech Transmission". *Proceedings of European Signal Processing Conference (EUSIPCO)*. EURASIP, September 2006.

[HV07] C. Hoelper and P. Vary. "A New Modulation Concept for Mixed Pseudo Analogue-Digital Speech and Audio Transmission". *Proceedings of IEEE International Conference on Acoustics, Speech, and Signal Processing (ICASSP)*, Honolulu, Hawai'i, USA, April 2007.

[ILZF08] A. Ingber, I. Leibowitz, R. Zamir, and M. Feder. "Distortion Lower Bounds for Finite Dimensional Joint Source-Channel Coding". *IEEE International Symposium on Information Theory, 2008. ISIT 2008.*, pp. 1183 –1187, Toronto, July 2008.

[JN84] N. Jayant and P. Noll. "Digital Coding of Waveforms: Principles and Applications to Speech and Video". *Englewood Cliffs, New Jersey*, 1984.

[Kay93] S. M. Kay. *Fundamentals of Statistical Signal Processing: Estimation Theory*. Prentice-Hall Signal Processing Series, 1993.

[KR09] M. Kleiner and B. Rimoldi. "Asymptotically Optimal Joint Source-Channel Coding with Minimal Delay". *Global Telecommunications Conference, 2009. GLOBECOM 2009. IEEE*, pp. 1 –5, November 2009.

[Krü10] H. Krüger. *Low Delay Audio Coding Based on Logarithmic Spherical Vector Quantization*. Phd thesis, Institute of Communication Systems and Data Processing (IND), RWTH Aachen University, Templergraben 55, 52056 Aachen, March 2010.

[LG89] T. Lookabaugh and R. Gray. "High-Resolution Quantization Theory and the Vector Quantizer Advantage". *IEEE Transactions on Information Theory*, vol. 35, no. 5, pp. 1020–1033, September 1989.

[LLL82] A. K. Lenstra, H. W. Lenstra, and L. Lovász. "Factoring Polynomials with Rational Coefficients". *Mathematische Annalen*, vol. 261, no. 4, pp. 515–534, 1982.

[Lüd10] H. Lüders. *Current and Evolved Physical Layer Concepts: Potentials and Limitations of Mobile Broadband Wireless Access*. Phd thesis, Institute of Communication Systems and Data Processing (IND), RWTH Aachen University, October 2010.

[MAR13] M. S. Mehmetoglu, E. Akyol, and K. Rose. "A Deterministic Annealing Approach to Optimization of Zero-delay Source-Channel Codes". *CoRR*, vol. abs/1304.6969, 2013.

[Moo05] T. Moon. *Error Correction Coding: Mathematical Methods and Algorithms*. Wiley-Blackwell, 2005.

[NI03] P. R. Norvig and S. A. Intelligence. *Artificial Intelligence: A Modern Approach (2nd ed.)*. Prentice Hall, 2003.

[OL07] J. Ohm and H. Lüke. *Signalübertragung: Grundlagen der digitalen und analogen Nachrichtenübertragungssysteme*. Springer, 2007.

[PPV10] Y. Polyanskiy, H. Poor, and S. Verdú. "Channel Coding Rate in the Finite Blocklength Regime". *IEEE Transactions on Information Theory*, vol. 56, no. 5, pp. 2307 –2359, May 2010.

[Pro95] J. Proakis. *Digital Communications*. McGraw-Hill, 1995.

[RBV14] M. Püngeler, J. Bunte, and P. Vary. "Design and Evaluation of Hybrid Digital-Analog Transmission Outperforming Purely Digital Concepts". *Communications, IEEE Transactions on*, vol. 62, no. 11, pp. 3983–3996, Nov 2014.

[Rez03] Z. Reznic. *Broadcasting Analog Sources over Gaussian Channels*. PhD thesis, Tel-Aviv Univ., Tel-Aviv, Israel, August 2003.

[RKBV13] M. Püngeler, H. Krüger, G. Behler, and P. Vary. "HD-Voice-3D: Herausforderungen und Lösungen bei der Audiosignalverarbeitung". *Workshop Audiosignal- und Sprachverarbeitung (WASP)*, pp. 2972–2986. Köllen Druck + Verlag GmbH, 2013.

[RSV09] M. Püngeler, B. Schotsch, and P. Vary. "Properties and Performance Bounds of Linear Analog Block Codes". *2009 Conference Record of the Forty-Third Asilomar Conference on Signals, Systems and Computers*, pp. 962 –966, November 2009.

[RSV10a] M. Püngeler, B. Schotsch, and P. Vary. "Improved Decoding of Shannon-Kotel'nikov Mappings". *IEEE 2010 International Symposium on Information Theory and its Applications (ISITA)*, pp. 633–638, Taichung, Taiwan, 2010. Society of Information Theory and its Applications (SITA).

[RSV10b] M. Rüngeler, B. Schotsch, and P. Vary. "Semi-Analytical Solution for Rate Distortion Function and OPTA for Sources with Arbitrary Distribution". *8th International ITG Conference on Source and Channel Coding*, January 2010.

[RV13a] M. Rüngeler and P. Vary. "Surpassing Purely Digital Transmission: A Simplified Design of Hybrid Digital Analog Codes". *9th International ITG Conference on Systems, Communications and Coding 2013 (SCC'2013)*, Munich, Germany, January 2013.

[RV13b] M. Rüngeler and P. Vary. "Hybrid Digital Analog Transform Coding". *2013 IEEE International Conference on Acoustics, Speech and Signal Processing (ICASSP)*, pp. 5109–5113, Vancouver, May 2013. IEEE.

[RV15] M. Rüngeler and P. Vary. "Hybrid Digital–Analog transmission for wireless acoustic sensor networks". *Signal Processing*, vol. 107, no. 0, pp. 164 – 170, 2015. Special Issue on ad hoc microphone arrays and wireless acoustic sensor networks Special Issue on Fractional Signal Processing and Applications.

[Rü09] M. Rüngeler. "Digital-analoge Quellen- und Kanalcodierung". Diplomarbeit, Institute of Communication Systems and Data Processing (IND), RWTH Aachen University, Templergraben 55, 52056 Aachen, March 2009.

[SACV11] L. Schmalen, M. Adrat, T. Clevorn, and P. Vary. "EXIT Chart Based System Design for Iterative Source-Channel Decoding with Fixed-Length Codes". *IEEE Transactions on Communications*, vol. 59, no. 9, pp. 2406–2413, September 2011.

[Sak70] D. Sakrison. *Notes on Analog Communication.* Van Nostrand Reinhold, 1970.

[Sch11] L. Schmalen. *Iterative Source-Channel Decoding: Design and Optimization for Heterogeneous Networks.* Phd thesis, Institute of Communication Systems and Data Processing (IND), RWTH Aachen University, July 2011.

[Sch13] T. Schmitz. "Analyse und Entwurf von Modulo-Codes". Masterarbeit, Institute of Communication Systems and Data Processing (IND), RWTH Aachen University, September 2013.

[Sha48] C. Shannon. "A Mathematical Theory of Communication". *Bell System Technical Journal*, vol. 27, pp. 623–656, 1948.

[Sha59a] C. Shannon. "Coding Theorems for a Discrete Source with a Fidelity Criterion". *IRE Nat. Conv. Rec*, vol. 7, no. 4, pp. 142–163, 1959.

[Sha59b] C. Shannon. “Probability of Error for Optimal Codes in a Gaussian Channel”. *Bell System Technical Journal*, vol. 38, no. 3, pp. 611–656, May 1959.

[SPA02] M. Skoglund, N. Phamdo, and F. Alajaji. “Design and Performance of VQ-based Hybrid Digital-Analog Joint Source-Channel Codes”. *IEEE Transactions on Information Theory*, vol. 48, no. 3, pp. 708–720, March 2002.

[SRV15] T. Schmitz, M. Rüngeler, and P. Vary. “Analysis of Analog Modulo Block Codes”. *Proceedings of International ITG Conference on Systems, Communications and Coding (SCC)*. ITG, VDE Verlag GmbH, February 2015.

[Tim70] U. Timor. “Design of Signals for Analog Communication”. *IEEE Transactions on Information Theory*, vol. 16, no. 5, pp. 581–587, September 1970.

[TK12] M. Taherzadeh and A. K. K. Khandani. “Single-Sample Robust Joint Source-Channel Coding: Achieving Asymptotically Optimum Scaling of SDR Versus SNR”. *IEEE Transactions on Information Theory*, vol. 58, no. 3, pp. 1565 –1577, March 2012.

[VC03] V. Vaishampayan and S. Costa. “Curves on a Sphere, Shift-Map Dynamics, and Error Control for Continuous Alphabet Sources”. *IEEE Transactions on Information Theory*, vol. 49, no. 7, pp. 1658–1672, July 2003.

[WSJM11] D. Wübben, D. Seethaler, J. Jaldén, and G. Matz. “Lattice Reduction: A Survey with Applications in Wireless Communications”. *IEEE Signal Processing Magazine*, vol. 28, no. 3, pp. 70–91, May 2011.

[WSR09] N. Wernersson, M. Skoglund, and T. Ramstad. “Polynomial Based Analog Source-Channel Codes”. *IEEE Transactions on Communications*, vol. 57, no. 9, pp. 2600–2606, September 2009.